ELECTROOSMOTIC FLOW STRUCTURE IN MICROCHANNEL WITH NONUNIFORM WALL ZETA-POTENTIAL MEASURED BY FLUORESCENCE IMAGING TECHNIQUE

by

Yutaka Kazoe

School of Integrated Design Engineering
Graduate School of Science and Technology
Keio University

September 2008

Abstract

Microscale liquid flows under electric field, i.e., electroosmotic flows, have been widely used in the microscale flow systems: capillary electrophoresis system, and microfluidic devices such as micro total analysis systems and lab-on-a-chip. Electroosmotic flows are easily controlled by switching the electric field through electrode arrays, and useful for the miniaturization of systems by recent microfabrication techniques. However, the absence of two-dimensional measurement techniques for key parameters of electroosmotic flow, i.e., the time dependent flow velocity and the wall zeta-potential, has prevented experimental approaches to the flow with nonuniform wall zeta-potential by the material heterogeneity in a channel and the ion and thermal transport with mixing and chemical reaction. The present study developed a velocity measurement technique and a nanoscale laser induced fluorescence imaging for the zeta-potential measurement, and investigated electroosmotic flow with nonuniform wall zeta-potential. The momentum transport in the flow field and the effect of the ion motion on the zeta-potential distribution were evaluated.

A time-resolved velocity measurement technique for transient electroosmotic flow was developed using fluorescent submicron particles and a high speed CMOS camera. Particle tracking velocimetry with low particle number density was employed in the present technique. The high spatial resolution was achieved by an iterative measurement method based on the reproducibility of low Reynolds number flows. The combined measurement of near-wall and bulk velocities were realized by a measurement system using the evanescent wave and the volume illumination.

A novel measurement technique for nonuniform wall zeta-potential, termed nanoscale laser induced fluorescence imaging, was developed using fluorescent dye and the evanescent wave generated near the wall about 100 nm. The fluorescent dye, which ionizes in the electrolyte solution, was selected for the measurements. Since the fluorescence ions are distributed depending on the wall zeta-potential, the fluorescent intensity excited by the evanescent wave is related to the wall zeta-potential. An evanescent wave illumination system using two prisms was developed to achieve the large area measurement with the low magnification. The evanescent wave is generated using the microchannel substrates and prisms as an optical waveguide.

Transient electroosmotic flows in microchannels with uniform zeta-potential and nonuniform zeta-potential by material heterogeneity and the surface modification on the channel wall were examined using the developed velocity measurement technique. Electroosmotic flows with the channel scale of 10^{-4} m reached to the steady state at the time about 10^{-3} s after the electric field was applied. Electroosmotic flows have different velocity profiles by the pattern and magnitude of wall zeta-potential, but the volumetric flow rate and the averaged zeta-potential shows a proportional relationship.

Electroosmotic flow with mixing of two electrolyte solutions at different ion concentrations was investigated. The zeta-potential at the microchannel wall was measured by the nanoscale laser induced fluorescence imaging. The flow velocity was obtained using the conventional measurement technique, micron-resolution particle image velocimetry. The ion concentration in the flow field was estimated by the numerical analysis using the experimentally obtained velocity information. The measured zeta-potential distribution at the wall shows a quantitative relationship with the local ion concentration governed by the convection and diffusion with the mixing. Electroosmotic flow in the mixing flow field was induced by the zeta-potential distribution at the wall dependent on the ion motion.

The developed measurement techniques and the knowledge obtained from this work will contribute to the optimal design of the devices, the precise flow control technique using electrokinetics, and the novel applications such as mixing and separation by regulating the electric field and the zeta-potential.

Contents

List of Tables

List of Figures

Nomenclature

Roman Symbols

a	(m)	half of channel width
A	(m^2)	area
A_{cross}	(m^2)	area of cross-section
A_{total}	(m^2)	total area of wall in microchannel
b	(m)	half of channel depth
c	(mol/m^3)	concentration
c_0	(mol/m^3)	bulk concentration
c_f	(mol/m^3)	fluorescence concentration
c_{f0}	(mol/m^3)	bulk concentration of fluorescent dye
C_D	(-)	drag coefficient
d_e	(m)	effective particle diameter captured on digital imaging device
d_p	(m)	diameter of particle
d_s	(m)	diameter of the diffraction-limited point spread function
D	(m^2/s)	diffusion coefficient
D_h	(m)	hydraulic diameter
Du	(-)	Dukhin number
$\boldsymbol{D}$	(m^2/s)	diffusion coefficient tensor
e	(m)	smallest distance resolved by imaging device (pixel size)
E_x	(V/m)	electric field in the X-direction
E_y	(V/m)	electric field in the Y-direction
E_z	(V/m)	electric field in the Z-direction
$\boldsymbol{E}$	(V/m)	electric field
$\boldsymbol{f_E}$	(N/m^3)	electric body force per unit volume
f_{obj}	(m)	focal length of objective lens
F	(C/mol)	Faraday's constant
$\boldsymbol{F}$	(N)	external force

$\boldsymbol{F_D}$	(N)	viscous drag force
g	(m/s^2)	gravitational acceleration
h	(m)	distance between the wall and the nearest edge of the particle
H_c	(m)	channel height
$\boldsymbol{i}$	(A/m^2)	current density
I_0	(W/m^3)	evanescent wave intentisy at interface
I_e	(W/m^3)	excitation light intensity
I_{eva}	(W/m^3)	evanescent wave intensity
I_f	(W/m^3)	fluorescent intensity
$\boldsymbol{j}$	(mol/m^{2}s)	molar flux
k	(-)	aspect ratio of channel
k_b	(J/K)	Boltzmann constant
K	(-)	collection efficiency
Kn	(-)	Knudsen number
L	(m)	characteristic length
L_c	(m)	channel length
L_e	(m)	entrance length
m	(kg)	mass
L_s	(m)	length of sampling volume
M	(-)	total magnification of microscope
n	(-)	refractive index
n_1	(-)	refractive index of first medium
n_2	(-)	refractive index of second medium
n_g	(-)	refractive index of glass
n_m	(-)	refractive index of immersing medium between objective lens and cover glass
n_s	(-)	refractive index of solution
N	(-)	number of particle velocities
NA	(-)	numerical aperture of objective lens
p	(Pa)	pressure
Pe	(-)	Peclet number
q	(C)	particle charge
q_E	(C/m^2)	charge per unit area
Q_{2D}	(m^2/s)	two-dimensional flow rate
Q_{3D}	(m^3/s)	volumetric flow rate
r	(-)	correlation coefficient
r_p	(m)	particle radius

R	(J/mol K)	gas constant
R_{off}	(m)	off-center location of laser beam in the optical pathway of microscope
Re	(-)	Reynolds number
Re_p	(-)	particle Reynolds number
Sr	(-)	Strouhal number
t	(s)	time
t_c	(s)	time required for buffer exchange
t_g	(m)	thickness of glass plate
T	(K)	temperature
u	(m/s)	velocity in the X-direction
u_{cell}	(m/s)	particle velocity in closed cell
$\boldsymbol{u_p}$	(m/s)	particle velocity
$\boldsymbol{u}$	(m/s)	Velocity
U	(m/s)	characteristic velocity
U_0	(m/s)	initial velocity
U_{ave}	(m/s)	average velocity
v	(m/s)	velocity in the Y-direction
w	(m/s)	velocity in the Z-direction
W_c	(m)	channel width
x	(m)	Cartesian coordinate in the streamwise direction
$\boldsymbol{x}$	(m)	Spatial coordinate vector
y	(m)	Cartesian coordinate in the spanwise direction
z	(m)	Cartesian coordinate in the depthwise direction
z_v	(-)	ion valence
z_{vf}	(-)	ion valence of fluorescent dye
z_p	(m)	penetration depth of the evanescent wave

Greek Symbols

α	(°)	half-angle of the maximum collection cone of light
β	(°)	angle from the central axis of partice
χ	(-)	collection efficiency of the imaging device
δ	(m)	small distance
δ_p	(m)	penetration distance of diffusion
δz	(m)	depth of field of microscopic optical system
δz_{eva}	(m)	measurement depth in the near-wall velocity measurement

δz_m	(m)	measurement depth in the velocity measurement using tracer particle
$\mathit{\Delta} t$	(s)	time interval
$\mathit{\Delta} x$	(m)	displacement during the time interval
ϵ	(C/V m)	permittivity
ϵ_0	(C/V m)	permittivity of vacuum
ϵ_m		measurement error
ϵ_r	(-)	relative permittivity
ϕ	(-)	quantum yield
γ	(m^2/mol)	molar absorption coefficient
η	(m)	position coordinate in particle
φ	(°)	inclination angle of laser beam
λ	(m)	wavelength
λ_D	(m)	Debye length
λ_l	(m)	length of the order of molecular diameter
$\lambda_{\|}$	(-)	correction factor for the diffusion coefficient parallel to the wall
$\lambda_{\perp}$	(-)	correction factor for the diffusion coefficient perpendicular to the wall
$\mathit{\Lambda}$	(S m^2/mol)	molar conductivity
μ	(Pa s)	viscosity
μ_{eof}	(m^2/V s)	electroosmotic mobility
μ_{ep}	(m^2/V s)	electrophoretic mobility
ν	(m^2/s)	kinematic viscosity
θ	(°)	angle
θ_c	(°)	critical angle
θ_i	(°)	incident angle
θ_p	(°)	incident angle at the prism-oil interface
θ_r	(°)	refractive angle
ρ	(kg/m^3)	fluid density
ρ_E	(C/m^3)	electric charge density
ρ_p	(kg/m^3)	particle density
σ	(S/m)	electrical conductivity
σ_s	(S)	surface conductivity
τ	(s)	charasteristic time
τ	(Pa)	shear stress
τ_c	(s)	convective time scale
τ_{dl}	(s)	charasteristic time for double-layer polarization

τ_{eof}	(s)	charasteristic time for electroosmotic flow
τ_{ep}	(s)	charasteristic time for hydrodynamic relaxation
τ_p	(s)	particle relaxation time
τ_υ	(s)	viscous time scale
υ	(mol s/kg)	mobility
ψ	(V)	electrostatic potential
ψ_S	(V)	electrostatic potential at solid surface
ζ	(V)	zeta-potential

Subscripts

ave	average value
eva	excited by the evanescent wave
eof	electroosmotic flow
ep	electrophoresis
i	ith
max	maximum value
p	particle
pre	pressure-driven flow
ref	reference
vol	excited by the volume illumination
$\parallel$	parallel to the wall
$\perp$	perpendicular to the wall
$+$	positive ion
$-$	negative ion

Superscripts

$*$	dimensionless variable

Mathematical

$\langle\,\rangle$	time average value

Chapter 1

Introduction and Objectives

1.1 Introduction

Microscale fluid flows are observed in blood capillaries and microorganisms (biological field), porous media like mineral substrates (geophysical field), and industrial applications: ink-jet nozzles, capillary electrophoresis (Li, 1992; Quigley & Dovichi, 2004; Ghosal, 2006), electrical chromatography (Heftmann, 1992), and microfluidic devices such as micro total analysis systems and lab-on-a-chip (Geschke *et al.*, 2004; Vilkner *et al.*, 2004; Stone *et al.*, 2004; Dittrich & Manz, 2006). They are generally laminar flows, and interfaces between fluids (solid-liquid, liquid-liquid, gas-liquid) are stably existing since the surface tension is dominant. Especially, microscale liquid flows under electric field, i.e., electroosmotic flows, have been used as driving forces of liquids and samples in the electrochemical and biochemical applications. Since electric circuits are easily miniaturized by recent micro fabrication techniques developed in micro electro mechanical systems (MEMS), electroosmotic flows are useful for the microscale flow systems alternative to microscale pressure-driven flows, which require mechanical pumps and valves preventing miniaturization, and larger pressure loss than the macroscale flow systems (Dutta *et al.*, 2006).

Electroosmotic flows are generated by the electric body force exerted on the liquid, and typical flow velocities are up to 1 cm/s. Figure 1.1 illustrates the schematic diagram of electroosmotic flow. When the liquid is filled in the channel, surface of the channel wall is charged, and near-wall region is electrically polarized by attracted ions with opposite charge to the wall, i.e., the electric double layer with a thickness about 1 $\sim$ 10 nm (Probstein, 1994; Lyklema, 1995). Hence, the liquid is driven by the drag of ions in the electric double layer migrated under the electric field. The flow velocity is proportional to the magnitude of electric field due to the electric body force, and the flow direction is easily controlled by switching the electric field. The electric body force also depends on the magnitude of near-wall electric

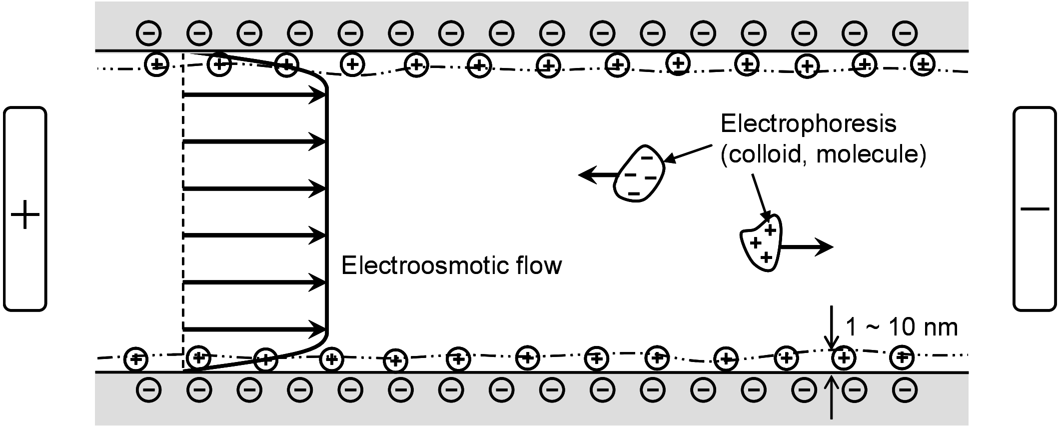

Figure 1.1. Schematic of electroosmotic flow induced by an external electric field. Particles such as colloid and molecule is driven by electrophoresis.

polarization, which is determined by the electric charge at the wall characterized by the zeta-potential (Hunter, 1981; Kirby & Hasselbrink, 2004*a*,*b*). In the channel with the scale of 10^{-4} m (microchannel), the thickness of the electric double layer is generally negligible compared with the channel scale. Only the near-wall region (inside the electric double layer) is dominated by viscous and electrostatic forces, while the bulk region is dominated by vicous and inertial forces. Thus, electroosmotic flows in the bulk region are described using the slip boundary condition with a velocity at a plane separating near-wall and bulk regions. When the wall charge characterized by the zeta-potential is uniform, the slip velocity is given by the Helmholtz-Smoluchowski equation, $u_{eof} = -\epsilon\zeta E/\mu$ where u_{eof} (m/s) is the electroosmotic velocity, ϵ (C/V m) is the liquid permittivity, ζ (V) is the wall zeta-potential, E (V/cm) is the electric field magnitude and μ (Pa s) is the liquid viscosity. In addition, if all the channel walls have a same zeta-potential, electroosmotic flow in the bulk region has uniform velocity profile, i.e., the plug flow (Probstein, 1994). On the other hand, particles such as colloids and molecules suspended in the liquid have own charges and migrate under the electric field, i.e., electrophoresis (Probstein, 1994; Lyklema, 1995). The flows involving electroosmotic flow and electrophoresis are termed electrokinetic flows.

Figure 1.2 shows applications of electroosmotic flow to the microfluidic devices and contribution of the present study. Electroosmotic flows have been used in various applications of the microfluidic devices: capillary electrophoresis microchip (Harrison *et al.*, 1992, 1993; Jacobson *et al.*, 1994; Chabinyc *et al.*, 2001), cell sorting (Li & Harrison, 1997; Sun *et al.*, 2007), cell lysis (Lee & Cho, 2007), micro-reactors (Fletcher *et al.*, 2001; Nelstrop *et al.*, 2001; Debusschere *et al.*, 2003), pumping and flow switching (Seller *et al.*, 1994; Wu *et al.*, 2007), sample stacking (Osbourn *et al.*, 2000; Jung *et al.*, 2003), mixing (Oddy & Santiago, 2001; Lin *et al.*, 2004; Leong *et al.*, 2007) and separation (Devasenathipathy *et al.*, 2003).

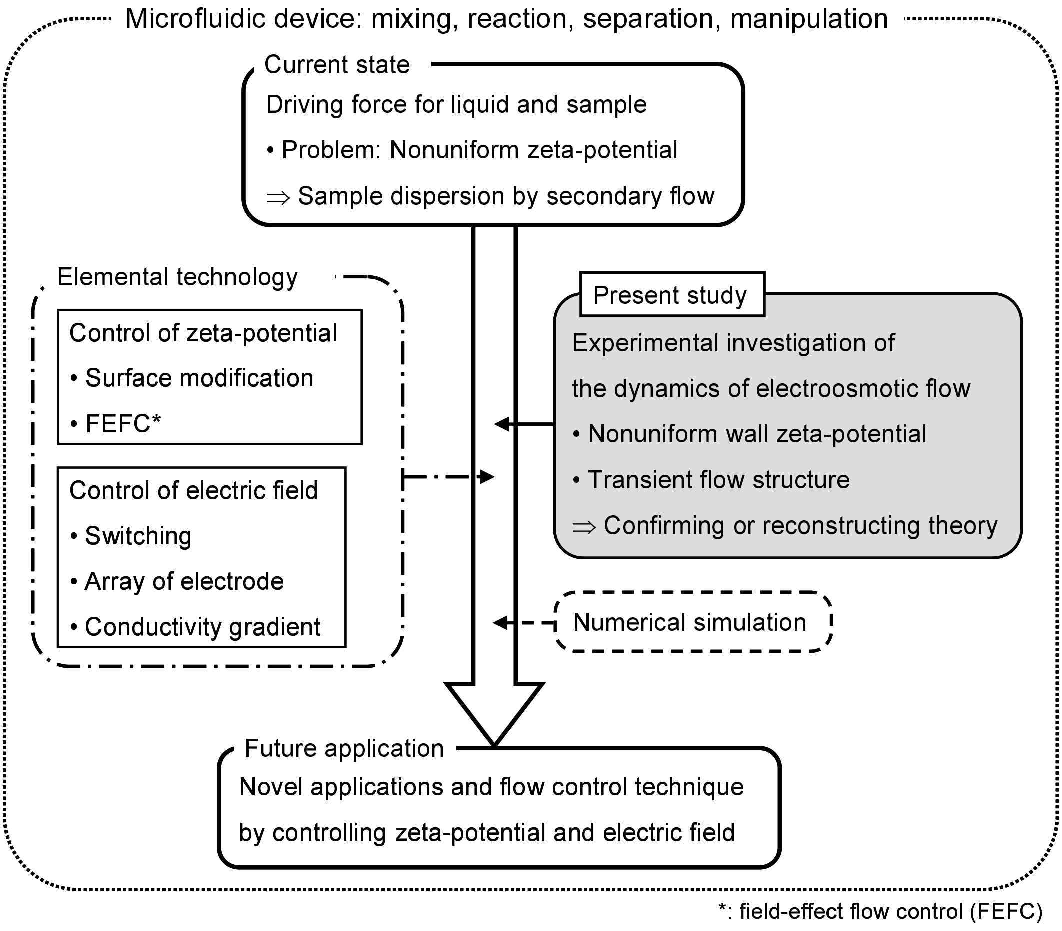

Figure 1.2. Applications of electroosmotic flow to the microfluidic devices and contribution of the present study.

Several applications using electrokinetics are achieved by temporally regulating the electric field. The flows with the plug profile effectively transport the samples without the advective dispersion compared with pressure-driven flows with the parabolic profile. Furthermore, the separation of samples by their own charges is easily achieved due to electrophoresis in electrokinetic flows. However, there is a critical problem that the wall zeta-potential is often nonuniform in the devices with practical application. Generally, the zeta-potential strongly depends on the ion concentration, pH and temperature of the liquid and the material properties (Kirby & Hasselbrink, 2004*a*,*b*). Thus, the nonuniform zeta-potential occurs in microfludic devices by the ion transport with mixing (Shinohara *et al.*, 2004, 2005) and chemical reaction (Baroud *et al.*, 2003; Ichiyanagi *et al.*, 2007), the thermal transport with mixing (Sato *et al.*, 2003*b*) and the Joule heating (Erickson *et al.*, 2003), heterogeneity of materials in the microchannel, and the surface chemical modification to the wall avoiding sample adhesion and controlling wettability (Whitesides *et al.*, 2001; Pallandre *et al.*, 2006). This heterogeneous wall zeta-potential significantly affects the flow profile and flow rate of electroosmotic flow, and unexpectedly changes the sample dispersion and quantity of products in the chemical reaction. In contrast, several works have made attempts to control the electroosmotic flow profile and the sample dispersion in the microchannel by controlling the local zeta-potential at the channel wall. A typical approach to control the wall zeta-potential is the surface modification by coating or patterning. Electroosmotic flows with opposite directions in the same channel or recirculating flow profiles have been generated by coating or patterning chemical materials on the channel wall to change the zeta-potential (Barker *et al.*, 2000; Stroock *et al.*, 2000; Stroock & Whitesides, 2003). Another approach is using a technique for the dynamic control of wall zeta-potential, i.e., field-effect flow control (FEFC) developed by Schasfoort *et al.* (1999). FEFC modifies the wall zeta-potential using a transverse electric field applied through the insulating microchannel wall. The voltage applied from an electrode embedded inside the wall increases or decreases the zeta-potential without affecting the axial electric field to generate electroosmotic flow (Buch *et al.*, 2001). Suppressing the sample dispersion in a U-shaped microchannel (Lee *et al.*, 2004), flow switching (Sniadecki *et al.*, 2004) and enhanced mixing (Wu & Liu, 2005) were achieved by spatial and temporal control of local electroosmotic flow using FEFC.

The dynamics of steady and transient electroosmotic flows at the nonuniform wall zeta-potential is fundamental for the development of microfluidic devices. Numerical simulation using the current theory has been conducted to understand the structure of electroosmotic flow with the nonuniform wall zeta-potential (Ajdari, 1995; Ren & Li, 2001; Erickson & Li, 2003; Fu *et al.*, 2003; Park *et al.*, 2007). Since the approximation using the Helmholtz-Smoluchowski equation can not be applied when the wall zeta-potential is inhomogeneous, the mass transport of charged species in the electric double layer must be considered to obtain the near-wall flow structure. However, it is difficult to estimate the mass transport in the electric double layer of $1 \sim 10$ nm thickness due to the resolution of numerical simulation in the microchannel. In addition, there is a question on the continuum assumption of fluid flow in such a nanometer order scale. Thus, experimental approaches are strongly required to confirm or reconstruct the current theory, and to realize a novel application and a flow control technique by regulating the wall zeta-potential and the electric field in the microchannel.

The present study experimentally investigates electroosmotic flow with nonuniform wall zeta-potential. Key elements for the experimental approaches are (i) time-resolved velocity measurement of transient electroosmotic flow, (ii) near-wall velocity measurement and (iii) measurement of the spatial and temporal distribution of wall zeta-potential.

1.2 Literature Survey

This section examines previous work related to the present study focusing on measurement techniques for the electroosmotic velocity and the wall zeta-potential, and experimental investigations of electroosmotic flow with nonuniform zeta-potential.

1.2.1 Velocity Measurement of Electroosmotic Flow

A method for the velocity measurement of electroosmotic flow is the current monitoring technique proposed by Huang *et al.* (1988). The electroosmotic velocity is obtained by measuring a time required for the current in the microchannel to be plateau with exchanging an electrolyte solution to another at a slightly different concentration, which is proportional to the electrical conductivity of solution. Spehar *et al.* (2003) measured the electroosmotic mobilities, $\mu_{eof} = u_{eof}/E$ (m^2/V s), in the microchannels made of fused silica, poly(dimethylsiloxane) (PDMS), and PDMS and glass (heterogeneous material) at different pH and electrolyte concentrations. Liu *et al.* (2000) conducted the measurements using the microchannels coated by polyelectrolyte multilayers and evaluated the electroosmotic mobilities at different pH. Since the obtained electroosmotic velocity or mobility is the averaged value along the microchannel, major application of this technique is evaluating the electrokinetic characteristic of the microchannel rather than investigating the electroosmotic flow structure.

Spatially-resolved velocity measurements using flow tracers such as dye and particles (Sinton, 2004) have been conducted to examine the electroosmotic flow field in the microchannel. Minor *et al.* (1997) measured the velocity of silicon iodide particles in electrokinetic flow in a closed 2 mm diameter capillary using laser Doppler velocimetry (LDV), which is a conventional technique for macroscale flow. However, it is difficult to achieve a micrometer order spatial resolution by LDV due to the size of probe volume. Tsuda *et al.* (1993) and Taylor

& Yeung (1993) performed the flow imaging using a fluorescent dye by monitoring the front of fluorescence-labeled solvent in the capillary. The interface between the labeled and non-labeled solutions was significantly blurred due to the diffusion of fluorescent molecules along the capillary, and thus this technique did not achieve the quantitative measurement of velocity profile. Taylor & Yeung (1993) also examined electrokinetic flow using fluorescent submicron particles and a CCD camera, and roughly estimated a velocity profile from captured particle streaks resulting from the motion of particles during a single exposure. However, the velocity of electroosmotic flow was not obtained because the motion of particles in electrokinetic flow is the superposition of electroosmotic and electrophoretic components.

Paul *et al.* (1998) developed a velocity measurement technique using a caged fluorescent dye, and performed the measurement in a fused-silica capillary. An ultraviolet laser pulse is irradiated to generate a fluorescence-tagging pattern into the flow by uncaging the fluorescent dye. The velocity profile is obtained from the transport and distortion of the uncaged region. The electroosmotic velocity is estimated by subtracting the electrophoretic velocity of dye from the observed velocity. Ross *et al.* (2001*b*) conducted the measurement using caged fluorescent dye in plastic microchannels. Sinton *et al.* (2002) measured the electroosmotic velocities in a capillary, which quantitatively agreed with the results obtained by the current monitoring. Sinton & Li (2003) investigated electroosmotic velocity profiles in microchannels of circular and rectangular shapes at different channel scales. Mosier *et al.* (2002) developed a photobleached-fluorescence imaging technique for microchannel flow. The photobleached region of the fluorescent dye solution in the microchannel is traced to obtain the flow velocity. These dye-based techniques, called molecular tagging velocimetry, is a strong method for the quantitative velocity measurement for electroosmotic flow. However, the measurement error is significantly increased in the flow with large velocity gradients due to the advective dispersion of dye caused by the shear rate. In addition, the depthwise resolution of the measurement is relatively low due to out-of-focus fluorescence.

Micron-resolution particle image velocimetry (micro-PIV) proposed by Santiago *et al.* (1998) is a most broadly used technique for the spatially-resolved velocity measurement in the microchannel. Microscopic images of fluorescent particles suspended in the liquid are captured by a digital imaging device, and the flow velocity is obtained by tracing patterns of particles in interrogation regions. Kim *et al.* (2002) conducted the micro-PIV measurement in electrokinetic flow in a T-junction microchannel made of PDMS, and compared the velocity profiles with those obtained by the numerical simulation. Devasenathipathy & Santiago (2002) firstly measured the electroosmotic velocity using micro-PIV by subtracting the electrophoretic velocity of particles from the observed velocities. Measurements were performed using an acrylic cross-microchannel and a microchannel composed of PDMS and glass, and the electroosmotic mobilities at material surface were obtained. Ichiyanagi *et al.* (2005) measured electroosmotic velocity in a microchannel composed of PDMS and glass, and investigated electroosmotic flow with exchange of a buffer solution to another at different pH. Sasaki & Sato (2006) evaluated the effect of surface modification to the microchannel wall on electroosmotic flow. In standard micro-PIV, the instantaneous velocities are temporally averaged to eliminate an error due to the Brownian motion of tracer particles, thus the measurement object is limited to the steady flow. On the other hand, Yan *et al.* (2006) examined transient electroosmotic flow in a submillimeter channel made of glass by using time-resolved micro-PIV. Although the measurement error due to the Brownian motion remained, the transient structure of electroosmotic flow with homogeneous zeta-potential was firstly obtained. They also examined transient electroosmotic flow in a closed channel (Yan *et al.*, 2007).

In order to investigate the near-wall structure of electroosmotic flow, Sadr *et al.* (2004) and Sadr *et al.* (2006) measured the velocity of electroosmotic flow in the vicinity of glass wall in a microchannel by nano-particle image velocimetry (nano-PIV). Nano-PIV enables the near-wall velocity measurement by using the evanescent wave generated by the total internal reflection of laser beam at the wall-solution interface (Zettner & Yoda, 2003). The evanescent wave is a light decaying exponentially from the wall with the order of 100 nm, and illuminates the tracer particles only in the vicinity of the wall. The near-wall electroosmotic mobilities were obtained from the measurement results, but the spatial resolution and the measurement accuracy are lower than micro-PIV due to escape of tracer particles from very thin illumination area by the Brownian motion.

For a turbid media where the spatially-resolved velocity measurement techniques based on the fluorescence imaging can not be applied, Wang *et al.* (2004*a*,*b*) developed phase-resolved optical Doppler tomography and conducted velocity measurements of electroosmotic flow in a microchannel. The cross-sectional velocity profile was obtained by collecting the backscattered light from tracer particles at different depths through an objective lens.

1.2.2 Measurement of Wall Zeta-Potential

Measurement techniques for the zeta-potential at a solid-liquid interface has been mainly based on electrophoresis of particles suspended in the liquid in a closed cell (Probstein, 1994; Hunter, 1981; Minor *et al.*, 1997; Mori & Okamoto, 1980). A method for the zeta-potential measurement using a sound wave induced by oscillating motion of particles due to electrophoresis in AC electric field was also proposed (Carasso *et al.*, 1995; Walldal, 2001). Oddy & Santiago (2004) developed a measurement technique for electrophoretic and electroosmotic mobilities using the particle displacements in AC and DC electric field.

A conventional technique for measuring the wall zeta-potential is the streaming potential measurement (Oldham *et al.*, 1963). Streaming potential is an electric potential related to the wall zeta-potential, induced by the motion of diffused ions in the electric double layer actuated by a high pressure applied into a channel. van Wagenen *et al.* (1981) evaluated the wall zeta-potential of various polymer materials. Scales *et al.* (1992) investigated the zeta-potential at the silica glass wall at different pH and electrolyte concentrations, and analyzed the results on the basis of a theoretical model of the electric double layer. In principle, the zeta-potential obtained by the steaming potential measurement is spatially averaged value in the channel.

Recent studies have measured the electroosmotic velocity or mobility, and estimated the wall zeta-potential using the Helmholtz-Smoluchowski equation, $\zeta = -(\mu/\epsilon E)u_{eof}$ or $\zeta = -(\mu/\epsilon)\mu_{eof}$. Sinton *et al.* (2002) evaluated the wall zeta-potential in the capillary from the electroosmotic velocity measured by the technique using the caged fluorescent dye. However, since the caged fluorescent dye significantly adsorbs to polymer materials and affects the wall zeta-potential, this technique is unsuitable for the zeta-potential measurement in polymer microchannels (Ross & Locascio, 2003). Sze *et al.* (2003) measured the zeta-potential at glass and PDMS surfaces by the current monitoring technique. Because of the current monitoring technique to measure the average velocity of electroosmotic flow, the obtained zeta-potetnial is also the spatially averaged value in the microchannel. Ichiyanagi *et al.* (2005) and Sasaki & Sato (2006) estimated the wall zeta-potential from the electroosmotic velocity measured by micro-PIV. Even in the microchannel composed of different materials, the wall zeta-potential can be evaluated by measuring the electroosmotic velocity near the each wall. However, due to use of the Helmholtz-Smoluchowski equation, the measurement regions are restricted to areas where the zeta-potential is assumed to be uniform at the wall. On the other hand, Park & Lee (2007) proposed a method estimating an inhomogeneous wall zeta-potential from the measured electroosmotic velocities, by solving the inverse problem using the governing equations for electroosmotic flow. This method was examined by the simulated velocity measurements but has not been applied to the real experiments.

1.2.3 Experimental Investigation of Electroosmotic Flow with Nonuniform Zeta-Potential

Herr *et al.* (2000) coupled two capillaries to generate an axial distribution of wall zeta-potential, and examined electroosmotic flow and the sample dispersion by the velocity measurement technique using the caged fluorescent dye. An internal pressure was generated by the axial variation of wall zeta-potential, and affected the flow profile and the dye dispersion.

Barker *et al.* (2000) modified the channel wall by polyelectrolytes to induce the step change zeta-potential along a direction perpendicular to the electric field, and generated a flow in opposite directions in the same channel. The sample dispersion and the motion of particles were observed by the flow imaging using the caged fluorescent dye and the velocity measurement using the streaks of fluorescent particles, respectively.

Stroock *et al.* (2000) and Stroock & Whitesides (2003) conducted the velocity measurement using particle streaks to examine the flows with the step change zeta-potential perpendicular and parallel to the electric field. The step change zeta-potential perpendicular to the electric field generated the co-flows in opposite directions as same as Barker *et al.* (2000), and the step change zeta-potential varying parallel to the electric field generated a recirculating flow profile.

Krishnamoorthy *et al.* (2006) experimentally and numerically investigated the structure of electroosmotic flow with nonuniform wall zeta-potential patterned by surface oxidation procedures. The mass flow rate obtained by the current monitoring and the sample dispersion calculated by the numerical simulation were affected by the magnitude of surface oxidation.

Horiuchi & Dutta (2006) conducted the micro-PIV measurement to investigate electroosmotic flow controlled by FEFC, and developed a flow control device using a T-junction microchannel.

1.3 Motivation and Objectives

The motivation of the present study is to experimentally investigate the dynamics of electroosmotic flow in a microchannel with nonuniform wall zeta-potential. The key parameters for the investigation are the wall zeta-potential, the near-wall velocity by the zeta-potential and the time dependent bulk flow velocity. In the current state, experimental studies are limited to steady electroosmotic flow with typical patterns of surface modification or FEFC, where the distribution of wall zeta-potential is easily predicted. A critical problem is the absence of measurement techniques for the quantitative evaluation of the key parameters. The absence of the measurement technique for inhomogeneous wall zeta-potential prevents the investigation of flows with mixing and chemical reaction, in which the wall zeta-potential will distribute by the ion and thermal transport in the flow field. Investigations of near-wall flow structure are indispensable to evaluate the effect of nonuniform wall zeta-potential on the flow field through the electric body force. Examing the transient flow structure leads to understand the momentum transport to form the flow field.

Figure 1.3 depicts the objectives of the present study and outline of the dissertation. The objective of the present study is to develop measurement techniques based on fluorescence imaging for the flow velocity and the wall zeta-potential. These techniques enable the time-resolved combined measurement of near-wall and bulk flow velocities, and the two-dimensional measurement of wall zeta-potential. Another objective is to investigate electroosmotic microchannel flow with nonuniform wall zeta-potential using the developed measurement techniques. Figure 1.4 illustrates the application of the measurement techniques to the electroosmotic flow field. Two approaches are conducted to generate the nonuniform wall zeta-

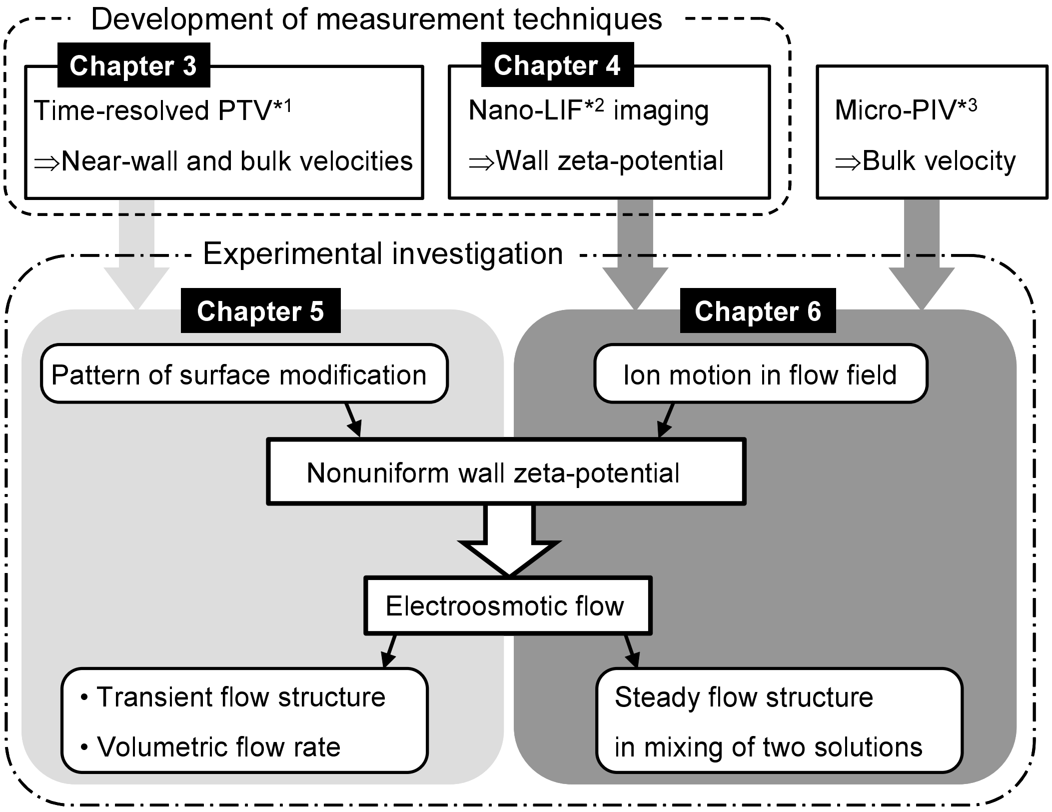

*1: particle tracking velocimetry (PTV), *2: laser induced fluorescence (LIF)
*3: particle image velocimetry (PIV)

Figure 1.3. Objectives of the present study and outline of the dissertation.

potential. The first approach is the surface modification to pattern the wall zeta-potential, and the experimental investigation focuses on the transient flow structure with typical patterns of zeta-potential. The second approach is the ion motion in a mixing flow field to make the zeta-potential nonuniform. A relationship between the ion motion and the wall zeta-potential, which has not been focused in previous work, is investigated using the zeta-potential measurement technique.

Chapter 2 describes the governing equations for microscale flows, fabrication techniques of microchannels, and fundamentals of measurement techniques based on fluorescence imaging.

Chapter 3 presents the development of a time-resolved velocity measurement technique using fluorescent submicron particles for near-wall and bulk electroosmotic flow structure in the transient and steady state. Figure 1.5 shows the concept of the velocity measurement technique. Conventional particle-based techniques based on fluorescence imaging, i.e., micro-PIV and nano-PIV, enable to measure the bulk velocity by the volume illumination of excitation light and the near-wall velocity by the evanescent wave illumination, respectively. On the other hand, the present technique accomplishes the combined measurement of bulk and near-

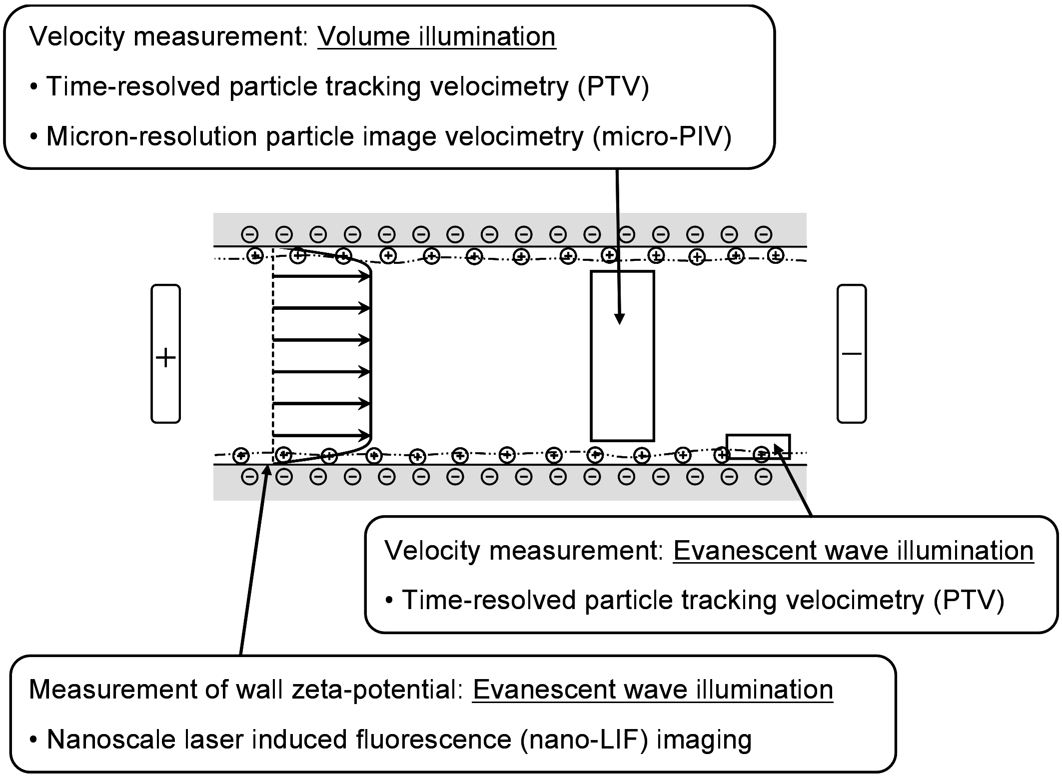

Figure 1.4. Experimental approaches to electroosmotic flow in the present study.

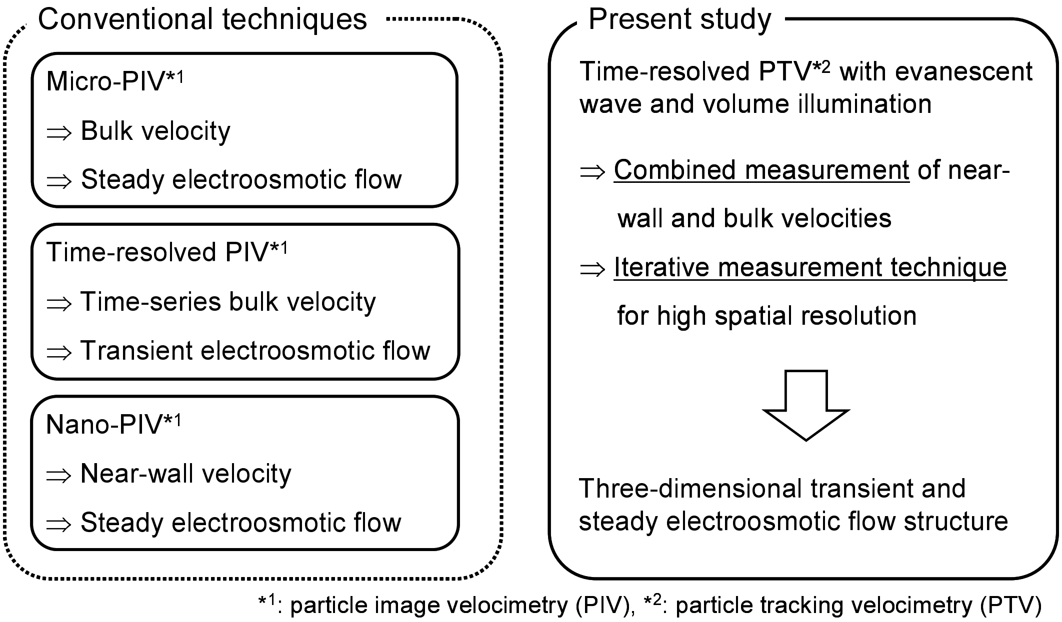

Figure 1.5. Concept of the velocity measurement technique using tracer particles developed in the present study compared with the conventional techniques.

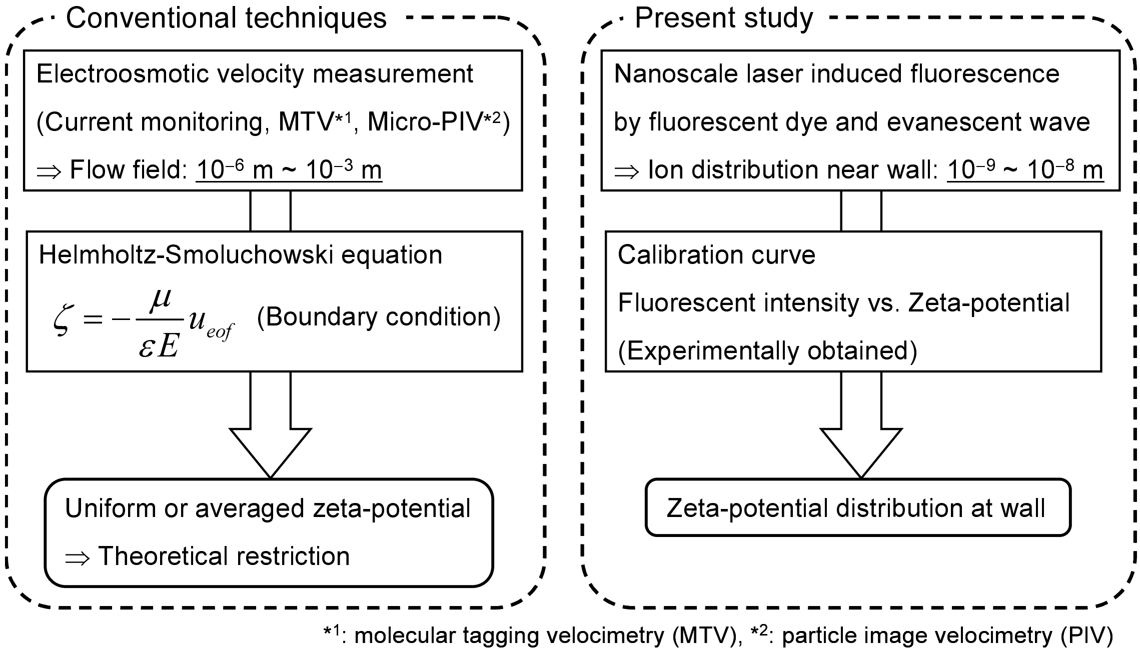

Figure 1.6. Concept of the zeta-potential measurement technique developed in the present study compared with the conventional techniques.

wall flow velocities by developing a measurement system with an optical system for both the volume and evanescent wave illuminations. Particle tracking velocimetry (PTV) is employed for the velocity measurement. The PTV measurement is achieved using tracer particles suspended in the liquid at relatively lower number density than that in PIV, and the velocity is obtained by tracing the individual particles. In order to improve the low spatial resolution of PTV, iterative measurement considering the reproducibility of low Reynolds number flow in the microchannel are conducted.

Chater 4 presents the development of a novel optical measurement technique using a fluorescent dye and the evanescent wave for inhomogeneous zeta-potential at the microchannel wall. This technique is termed nanoscale laser induced fluorescence (nano-LIF) imaging. Figure 1.6 shows the concept of the proposed measurement technique. In conventional techniques, the wall zeta-potential is estimated from the electroosmotic velocity with the scale of $10^{-6} \sim 10^{-3}$ m, however, the use of the Helmholtz-Smoluchowski equation restricts the measurement region to the area where the zeta-potential is uniform. On the other hand, the nano-LIF imaging focuses on the ion concentration in the vicinity of the wall related to the near-wall electric polarization with the scale of $10^{-9} \sim 10^{-8}$ m. Fluorescent dye, which ionized in the liquid, are selected for the measurement. In the vicinity of the wall, the fluorescence ions are distributed by the electric charge at the wall, i.e., the zeta-potential. Hence, the fluorescent intensity related to the zeta-potential is detected by exciting the fluorescence only near the wall using the evanescent wave decaying from the wall with the order of 100 nm. A relationship between the fluorescent intensity and the zeta-potential is experimentally examined, and the zeta-potential distribution at the wall is measured using the obtained relationship as a calibration curve. An evanescent wave illumination system is developed to expand the measurement area compared with the conventional system.

Chapter 5 presents the investigation of transient electroosmotic flow structure with nonuniform wall zeta-potential by the time-resolved velocity measurement technique. A relationship between the distribution of wall zeta-potential and the transient structure of electroosmotic flow is examined. Microchannels with uniform zeta-potential, nonuniform zeta-potential by material heterogeneity and patterned zeta-potential by surface modification are employed. The flow structure by the nonuniform zeta-potential is examined focusing on the momentum transport in the flow field and the volumetric flow rate.

Chapter 6 presents the investigation of electroosmotic flow with mixing of two solutions at different electrolyte concentrations. The effect of the ion motion with the mixing on the zeta-potential distribution at the wall is quantitatively evaluated. A T-shaped microchannel composed of PDMS and silica glass is employed. Two kinds of electrolyte solutions are injected by pressure-driven flow to conduct the mixing in the microchannel. The zeta-potential distribution at the wall is measured by the nano-LIF imaging. The ion motion in the flow field is estimated by the numerical analysis using the velocity information experimentally obtained by micro-PIV. Micro-PIV measurements are also conducted to examine the electrokinetic flow field induced by a DC electric field. A relationship between the ion motion, the zeta-potential distribution and the electroosmotic flow structure is investigated.

Chapter 7 describes the conclusions, and shows potential applications of the developed measurement techniques and the knowledge obtained in this work for the future researches.

Chapter 2

Fundamentals of Microfluidics

This chapter describes fundamentals of microfluidics, i.e., the behavior, precise control and manipulation of fluids in a channel with a small, typically sub-millimeter, scale (Geschke *et al.*, 2004). The present study experimentally investigates electrokinetic flow in a microchannel induced by an external electric field. A section for theory of microfluidics consists of that of microscale fluid mechanics and electrokinetics. Materials and fabrication techniques of microchannel used in the experiments are also described. The later section describes fundamentals of measurement technique based on fluorescence microscopy.

2.1 Theory of Microfluidics

2.1.1 Motion of Fluid

The present study focuses on a fluid flow, especially a flow of an aqueous electrolyte solution, which is geometrically constrained to a small scale with a characteristic length, $L = 10^{-4}$ m, with a characteristic velocity, $U = 10^{-3}$ m/s. Since the electrolyte concentration is dilute, properties of water as listed in table 2.1 are used as those of electrolyte solution in the experimental analyses. Validity of the continuum approximation of fluid is described by the Knudsen number, Kn (-), which is the ratio of the molecular length scale characterizing the fluid structure to the characteristic flow scale (White, 1986). The Knudsen number for the liquid is given by $Kn = \lambda_l / L$, where λ_l (m) is the length of the order of molecular diameter (Deen, 1998). In water with the molecular diameter of 3×10^{-10} m, the continuum approximation holds down to the flow scale of 10^{-8} m ($Kn < 10^{-2}$). The liquid flow is nearly incompressible and thus the fluid density, ρ (kg/m^3), is constant, and the liquid such as water is regarded as the Newtonian fluid, where the shear stress is proportional to the strain rate (the velocity gradient) (White, 1986, 2006). Therefore, the equation of continuity and the momentum equation, i.e., the Navier-Stokes equation, at the position, $\boldsymbol{x} = (x, y, z)$ (m), in the rectangular Cartesian coordinate system are given by

$$\boldsymbol{\nabla} \cdot \boldsymbol{u} = 0 \tag{2.1}$$

$$\rho\left(\frac{\partial \boldsymbol{u}}{\partial t} + \boldsymbol{u} \cdot \boldsymbol{\nabla}\boldsymbol{u}\right) = -\boldsymbol{\nabla}p + \rho_E \boldsymbol{E} + \mu \boldsymbol{\nabla}^2 \boldsymbol{u} \tag{2.2}$$

where $\boldsymbol{u} = (u, \upsilon, w)$ (m/s) is the fluid velocity, t (s) is the time, p (Pa) is the pressure, ρ_E (C/m^3) is the electric charge density, $\boldsymbol{E} = (E_x, E_y, E_z)$ (V/m) is the electric field and μ (Pa s) is the viscosity expressed as $\mu = \rho\nu$, where ν (m^2/s) is the kinematic viscosity. $\boldsymbol{f_E} = \rho_E \boldsymbol{E}$ (N/m^3) is the electric body force per unit volume, which induces the electrokinetic flow. The Cartesian coordinates in the fluid system, x, y and z, are set to be the streamwise, spanwise and depthwise components, respectively. By using dimensionless variables, $\boldsymbol{x^*} = \boldsymbol{x}/L$, $t^* = t/\tau$, $\boldsymbol{u^*} = \boldsymbol{u}/U$ and $p^* = pL/\mu U$, where τ (s) is the characteristic time, equations (2.1) and (2.2) are normalized as follow

$$\boldsymbol{\nabla^*} \cdot \boldsymbol{u^*} = 0 \tag{2.3}$$

$$Re\left(\frac{1}{Sr}\frac{\partial \boldsymbol{u^*}}{\partial t^*} + \boldsymbol{u^*} \cdot \boldsymbol{\nabla^*}\boldsymbol{u^*}\right) = -\boldsymbol{\nabla^*}p^* + \boldsymbol{f^*_E} + \boldsymbol{\nabla^{*2}}\boldsymbol{u^*} \tag{2.4}$$

where $\boldsymbol{f^*_E} = \left(L^2/\mu U\right)\rho_E \boldsymbol{E}$ (-) is the dimensionless electric body force. $Re = UL/\nu$ (-) is the Reynolds number, i.e., the ratio of the inertial to the viscous effects, and $Sr = \tau U/L$ (-) is the Strouhal number, the ratio of the characteristic time to the convective time scale, $\tau_c = L/U$ (s) (Deen, 1998). Due to the order of the Reynolds number of $Re = 10^{-1}$, the flow is the laminar flow, where the flow moves as if it were layered (Probstein, 1994; Brody *et al.*, 1996). Two types of the momentum equation are generally used for analyzing the low Reynolds number flow. When $Re << 1$, equation (2.4) reduces to the time-dependent Stokes equation

$$\frac{Re}{Sr}\frac{\partial \boldsymbol{u^*}}{\partial t^*} = -\boldsymbol{\nabla^*}p^* + \boldsymbol{f^*_E} + \boldsymbol{\nabla^{*2}}\boldsymbol{u^*} \tag{2.5}$$

Hence, the inertial force also contributes to the fluid dynamics at $Sr << 1$ (extremely short timescale). When $Re/Sr << 1$ or the flow is in the steady state, all inertial terms are negligible and equation (2.5) reduces to the Stokes equation

$$0 = -\boldsymbol{\nabla^*}p^* + \boldsymbol{f^*_E} + \boldsymbol{\nabla^{*2}}\boldsymbol{u^*} \tag{2.6}$$

Equations (2.5) and (2.6) are linear and superposable in the theoretical analysis.

Couette flow is well known as a flow between a fixed and a moving plates as shown in figure 2.1(*a*). Consider a sudden acceleration of the plane to a constant velocity, U_0 (m/s) at $\boldsymbol{\nabla p} = 0$ and $\boldsymbol{E} = 0$. Equation (2.5) is simplified to the diffusion equation

$$\frac{\partial u}{\partial t} = \nu \frac{\partial^2 u}{\partial y^2} \tag{2.7}$$

For short times from the start-up, the order-of-magnitude estimates of the derivatives in the equation are $\partial u/\partial t \sim U_0/t$ and $\partial^2 u/\partial y^2 \sim U_0/\delta^2$. Setting $\delta(t) = L$, the viscous time scale, τ_υ

Table 2.1. Properties of water at $T = 298$ K

Relative permittivity	ϵ_r	(-)	78.3
Viscosity	μ	(Pa s)	0.891×10^{-3}
Kinematic viscosity	ν	(m^2/s)	0.891×10^{-6}
Density	ρ	(kg/m^3)	997

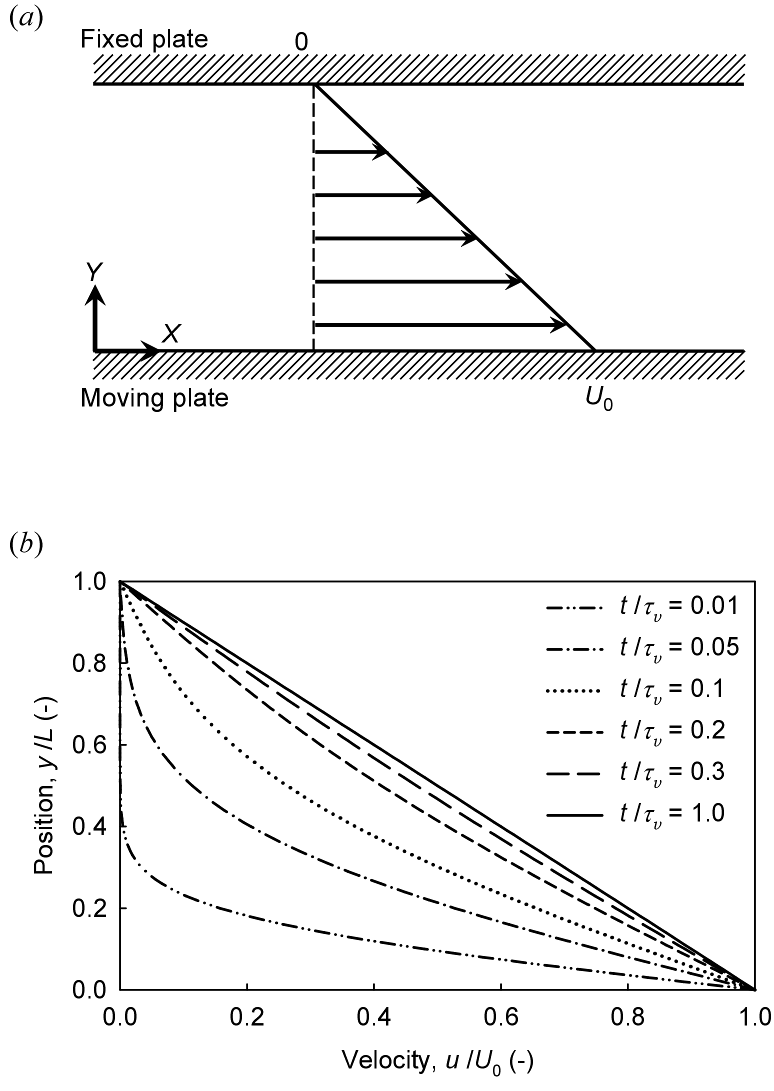

Figure 2.1. (*a*) Schematic of the Couette flow between a fixed and a moving plate. (*b*) Development of the Couette flow by the sudden acceleration of the plane to U_0 (m/s) at $t = 0$.

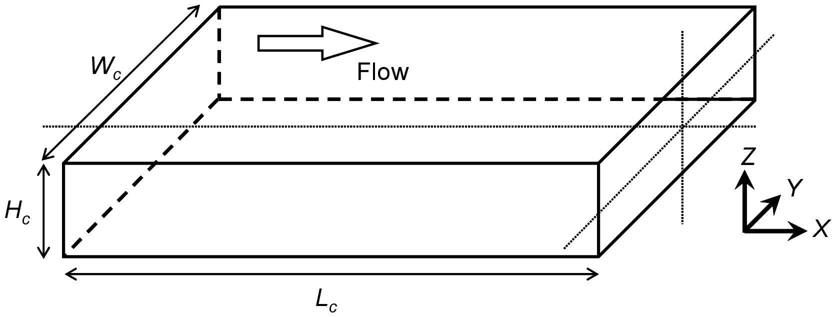

Figure 2.2. Geometry of a rectangular microchannel with the width of 2*a* (m), the depth of 2*b* (m) and the length of *l* (m).

(s), i.e., the time required for the momentum transport over the characteristic length, is given by

$$\tau_v = \frac{L^2}{\nu} \tag{2.8}$$

The order of the viscous time scale at $L = 10^{-4}$ m is $\tau_v = 10^{-2}$ s. The time-dependent solution for the Couette flow is (White, 2006)

$$\frac{u(y,t)}{U_0} = \left(1 - \frac{y}{L}\right) - \frac{2}{\pi}\sum_{n=1}^{\infty}\frac{1}{n}\exp\left(\frac{-n^2\pi^2 t}{\tau_v}\right)\sin\frac{n\pi y}{L} \tag{2.9}$$

Figure 2.1(*b*) shows the development of the Couette flow. The flow nearly approaches to the steady state with a linear velocity profile at $t/\tau_v \approx 0.3$.

Pressure-driven flow is a flow generated by a pressure gradient. In a rectangular microchannel with the width of $W_c = 2a$ (m), the height of $H_c = 2b$ (m) and the length of L_c (m) as illustrated in figure 2.2, when no external electric field is applied ($\boldsymbol{E} = 0$), the velocity profile of pressure-driven flow in the steady state is solved from equation (2.6) at non-slip boundary conditions ($\boldsymbol{u} = 0$ at the walls) (Brody *et al.*, 1996; White, 2006)

$$u(y,z) = -\frac{16b^2}{\mu\pi^3}\frac{\partial p}{\partial x}\sum_{n=1}^{\infty}\frac{(-1)^n}{(2n-1)^3}\frac{\cosh\left[\dfrac{(2n-1)\pi y}{2b}\right]}{\cosh\left[\dfrac{(2n-1)\pi a}{2b}\right]}\cos\left[\frac{(2n-1)\pi z}{2b}\right] \tag{2.10}$$

It is noted that the characteristic length of the rectangular microchannel is the hydraulic diameter, $D_h = 4 \times \text{area}/\text{wetted perimeter} = 4ab/(a+b)$ (m) (White, 1986, 2006). Figure 2.3 shows the velocity profile of the pressure-driven flow in the microchannel with the aspect ratio, $k = a/b$ (-), of 10. For the microchannel with the large aspect ratio, the velocity profile in the *Y*-direction is plug-like, and that in the *Z*-direction is parabolic. Thus, the flow in the area

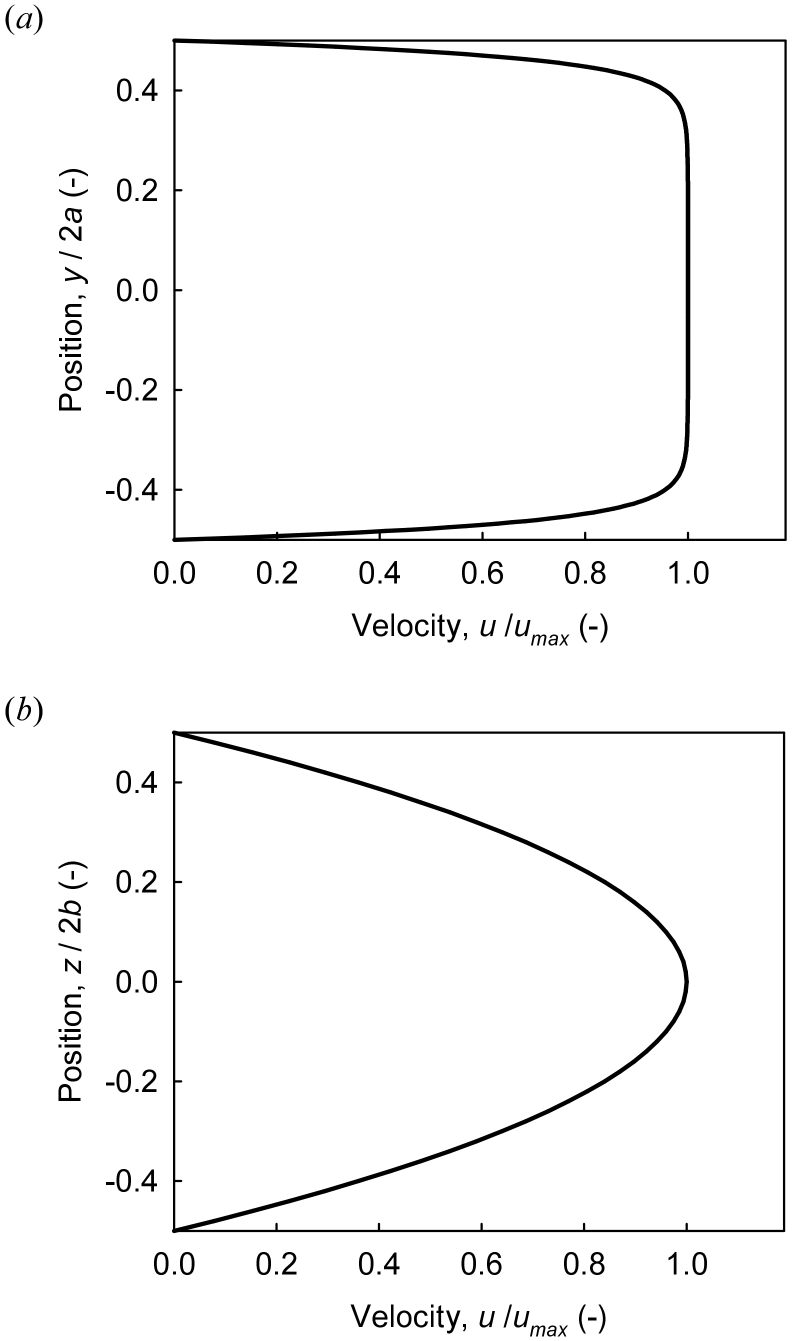

Figure 2.3. Velocity profiles of pressure-driven flow in the rectangular microchannel with $k = 10$ at (*a*) $z/2b = 0$ and (*b*) $y/2a = 0$.

Table 2.2. Properties of ion species at $T = 298$ K

Ion	Diffusivity D ($\times 10^{-9}$ m^2/s)	Mobility υ ($\times 10^{-13}$ mol s/kg)	Molar conductivity Λ ($\times 10^{-3}$ S m^2/mol)
H^+	9.31	37.6	35.0
K^+	1.96	7.90	7.35
Na^+	1.33	5.38	5.01
Cl^-	2.03	8.19	7.63
OH^-	5.27	21.3	19.8

except near the side walls (walls at $y/2a = \pm 0.5$) is independent of the spanwise position, y (m), and regarded as the Poiseuille flow with the parabolic velocity profile (Deen, 1998)

$$u(z) = -\frac{b^2}{2\mu}\frac{\partial p}{\partial x}\left[1 - \left(\frac{z}{b}\right)^2\right] \tag{2.11}$$

2.1.2 Mass Transport

When a species is present in the liquid flow with a dilute concentration, c (mol/m^3), and no chemical reaction takes place, the mass transport with the diffusive flux depending on the Fick's law is governed by the convective diffusion equation (Probstein, 1994; Deen, 1998)

$$\frac{\partial c}{\partial t} + \boldsymbol{u} \cdot \boldsymbol{\nabla} c = D \boldsymbol{\nabla}^2 c \tag{2.12}$$

where D (m^2/s) is the diffusion coefficient. By using the dimensionless concentration, $c^* = c/c_0$ (-), where c_0 (mol/m^3) is the bulk concentration, the equation becomes

$$Pe\left(\frac{1}{Sr}\frac{\partial c^*}{\partial t^*} + \boldsymbol{u}^* \cdot \boldsymbol{\nabla}^* c^*\right) = \boldsymbol{\nabla}^{*2} c^* \tag{2.13}$$

where $Pe = UL/D$ is the Peclet number, i.e., the ratio of the convective to the diffusive mass transports. Table 2.2 shows properties of ion species examined in the present study (Probstein, 1994; Lide, 2007). From $L = 10^{-4}$ m, $U = 10^{-3}$ m/s and $D = 10^{-9}$ m^2/s, the order of the Peclet number is $Pe = 10^2$. Hence, the convection dominates over the diffusion even in the low Reynolds number flow.

Due to an electric charge, the ion species is migrated under an electric field, i.e., the negative gradient of the electrostatic potential: $\boldsymbol{E} = -\boldsymbol{\nabla}\psi$. The molar flux of the ith charged species, $\boldsymbol{j}_i$ (mol/m^{2}s), by diffusion, electromigration, and convection is obtained by the Nernst-Planck equation (Probstein, 1994)

$$\boldsymbol{j}_i = -\upsilon_i z_{\upsilon,i} F c_i \boldsymbol{\nabla}\psi - D_i \boldsymbol{\nabla} c_i + c_i \boldsymbol{u} \tag{2.14}$$

Table 2.3. List of physical constants

Faraday's constant	F	(C/mol)	9.65×10^{4}
Boltzmann constant	k_b	(J/K)	1.38×10^{-23}
Gas constant	R	(J/mol K)	8.31
Permittivity of vacuum	ϵ_0	(C/V m)	8.85×10^{-12}

where υ (mol s/kg) is the mobility interpreted as the average velocity of a charged particle in solution accelerated by a force of 1 N/mol, z_υ (-) is the ion valence, F (C/mol) is the Faraday's constant as listed in table 2.3. The mobility is related to the diffusion coefficient by the Nernst-Einstein equation (Probstein, 1994)

$$D_i = RT\upsilon_i \tag{2.15}$$

where R (J/mol K) is the gas constant as listed in table 2.3. From the expression of the molar flux, conservation of the species by equation (2.12) is expanded for the charged species

$$\frac{\partial c_i}{\partial t} + \boldsymbol{u} \cdot \boldsymbol{\nabla} c_i = z_{\upsilon,i}\upsilon_i F\ \boldsymbol{\nabla}\cdot (c_i \boldsymbol{\nabla}\psi) + D_i \boldsymbol{\nabla}^2 c_i \tag{2.16}$$

The mass transport of the charged species gives rise to a current with the current density, $\boldsymbol{i}$ (A/m^2), expressed by using equation (2.15)

$$\begin{aligned} \boldsymbol{i} &= F \sum z_{\upsilon,i}\boldsymbol{j}_i \\ &= -F^2 \boldsymbol{\nabla}\psi \sum z_{\upsilon,i}^2 \upsilon_i c_i - F \sum z_{\upsilon,i} D_i \boldsymbol{\nabla} c_i + F\boldsymbol{u} \sum z_{\upsilon,i} c_i \end{aligned} \tag{2.17}$$

If there are no concentration gradients and no flow, the equation reduces to the Ohm's law

$$\boldsymbol{i} = \sigma \boldsymbol{E} = -\sigma \boldsymbol{\nabla}\psi \tag{2.18}$$

where σ (S/m) is the electrical conductivity of the solution given by

$$\sigma = F^2 \sum z_{\upsilon,i}^2 \upsilon_i c_i \tag{2.19}$$

It is noted that the molar conductivity, Λ_i (S m^2/mol), listed in table 2.2 is given by $\Lambda_i = \sigma_i / c_i = F^2 z_{\upsilon,i}^2 \upsilon_i$.

As shown in the Navier-Stokes equation (equation (2.2)), the mass transport of the charged species in the electric field affects the liquid flow through the Lorentz force as the body force, $\boldsymbol{f_E} = \rho_E \boldsymbol{E}$ (N). The electric charge density of the fluid is given by

$$\rho_E = F \sum z_{\upsilon,i} c_i \tag{2.20}$$

Generally, the aqueous electrolyte solution is closely electrically neutral, $\sum z_{v,i} c_i = 0$, thus $\boldsymbol{f_E} = 0$, everywhere except in the vicinity of charged boundaries, i.e., a region of the electric double layer, as described later. The charge distribution relates to the spatial variation in the electric field by the Poisson's equation (Hunter, 1981; Probstein, 1994)

$$\boldsymbol{\nabla}^2 \psi = -\frac{\rho_E}{\epsilon} \tag{2.21}$$

ϵ (C/V m) is the permittivity of the liquid given by $\epsilon = \epsilon_r \epsilon_0$, where ϵ_r (-) is the relative permittivity and ϵ_0 (C/V m) is the permittivity of a vacuum (table 2.3).

2.1.3 Motion of Particle

When an externally-forced spherical particle with a velocity, $\boldsymbol{u_p}$ (m/s), is present in the fluid flow, because acceleration of the particle accompanies that of the fluid, the Newton's law of motion for the particle with the added mass by the fluid is expressed as (Clift *et al.*, 1978; Rudinger, 1980)

$$\frac{1}{6}\pi d_p^3 \left(\rho_p + \frac{1}{2}\rho\right) \frac{d\boldsymbol{u_p}}{dt} = \boldsymbol{F} - \boldsymbol{F_D} \tag{2.22}$$

where d_p (m) is the particle diameter, ρ_p (kg/m^3) is the particle density, $\boldsymbol{F}$ (N) is the external force and $\boldsymbol{F_D}$ (N) is the viscous drag force dependent on the relative velocity, $\boldsymbol{u_p} - \boldsymbol{u}$ (m/s),

$$\boldsymbol{F_D} = \frac{1}{8}\pi d_p^2 \rho C_D \left(\boldsymbol{u_p} - \boldsymbol{u}\right) \left|\boldsymbol{u_p} - \boldsymbol{u}\right| \tag{2.23}$$

C_D (-) is the drag coefficient, which is a function of the particle Reynolds number, $Re_p = \left|\boldsymbol{u_p} - \boldsymbol{u}\right| d_p / \nu$ (-). Due to the order of Re_p of 10^{-5} in the present study, the drag coefficient is given by the Stokes law, $C_D = 24/Re_p$ (for $Re_p < 1$) (White, 2006), and equation (2.23) becomes

$$\boldsymbol{F_D} = 3\pi\mu d_p \left(\boldsymbol{u_p} - \boldsymbol{u}\right) \tag{2.24}$$

When the spherical particle is released from rest at $t = 0$ in the steady flow of U (m/s) and no external force is applied ($\boldsymbol{F} = 0$), the particle velocity is obtained by substituting equation (2.24) into equation (2.22)

$$u_p = U\left[1 - \exp\left(-\frac{t}{\tau_p}\right)\right] \tag{2.25}$$

$$\tau_p = \frac{\rho_p + \rho/2}{18\mu} d_p^2 \tag{2.26}$$

τ_p (s) is the particle relaxation time, i.e., the time required for the particle to follow the fluid flow.

The random thermal motion of particles suspended in the fluid is called the Brownian motion (Probstein, 1994). The fluctuations of the particles are caused by the collisions of the solvent molecules with the particles. Since the Brownian motion is spatially and temporally random by the probability of the displacement with the Gaussian distribution, the mean displacement is zero. The diffusion coefficient for a dilute suspension of particles is obtained by considering the balance of the thermal motion with the viscous drag (the Stokes-Einstein equation)

$$D = \frac{k_b T}{3\pi\mu d_p} \tag{2.27}$$

where k_b (J/K) is the Boltzmann constant as listed in table 2.3. The displacements are generally estimated by the stochastic equation for the motion of particle undergoing the Brownian motion, i.e., the Langevin equation (Probstein, 1994). When the time interval, Δt (s), is sufficiently large compared with the particle relaxation time without considering the acceleration of fluid, $\tau_p = m/3\pi\mu d_p$ (s) (about 10^{-8} s in the present study), where m (kg) is the mass of particle, the mean square displacement in one-dimension is given by

$$\langle \Delta x^2 \rangle = 2D\Delta t \tag{2.28}$$

In the vicinity of the solid wall, the Brownian motion is hindered with increasing the viscous drag force, and the displacements are non-Gaussian and anisotropic (Kihm *et al.*, 2004; Banerjee & Kihm, 2005; Sadr *et al.*, 2005). The diffusion coefficient tensor, $\boldsymbol{D}$ (m^2/s), is obtained by (Sadr *et al.*, 2005)

$$\boldsymbol{D} = D \begin{bmatrix} \lambda_{\parallel} & 0 & 0 \\ 0 & \lambda_{\parallel} & 0 \\ 0 & 0 & \lambda_{\perp} \end{bmatrix} \tag{2.29}$$

$\lambda_{\parallel}$ is the correction factor for the diffusion coefficient parallel to the wall bounding a semi-infinite, quiescent, viscous fluid given by Goldman *et al.* (1967)

$$\lambda_{\parallel} = 1 - \frac{9}{16}\frac{r_p}{r_p + h} + \frac{1}{8}\left(\frac{r_p}{r_p + h}\right)^3 - \frac{45}{256}\left(\frac{r_p}{r_p + h}\right)^4 - \frac{1}{16}\left(\frac{r_p}{r_p + h}\right)^5 \tag{2.30}$$

where r_p (m) is the particle radius and h (m) is the distance between the wall and the nearest edge of the particle. $\lambda_{\perp}$ is the correction factor in the form of an infinite series for the diffusion coefficient perpendicular to the wall given by Brenner (1961). The approximation of the correction factor is expressed as (Bevan & Prieve, 2000)

$$\lambda_{\perp} = \frac{6h^2 + 2r_p h}{6h^2 + 9r_p h + 2r_p^2} \tag{2.31}$$

Figure 2.4 shows the diffusion coefficient of the particle with the diameter of 500 nm in the vicinity of the wall at $T = 298$ K, which is calculated by equations (2.27) and (2.29) to (2.31). The bulk diffusion coefficient is 9.79×10^{-13} m^2/s. The diffusion coefficient reduces with decreasing h (m). The diffusion coefficient parallel to the wall is always larger than that perpendicular to the wall.

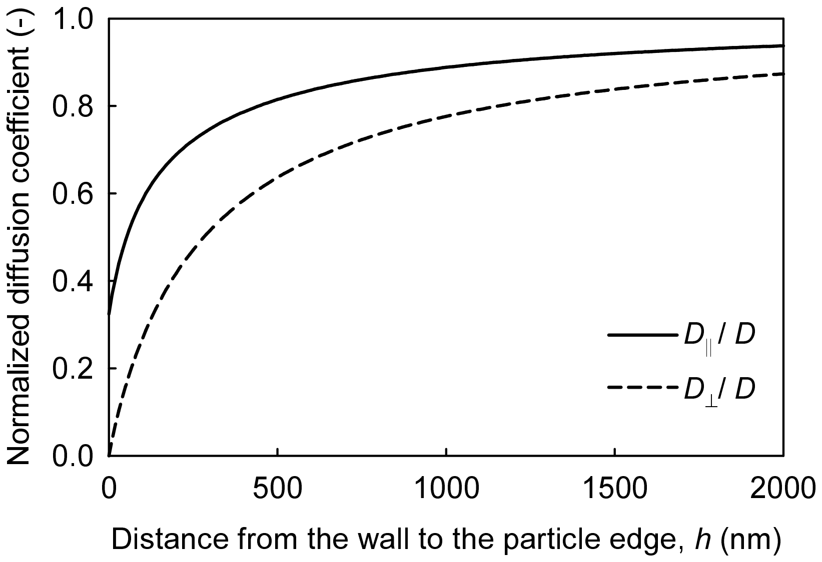

Figure 2.4. The diffusion coefficient of the particle in the vicinity of the wall at $T = 298$ K ($d_p = 500$ nm, $D = 9.79 \times 10^{-13}$ m^2/s).

2.1.4 Electric Double Layer

When a liquid contacts a solid surface, the solid surface is electrically charged by ionization, ion adsorption, and ion dissolution (Probstein, 1994). Then, ions in the liquid with opposite charge to the solid charge (counterion) are attracted toward the solid surface while ions with same charge (coion) are repelled from the surface. As a result, a region very near the solid surface is electrically polarized by an ionic layer mainly formed by counterions, i.e., the electric double layer with the thickness on the order of 10^{-9} m (Probstein, 1994). Since the materials of microfluidic devices such as glass and silicon polymer are negatively charged, the electric double layer in the devices consists of positive ions.

Most typical and practical model to describe the electric double layer is the Gouy-Chapman-Stern model as depicted in figure 2.5 (Hunter, 1981). The electric double layer is composed of the solid layer next to the surface (Stern layer) and the diffuse layer (Gouy-Chapman layer). The Stern layer is an ionic layer of ions adsorbed to the surface by van der Waals forces and chemical bindings, and it is considered that the thickness is about the scale of ion size, 3 – 5 Å (Revil *et al.*, 1999). Since the Stern layer behaves like solid, the non-slip boundary condition is applied to a surface separating the solid and diffuse layer, i.e., the shear plane. The zeta-potential, ζ (V), is defined as an electric potential at the shear plane, and is a characteristic parameter of the electric double layer for the electrokinetic phenomena such as electroosmotic flow and electrophoresis (Hunter, 1981; Probstein, 1994; Lyklema, 1995; Revil *et al.*, 1999; Kirby & Hasselbrink, 2004*a*,*b*; Wilkes, 2006). The ions in the Gouy-Chapman layer distributes

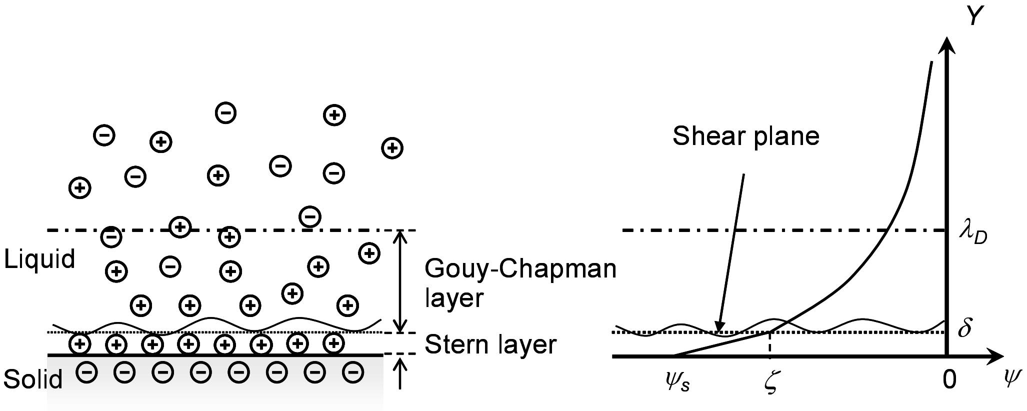

Figure 2.5. The theoretical model for the electric double layer, when the solid surface is charged negatively. ψ_S (V) is the electrostatic potential at the solid surface.

by the balance between the electric potential and thermal energy, given by the Nernst-Planck equation (equation (2.14)) with no net flux of ions and no flow normal to the flat solid surface

$$0 = -\upsilon_i z_{\upsilon,i} F c_i \frac{d\psi}{dy} - D_i \frac{dc_i}{dy} \tag{2.32}$$

Substituting the Nernst-Einstein equation (equation (2.15)) into the above equation and using the boundary conditions, $\psi = 0$ (bulk is electrically neutral) and $c_i = c_{0,i}$ as $y \to \infty$, yield the Boltzmann distribution of ith ion (Probstein, 1994)

$$c_i(y) = c_{0,i} \exp\left(-\frac{z_{\upsilon,i} F \psi(y)}{RT}\right) \tag{2.33}$$

The electric potential associated with the electric double layer on the solid surface is expressed by the Poisson-Boltzmann equation, which is obtained by substituting equations (2.20) and (2.33) into equation (2.21)

$$\frac{d^2\psi}{dy^2} = -\frac{F}{\epsilon} \sum z_{\upsilon,i} c_{0,i} \exp\left(-\frac{z_{\upsilon,i} F \psi(y)}{RT}\right) \tag{2.34}$$

In order to solve the non-linear Poisson-Boltzmann equation, the Debye-Hückel approximation is widely examined. When the electric potential, ψ (V), is enough small as $z_\upsilon F\psi/RT << 1$ ($\psi << 25.7$ mV at $z_\upsilon = 1$ and $T = 298$ K), the equation is simplified due to $e^{-x} \approx 1 - x$ for small x and the bulk electroneutrality condition (Hunter, 1981)

$$\frac{d^2\psi}{dy^2} = \frac{\psi(y)}{\lambda_D^2} \tag{2.35}$$

where λ_D (m) is the Debye length, i.e., the thickness of the electric double layer, given by

$$\lambda_D = \left(\frac{\epsilon RT}{F^2 \sum z_{\upsilon,i}^2 c_{0,i}}\right)^{\frac{1}{2}} \tag{2.36}$$

The Debye length also indicates the plane where the electric potential energy is equal to the thermal energy. Integrating equation (2.35) subject to the conditions that $\psi = \zeta$ at $y = \delta \approx 0$ and $d\psi/dy = 0$ as $y \rightarrow \infty$ yields (Kirby & Hasselbrink, 2004*a*)

$$\psi(y) = \zeta \exp\left(-\frac{y}{\lambda_D}\right) \tag{2.37}$$

The electric potential decays exponentially from the shear plane in the Debye-Hückel approximation. The total charge per unit area in the electric double layer on the solid surface, q_E (C/m^2), is obtained by

$$q_E = -\int_0^\infty \rho_E dy \tag{2.38}$$

For a symmetric electrolyte ($z_{v,+} = z_{v,-}$ and $c_+ = c_-$), by substituting the Poisson-Boltzmann equation (equation (2.34)) into equation (2.38) and using the boundary condition, $\psi = \zeta$ at $y = 0$,

$$\sinh\left(\frac{-F\zeta}{2RT}\right) = \frac{q_E F \lambda_D}{2\epsilon RT} \tag{2.39}$$

From $\sinh x \approx e^x/2$ for large x, when the charge at the solid surface is unaffected by the counterion concentration and is shielded by the ions in the electric double layer, the following relationship is obtained (Kirby & Hasselbrink, 2004*a*)

$$\zeta \sim \log \lambda_D \sim C_0 + C_1 \log c_0 z_v^2 \tag{2.40}$$

where C is the coefficient of the equation and c_0 (mol/m^3) is the bulk counterion concentration. The above relationship shows that the surface zeta-potential is dependent on the bulk electrolyte concentration, especially counterion concentration (Spehar *et al.*, 2003; Kirby & Hasselbrink, 2004*a*). In the real system, the charge at the solid surface is also affected by the counterion concentration due to adsorption or chemical binding.

2.1.5 Electroosmotic Flow

Electroosmotic flow is a fluid flow caused by the electric double layer on an application of electric field (Hunter, 1981; Probstein, 1994). When an electric field is applied, the migration of diffused ions in the electric double layer induces the motion of fluid by the electric body force, $\boldsymbol{f_E} = \rho_E \boldsymbol{E}$ (N). Then, the fluid in the electric double layer exerts a viscous force on that in the bulk region (electrically neutral).

In the microchannel, electroosmotic flow is described by the Stokes equation (equations (2.5) and (2.6)) and the Poisson's equation (equation (2.21)). When the electric charge of the wall is uniform (uniform zeta-potential) at no pressure, $p = 0$, the electroosmotic flow velocity at the steady state is given by

$$u_{eof}(y) = -\frac{\epsilon\zeta E}{\mu}\left(1 - \frac{\psi(y)}{\zeta}\right) \tag{2.41}$$

Since the electroosmotic velocity is proportional to the magnitude of electric field, the electroosmotic mobility, $\mu_{eof} = u_{eof}/E$ (m^2/V s), i.e., the electroosmotic velocity generated by the electric field of 1 V/m, is often used for the analysis. Figure 2.6 shows the velocity profile of electroosmotic flow obtained by using the Debye-Hückel solution (equation (2.37)) at $L/\lambda_D = 100$. Electroosmotic flow has the velocity gradient only in the vicinity of the electric double layer. Therefore, when $L/\lambda_D >> 1$, the flow field can be separated into the near-wall region dominated by viscous and electrostatic forces and the bulk region dominated by inertial and pressure forces (Santiago, 2000; Yang *et al.*, 2004). The flow outside the electric double layer is expressed with a slip velocity condition determined by the Helmholtz-Smoluchowski equation

$$u_{eof} = -\frac{\epsilon\zeta E}{\mu} \tag{2.42}$$

Under the slip velocity approach, electroosmotic flow is regarded as the Couette flow. Thus, the time for electroosmotic flow to become steady, τ_{eof} (s), is equal to the viscous timescale by equation (2.8) (Minor *et al.*, 1997)

$$\tau_{eof} = \tau_v = \frac{L^2}{\nu} \tag{2.43}$$

This assumption is considered to be valid since the fluid inside the electric double layer responds nearly instantaneously to the external electric field (Minor *et al.*, 1997). In the rectangular microchannel, the velocity profile of transient electroosmotic flow with uniform zeta-potential is given by solving the Stokes equation (equation (2.5)) under the slip velocity approach

$$\begin{aligned} \frac{u(y,z,t)}{-\epsilon\zeta E/\mu} =& 1 - \frac{16}{\pi^2}\sum_{m=1}^{\infty}\sum_{n=1}^{\infty}\frac{(-1)^{m+n}\cos\left[\frac{(2m-1)\pi y}{2a}\right]\cos\left[\frac{(2n-1)\pi z}{2b}\right]}{(2m-1)(2n-1)} \\ & \times \exp\left\{-D_h^2\left[\left(\frac{2m-1}{2a}\pi\right)^2+\left(\frac{2n-1}{2b}\pi\right)^2\right]\frac{t}{\tau_{eof}}\right\} \end{aligned} \tag{2.44}$$

where $\tau_{eof} = D_h^2/\nu$ (s) (Tay, 2002; Yang *et al.*, 2004).

2.1.6 Electrophoresis

Electrophoresis is the electromigration of molecules and particles in the fluid as illustrated in figure 2.7. The electrophoretic velocity, u_{ep} (m/s) is proportional to the electric field, expressed as $u_{ep} = \mu_{ep}E$, where μ_{ep} (m^2/V s) is the electrophoretic mobility.

When the particle radius is much smaller than the Debye length (electrophoresis of ions or molecules), $r_p/\lambda_D << 1$, the electrophoretic velocity is simply obtained by using the Stokes

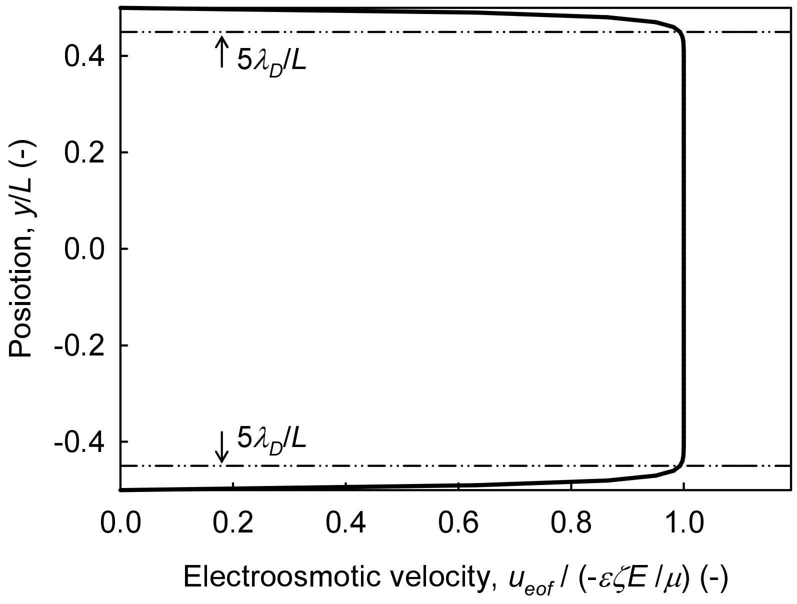

Figure 2.6. Velocity profile of electroosmotic flow at $L/\lambda_D = 100$.

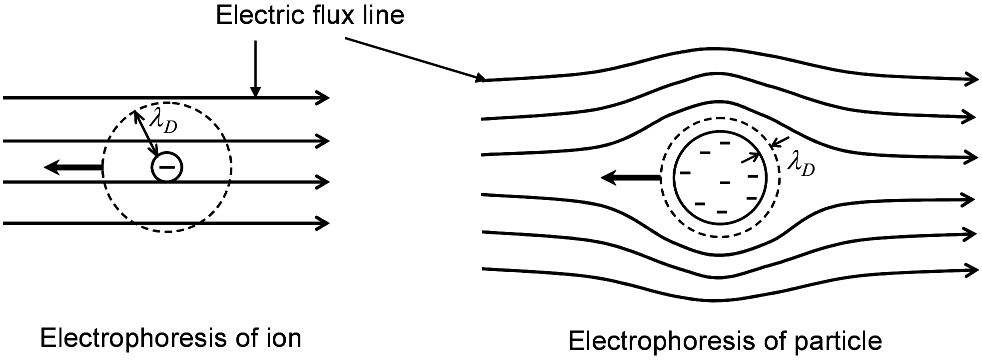

Figure 2.7. Schematic of particle electrophoresis with different size compared to the Debye length.

law (equation 2.24)

$$u_{ep} = \frac{q}{6\pi\mu r_p}E \tag{2.45}$$

where q (C) is the charge of particle.

For the electrophoresis of dielectric particle with a radius larger than the Debye length, the electric flux lines are detoured by the presence of particle, and the electrostatic force exerted on the surface charges balances with the fluid drags related to the Stokes law and the motion of ions in the electric double layer around the particle at the steady state (Probstein, 1994; Lyklema, 1995). The electric flux lines are also affected by the surface conductance, which is caused by the excess ions in the electric double layer compared with the bulk region. The effect of the surface conductance on the electric field is described by the Dukhin number, $Du = \sigma_s / r_p \sigma$ (-), where σ_s (S) is the surface conductivity (Lyklema, 1995; Lyklema & Minor, 1998). The electrophoretic velocity of the particles is expressed as (Lyklema, 1995)

$$u_{ep} = \frac{2}{3}\frac{\epsilon\zeta}{\mu} f\left(\frac{r_p}{\lambda_D}, Du\right)E \tag{2.46}$$

where f (-) is the function depending on r_p/λ_D and Du. When $r_p/\lambda_D >> 1$, $f \rightarrow 1.5$ and equation (2.46) becomes the Helmholtz-Smoluchowski equation.

The relaxation of particle electrophoresis is divided into three components: the hydrodynamic relaxation, the double-layer polarization and the concentration polarization (Minor *et al.*, 1997; Oddy & Santiago, 2004). The hydrodynamic relaxation is caused by the relaxation of the local electroomotic flow around the particle and the relaxation of particle motion suspended in the fluid with the Stokes law. When the particle density is close to the fluid density, the characteristic time for this process is given by (Minor *et al.*, 1997)

$$\tau_{ep} = \frac{r_p^2 \rho_p}{\mu} \tag{2.47}$$

Under the applied electric field, the electromigration of ions distorts the electric double layer from the sphericity as illustrated in figure 2.8 (Probstein, 1994). This polarization is strongly affected by the electric flux lines and governed by the conservation of charged species (equation (2.16)). The polarization process continues until the electromigration and the diffusion are balanced. The relaxation time for the double-layer polarization is given by (Lyklema, 1995; Minor *et al.*, 1997)

$$\tau_{dl} = \frac{\lambda_D^2}{D} \tag{2.48}$$

The distribution of ions in the electrolyte around the particle is also affected by the double-layer polarization (concentration polarization). The characteristic time for the concentration polarization is given by (Lyklema, 1995; Minor *et al.*, 1997)

$$\tau_{cp} = \frac{r_p^2}{D} \tag{2.49}$$

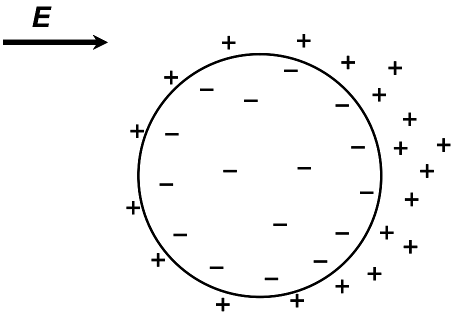

Figure 2.8. Schematic of the polarized electric double layer around the particle on an application of electric field.

However, when $r_p/\lambda_D >> 1$, the magnitude of the double-layer polarization and the concentration polarization are negligible, and the relaxation time for the particle electrophoresis is given by equation (2.47) (Lyklema, 1995; Minor *et al.*, 1997).

When an electric field is applied in the microchannel, the fluid is driven by electroosmotic flow, on the other hands, the particles undergo electrophoresis. Therefore, the velocity of particles suspended in the fluid is the superposition of the electroosmotic and electrophoretic velocity (Santiago, 2000; Devasenathipathy & Santiago, 2002).

$$\boldsymbol{u_p} = \boldsymbol{u_{eof}} + \boldsymbol{u_{ep}} \tag{2.50}$$

2.2 Microchannel

This section describes fabrication of microchannel by soft lithography (McDonald *et al.*, 2000; Whitesides *et al.*, 2001; McDonald & Whitesides, 2002; Ng *et al.*, 2002). Soft lithography is a set of microfabrication techniques using an elastomeric material: replica molding, microcontact printing, microtransfer molding, micromolding in capillaries and solvent-assisted micromolding (Xia & Whitesides, 1998). An elastomeric substrate with a mold fabricated by replica molding is used as the microstructure in the system, or as the pattern transfer elements to the substrate. A siloxane-based polymer, poly(dimethylsiloxane) (PDMS) is widely used as the elastomeric material. In the present study, the microchannel is mainly fabricated by replica molding and composed of PDMS and glass walls. For patterning the wall zeta-potential, self-assembled monolayers (Mrksich & Whitesides, 1996; Schreiber, 2000) is modified on the glass surface by microcontact printing.

2.2.1 Materials of Microchannel

Glass, which is an amorphous solid (Doremus, 1973), has been the dominant material for the microfluidic devices in the early 1990s as well as silicon since the fabrication techniques were well developed in the semiconductor industry and the surface properties were well characterized (Harrison *et al.*, 1992, 1993; Jacobson *et al.*, 1994). Its optical transparency is suitable for the optical detection, and its electric insulation enables the applications using electrokinetics inside the microchannel. The glass microchannel is fabricated by chemical etching, and sealing the materials requires high voltage or temperature (Geschke *et al.*, 2004). The glass surface is hydrophilic by the silanol groups, SiOH, present on the surface, and charged negatively by deprotonation of silanol groups: $\mathrm{SiOH} \rightleftharpoons \mathrm{SiO}^- + \mathrm{H}^+$. This electrostatic charge at the surface generates the negative zeta-potential. Hence, the zeta-potential at the glass surface is strongly dependent on pH of the solution by the chemical equilibrium of silanol groups (Hunter, 1981; Scales *et al.*, 1992; Revil *et al.*, 1999; Gu & Li, 2000; Kirby & Hasselbrink, 2004*a*). The magnitude of the negative zeta-potential becomes larger with higher pH of the solution since the number of dissociated silanol group (SiO^-) is increased. The zeta-potential at the glass surface also depends on the electrolyte concentration related to the Debye length, λ_D (m), by equation (2.36) and the species of metal cation (Me) in the electrolyte due to the chemical equilibrium with binding affinity for the silanol groups: $\mathrm{SiOH} + \mathrm{Me}^+ \rightleftharpoons \mathrm{SiOMe} + \mathrm{H}^+$ (Revil *et al.*, 1999; Gu & Li, 2000; Kirby & Hasselbrink, 2004*a*). The binding affinities of metal cation for the silanol groups are ordered as $\mathrm{Ca}^{2+} > \mathrm{Ba}^{2+} >> \mathrm{K}^+ > \mathrm{Na}^+ > \mathrm{Li}^+$ (Revil *et al.*, 1999; Kirby & Hasselbrink, 2004*a*). The species with strong binding affinity decreases the number of SiOH at the glass surface, and thus the magnitude of zeta-potential, $|\zeta|$ (V), in contact with the electrolyte solution of different metal ions (Ca^{2+}, K^+ and Na^+) can be sequenced as follow: $\left|\zeta\left(\mathrm{Na}^+\right)\right| > \left|\zeta\left(\mathrm{K}^+\right)\right| >> \left|\zeta\left(\mathrm{Ca}^{2+}\right)\right|$. In previous work, several models for the zeta-potential at the silica glass-solution interface were proposed from the results of experimental and theoretical analysis (Scales *et al.*, 1992; Revil *et al.*, 1999). These models are quite accurate but limited to specific conditions. This limitation is caused by the ambiguity in the model of the electric double layer and the dissociation constant of ions for the silanol groups.

Polymers such as poly(dimethylsiloxane) (PDMS), polycarbonate, poly(methyl methacrylate), poly(ethylene terephthalate glycol) and polyethylene have been used as a material for the microfluidic devices alternative to glass because of a reduced cost and a simplified fabrication process (molding or embossing rather than etching) (Becker & Locascio, 2002; Ng *et al.*, 2002; Kirby & Hasselbrink, 2004*b*). Especially, PDMS is the most actively developed material for the microchannel. Using PDMS for the microchannel material have great advantages: simple fabrication process by soft lithography, optical transparency down to 300 nm, reversible sealing with a flat surface by van der Waals contact, low permeability to water and low electrical conductivity. However, its low thermal conductivity, 0.18 W/K m, which is an order of magnitude lower than that of glass, can lead to significant increase in the temperature of the aqueous solution in the microchannel by Joule heating on an application of electric field (Ross *et al.*, 2001*a*; Erickson *et al.*, 2003). In addition, since PDMS swells in contact with nonpolar organic solvents like toluene, it is not useful in the application using some organic solvents (Lee *et al.*, 2003). PDMS is supplied from two components: a base and a curing agent. Silicon hydride groups in the curing agent react with vinyl groups in the base and form a cross-linked elastomeric solid (McDonald & Whitesides, 2002). Thus, PDMS is composed of repeating units of -O-Si$(CH_3)_2$- groups and this chemical structure induces a hydrophobicity of surface. It is known that the surface of PDMS is charged negatively (van Wagenen *et al.*, 1981). The dependence of the zeta-potential (electroosmotic mobility) at the PDMS surface on pH and ion concentration shows the same tendency as that at the glass surface but the magnitude is smaller (Liu *et al.*, 2000; Ocvirk *et al.*, 2000; Spehar *et al.*, 2003; Kirby & Hasselbrink, 2004*b*). However, a source of the negative charge at the PDMS surface is yet unknown despite the experimental researches by the measurement of electroosmotic mobility, infrared absorption spectra or chemical force titration using atomic force microscopy (Ren *et al.*, 2001; Wang *et al.*, 2003; Wheeler *et al.*, 2004; Bao *et al.*, 2005). Irradiation of an oxygen or air plasma to PDMS is often performed to destroy methyl groups ($SiCH_3$) and introduce silanol groups (SiOH) at the PDMS surface. This results in an increased electroosmotic mobility compared with the native PDMS, a hydrophilic surface, and enables irreversible sealing of PDMS with the material containing hydroxy groups (-OH) such as PDMS, glass, silicon and polystyrene, which are also exposed to the plasma, by forming -O-Si-O- bonds (Ng *et al.*, 2002). These properties of oxidized PDMS is preserved as long as the substrate is filled with an aqueous solution but reduced by exposing to air (Ren *et al.*, 2001).

In the present study, the microchannel is fabricated by the process as described below and made of glass and PDMS. This hybrid microchannel prevents increase of the solution temperature by Joule heating on an application of electric field since the glass has a high thermal conductivity (Erickson *et al.*, 2003).

2.2.2 Microchannel Fabrication by Replica Molding

Replica molding easily duplicates a microstructure to the elastomeric substrate by using a master (Xia & Whitesides, 1998). Thus, fabricating the microchannel by this technique has an advantage in verifying the repeatability of experiments. The master is prepared by photolithography (Moreau, 1988; Deng *et al.*, 2000). Figure 2.9 shows the fabrication process of the microchannel by replica molding (Hosokawa & Maeda, 2001; Sato *et al.*, 2003*b*).

Figure 2.9(*a*) illustrates the process of photolithography: spin coat, softbake, expose, post expose bake, followed by develop (Moreau, 1988). A slide glass (Matsunami Glass Ind., Ltd., Micro Slide Glass) is used as a wafer in the present study. The glass wafer is cleaned by

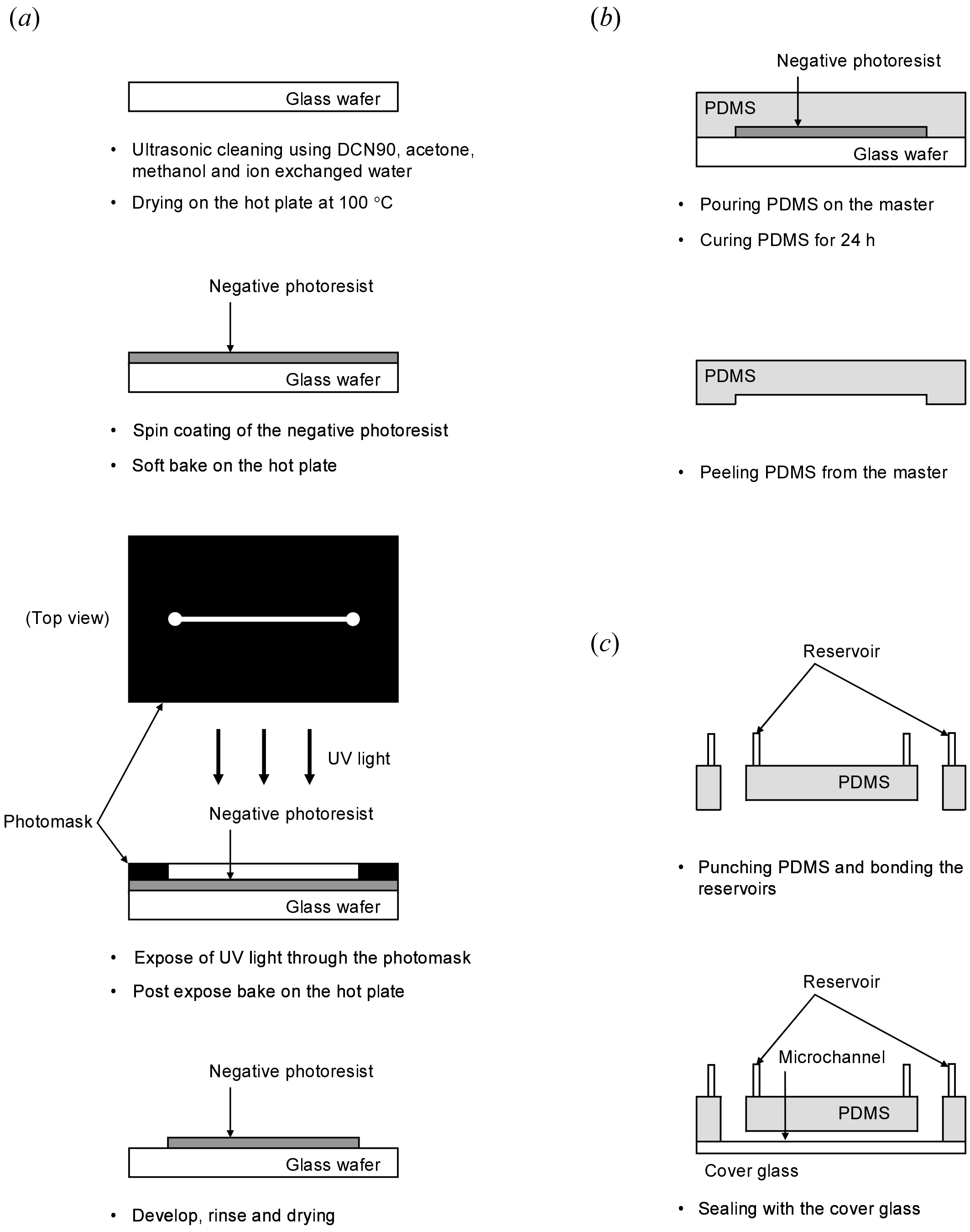

Figure 2.9. Fabrication process of the microchannel by replica molding. (*a*) Master preparation by photolithography. (*b*) Molding the microstructure to PDMS by replica molding. (*c*) Fabricating the microchannel used in the experiments.

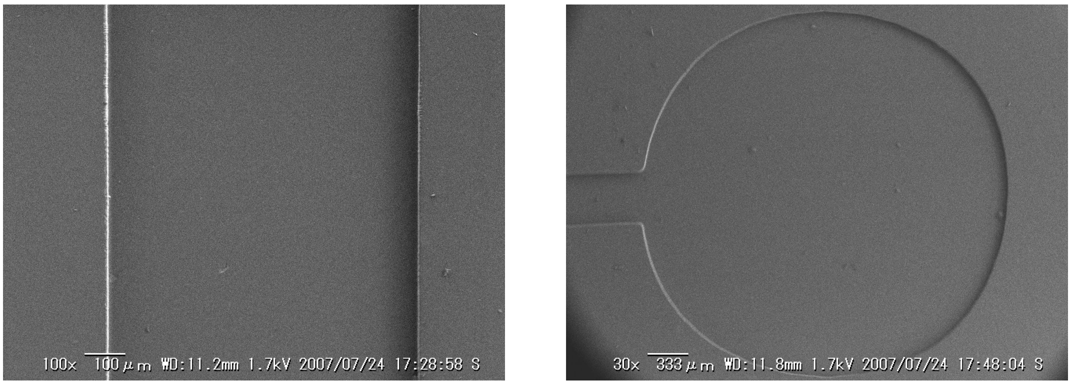

Figure 2.10. SEM images of PDMS microchannels fabricated by replica molding.

ultrasonic cleaning with a detergent surfactant (AR BROWN Co. Ltd., DCN90), acetone, methanol and ion exchanged water followed by drying on a hot plate at 100 °C. An epoxy based negative photoresist (MicroChem Corp., SU-8 3000) is coated on the wafer by a spin coater (Misaka Co. Ltd., 1H-D7). The photoresist-coated wafer is soft baked on the hot plate to evaporate the solvent and densify the film. The wafer is exposed to a UV light through a photomask with a microstructure image by using a mask aligner (Union Optical Co. Ltd., EMA-400). The exposed wafer is baked on the hot plate to selectively cross-link the exposed portion of the photoresist (post expose bake). The photoresist is developed in a developer (MicroChem Corp., SU-8 Developer) to dissolve the unexposed portion. Finally, the wafer is rinsed with isopropyl alcohol and dried with a stream of nitrogen. Detail parameters about the process of photolithography (spin speed of coating, temperature and time for baking, UV exposure time and develop time) are optimized with a desired thickness of the photoresist film.

The process of replica molding is shown in figure 2.9(*b*). A prepolymer solution of PDMS (Shin-Etsu Chemical Co. Ltd., KE-1606, base : curing agent = 10 : 1) is poured on the master with a frame for holding the solution and cured for 24 h. The cured PDMS chip with the molded microstructure is peeled from the master. Figure 2.10 shows scanning electron micrograph (SEM) images of PDMS microchannels captured by a scanning electron microscope (Keyence Corp., VE-7800).

For fabricating the microchannel used in the experiments, access holes for inlet and outlet of the microchannel are prepared by punching the PDMS chip, and reservoirs (Sigma-Aldrich Corp., Cloning Cylinders, polystyrene, height: 9.5 mm, inner diameter: 11 mm) are bonded as illustrated in figure 2.9(*c*). Finally, the PDMS chip is sealed with the cover glass by bringing both the surfaces into contact.

2.2.3 Surface Modification by Microcontact Printing

Microcontact printing is a simple method for patterning a material using a PDMS stamp (Kumar & Whitesides, 1993; Xia & Whitesides, 1998). The material for patterning is inked to the stamp and transferred to a substrate surface by stamping. This procedure has been widely used for the patterning of self-assembled monolayers (SAMs) to change the surface properties such as adhesion and wettability (Whitesides *et al.*, 2001). SAMs are ordered molecular assemblies, which are formed spontaneously on the substrate surface by the chemical adsorption with covalent grafting (Schreiber, 2000). They are made of organic molecules with lengths about a few nanometers, which consist of headgroup with a specific affinity to the substrate, backbone (alkyl chain) and endgroup (terminal functional group) as illustrated in figure 2.11 (Schreiber, 2000). The organic molecules on the substrate surface are tilted to maximize the van der Waals interactions between the alkyl chains. The surface properties with SAMs are characterized by the terminal functional groups of the organic molecules. Typically, there are two classes of SAMs, alkanethiolates with a specific affinity for gold and silver surfaces and alkylsiloxanes with that for hydroxylated surfaces such as glass and oxidized silicon. In the present study, microcontact printing using SAMs is performed to pattern the zeta-potential at the glass surface. Thus, an alkylsiloxane, octadecyltrichlorosilane (OTS) of a chemical structure, $Cl_3Si\text{-}(CH_2)_{17}\text{-}CH_3$ (McGovern *et al.*, 1994; Schreiber, 2000; Pallandre *et al.*, 2006; Benor *et al.*, 2007), is selected for the surface modification. Since OTS has a nonpolar methyl group ($\text{-}CH_3$) as the terminal functinonal group, the substrate surface modified by SAMs of OTS is hydrophobic (McGovern *et al.*, 1994; Benor *et al.*, 2007). Figure 2.12 shows a schematic model for the formation of SAMs by OTS on the glass surface through physisorption, hydrolysis in an adsorbed water layer, covalent binding to the glass surface and lateral polymerization with other OTSs (Pallandre *et al.*, 2006). It is noted that a small amount of residual water on the glass surface, which is present on the surface unless the condition is at a temperature above 400 °C and at reduced pressure, is essential for the reaction of alkylsiloxane SAMs (Wasserman *et al.*, 1989; Tripp *et al.*, 1993; McGovern *et al.*, 1994; Pallandre *et al.*, 2006).

Figure 2.13 shows a schematic outline of the process for microcontact printing of SAMs by OTS to the glass surface using a PDMS stamp. The glass plate is pretreated by ultrasonic cleaning with ion exchanged water, ethanol and sodium hydrate (NaOH) solution, followed by drying on the hot plate at 120 °C. Then, an oxygen plasma is irradiated to the glass plate for 1 min by a plasma etching system (Samco Inc., FA-1) to chemically activate the glass surface. The PDMS stamp is fabricated by replica molding as illustrated in figure 2.9(*a*) and (*b*). A 5 mmol/*l* solution of OTS (Shin-Etsu Chemical Co. Ltd.) in dehydrated toluene, which avoids the polymerization of OTS before the stamping process, is prepared. The PDMS stamp is liquored in the OTS solution and dried to evaporate dehydrated toluene under nitrogen condition for 30 min. After the drying process, the stamp is brought into conformal contact

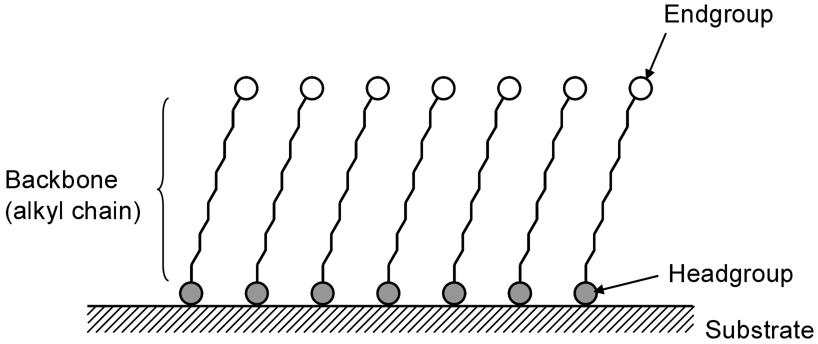

Figure 2.11. Schematic of SAM formed on the substrate.

with the glass plate for the covalent grafting of OTS to the glass surface. The OTS-transferred glass plate is baked on the hot plate at 120 °C for 5 min to sufficiently bond SAMs on the glass surface. Unreacted OTSs are removed from the glass plate by ultrasonic cleaning using ethanol and hydrochloric acid (HCl) solution with making the glass surface chemically inert to prevent the pattern of SAMs from blurring. Finally, the glass plate is rinsed by ion exchanged water and dried on the hot plate.

Patterned SAMs have been visualized using various techniques such as SEM (López *et al.*, 1993*b*), scanning probe microscopy (Wilbur *et al.*, 1995), fluorescence microscopy, in which case a fluorophore is present in SAMs (Chi *et al.*, 1991), secondary ion mass spectrometry (López *et al.*, 1993*a*), condensation figures with an array of droplets on a cold surface exposed to warm air (López *et al.*, 1993*a*), and surface-enhanced Raman microscopy (Yang *et al.*, 1996). In the present study, SAMs of OTS on the glass surface patterned by microcontact printing was evaluated by an optical profiler based on noncontact and three-dimensional scanning white light interferometry for the measurement of surface roughness with a resolution of 0.1 nm (Zygo Corp., NewView 6200). The measured thickness of patterned SAMs formed by OTS was 5−7 nm. It is noted that the theoretical thickness of OTS monolayer, which quantitatively agrees with the experimental results obtained by ellipsometry (Wasserman *et al.*, 1989) and X-ray scattering techniques (Maoz *et al.*, 1995), is 2.62 nm from the molecular structure (Wasserman *et al.*, 1989) and 2.29 nm not considering the projections for Si-O bonds (Maoz *et al.*, 1995). Thus, SAMs of OTS patterned by the process shown in figure 2.13 have two- or three-fold larger thickness compared with the results of previous studies. It is presumed that vertical polymerization of OTS occurs in the process of microcontact printing and increases the thickness of SAMs. Measurement of the contact angle (Dubois & Nuzzo, 1992; Probstein, 1994; Pashley & Karaman, 2004) was also conducted to verify the surface wettability from the photograph of water droplet on the flat substrate surface. The contact angle of OTS-modified

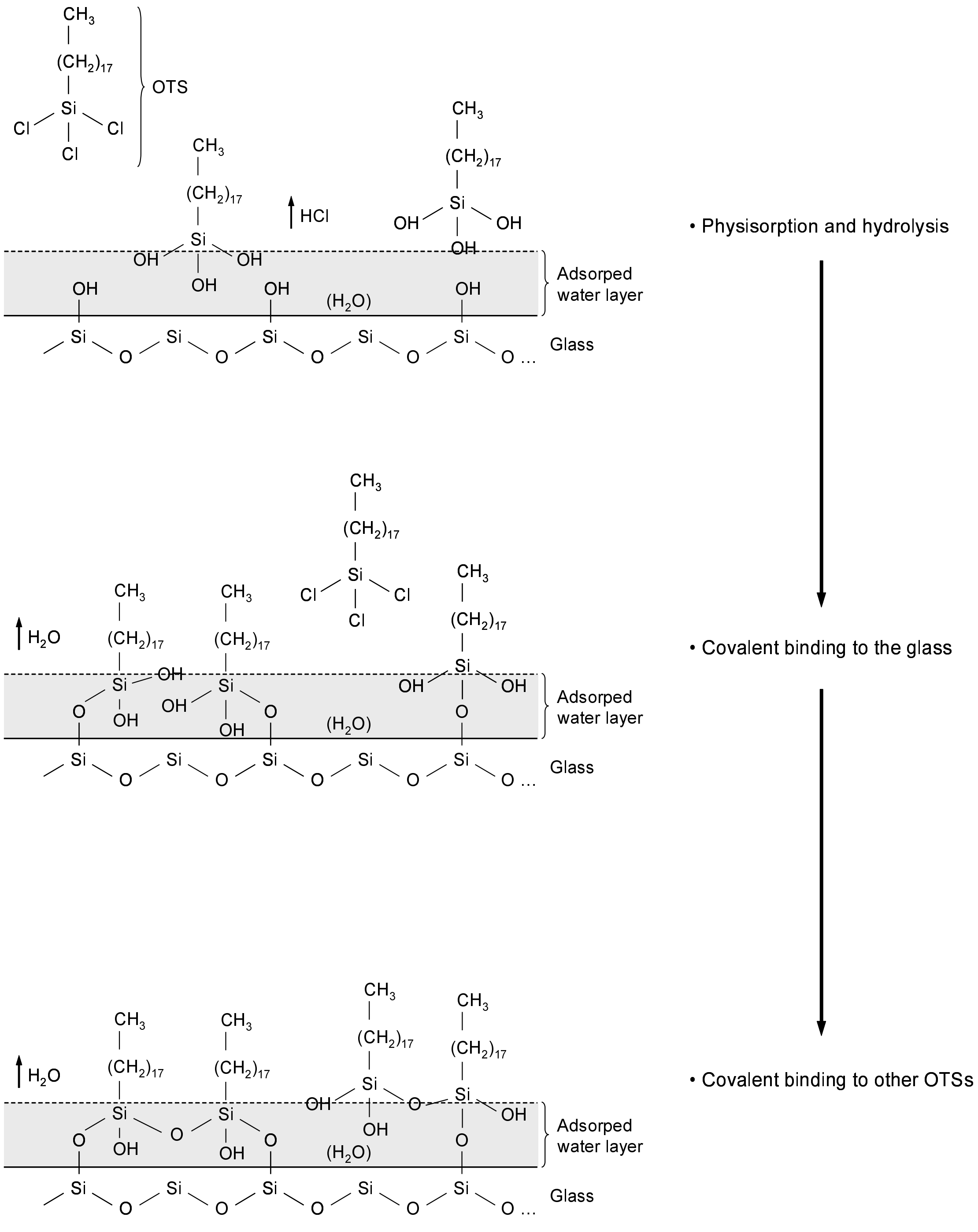

Figure 2.12. Formation of SAMs by OTS on the glass surface through physisorption, hydrolysis in the adsorbed water layer, covalent binding to the glass surface and lateral polymerization with other OTSs.

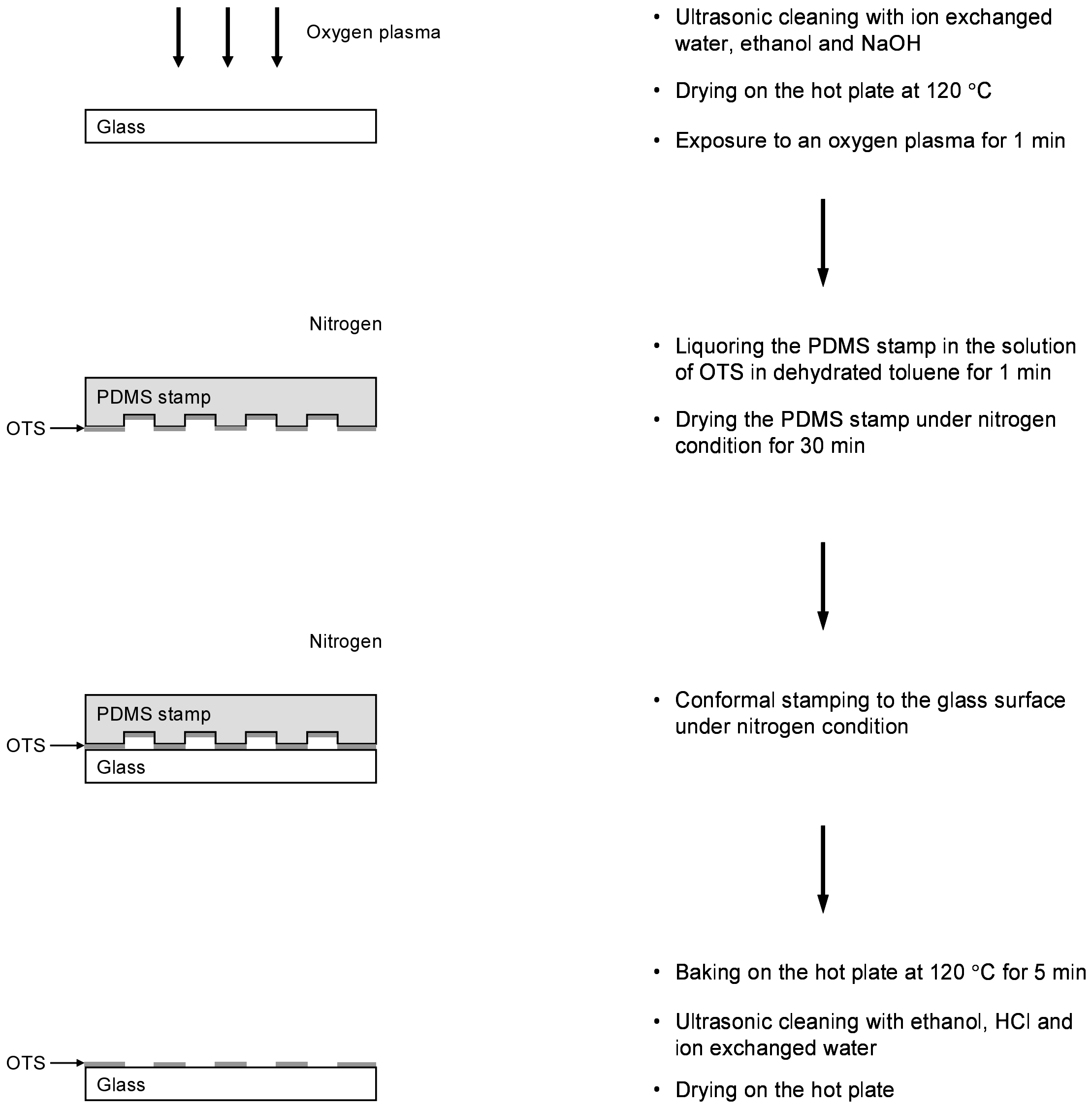

- Ultrasonic cleaning with ion exchanged water, ethanol and NaOH
- Drying on the hot plate at 120 °C
- Exposure to an oxygen plasma for 1 min

- Liquoring the PDMS stamp in the solution of OTS in dehydrated toluene for 1 min
- Drying the PDMS stamp under nitrogen condition for 30 min

- Conformal stamping to the glass surface under nitrogen condition

- Baking on the hot plate at 120 °C for 5 min
- Ultrasonic cleaning with ethanol, HCl and ion exchanged water
- Drying on the hot plate

Figure 2.13. Schematic outline of the process for microcontact printing of OTS to the glass surface using a PDMS stamp.

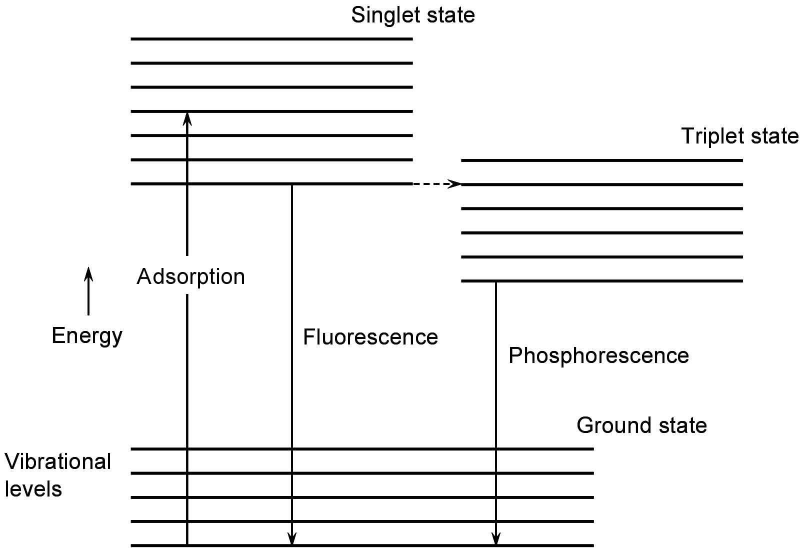

Figure 2.14. Schematic of the energy-level diagram.

glass surface was 112° (hydrophobic), and that of glass and PDMS surfaces are 27° (hydrophilic) and 104° (hydrophobic), respectively. These measured contact angles show quite agreement with those obtained by previous studies (Wasserman *et al.*, 1989; McGovern *et al.*, 1994; Lee *et al.*, 2003; Benor *et al.*, 2007).

2.3 Microscopic Measurement Using Fluorescence

The present study performs microscopic measurements focusing on the fluid flow in the microchannel based on fluorescence imaging techniques. Fluorescent dyes and submicron fluorescent particles are used for the scalar and velocity measurements, respectively. This section describes fundamentals of measurements using fluorescence microscope. Most widely used method is epi-fluorescence microscopy, in which an excitation light for the fluorescence is provided to a sample through an objective lens. For improving the measurement resolution to the order of nanometers, total internal reflection fluorescence microscopy using the evanescent wave as the excitation light is utilized.

2.3.1 Fluorescence

Fluorescence is the radiation processes, which is induced by molecules or atoms excited by the absorption of radiation (Becker, 1969). Figure 2.14 shows schematic of the energy level diagram. When a molecule is excited, an outer electron jumps from the ground state to the excited singlet state. From this state, there can occur de-excitation to the ground state by fluorescence emission or by radiationless collision, or crossing to the triplet state. Because fluorescence occurs from the lowest singlet excitation state, which is lower than the initial excited state by the absorption, the fluorescence wavelength is longer than the absorption wavelength. A time about 10^{-10}–10^{-7} s is required for the fluorescence processes. Since the molecule randomly rotates during this lifetime by the Brownian motion, fluorescence is partially (or totally) depolarized and the intensity is independent of direction (Walker, 1987; Valeur, 2002).

When a fluorescent solution at low enough concentration, c_f (mol/m^3), is irradiated by the excitation intensity, I_e (W/m^3), the fluorescent intensity, I_f (W/m^3), is given by (Walker, 1987; Coppeta & Rogers, 1998)

$$I_f(\lambda) = I_e(\lambda) c_f \phi \gamma(\lambda) L_s \tag{2.51}$$

where λ (m) is the excitation wavelength, ϕ (-) is the quantum yield and γ (m^2/mol) is the molar absorption coefficient, and L_s (m) is the length of the sampling volume. The fluorescence is widely used for the scalar measurement, i.e., laser induced fluorescence, by the dependence of the quantum yield and the molar absorption coefficient on the temperature and pH, respectively (Sakakibara & Adrian, 1999; Ross *et al.*, 2001*a*; Erickson *et al.*, 2003; Sato *et al.*, 2003*b*; Shinohara *et al.*, 2004, 2005; Ichiyanagi *et al.*, 2007). However, since the fluorescence characteristics are different in each species of molecule, a fluorescence molecule should be optimally selected with a system and an objective of the measurement (Coppeta & Rogers, 1998).

2.3.2 Evanescent Wave

Evanescent wave is an electromagnetic field, which decays exponentially with the distance from an interface separating two media of different refractive indices, n (-).

When a light passes through the interface, the light is partially reflected back into the first medium ($n = n_1$) and partially transmitted into the second medium ($n = n_2$) as shown in figure 2.15. The angles of incidence and refraction, θ_i (°), and θ_r (°), respectively, are related by the Snell's law (de Fornel, 2001),

$$n_1 \sin\theta_i = n_2 \sin\theta_r \tag{2.52}$$

When the refractive index of the first medium is larger than that of the second medium ($n_1 > n_2$), the refractive angle is always larger than the incident angle ($\theta_r > \theta_i$). Thus, an increase in the incident angle results in the refractive angle of $\theta_r = 90°$. The incident angle at $\theta_r = 90$ is defined as the critical angle, θ_c (°), given by

$$\theta_c = \sin^{-1}\frac{n_2}{n_1} \tag{2.53}$$

When the incident angle is larger than the critical angle, θ_c (°), the light is totally reflected at the interface. However, the electromagnetic field of the incident light penetrates into the second medium and propagates parallel to the surface in the plane of incidence, i.e., the evanescent

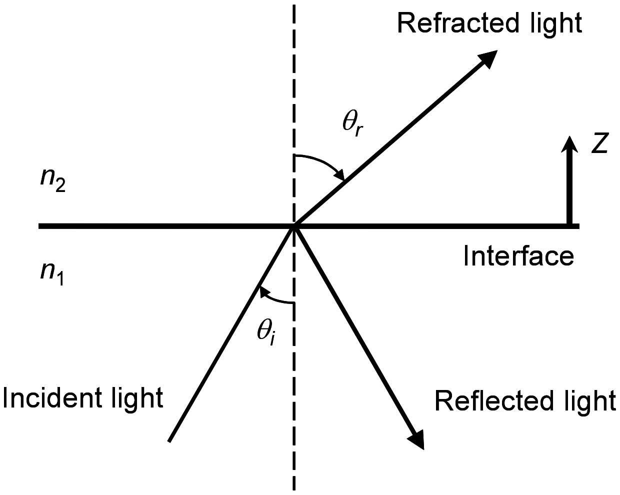

Figure 2.15. Schematic of refraction of light at an interface between two media of different refractive indices ($n_1 > n_2$).

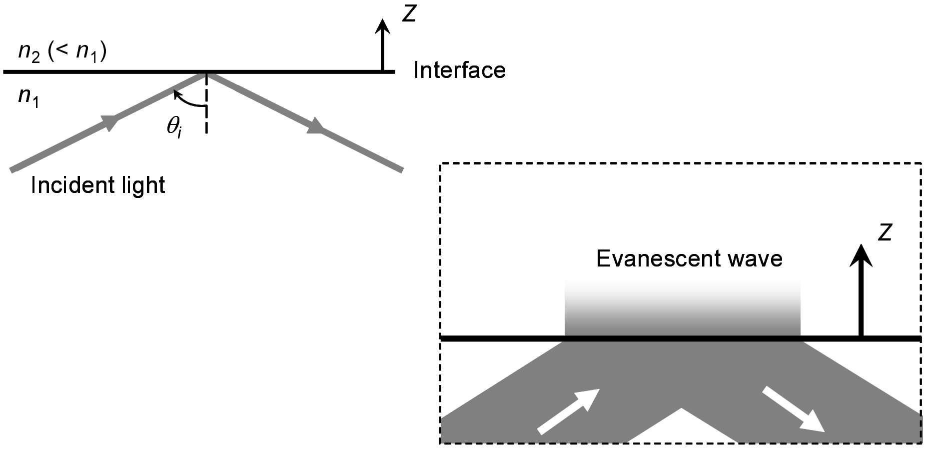

Figure 2.16. Schematic of the evanescent wave generated by total internal reflection of light at the interface.

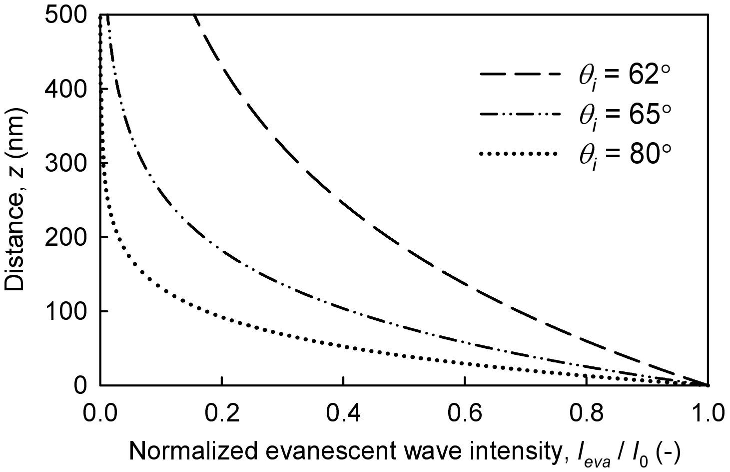

Figure 2.17. The profiles of evanescent wave intensity at different incident angles, when the light of $\lambda = 488$ nm is totally reflected at an interface between borosilicate glass ($n_1 = 1.522$) and water ($n_2 = 1.336$).

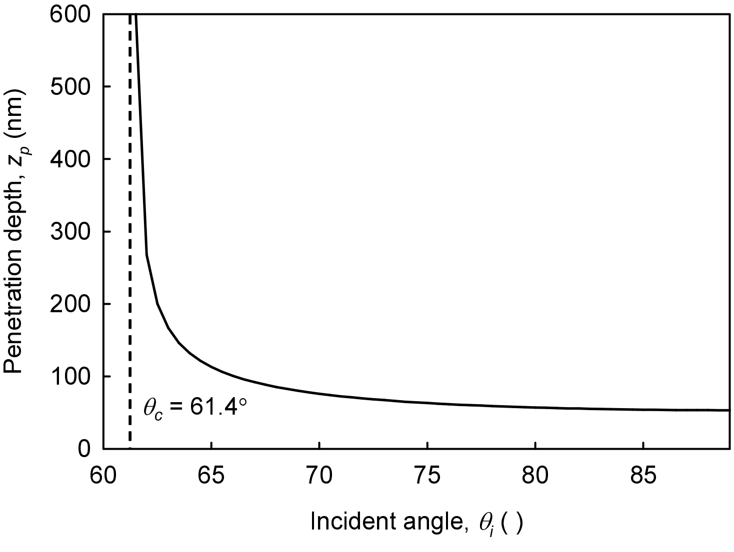

Figure 2.18. Relationship between the incident angle and the penetration depth of the evanescent wave, when the light of $\lambda = 488$ nm is totally reflected at an interface between borosilicate glass ($n_1 = 1.522$) and water ($n_2 = 1.336$).

wave as shown in figure 2.16 (Axelrod *et al.*, 1984; Prieve & Frej, 1990; de Fornel, 2001). The evanescent wave intensity, I_{eva} (W/m^3), decays exponentially with the distance, z (m), from the interface, defined as

$$I_{eva}(z) = I_0 \exp\left(-\frac{z}{z_p}\right) \tag{2.54}$$

where I_0 (W/m^3) is the intensity at the interface and z_p (m) is the penetration depth given by

$$z_p = \frac{\lambda}{\sqrt{n_1^2 \sin^2\theta_1 - n_2^2}} \tag{2.55}$$

where λ (m) is the wavelength in a vacuum. The penetration depth, z_p (m), is independent of the polarization of the incident light. Figure 2.17 shows the profiles of evanescent wave intensity at different incident angles, when the light of $\lambda = 488$ nm is totally reflected at an interface between borosilicate glass ($n_1 = 1.522$) and water ($n_2 = 1.336$). The evanescent wave decays exponentially from the interface more significantly with increasing the incident angle. Figure 2.18 shows a relationship between the incident angle of total internal reflection and the penetration depth of the evanescent wave at the borosilicate glass-water interface. The penetration depth is significantly decreased with increasing the incident angle near the critical angle, $\theta_c = 61.4°$, but slightly decreased near the incident angle of 90° (Kihm *et al.*, 2004).

2.3.3 Fluorescence Microscopy

The present study develops the micro- and nanoscale optical measurement techniques based on fluorescence microscopy. Figure 2.19 illustrates fundamental setup of a fluorescence microscope (Nikon Corp., E800) and an inverted fluorescence microscope (Nikon Corp., TE2000U), i.e., epi-fluorescence microscopy. A continuous mercury lamp is used as an excitation light source. A filter block, which is composed of an excitation filter, a dichroic mirror and a barrier filter, is selected considering absorption and emission wavelengths of fluorescence. Table 2.4 lists two kinds of filter block for blue and green excitation used in the present study. The excitation light from the mercury lamp is routed through the excitation filter to provide excitation wavelengths, reflected by the dichroic mirror and illuminated to the fluorescence molecules in the microchannel. An excited fluorescence is collected through an objective lens, the dichroic mirror and the barrier filter to provide wavelengths longer than the excitation wavelengths, and finally captured by an imaging device.

Figure 2.20 shows a schematic of the recording optical system of the fluorescence microscope. Generally, the microscopic optical imaging is affected by the diffraction of light. The diameter of the diffraction-limited point spread function in the image plane, d_s (m), is given by

$$d_s = 2.44M\frac{\lambda}{2NA} \tag{2.56}$$

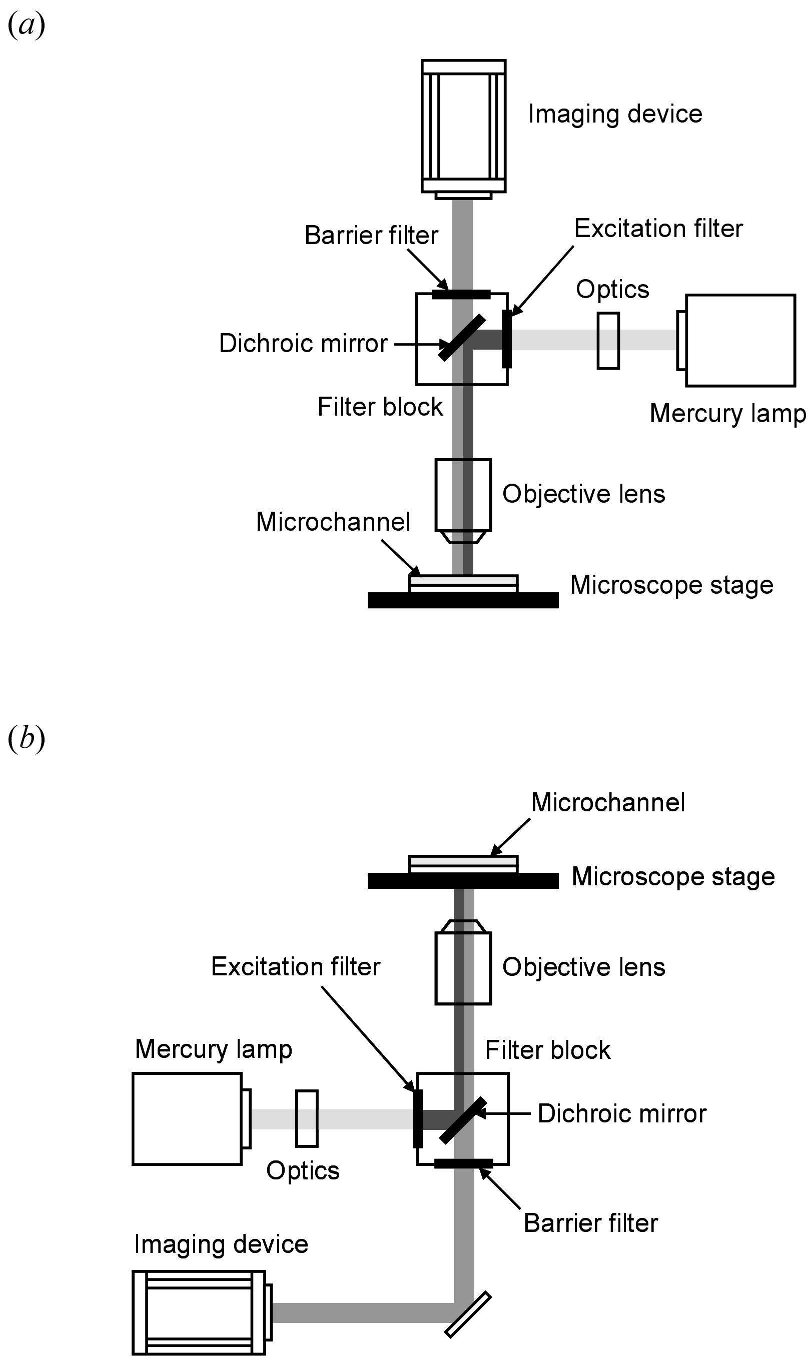

Figure 2.19. Schematic diagrams of (*a*) a fluorescence microscope and (*b*) an inverted fluorescence microscope.

Table 2.4. Properties of filter blocks for blue and green excitaiton (Nikon Corp.)

Filter block	Excitation filter (nm)	Dichroic mirror (nm)	Barrier filter (nm)
Blue excitation	450 – 490	505	515
Green excitation	510 – 560	575	590

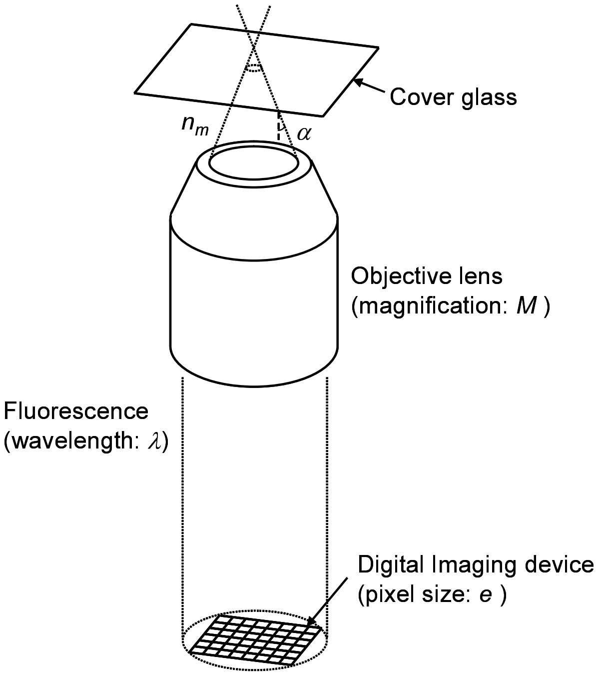

Figure 2.20. Schematic of the recording optical system of the fluorescence microscope.

where M (-) is the total magnification of the microscope and NA (-) is the numerical aperture of the objective lens, which is given by

$$NA = n_m \sin\alpha \tag{2.57}$$

where n_m (-) is the refractive index of the immersing medium between the objective lens and the cover glass, and α (°) is the half-angle of the maximum collection cone of light (Born & Wolf, 1999; Meinhart *et al.*, 1999). In the imaging of a finite-diameter particle, the particle image is the convolution of the diffraction-limited image with the geometric image (Adrian, 1991). Approximating both the diffraction-limited and geometric images as Gaussian functions, an effective particle diameter captured on the imaging device, d_e (m), is given by

$$d_e = \left(M^2 {d_p}^2 + {d_s}^2\right)^{1/2} \tag{2.58}$$

On the other hand, since the entire test section in the depthwise direction is illuminated by the volume of excitation light, i.e., the volume illumination, the depthwise resolution of the image plane is defined by the characteristic of the recording optical system. The depth of field of the microscope, which is the summation of the depth of fields by the diffraction and geometric effects, is given by Inoué & Spring (1997) as

$$\delta z = \frac{n_m \lambda}{NA^2} + \frac{n_m e}{NA\, M} \tag{2.59}$$

where e (m) is the smallest distance resolved by the imaging device (pixel size). Meinhart *et al.* (2000*a*) proposed the measurement depth in the velocity measurement using tracer particles, δz_m (m), given by

$$\delta z_m = \frac{3 n_m \lambda}{NA^2} + \frac{2.16 d_p}{\tan\alpha} + d_p \quad \text{for } d_p > \frac{e}{M} \tag{2.60}$$

Equation (2.60) is the summation of the measurement depths due to diffraction and geometrical optics and the particle diameter.

Tables 2.5 and 2.6 list the objective lenses and the imaging devices, respectively, which are used in the present study. Since the fluorescence lifetime about 10^{-10}–10^{-7} s is extremely shorter than the frame rate of the cameras, the temporal resolution of measurement is determined by the frame rate. Combination of the objective lens and the imaging device for the recording optical system is selected with the experimental condition. The present study performs two types of the measurement using fluorescence. One is the zeta-potential measurement using a fluorescent dye, which focuses on the distribution of the fluorescent intensity as described in chapter 4. Thus, for the fluorescence imaging, the CCD camera is selected for the experiments considering their superiority in the signal to noise ratio (S/N), the image uniformity and the linearity toward the intensity compared with CMOS camera (Golden & Ligler, 2002; Hain *et al.*, 2007). The other is the velocity measurement using fluorescent tracer particles, which focuses on the particle displacement in a flow field, as described in chapter 3.

Table 2.5. Specifications of the objective lenses (Nikon Corp.)

Objective lens	Magnification M (-)	Numerical aperture NA (-)
Dry lens		
CFI S Fluor	10	0.5
Oil immersion lens		
CFI Plan Fluor	40	1.3
CFI Plan Apo	60	1.4
TIRF	60	1.45

Table 2.6. Setups of the digital imaging devices

Camera	Device	Resolution (pixels)	Pixel size e (μm)	Depth (bit)	fps (1/s)
Hamamatsu Photonics K. K.					
C4880-80	CCD	656×494	9.9	12	27
Vision Research Inc.					
Phantom V7.1	CMOS	800×600	22	10	2500

In order to obtain the enough spatial resolution for the particles, the objective lens and the camera are selected to implement a condition that the effective particle diameter captured on the camera, d_e (m), given by equation (2.58) is larger than the single pixel size, e (m). The CMOS camera is used for the near wall velocity measurement using the evanescent wave and the time-resolved velocity measurement of the transient electroosmotic flow because of their high temporal resolution (Hain *et al.*, 2007).

2.3.4 Total Internal Reflection Fluorescence Microscopy

Total internal reflection fluorescence microscopy (TIRFM) (Axelrod *et al.*, 1984; Axelrod, 2001) is an advanced technique of fluorescence microscopy. The evanescent wave is used as the excitation light of fluorescence and enables the selective illumination with nanometer-resolution in the vicinity of a solid surface. Thus, compared with the epi-fluorescence microscopy, TIRFM enables the nanoscale optical measurement near the solid surface and the clear fluorescence imaging with low background intensity. Figure 2.21 illustrates several configurations of TIRFM (Conibear & Bagshaw, 2000).

The most popular configuration is the objective lens-based TIRFM shown in figure 2.21(*a*), which is based on an oil immersion objective lens with a high numerical aperture (Axelrod, 2001). A laser beam is focused on the back focal plane at the peripheral region of the objective lens, refracted at the lens and introduced into a cover glass through an immersion oil. The evanescent wave is generated by the total internal reflection of the collimated laser beam at an interface between the cover glass and aqueous solution. The maximum incident angle, θ_i (°), is determined by the numerical aperture of the objective lens, NA (-), given by equation (2.57). Considering the Snell's law and the critical angle, θ_c (°), as shown in equations (2.52) and (2.53), respectively, in order to occur total internal reflection at the interface between borosilicate glass ($n_1 = 1.522$) and water ($n_2 = 1.336$), NA must be higher than $n_1 \sin\theta_c = n_2 = 1.336$. The advantages of this configuration is that it enables the high S/N and detailed measurement, and is easy to access the sample and mount other optical components. However, due to the limitation of the numerical aperture, the magnification of objective lens is restricted to be $M \geq 60$. Another disadvantage is that the thickness of the cover glass is determined by the glass material to locate the spot of total internal reflection at the imaging region (for example, borosilicate cover glass of 0.17 mm thickness).

Another typical configuration is the prism-based TIRFM shown in figure 2.21(*b*) and (*c*). The laser beam is guided by the prism to generate the evanescent wave at the interface. A major advantage of this configuration is wide selectivity for the magnification of measurements because the optical system to generate the evanescent wave is independent of the objective lens. Figure 2.21(*b*) shows a conventional prism-based TIRFM, in which the prism is located in the opposite side toward the objective lens. It enables the high S/N measurement with single

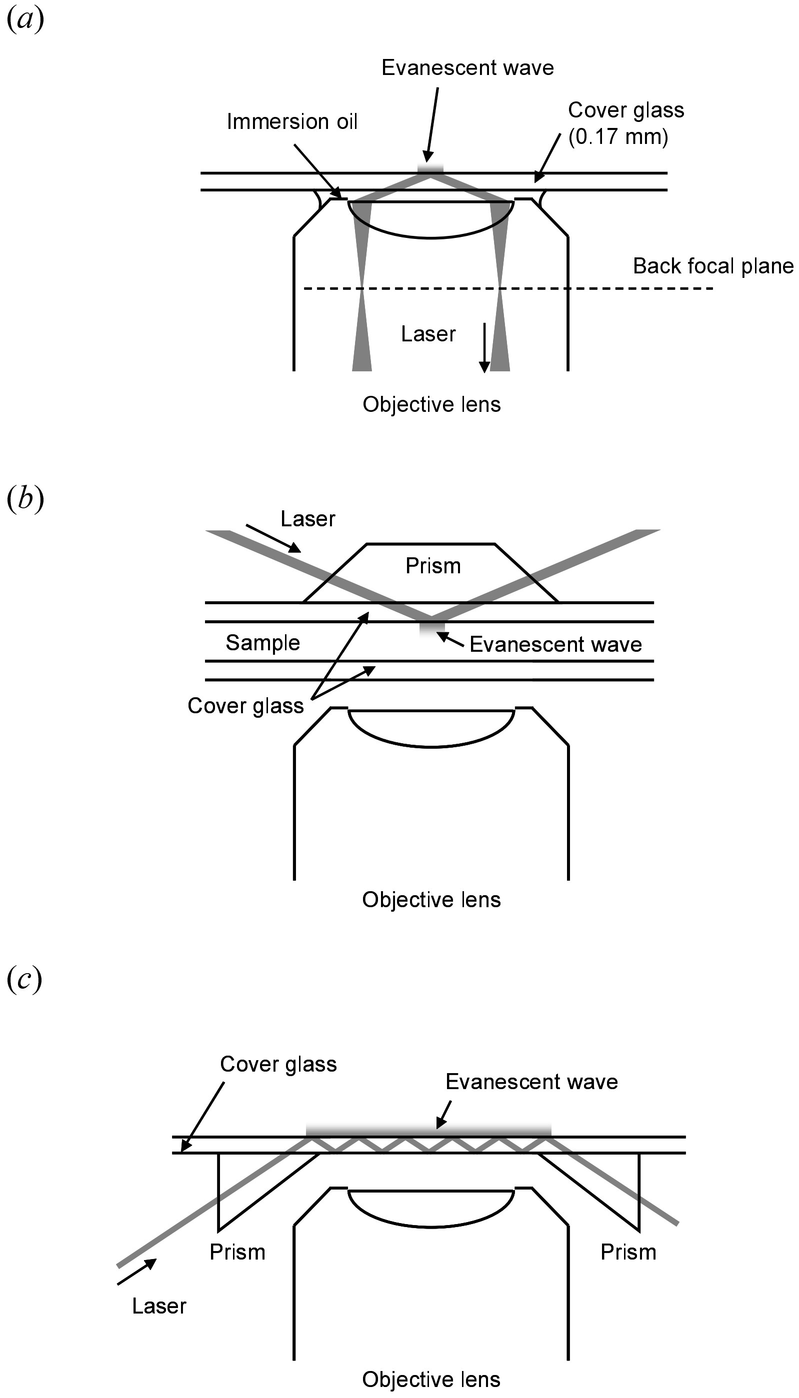

Figure 2.21. Schematics of (*a*) the objective lens-based TIRFM, and the prism-based TIRFMs, in which (*b*) the prism is located in the opposite side toward the objective lens and (*c*) entry and exit prisms are located in the same side as the objective lens.

total internal reflection but has difficulty in access to the sample. Figure 2.21(*c*) shows another prism-based TIRFM, in which entry and exit prisms are located in the same side as the objective lens to allow multiple total internal reflections inside the coverglass. This configuration is easy to access the sample but signal to noise ratio is decreased because of the light scatter from the adjacent reflections close to the objective lens (Conibear & Bagshaw, 2000). Since the two prisms are glued to the coverglass, it is difficult to adjust the light path of laser beam.

In a standard practice, the penetration depth of the evanescent wave is calculated from the geometry of optical system in the microscope. However, the estimated penetration depth has an uncertainty because of an intrinsic error in the optical system (Harlepp *et al.*, 2004). Considering the relationship between the incident angle of the total internal reflection and the penetration depth as shown in figure 2.18, in order to minimize the uncertainty in the penetration depth, the incident angle must be enough larger than the critical angle.

2.3.5 Micron-Resolution Particle Image Velocimetry

The present study performs the velocity measurements of fluid flow in a microchannel by particle image velocimetry (PIV) (Adrian, 1991; Tropea *et al.*, 2007). Small tracer particles are seeded into the fluid and images of the test section are captured by a digital imaging device. The fluid velocity is obtained by measuring the displacement of tracer particles during a short time interval as illustrated in figure 2.22.

In PIV, patterns of tracer particles in interrogation windows are used to obtain an array of velocity vectors (figure 2.22(*a*)). Generally, the interrogation windows are overlapped by 50% to satisfy the Nyquist sampling theorem. The particle image in the interrogation window in the first frame is used as a reference for the match candidates in the second frame. The most likely particle-image pairing between the first and second frame is determined by the spatial cross-correlation of the interrogation images (Westerweel, 1997; Tropea *et al.*, 2007). This cross-correlation pattern matching is implemented by the hierarchical computational scheme (Roesgen & Totaro, 1995; Kumar & Banerjee, 1998). Each image is subsampled to obtain a set of images progressively decreasing in resolution and size. The displacements obtained from image pairs of lower resolution are used for more accurate predictions at the higher resolution level. Since the particle images captured by the digital imaging device are discrete, the obtained displacement has the uncertainty of ±0.5 pixel. Hence, a subpixel interpolation based on Gaussian peak fit is performed to determine the subpixel displacement (Westerweel, 1997; Tropea *et al.*, 2007). When the particle diameter captured on the digital imaging device, d_e/e (-), calculated by equation (2.58) is 2~4 pixel, both the bias and random errors by the Gaussian peak fit is minimized (Tropea *et al.*, 2007). On the other hands, the velocity measurenment using the displacement of individual tracer particles is especially termed particle tracking velocimetry (PTV) as shown in figure 2.22(*b*). First, particles in the each image are

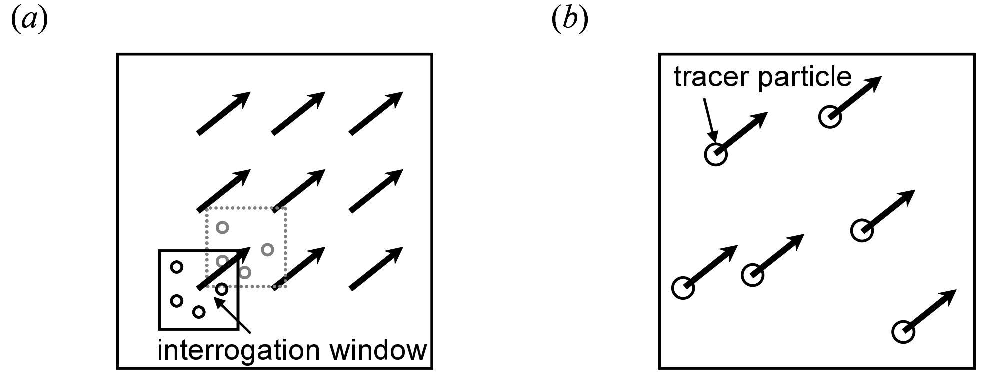

Figure 2.22. Schematics of (*a*) particle image velocimetry and (*b*) particle tracking velocimetry.

detected by the dynamic threshold binarization (Ohmi & Li, 2000; Sato *et al.*, 2003*a*). The centroid of the particles in the digital image is estimated by the subpixel interpolation based on the Gaussian peak fit. Then, particle pairs between the first and second frame are determined by the spatial cross-correlation of the particle images. The array of velocity vectors obtained by PIV performed prior to PTV is used as guides in the cross-correlation particle matching process (Cowen & Monismith, 1997; Stitou & Riethmuller, 2001; Sato *et al.*, 2003*a*).

Santiago *et al.* (1998) proposed micron-resolution particle image velocimetry (micro-PIV) for the velocity measurement in microspace using fluorescence microscope. Submicron particles labeled with a fluorescent dye are used to trace the fluid flow. Due to the small particle diameter and the small scale of test section, the Brownian motion of tracer particles become obvious in the measurement. The measured particle velocity is given by using the mean square displacement of the Brownian motion (equation (2.28))

$$u_p = u \pm \frac{1}{\mathit{\Delta} t}\sqrt{\langle \mathit{\Delta} x^2 \rangle} \tag{2.61}$$

When the fluid velocity is 10^{-3} m/s, the particle diameter is 10^{-7} m and the time interval is 10^{-2} s, the relative error due to the Brownian motion, i.e., the ratio of the fluid velocity to the Brownian velocity, is 3%. Since the displacement of the Brownian motion is unbiased and random, the temporally averaging over the instantaneous velocities is applied to eliminate the measurement error due to the Brownian motion (Santiago *et al.*, 1998; Meinhart *et al.*, 2000*b*). When the fluid velocity is constant over the measurements (flow is at the steady state) and the each measurement is statistically independent, the velocity obtained by the ensemble averaging over N particle velocities is expressed as (Santiago *et al.*, 1998)

$$\frac{1}{N}\sum u_p = u \pm \frac{1}{\mathit{\Delta} t}\sqrt{\frac{\langle \mathit{\Delta} x^2 \rangle}{N}} \tag{2.62}$$

Therefore, the terms by the Brownian motion is nearly zero at substantially large N and the obtained velocity closes to the fluid velocity. When the ensemble averaging over 100 vectors is applied ($u = 10^{-3}$ m/s, $d_p = 10^{-7}$ m and $\Delta t = 10^{-2}$ s), the relative error due to the Brownian motion is reduced to 0.3%.

Chapter 3

Velocity Measurement Technique for Transient Electroosmotic Flow Using Fluorescent Submicron Particles

This chapter presents a time-resolved velocity measurement technique for transient electroosmotic flow using fluorescence microscope and fluorescent submicron particles. This technique employs particle tracking velocimetry at low particle number density to reduce errors in the measurement of electroosmotic velocity. An iterative measurement is conducted to achieve the high spatial resolution of the measurement. The combined measurement of near-wall and bulk velocities is achieved by the measurement system with the evanescent wave and volume illumination.

3.1 Fluorescent Submicron Particle

Fluorescence-labeled polystyrene particles with a diameter of 500 nm, a density of 1055 kg/m^3 and an electrical conductivity of 1.0×10^{-13} μS/cm (Invitrogen, Corp., FluoSpheres) (Haugland, 2005) were used as tracer particles. A peak of the absorption and emission wavelength of fluorescence is 505 nm and 515 nm, respectively. Because the particle surface is modified by carboxyl groups, it is negatively charged by the ionization of carboxyl groups in the electrolyte solution: $\text{-COOH} \rightleftharpoons \text{-COO}^- + \text{H}^+$. The particle relaxation time to the liquid calculated by equation (2.26) is 24 ns. Magnitude of the particle sedimentation is evaluated by a ratio of the gravitational to the diffusive forces, which is described by the Peclet number (Banerjee & Kihm, 2005)

$$Pe = \frac{UL}{D} = \frac{\left(\rho_p - \rho\right) d_p^3 g}{18\mu D} \tag{3.1}$$

where $U = (\rho_p - \rho)d_p^2 g/18\mu$ (m/s) is the sedimentation velocity given by using the Stokes law (equation (2.24)) (Probstein, 1994), $L = d_p$ (m), D (m^2/s) is the particle diffusivity by the Stokes-Einstein equation (equation (2.27)), and $g = 9.8$ m/s^2 is the gravitational acceleration. In the present study, due to the Peclet number of 4.5×10^{-3} at the sedimentation velocity of 8.8 nm/s, the Brownian motion of tracer particles is dominant in the stationary fluid. Thus, the effect of the sedimentation on the velocity measurement is negligible.

3.2 Working Fluid

An electrolyte aqueous solution was prepared as a working fluid for the velocity measurement of transient electroosmotic flow. The electrolyte solution was composed of a 5 mmol/*l* HEPES buffer (4-(2-hydroxyethyl)-1-piperazineethanesulfonic acid) to keep pH in constant (Beynon & Easterby, 1996). Potassium chloride (KCl) was dissolved at 1 mmol/*l*. pH and the electrical conductivity of the solution were 7.18 and 284 μS/cm, respectively. Fluorescent submicron tracer particles are added into the electrolyte solution at a number density of 1.22×10^{10} particles/m*l*. The thickness of the electric double layer at solid-liquid interfaces, i.e., the Debye length was calculated to be 9.6 nm by equation (2.36).

3.3 Velocity Measurement of Transient Electroosmotic Flow by Particle Tracking Velocimetry

The time-resolved velocity measurement technique for transient electroosmotic flow by particle tracking velcimetry (PTV) was developed.

3.3.1 Measurement Principle for Transient Electroosmotic Flow

The time resolution of the velocity measurement was determined considering the relaxation time of electroosmotic flow and particle electrophoresis (Yan *et al.*, 2006, 2007). The particle motion in the liquid on an application electric field is the superposition of electroosmotic and electrophoretic components (equation (2.50)). Hence, the electroosmotic velocity is obtained by subtracting the electrophoretic velocity from the observed velocity

$$\boldsymbol{u_{eof}} = \boldsymbol{u_p} - \mu_{ep}\boldsymbol{E} \tag{3.2}$$

where μ_{ep} (m^2/V s) is the electrophoretic mobility at the steady state, which is obtained preliminarily (details are described in section 3.5). The order of the relaxation time of electroosmotic flow is $\tau_{eof} = 10^{-2}$ s because of the channel scale of 10^{-4} m, given by equation (2.43). The relaxation time of electrophoresis by the hydrodynamic relaxation, the double-layer polarization and the concentration polarization are $\tau_{ep} = 10^{-7}$ s, $\tau_{dl} = 10^{-8}$ s and $\tau_{cp} = 10^{-5}$ s, respectively, calculated by equations (2.47) to (2.49) using the properties of tracer particles and working fluid (sections 3.1 and 3.2). Since the magnitude of the double-layer and concentration polarization are considered to be small due to the ratio of the particle radius to the Debye length of $r_p/\lambda_D = 26$ (section 2.1), the hydrodynamic relaxation time is regarded as the characteristic time of electrophoresis. Therefore, the order of the time resolution is set to be 10^{-4} s to satisfy a following condition: $\tau_{ep} << \Delta t < \tau_{eof}$ where Δt (s) is the time resolution. The electrophoresis is assumed to be at the quasi-steady state in this condition, and thus the electroosmotic velocity can be obtained by equation (3.2). It is noted that the relaxation of particle electrophoresis will be affected by the Brownian motion. Hunter (1981) concluded that the effect of the Brownian motion on the particle electrophoresis is generally small and negligible.

3.3.2 Time-Resolved Velocity Measurement Technique

PTV at a low particle number density, which measures the flow velocity by tracing individual particles, was employed to the time-resolved velocity measurement. In the velocity measurement of electrokinetic flow, the low particle number density can reduces the errors caused by the particle agglomeration and particle adhesion to the microchannel wall, which result in the local change of electrophoretic and electroosmotic mobilities. On the other hand, a shortage in the use of PTV is that the spatial resolution is not enough owing to the low particle number density. In order to achieve the high spatial resolution, an iterative measurement method focusing on the reproducibility of the laminar flow at low Reynolds number was proposed.

Figure 3.1 depicts a schematic diagram of the iteration measurement. Acquisition of time-series n images is triggered at a timing when the fluid starts to move by unsteady flow. m sets of the images are obtained by the iterative acquisitions, and the particle displacements at each image are measured by the PTV algorithm (section 2.3). Since the laminar flow at low Reynolds number has the reproducibility, the ith instantaneous vector maps in each sequence are considered to be the results at the same time. Thus, the vector maps at the same time are integrated over m iterations to obtain time-series vector maps with the high spatial resolution. The measured particle displacements involves errors due to the random Brownian motion of particles and the bias and random errors by PTV. In order to reduce the errors, the particle displacements are spatially averaged in reference regions to obtain an array of vectors (Sato *et al.*, 2003*a*). Therefore, the spatial resolution of the measurement is defined by the area of the reference region and increased to the maximum value equal to the diameter of tracer particles with increasing the number of iteration. It is noted that the reference regions are overlapped by 50% to satisfy the Nyquist sampling theorem. The time resolution is defined by the time interval of the image pair for the PTV result.

The particle velocity is calculated from the particle displacement, Δx (m), during the time

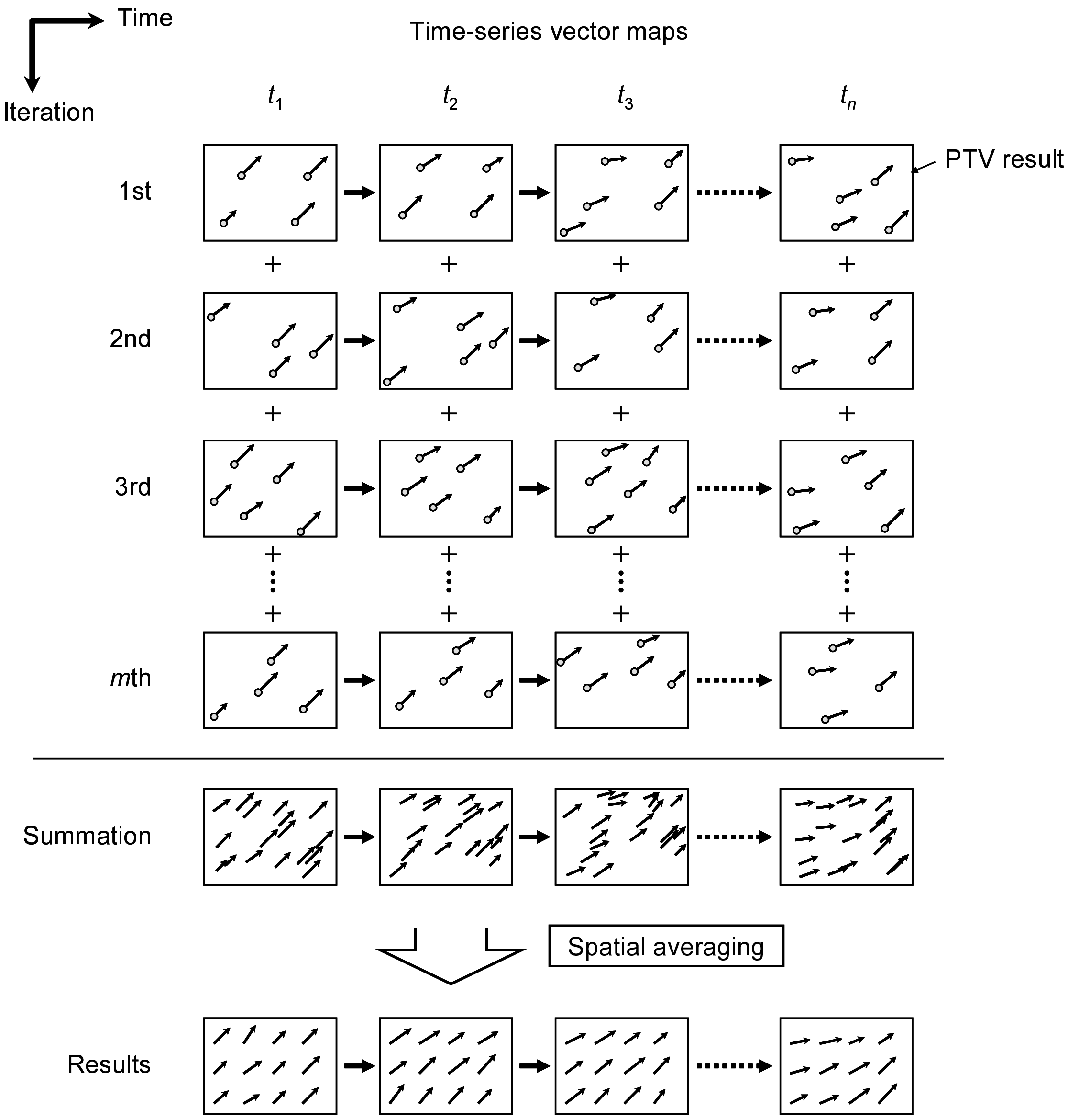

Figure 3.1. Schematic diagram of the iteration measurement method using PTV.

interval, Δt (s), on the basis of the central difference to minimize an error caused by the variation of the flow velocity during the time interval. From the Taylor expansion, the particle velocity is approximated as follows, using the particle displacement, $x = f(t)$ (m),

$$\begin{aligned} u = \frac{\partial f}{\partial t} &\approx \frac{f\left(t + \frac{\Delta t}{2}\right) - f\left(t - \frac{\Delta t}{2}\right)}{\Delta t} - \frac{1}{24}\frac{\partial^3 f}{\partial t^3}\Delta t^2 \\ &\approx \frac{\Delta x}{\Delta t} + O(\Delta t^2) \end{aligned} \tag{3.3}$$

The second term in the right-hand side is the error of the approximation, which decreases linearly by Δt^2. When the error of the approximation is negligible due to the small time interval, the particle velocity is obtained by $u = \Delta x/\Delta t$.

3.3.3 Bulk Velocity Measurement by Volume Illumination

The iterative method by PTV was applied to the bulk velocity measurement using the volume illumination. The present technique with the volume illumination has two advantages compared with micron-resolution particle image velocimetry (PIV) as described in section 2.3.

The first advantage is that the time resolution of the measurement is increased due to the spatial averaging of the velocities to reduce the measurement error by the Brownian motion. Standard micro-PIV performs the temporal velocity averaging, and thus the time resolution is defined by the number of the averaging of the instantaneous velocity. In contrast, the time resolution of the present technique is equal to the time interval of the image pair as mentioned above.

The second advantage is that the high spatial resolution is achieved with the particle images of high signal to noise ratio at low particle number density. This is because the spatial resolution of the present technique is dependent on the number of the iteration rather than the particle number density. On the other hand, micro-PIV requires high particle number density to achieve the high spatial resolution but this leads to decrease in the signal to noise ratio of images. The signal to noise ratio of the volume illumination images was evaluated at two different particle number densities, 1.22×10^{10} particles/ml and 4.58×10^{10} particles/ml. The experimental condition was set to be same as the measurements in the present study. Figure 3.2 shows the volume illumination images of fluorescent particles in a microchannel, captured by the CMOS camera (table 2.6) at different depths with a magnification of 90 and $NA = 1.45$. The depthwise coordinate is the distance from the cover glass sealed with a microchannel made of poly(dimethylsiloxane) (PDMS). Table 3.1 lists signal to noise ratios of each image. High signal to noise ratios over 1.9 were achieved in the images at the lower particle number density due to the low magnitude of out-of-focus fluorescence. In contrast, the signal to noise ratios of the images at the higher particle number density are obviously low, and it is difficult

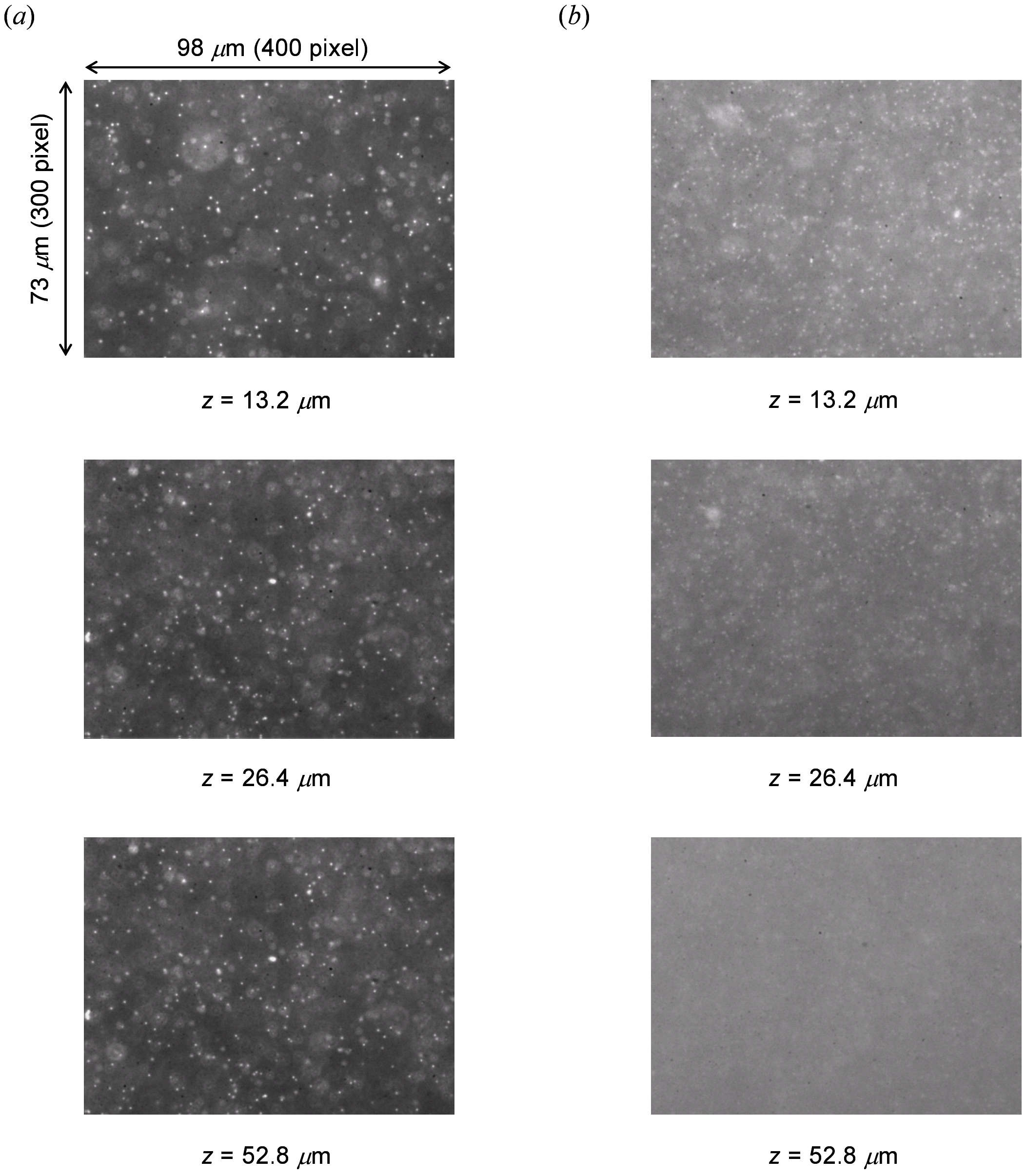

Figure 3.2. Sample particle images with the volume illumination. The particle number density is (*a*) 1.22×10^{10} particles/m*l* and (*b*) 4.58×10^{10} particles/m*l*.

Table 3.1. Signal to noise ratios of the volume illumination images

	Particle concentration (particles/ml)	
Depthwise position	1.22×10^{10}	4.58×10^{10}
z = 13.2 μm	2.93	1.52
z = 26.4 μm	2.39	1.31
z = 52.8 μm	1.91	1.05

to distinguish the individual particles at z = 52.8 μm due to further increase in out-of-focus fluorescence. Although an optimal particle number density is dependent on the magnification of measurements, the results shows that the particle number density is limited by the signal to noise ratio of images. Even if the particle number density is low, the present technique can realize the high spatial resolution by increasing the number of iteration.

3.3.4 Near-Wall Velocity Measurement by Evanescent Wave Illumination

The iterative method by PTV was also applied to the near-wall velocity measurement using the evanescent wave illumination. Figure 3.3 illustrates the schematic of the near-wall velocity measurement using the fluorescent submicron particles. The tracer particles only in the vicinity of the microchannel wall are illuminated by the evanescent wave decaying exponentially with the order of 100 nm, which is generated by the total internal reflection of a laser beam at the interface between the microchannel wall and the working fluid. The near-wall velocities are obtained from the particle displacements in the evanescent wave illumination area. Figure 3.4 shows the evanescent wave illumination image of fluorescent particles captured by the CMOS camera (table 2.6). The experimental condition was same as the measurements in the present study (90×, NA = 1.45, $\varDelta t$ = 400 μs). The penetration depth of the evanescent wave was 74 nm, and the evanescent wave intensity decays to 1% at z = 340 nm (given by equation (2.54)). Hence, considering the measurement depth of 1.94 μm by equation (2.60), the whole particles in the image were in-focus. The image obtained by the evanescent wave illumination has much higher signal to noise ratio than that by the volume illumination due to absence of out-of-focus fluorescence.

The measurement depth of the velocity measurement using the fluorescent particles and the evanescent wave illumination was approximately estimated from the theoretical analysis. Figure 3.5 depicts a fluorescent particle illuminated by the evanescent wave. The fluorescent intensity depends on the amount of fluorescent dye in tracer particles and proportional to the

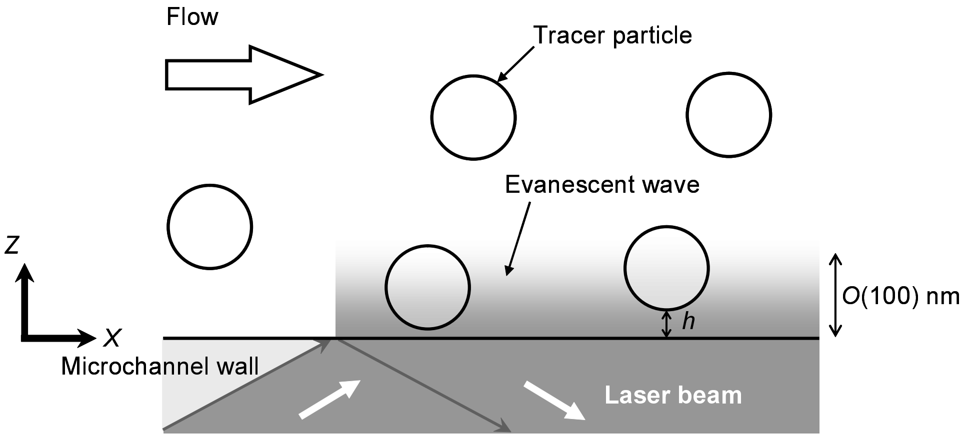

Figure 3.3. Schematic of the near wall velocity measurement using the evanescent wave illumination.

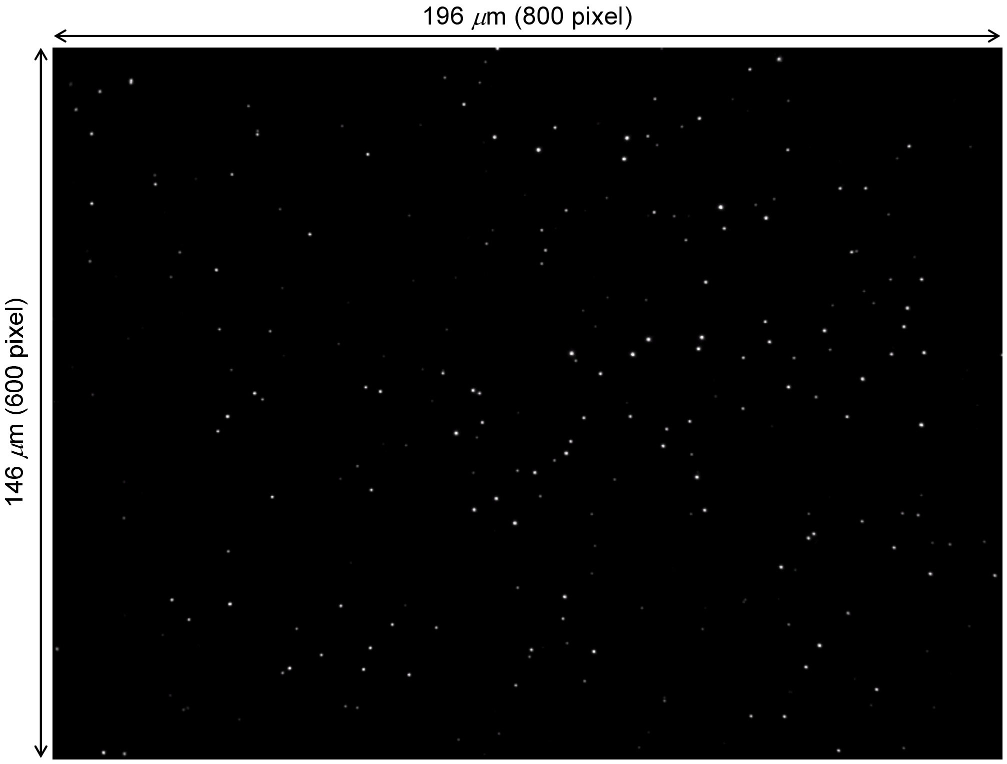

Figure 3.4. Sample images of fluorescent submicron particles with the evanescent wave illumination.

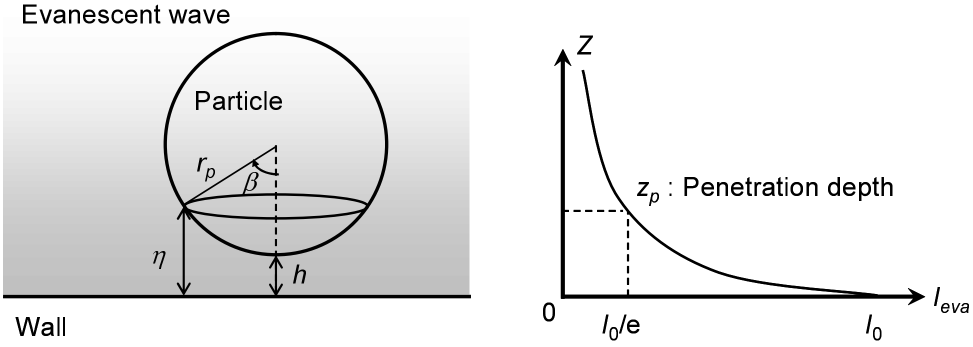

Figure 3.5. Fluorescent particle illuminated by the evanescent wave.

particle volume (Tropea *et al.*, 2007). Estimation of the measurement depth was conducted on assumptions as follows: (i) the particle is made of transparent material such as polystyrene, (ii) the fluorescent dye concentration is constant in the particle and the fluorescence is excited by the evanescent wave, (iii) the effects of the presence of the particle on the evanescent wave, i.e., light scattering, diffraction, refraction and reflection, are not considered, (iv) the evanescent wave intensity at the wall surface, I_0 (W/m^3), is constant. Since the evanescent wave intensity is only dependent on z (m) (equation (2.54)), the fluorescent intensity at the cross-section of the particle at $z = \eta$ (m) is obtained from equation (2.51), $c_f \phi \gamma I_{eva}(\eta) A_{cross}$, where A_{cross} (m^2) is the area of the cross-section given by using an angle, β (°),

$$A_{cross} = \pi r_p^2 \sin^2 \beta = \pi \left\{ r_p^2 - \left[r_p - (\eta - h) \right]^2 \right\} \tag{3.4}$$

Thus, the total fluorescent intensity emitted from the particle, $I_{f,p}$ (W), which is detected through an objective lens, is estimated by the integral,

$$\begin{aligned} I_{f,p} &= K \int_h^{h+2r_p} I_{eva}(\eta) A_{cross} d\eta \\ &= K\pi I_0 \int_h^{h+2r_p} \left\{ r_p^2 - \left[r_p - (\eta - h) \right]^2 \right\} \exp\left(-\frac{\eta}{z_p}\right) d\eta \\ &= 2K\pi I_0 z_p^3 \left[\left(\frac{r_p}{z_p} + 1 \right) \exp\left(-\frac{2r_p}{z_p} \right) + \frac{r_p}{z_p} - 1 \right] \exp\left(-\frac{h}{z_p} \right) \end{aligned} \tag{3.5}$$

where K (-) is the constant for the fluorescence and the collection efficiency by the objective lens. The total fluorescent intensity is the exponential function of the distance, h (m). Because the all particles in the evanescent wave illumination image are in-focus, the collection efficiency by the objective lens is assumed to be constant (Sadr *et al.*, 2005). Therefore, the measurement depth for the near-wall velocity measurement is simply defined as follows

$$\delta z_{eva} = -z_p \ln (1 - \chi) + d_p \tag{3.6}$$

where χ (-) is the collection efficiency of the imaging device. Equation (3.6) is the summation of the depth of the evanescent wave illumination area captured by the imaging device and the particle diameter. The depth of the evanescent illumination area is the value calculated on an assumption that the particle with the maximum intensity is located on the wall ($h = 0$).

There are several advantages of the present technique for the near-wall velocity measurement at the time resolution of 10^{-4} s over nano-partice image velocimetry (PIV) proposed by Zettner & Yoda (2003). Sadr *et al.* (2004) measured the near-wall electroosmotic velocity by nano-PIV with the image acquisition at the time interval of 10^{-3} s, and the measurement accuracy of nano-PIV was evaluated using artificial images by the Monte Carlo simulation (Sadr *et al.*, 2005). (i) Time-resolved velocity measurement is achieved by the spatial averaging of vectors to reduce the measurement error by the Brownian motion compared to nano-PIV with the temporal averaging. (ii) High spatial resolution is realized by the iterative measurement. In the near-wall velocity measurement, a measurement error occurs due to escape of tracer particles from the very thin illumination area by the Brownian motion. Furthermore, the particle number density is generally low in the evanescent wave illumination image because of the thinner measurement volume than the volume illumination. Sadr *et al.* (2005) pointed out that at least 30 particles in an interrogation region are required for nano-PIV to achieve an accuracy comparable to normal PIV. Thus, the spatial resolution becomes low to obtain the enough particle number, or the particle number density must be high. However, the high particle number density interrupts the combination with the measurement using the volume illumination due to the low signal to noise ratio as described above. In contrast, the iterative measurement by PTV at low particle number density can easily obtain the high spatial resolution by increasing the number of iteration, and can combine the measurements using the volume and evanescent wave illuminations. (iii) Measurement error by the Brownian displacements is low due to the short time interval. The maximum value of the Brownian displacement perpendicular to the wall in the evanescent wave was 20.7 nm in the evanescent wave illumination area, calculated by equations (2.27) to (2.29) and (2.31). Thus, the length scale of the Brownian motion is enough small compared to that of the particle diameter and the evanescent wave illumination depth. The small Brownian displacement prevents the escape of the tracer particles from the illumination area during the time interval.

3.4 Measurement System

3.4.1 Experimental Apparatus

Figure 3.6 shows schematics of the measurement system comprised of the inverted fluorescence microscope with the filter block for blue excitation (shown in table 2.4), the continuous

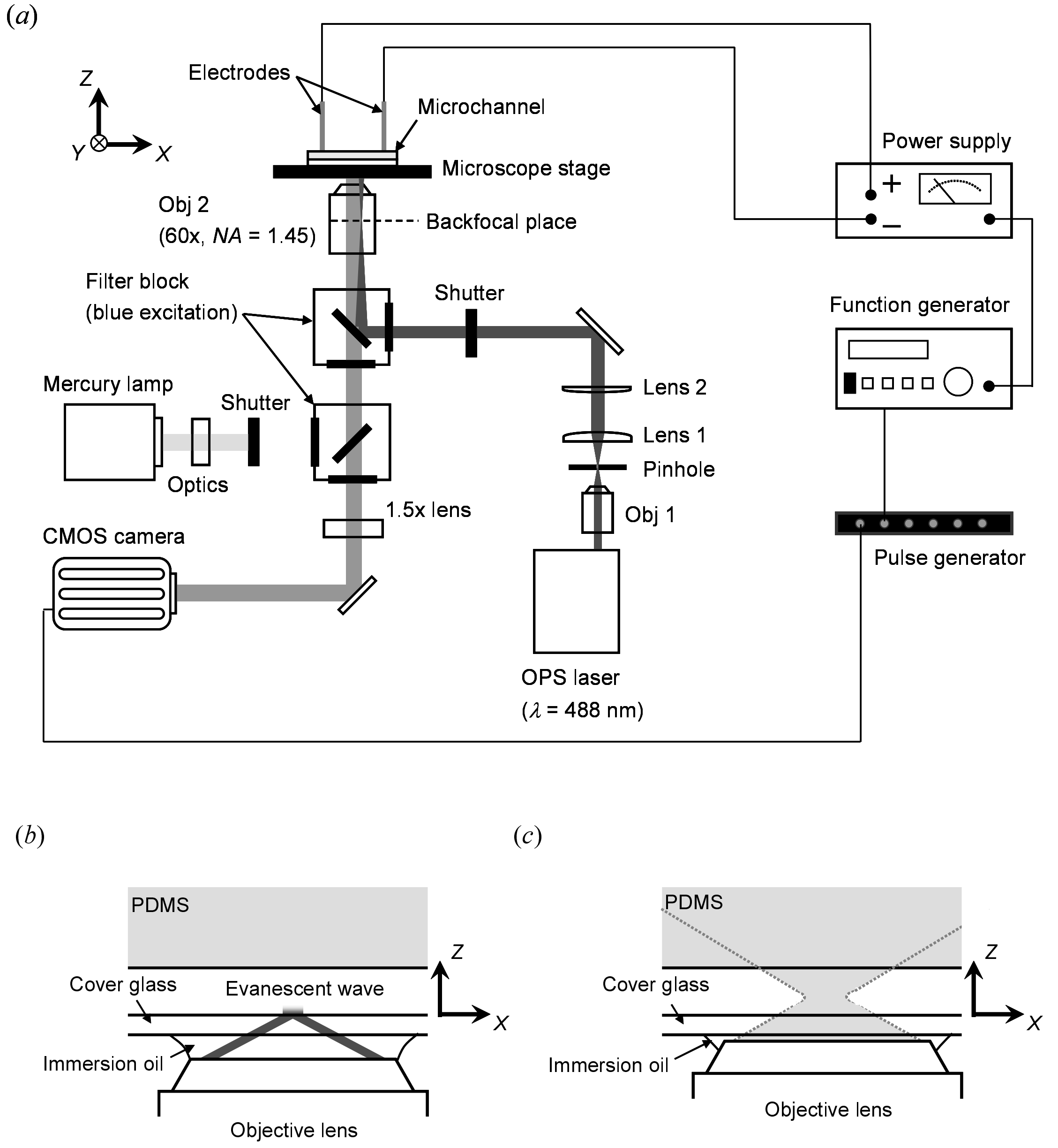

Figure 3.6. Schematics of (*a*) the measurement system for investigations of transient electroosmotic flow, (*b*) the evanescent wave illumination and (*c*) the volume illumination in the microchannel.

mercury lamp, an optically pumped semiconductor laser (Coherent Inc., Sapphire 488-30, laser power: 30 mW, $\lambda = 488$ nm) and the CMOS camera (shown in table 2.6). This system enables both the evanescent wave and volume illuminations for the velocity measurement. The iterative measurement for transient electroosmotic flow was performed by a timing control system using a pulse generator (Integrated Design Tools, Inc., MotionPro Timing Hub). A DC voltage, which induces electroosmotic flow in the microchannel, was applied through platinum electrodes by a power supply (KEPCO Inc., BOP 1000M).

The evanescent wave illumination as illustrated in figure 3.6(*b*) was conducted by objective lens-based total internal reflection fluorescence microscopy (section 2.3). A beam diameter was expanded by a beam expander combined with a spatial filter composed of an objective lens (Obj 1, 20×, $NA = 0.4$), a pinhole (diameter: 20 μm) and a convex lens (Lens 1, focal length: 500 mm). Then, the laser beam passed through a convex lens (Lens 2, focal length: 600 mm) and the excitation filter, was reflected by the dichroic mirror and focused on the back focal plane at the peripheral region of the oil immersion objective lens (Obj 2, 60×, $NA = 1.45$, table 2.5). The evanescent wave was generated by the total internal reflection of the collimated laser beam at the interface between the borosilicate glass ($n_1 = 1.522$) and the working fluid ($n_2 = 1.336$), and illuminated the tracer particles in the vicinity of the glass wall. The penetration depth of the evanescent wave was 74 nm by equation (2.55) using the incident angle of 70°. The incident angle was determined by $R_{off} = f_{obj} n_m \sin\theta_i$, where $R_{off} = 4.74$ mm is the off-center location of the laser beam in the optical pathway of the microscope and $f_{obj} = 3.33$ mm is the focal length of the objective lens (Kihm *et al.*, 2004). In the volume illumination as depicted in figure 3.6(*c*), the mercury lamp was selected as the light source by shutter units. The excitation light was provided by the mercury lamp into the microchannel through the excitation filter and the dichroic mirror.

The particle images of 196×146 μm^2 were captured by the CMOS camera at the frame rate of 2.5 kHz through the objective lens (Obj 2), the dichroic mirror, the barrier filter and a 1.5× magnification lens. Thus, the total magnification of the measurement system was 90, and the particle diameter captured on the CMOS camera calculated from d_e/e by equation (2.58) was 2.7 pixel. The temporal resolution of the velocity measurement was $\Delta t = 400$ μs equal to the frame rate. The depthwise resolution of the evanescent wave and volume illuminations were 0.72 μm and 1.94 μm, respectively, calculated by equations (3.6) and (2.60). The collection efficiency for the CMOS camera, χ (-), was 0.95 considering the background noise. The captured images by the evanescent wave and volume illuminations included 192 particles and 872 particles at the averaged value, respectively. The particle number in the evanescent wave illumination was too low considering the ratio of the measurement depths between the evanescent wave and volume illuminations. This is because the number of negatively charged particles was decreased by the repulsive coulomb force due to the negative charge of the wall

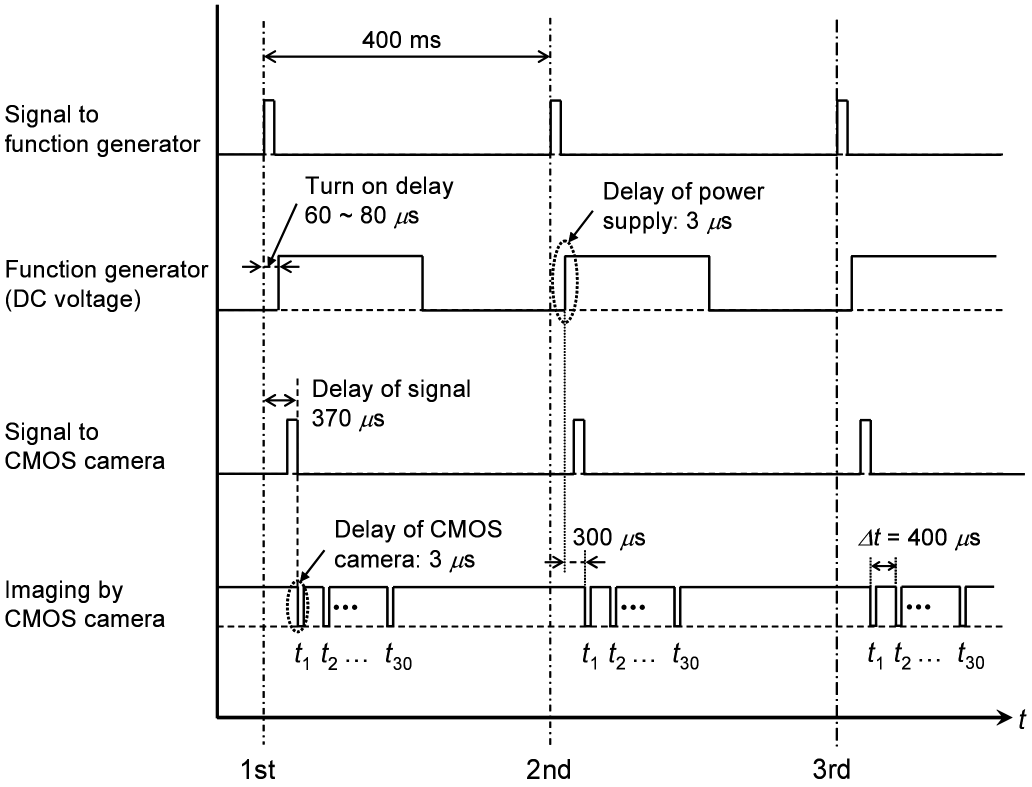

Figure 3.7. Timing chart of the iterative measurement.

(Prieve & Frej, 1990).

Figure 3.7 shows a timing chart for the iterative measurement with an interval of 400 ms. Timing of image acquisition was synchronized with that of applying a DC voltage generating electroosmotic flow in the microchannel. The start signal from the pulse generator was sent to a function generator (Pragmatic Instruments, Inc., 2711A), and the CMOS camera after the time delay of 370 μs. The function generator determined the profile of the DC voltage by the power supply. The delay time of the function generator from the start signal was 60 $\sim$ 80 μs, and that of the power supply toward the function generator was 3 μs. It is noted that the timing error occurred due to the fluctuation of the delay time of the function generator about 10 μs. On the other hand, the image acquisition of 30 images at Δt = 400 μs was started after 3 μs from the start signal to the CMOS camera. Therefore, the time delay from the application of the voltage to the start of image acquisition was 300 μs. Considering the particle number in an image, the number of iterative measurement was determined to be 12 in the evanescent wave illumination and 6 in the volume illumination. Time-series vector maps of the particle displacement during Δt = 400 μs were obtained by the PTV algorithm, and the displacement vectors in each acquisition were integrated over the iterations. Figure 3.8 shows (*a*) instantaneous vector map of the particle displacement obtained by PTV using the volume

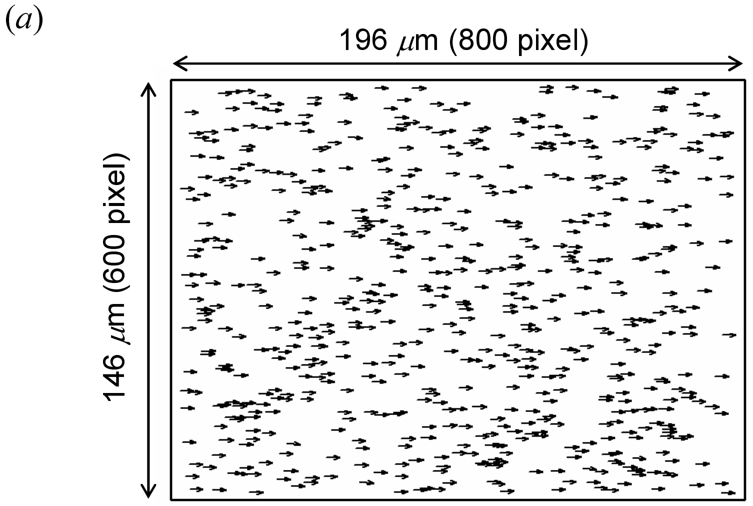

Instantaneous vector map

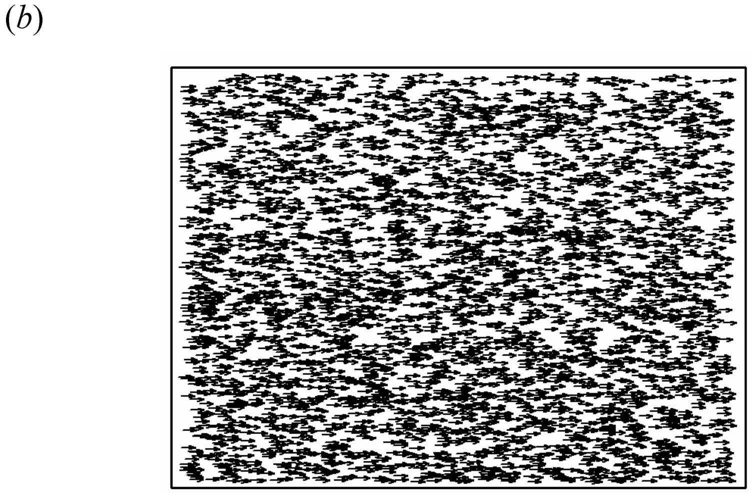

Instantaneous vector map × 6 iterations

Figure 3.8. (*a*) Instantaneous vector map of the particle displacement during the time interval of 400 μs obtained by PTV using the volume illuminaton images. (*b*) Instantaneous displacement vector map obtained after 6 iterative measurements.

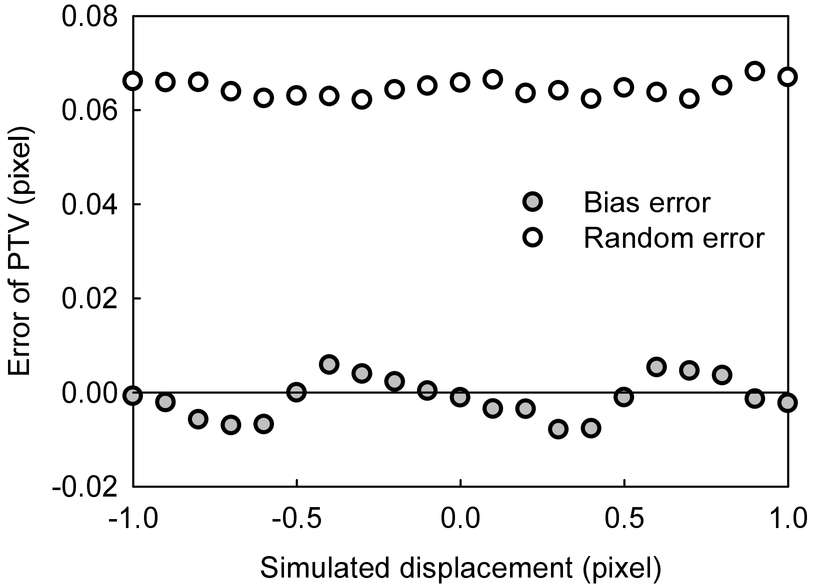

Figure 3.9. Bias and random errors of PTV at the volume illumination evaluated using the artificial images by the Monte Carlo simulation.

illumination image pair and (*b*) that obtained after 6 iterative measurements. The number of vectors was increased and the spatial resolution became higher by the iterative method. Finally, the displacement vectors were spatially averaged in reference regions to reduce the measurement errors by PTV. The particle velocities were calculated using $\varDelta t = 400\ \mu\mathrm{s}$ by $\varDelta x/\varDelta t$.

3.4.2 Evaluation of Measurement Uncertainty

Errors of the iterative velocity measurement using PTV was evaluated numerically and experimentally. The spatial resolution of the velocity measurement, which is equal to the area of the reference region for the averaging of velocities, was determined considering the evaluated measurement errors.

First, the measurement accuracy of PTV was examined using artificial particle images by the Monte Carlo simulation (Sato *et al.*, 2003*a*) and experimentally captured images. In the artificial images, particles were randomly distributed in the volume of imaging region with 256 grayscales. The intensity and shape of imaged particles with the three-dimensional diffraction pattern were calculated using the Lommel functions (Born & Wolf, 1999). The particle displacement was represented as the summation of the simulated displacement and the Brownian displacement with the probability density function of the Gaussian distribution. The variance of the Brownian motion was calculated from the mean square displacement (equation (2.28))

Table 3.2. Random errors of particle displacement obtained by the PTV measurements.

	Random error (pixel)	Random error (nm)
Volume illumination (Artificial)	0.065	15.6
Volume illumination ($z = 26.4\ \mu$m)	0.125	30.4
Evanescent wave illumination	0.183	44.8

depending on the particle diffusivity (equation (2.27)). All parameters in the artificial images were chosen to be the same as those of experiments. Figure 3.9 shows the bias and random errors of PTV evaluated using the artificial images. The bias errors with values less than 0.01 pixel have a period of 1 pixel due to the error of the subpixel interpolation based on the Gaussian peak fit, which determines the centroid of particles (section 2.3) (Westerweel, 1997; Tropea *et al.*, 2007). The random errors about 0.07 pixel are summations of the Brownian displacement and the random error of the Gaussian peak fit. Table 3.2 shows comparison of the random errors of the particle displacements obtained from the volume and the evanescent wave illumination images with those obtained from the artificial images. The random errors with the volume illumination is two-fold larger than that by the artificial images due to increase in the background noise and the effect of the agglomerated particles on the measurement. The random errors with the evanescent wave illumination is further increased compared to those with the volume illumination. They are due to the particle displacements perpendicular to the wall by the Brownian motion. Although the Brownian displacements normal to the wall are less than 21 nm and small compared to the particle diameter, these affect the total fluorescent intensity emitted from the particle illuminated by the evanescent wave with the exponential-decay function of the depthwise position. Thus, the brightness, shape and observed diameter of particles in the image were varied by the Brownian motion perpendicular to the wall, and the random errors of PTV were increased.

The effect of the iteration in the measurement on the errors of particle displacement was evaluated experimentally. Figure 3.10 shows the time dependent particle displacements and the random errors obtained by the PTV measurement and the iterative measurement without the spatial averaging of vectors. The obtained displacements and the random errors by the iterative measurement nearly correspond to those by PTV. This shows that the flow kept the reproducibility in the current condition and the iterative measurements were successfully conducted. In addition, since the random errors are kept constant despite the temporal variance of the displacements, the effect of the timing error in the iteration caused by the function generator is considered to be negligible.

The measurement errors of particle displacements obtained by the spatial averaging of

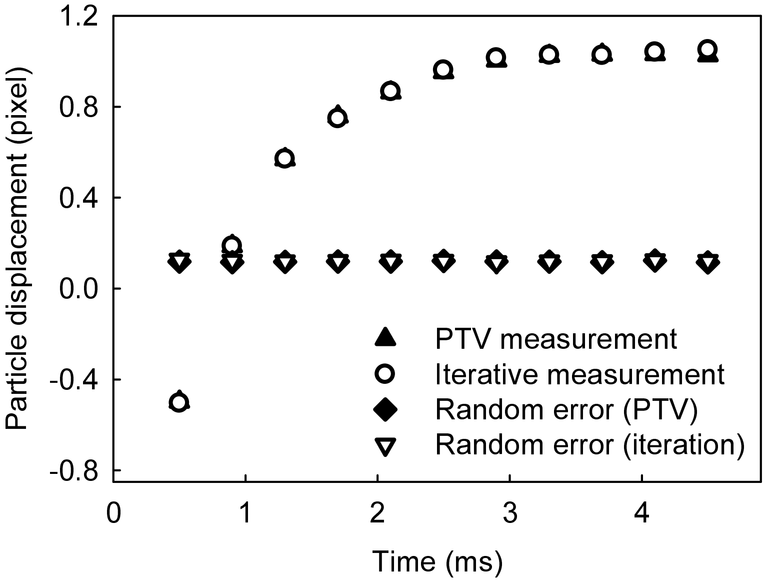

Figure 3.10. The time dependent particle displacements and the random errors obtained by the PTV and the iterative measurement without the spatial averaging. The obtained displacements are at z = 26.4 μm with the volume illumination and the number of iteration was 6.

PTV vectors were evaluated experimentally. Since the bias error is independent of the spatial averaging, only the random errors were estimated from the volume illumination images at z = 26.4 μm and the evanescent wave illumination images. Figure 3.11 shows the random errors of displacements obtained by the spatial averaging at different vector numbers, when the number of iteration was 6 and 12 in the volume illumination and evanescent wave illumination, respectively. The random errors in the volume and evanescent wave illumination are decreased to 0.024 pixel and 0.032 pixel, respectively, with increasing the number of vectors for averaging. Due to the characteristic velocity of 1 mm/s in the present study, the characteristic particle displacement is calculated to be 1.64 pixel. Therefore, in order to reduce the random errors by the spatial averaging less than 3% (0.05 pixel) compared with the characteristic displacement, about 10 and 30 particles are required in the bulk and near-wall velocity measurement, respectively. The spatial resolution of the iterative measurement is defined by the area of the reference regions for the averaging of the particle displacements. Figure 3.12 shows the random errors of particle displacement obtained by the spatial averaging at different areas of reference region. For the random errors less than 3%, the maximum spatial resolution is 900 pixel^2 (30$\times$30 pixel^2) in the bulk velocity measurement and 4900 pixel^2 (70$\times$70 pixel^2) in the near-wall velocity measurement.

The spatial resolutions and errors of the iterative measurement using PTV were compared

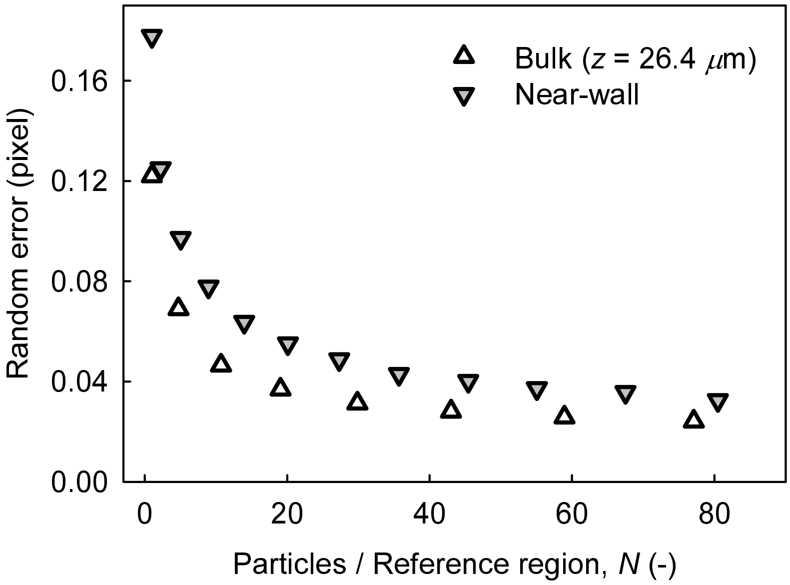

Figure 3.11. The random errors of particle displacement by the spatial averaging at different vector numbers in the volume illumination (z = 26.4 μm) and the evanescent wave illumination.

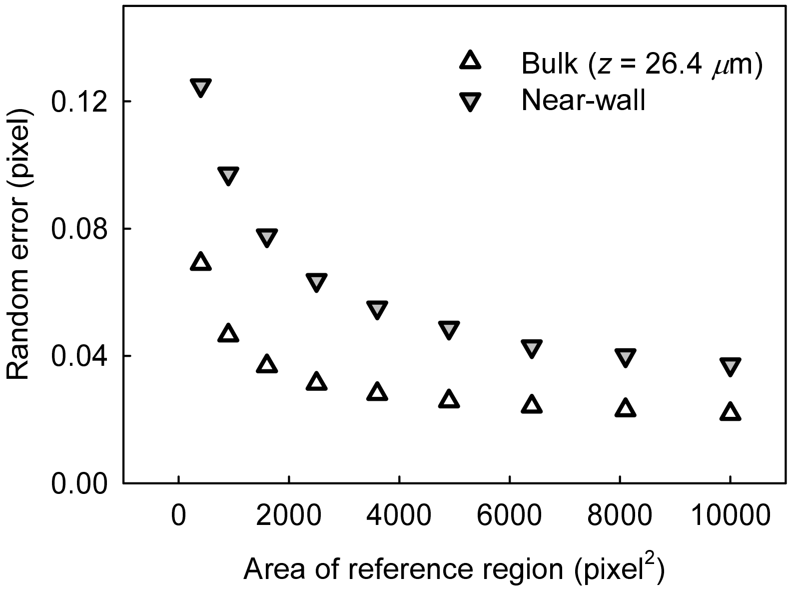

Figure 3.12. The random errors by the spatial averaging at different areas of the reference region, when the number of iterative measurement was 6 and 12 in the volume and evanescent wave illuminations, respectively.

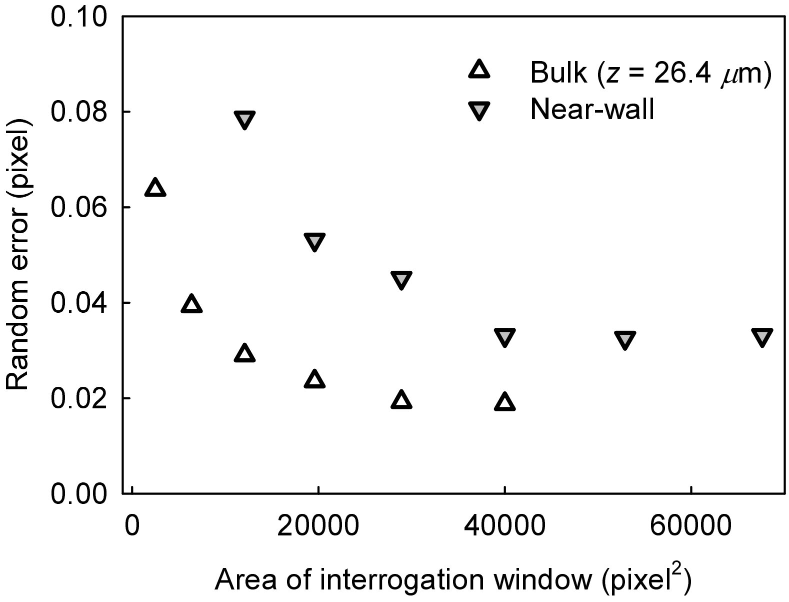

Figure 3.13. The random errors of PIV with the volume illumination and the evanescent wave illumination at different areas of the interrogation window.

with those of PIV. The bias error of PIV was evaluated to be 0.008 pixel from the artificial images. Figure 3.13 shows the random errors of PIV at different areas of the interrogation window. In order to achieve the random errors less than 3%, the interrogation window of 4624 pixel^2 (68 × 68 pixel^2) and 28900 pixel^2 (170 × 170 pixel^2) are required in the bulk and near-wall velocity measurements, respectively. Temporal averaging of 10 instantaneous vectors were conducted to reduce the errors by the Brownian motion, and the random errors were slightly reduced about 0.004 pixel but almost same order with those without the averaging. This shows that the effect of the Brownian motion is small and negligible due to the high time resolution of 400 μs. Table 3.3 shows the spatial resolutions and the measurement errors of PIV and the iterative measurement using PTV. Compared with the PIV measurements, the iteration measurements using PTV achieved about 5 times and 6 times higher spatial resolutions in the bulk and near-wall velocity measurements, respectively, with the measurement error of 0.05 pixel.

Finally, the spatial resolution of the combined measurement of bulk and near-wall velocities conducted in the present study was determined and the uncertainty of the velocity measurement was estimated. In order to sufficiently reduce the random errors, the area of reference region was determined to be 6400 pixel^2 (80 × 80 pixel^2 at square region). Hence, the spatial resolution of the velocity measurement was 383 μm^2 (19.6 × 19.6 μm^2 at the square region). The number of averaged vectors was 77 in the volume illumination and 36 in the evanescent

Table 3.3. The maximum spatial resolutions and the measurement errors of PIV and the iterative measurement using PTV

	Spatial resolution (pixel^2)	Measurement error (pixel)
Volume illumination		
PIV measurement	4624	0.047
6 iteration measurement	900	0.047
Evanescent wave illumination		
PIV measurement	28900	0.046
12 iteration measurement	4900	0.049

Table 3.4. List of parameters, uncertainties in 95% confidence level and the spatial resolutions in the combined measurement of bulk and near-wall velocities

Parameter			Bulk velocity	Near-wall velocity
Time interval	Δt	(μs)	400	400
Uncertainty of Δx	$\epsilon_m(\Delta x)$	(nm)	12.0	21.1
Uncertainty of u	$\epsilon_m(u)$	(μm/s)	30.1	52.8
Spatial resolution		($\mu\mathrm{m}^2$)	383	383

wave illumination. The random errors of the particle displacement in the volume and evanescent wave illumination were 0.024 pixel and 0.043 pixel, respectively. Considering the bias error of PTV of 0.0046 pixel, the total errors of the particle displacement in the volume and evanescent wave illumination were 0.025 pixel and 0.043 pixel, respectively. This shows that the bias error is negligible compared with the random errors. The uncertainty of the particle velocity was evaluated using parameters as listed in table 3.4. Since the velocity is calculated by $u = \Delta x/\Delta t$, the measurement error is estimated by the law of propagation of uncertainty (ISO, 1995) as follows

$$\epsilon_m(u) = \sqrt{\left[\frac{\partial u}{\partial \Delta x}\right]^2 \epsilon_m^2(\Delta x)} = \sqrt{\frac{1}{\Delta t^2}\epsilon_m^2(\Delta x)} \tag{3.7}$$

where ϵ_m is the measurement error. The measurement uncertainty in 95% confidence level was evaluated to be 30.1 μm/s in the bulk velocity and 52.8 μm/s in the near-wall velocity, using the time interval, $\Delta t = 400$ μs, and the measurement errors in the particle displacement, $\epsilon_m(\Delta x)$.

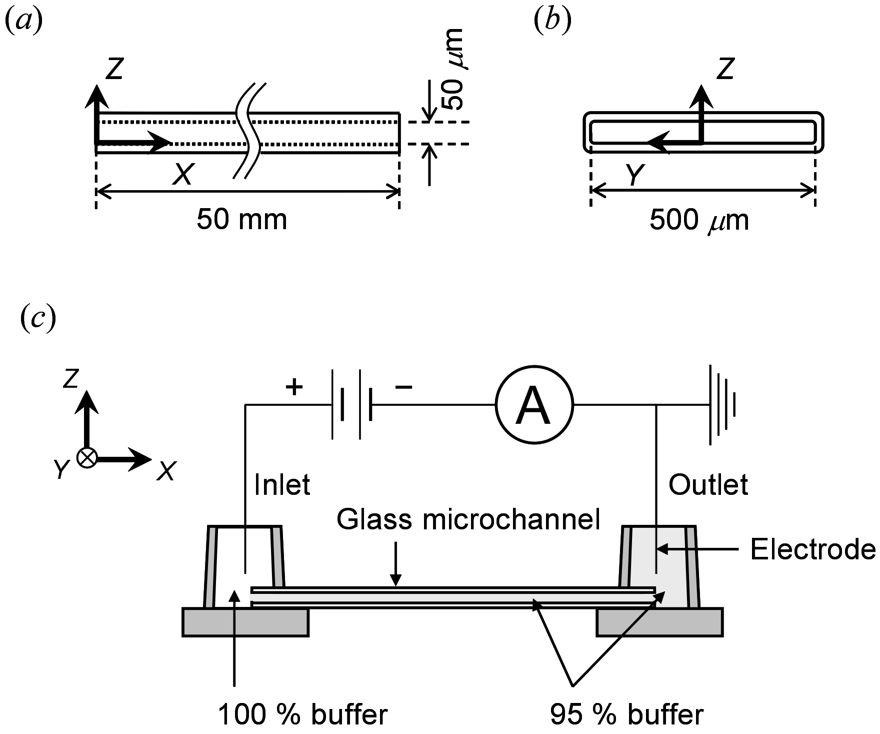

Figure 3.14. (*a*) Side and (*b*) cross-sectional views of the glass microchannel. (*c*) Schematic of the current monitoring setup.

3.5 Calibration of Electrophoretic Mobility

The electrophoretic mobility of tracer particles were evaluated for the velocity measurement of transient electroosmotic flow.

Simultaneous measurement by the current monitoring (Huang *et al.*, 1988) and PTV was conducted using a glass microchannel (VitroCom Inc., Vitrotubes Bolosilicate Glass 5005) at the width of 500 μm, height of 50 μm and length of 50 mm as illustrated in figure 3.14. Figure 3.14(*c*) shows a schematic of the current monitoring setup using an ampere meter (Advantest Corp., AD7461D). The experimental apparatus shown in figure 3.6 was used for the velocity measurement by PTV with the volume illumination. The frame rate of the CMOS camera was set to be 1000 Hz. 500 volume illumination images at $z = 4.4$ μm were captured, and the velocities obtained by PTV in whole imaging region were spatially and temporally averaged.

A buffer solution was prepared by diluting the working fluid to 95% and injected into the glass microchannel from the outlet reservoir. On the other hand, the inlet reservoir was filled with the working fluid (100% buffer). Heights of the aqueous surface in the inlet and outlet of the channel were adjusted to be equal, and thus the pressure at the inlet and outlet was the atmospheric pressure. A DC electric field of 100 V/cm was applied into the microchannel to

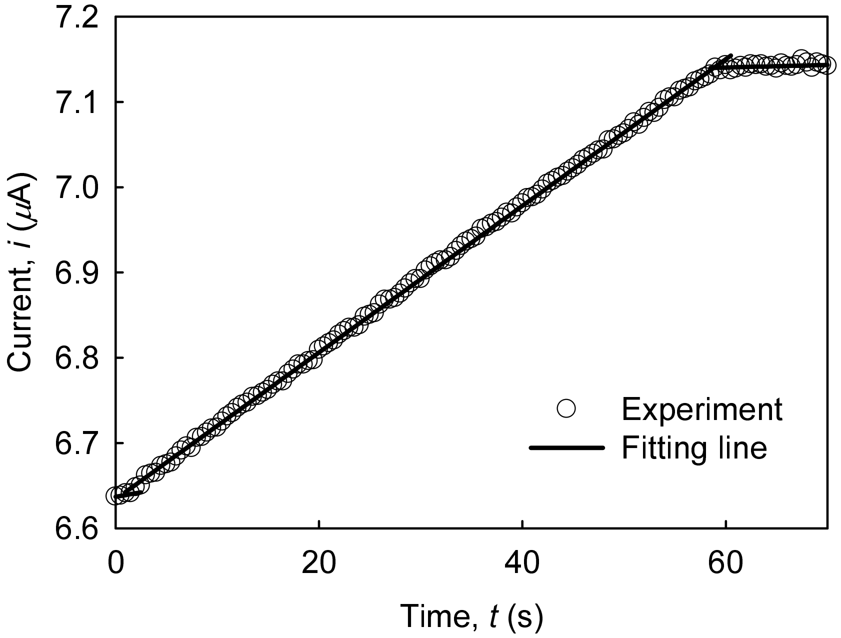

Figure 3.15. The current profile with the time from the application of electric field, measured at the time resolution of 2 Hz.

induce electroosmotic flow. The buffer solution in the microchannel was exchanged from the 95 % buffer to the 100 % buffer by electroosmotic flow. Since the electrical conductivity is proportional to the electrolyte concentration given by equation (2.19), the electrical conductivity in the microchannel was increased with the buffer exchange. Figure 3.15 shows the current profile with the time from the application of electric field, measured by the ampere meter of the time resolution of 2 Hz. The current in the microchannel was increased and became plateau when the buffer exchange was completed. From the intersecting points of fitting lines, the time required for the buffer exchange, t_c (s), was obtained to be 54.8 s. Thus, the averaged velocity of electroosmotic flow, which is equal to the electroosmotic velocity of the plug flow due to uniform zeta-potential, was 856 μm/s calculated by $u_{eof} = L_c/t_c$. During the buffer exchange, the velocity measurement by PTV was simultaneously conducted, and the averaged particle velocity was 331 μm/s. Since the particle velocity in electrokinetic flow is the summation of electroosmotic and electrophoretic velocities (equation (2.50)), the electrophoretic velocity was $-526\,\mu$m/s obtained by $u_{ep} = u_p - u_{eof}$. The electrophoretic mobility given by $\mu_{ep} = u_{ep}/E$ was calculated to be -5.26×10^{-4} cm^2/V s. From 5 measurements, the electrophoretic mobility of -5.34×10^{-4} cm^2/V s was obtained with the uncertainty of 0.39×10^{-4} cm^2/V s in 95 % confidence level, which was estimated using the coverage factor of 2.57.

3.6 Concluding Remarks

A time-resolved velocity measurement technique using particle tracking velocimetry (PTV) was developed to investigate the transient structure of electroosmotic flow in a microchannel. In order to improve the low spatial resolution of PTV, an iterative measurement method on the basis of the reproducibility of laminar flow at low Reynolds number was proposed. The iterative measurement technique achieves the time-resolved velocity measurements with the high spatial resolution. The volume illumination and the evanescent wave illumination were used for the bulk and near-wall velocity measurements, respectively.

Fluorescent polystyrene submicron particles of 500 nm were selected as the tracer particles. The particles are negatively charged in the electrolyte solution and the effect of the particle sedimentation on the velocity measurement is negligible. The time resolution of the measurement was determined to be 400 μs considering the relaxation times of electroosmotic flow and electrophoresis. In the bulk velocity measurement with the volume illumination, the high spatial resolution was achieved with the particle images of the high signal to noise ratio due to the low particle number density. In the near-wall velocity measurement, the time resolved velocity measurement with the high spatial resolution was firstly realized. The measurement depth of the near-wall velocity measurement was theoretically estimated considering the depth of the evanescent wave illumination are and the particle diameter.

A measurement system with a timing control system for the iterative measurement was developed. The objective lens-based total internal reflection fluorescence microscopy was employed to achieve the combined measurement of the bulk and near-wall velocities. The measurement depth was 1.94 μm in the volume illumination and 0.72 μm in the evanescent wave illumination. Considering the particle number density in the captured images, the measurements with 6 iteration was conducted in the bulk velocity measurement and that with 12 iteration was conducted in the near-wall velocity measurements.

Errors in the velocity measurement were evaluated using the artificial images and the experimentally captured images. The spatial resolution was determined to be 383 μm^2 (19.6×19.6 μm^2 at the square region) to sufficiently reduce the random error by the Brownian motion of particles and the subpixel interpolation by PTV. The uncertainty in 95 % confidence level was 30.1 μm/s in the bulk velocity and 52.8 μm/s in the near-wall velocity.

For the velocity measurement of electroosmotic flow, the electrophoretic mobility was examined by the simultaneous measurement by the current monitoring and PTV. The obtained electrophoretic mobility was -5.34×10^{-4} cm^2/V s with the uncertainty of 0.39×10^{-4} cm^2/V s.

Chapter 4

Nanoscale Optical Measurement Technique for Wall Zeta-Potential Using Fluorescent Dye

This chapter presents a novel optical measurement technique for wall zeta-potential. Nanoscale laser induced fluorescence imaging using fluorescent dye and the evanescent wave is proposed. This technique enables the measurement of wall zeta-potential by detecting the fluorescence excited by the evanescent wave in a microchannel. An evanescent wave illumination system based on two prisms is developed for the zeta-potential measurements. The key components of the evanescent wave illumination system are (i) the large area illumination using the microchannel substrate as an optical waveguide, (ii) wide selectivity for the microchannel materials and (iii) easy access to the microchannel.

4.1 Nanoscale Laser Induced Fluorescence Imaging

Nanoscale laser induced fluorescence (nano-LIF) using fluorescent dye and the evanescent wave was proposed. A fluorescent dye, which ionizes in an electrolyte solution, is selected. The evanescent wave illuminates the fluorescent dye in the vicinity of the microchannel wall as illustrated in figure 4.1. This technique enables the two-dimensional measurement of wall zeta-potential by the dependence of fluorescence on the concentration as shown in equation (2.51), which has not been achieved by the conventional techniques using the steaming potential and the electroosmotic velocity as described in section 1.2.

The fluorescent dye is dissolved into the electrolyte solution at a negligible concentration compared to the electrolyte concentration. Thus, effect of the fluorescent dye on the structure of electric double layer is considered to be negligible. The concentration of fluorescent dye, c_f

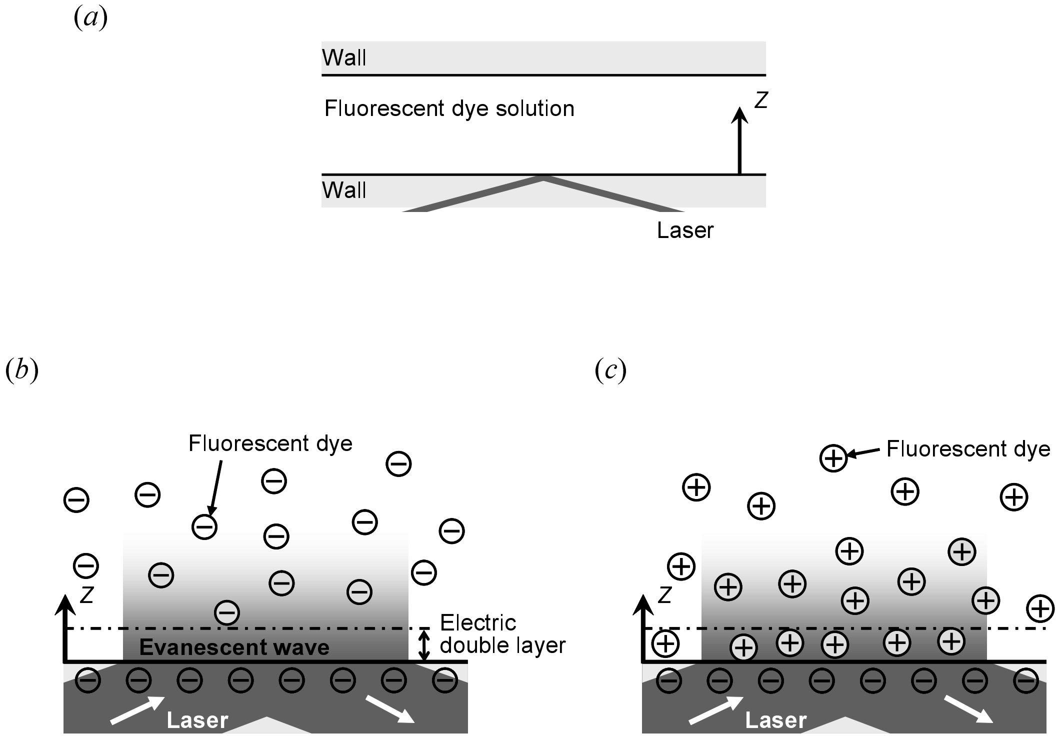

Figure 4.1. (*a*) Schematic of the total internal reflection at the wall-liquid interface in the microchannel. (*b*) Negative ion fluorescent dye and (*c*) positive ion fluorescent dye in the vicinity of the wall surface with a negative zeta-potential is illuminated by the evanescent wave.

(mol/m^3), at the distance from the wall, z (m), has the Boltzman distribution (equation 2.33)

$$c_f(z) = c_{f0} \exp\left(-\frac{z_{vf} F \psi(z)}{RT}\right) \tag{4.1}$$

where c_{f0} (mol/m^3) is the bulk concentration of fluorescent dye, z_{vf} (-) is the valence of fluorescent dye, and ψ (V) is the electric potential given by equation (2.37),

$$\psi(z) \approx \zeta \exp\left(-\frac{z}{\lambda_D}\right) \tag{4.2}$$

Equations (4.1) and (4.2) show that the zeta-potential electrically affects the distribution of fluorescent dye in the vicinity of the wall. When the wall surface is charged negatively (i.e., the negative zeta-potential), the near wall concentration of negative ion fluorescent dye becomes dilute by a repulsive Coulomb force as illustrated in figure 4.1(*b*), on the other hand, that of positive ion fluorescent dye becomes concentrated by an attractive Coulomb force as illustrated in figure 4.1(*c*).

The fluorescent dye in the vicinity of the wall is excited by the evanescent wave. The detected fluorescent intensity, $I_{f,eva}$ (W/m^3), is obtained by substituting equations (2.54) and (4.1) into equation (2.51),

$$\begin{aligned} I_{f,eva} &= \int I_{eva}(z) c_f(z) \phi\gamma \, dz \\ &= \int I_0 \exp\left(-\frac{z}{z_p}\right) c_{f0} \exp\left[-\frac{z_{vf} F}{RT} \zeta \exp\left(-\frac{z}{\lambda_D}\right)\right] \phi\gamma \, dz \end{aligned} \tag{4.3}$$

When the penetration depth of the evanescent wave, z_p (m), is constant, equation (4.3) reduces to

$$I_{f,eva} = I_e c_{f0} f(\zeta) \tag{4.4}$$

where $f(\zeta)$ (m^3/mol) is the function determined by the zeta-potential. Equation (4.4) shows that the fluorescent intensity is dependent on the excitation intensity, the bulk concentration of fluorescent dye and the zeta-potential at the wall. In order to obtain the zeta-potential distribution from the fluorescent intensity, the measurement errors associated with the distribution of excitation intensity and bulk fluorescent dye concentration must be corrected.

When the bulk concentration of fluorescent dye is constant over the measurement, the fluorescent intensity is normalized by that at the reference zeta-potential to correct the influence of excitation intensity.

$$I^*_{f,eva} = \frac{I_{f,eva}}{I_{f,eva,ref}} = \frac{f(\zeta)}{f(\zeta_{ref})} \tag{4.5}$$

On the other hand, when the bulk concentration of fluorescent dye distributes spatially and temporally, it is difficult to correct the measurement errors by equation (4.5). Thus, in the present study, the change in the bulk concentration of fluorescent dye is measured by laser induced fluorescence (LIF) using the volume illumination technique (Ross *et al.*, 2001*a*; Sato *et al.*, 2003*b*; Shinohara *et al.*, 2004). Because the fluorescent intensity excited by the volume illumination, $I_{f,vol}$ (W/m^3), is proportional to the bulk fluorescent dye concentration as shown in equation (2.51), the normalized fluorescent intensity, $I^*_{f,vol} = c_{f0}/c_{f0,ref}$ (-), is used for the correction as follows:

$$\frac{I^*_{f,eva}}{I^*_{f,vol}} = \frac{c_{f0}\,f(\zeta)}{c_{f0,ref}\,f(\zeta_{ref})}\frac{c_{f0,ref}}{c_{f0}} = \frac{f(\zeta)}{f(\zeta_{ref})} \tag{4.6}$$

4.2 Fluorescent Dye

As described in the above section, the fluorescent dye must be ionized in the aqueous solution to measure the wall zeta-potential by the nano-LIF imaging. Alexa Fluor 546 (Haugland, 2005; Chiuman & Li, 2007) (Invitrogen, Corp.) was selected as the fluorescent dye in the present study. The molecular structure is $C_{44}H_{45}Cl_3N_4NaO_{14}S_3$ and the molecular weight is 1079.39 g/mol. A peak of the absorption and emission wavelength is 554 nm and 571 nm, respectively. The fluorescence lifetime is 3.6 ns. Alexa Fluor 546 becomes monovalent anion by the ionization in the aqueous solution at neutral pH as shown in figure 4.2(*a*). It is noted that the fluorescence of Alexa Fluor 546 is nearly independent of pH (Haugland, 2005). In the nano-LIF imaging, Alexa Fluor 546 was dissolved into the electrolyte solution with a 15 μmol/*l*.

Dichlorotris(1,10-phenanthroline)ruthenium(II) hydrate (Ru(Phen)) (O'Neal *et al.*, 2004; Lee *et al.*, 2008) (Sigma-Aldrich Corp.) was also selected as the fluorescent dye. Ru(Phen) was not used for the quantitative measurement by the nano-LIF imaging, but for the visualization of the pattern of surface modification by octadecyltrichlorosilane (OTS) (section 2.2). The molecular structure is $C_{36}H_{24}Cl_2N_6Ru$ and the molecular weight is 712.61 g/mol. A peak of the absorption and emission wavelength is 449 nm and 582 nm, respectively. Ru(Phen) becomes divalent cation by the ionization in the aqueous solution as shown in figure 4.2(*b*). It was dissolved into the electrolyte solution with a 100 μmol/*l*.

4.3 Two-Prism-Based Evanescent Wave Illumination System

An evanescent wave illumination system is required to perform nanoscale optical measurements focusing on an area in the vicinity of the microchannel wall. In the present study, an optical system based on two prisms was developed as illustrated in figure 4.3.

The two prisms were made of borosilicate glass (n = 1.522). A microchannel, which is fabricated from a poly(dimethylsiloxane) PDMS chip and a glass plate ($n = n_g$), is located on the prisms with an immersion oil. A laser beam is introduced into the prism at an inclination

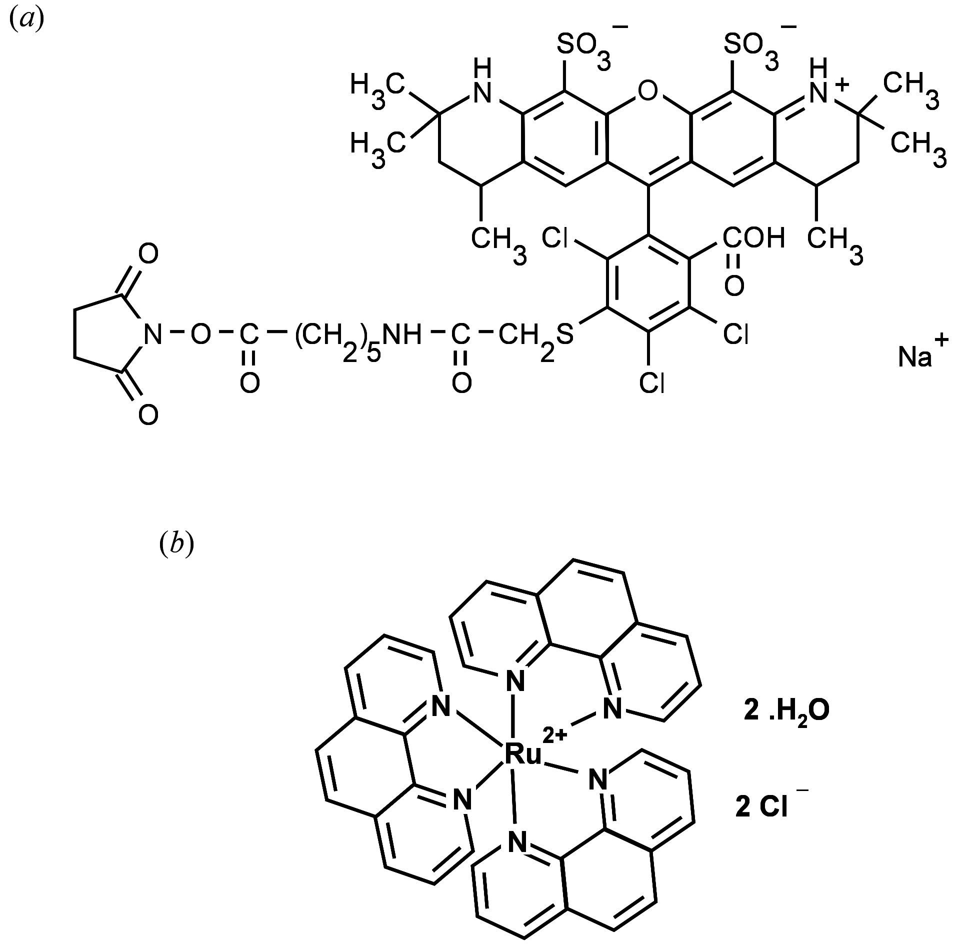

Figure 4.2. Structure of fluorescent dyes. (*a*) Alexa Fluor 546. (*b*) dichlorotris(1,10-phenanthroline)ruthenium(II) hydrate.

angle, φ (°), reflected at a reflection coating inside the prism, and directed to the glass plate with an incident angle, θ_p (°), at an interface between the prism and the immersion oil. A relationship between φ (°) and θ_p (°) is given by the geometrical optics and the Snell's law.

$$\theta_p = \sin^{-1}\left[\frac{\sin(65^\circ - \varphi)}{1.522}\right] \tag{4.7}$$

Then, the laser beam is introduced into the glass plate through the oil layer and guided with total internal reflections at an interface between the glass plate and the solution ($n = n_s$) with an incident angle, θ_i (°), larger than the critical angle. The light path inside the glass plate is dependent on the glass thickness, t_g (m), and θ_i (°). An interval between the total internal reflections inside the glass plate, d_t (m), is given by

$$d_t = 2t_g \tan\theta_i \tag{4.8}$$

The location of a movable prism in the opposite side is adjusted with the light path and the laser beam is finally thrown out from the movable prism through the oil layer to avoid the light scatter at the glass edge. The evanescent wave is generated at the glass-solution interface with the penetration depth given by

$$z_p = \frac{\lambda}{\sqrt{\left(n_g \sin\theta_i\right)^2 - n_s^2}} \tag{4.9}$$

Because of the conservation of $n \sin\theta$ by the Snell's law, $n_g \sin\theta_i$ in equation (4.9) is given by

$$n_g \sin\theta_i = 1.522 \sin\theta_p \tag{4.10}$$

Thus, by substituting equation (4.7) to equation (4.10),

$$n_g \sin\theta_i = 1.522 \sin\left\{\sin^{-1}\left[\frac{\sin(65^\circ - \varphi)}{1.522} + 65^\circ\right]\right\} \tag{4.11}$$

Equations (4.9) and (4.11) show that the penetration depth of the evanescent wave, z_p (m), is not dependent on the refractive index of glass, n_g (-), and the incident angle, θ_i (°), but on the inclination angle of the laser beam, φ (°).

The two-prism-based evanescent wave illumination system has several advantages toward conventional total internal reflection fluorescence microscopy (TIRFM) as described in section 2.3. Compared to the objective lens-based TIRFM, the large field of view with the low magnification objective lens is achieved by the evanescent wave illumination using the microchannel substrate as an optical waveguide. The optical system based on the two prisms has wide selectivity of the material and thickness of microchannel substrate such as borosilicate glass and silica glass. Compared to the conventional prism-based TIRFM, since the prisms are

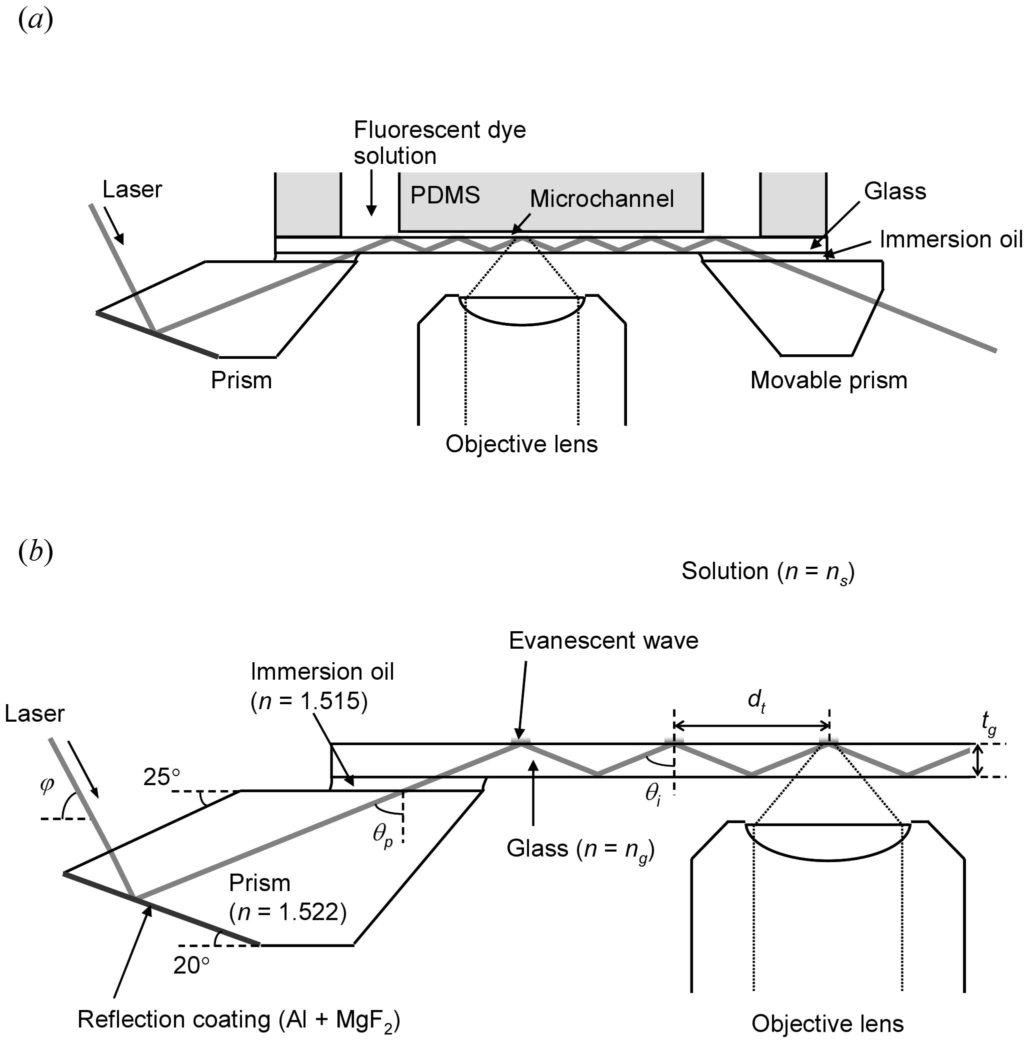

Figure 4.3. (*a*) Schematic of the two-prism-based optical system for the evanescent wave illumination in a microchannel. (*b*) Schematic of total internal reflections inside the glass plate.

located in the same side as the objective lens, free access to the microchannel is achieved. In addition, it is easy to adjust the light path of the laser beam by sliding the movable prism with the immersion oil.

In order to achieve the measurement with the high signal to noise ratio by the present system, a thick glass plate is desired within the restriction of the glass thickness, t_g (m), by the objective lens. Since the interval between the total internal reflections inside the glass plate, d_t (m), is proportional to the glass thickness as shown in equation (4.8), the number of total internal reflection inside the glass plate between two prisms decreases with increasing the glass thickness. This results in reduction of the background intensity caused by the light scatter at the spot of total internal reflection.

4.4 Experimental Apparatus

Figure 4.4(*a*) illustrates the two-prism-based evanescent wave illumination system comprised of the inverted fluorescence microscope with the filter block for green excitation (shown in table 2.4), the continuous mercury lamp, an Nd:YAG laser (Coherent Inc., Verdi V-5, $\lambda = 532$ nm) and the CCD camera (shown in table 2.6). A microchannel fabricated from a PDMS chip and a silica glass ($n_g = 1.461$, $t_g = 1$ mm), where fluorescent dye solution (Alexa Fluor 546) was injected, was located on the prisms with immersion oil. The refractive index of the fluorescent dye solution was assumed to be equal to that of water ($n_s = 1.336$).

The laser beam was diffracted by a pinhole with a diameter of 1 mm, focused by a convex lens (focal length: 1000 mm) with the intensity of 624 mW and directed into the prism at an inclination angle of $\varphi = 60.5°$ adjusted by the mirror. As illustrated in figure 4.4(*b*), the diffracted laser beam was introduced into the silica glass of the microchannel through the prism and guided with total internal reflection at an incident angle, $\theta_i = 75°$, calculated by equation (4.11). The laser beam was finally thrown out from the movable prism to avoid the light scatter at the silica glass edge. The evanescent wave was generated at the silica glass-solution interface and the fluorescent dye in the vicinity of the interface was excited as illustrated in figure 4.4(*c*). The penetration depth of the evanescent wave was $z_p = 93$ nm calculated by equation (4.9). The size of the illumination area in the Y-direction was adjusted to that less than the width of the microchannel in order to minimize the light scatter from the edge of the PDMS wall at the interface. Figure 4.5 shows the intensity profile of the diffracted laser beam in the Y-direction, which was measured from the fluorescence excited by the evanescent wave. The beam profile was generated by an out-of-focus diffracted beam with the central maximum and first sidelobes. The uniform intensity profile was obtained in comparison with the Gaussian distribution. Thus, the excitation efficiency of fluorescent dye was improved by the diffracted laser beam. Therefore, the fluorescence excited by the evanescent wave was

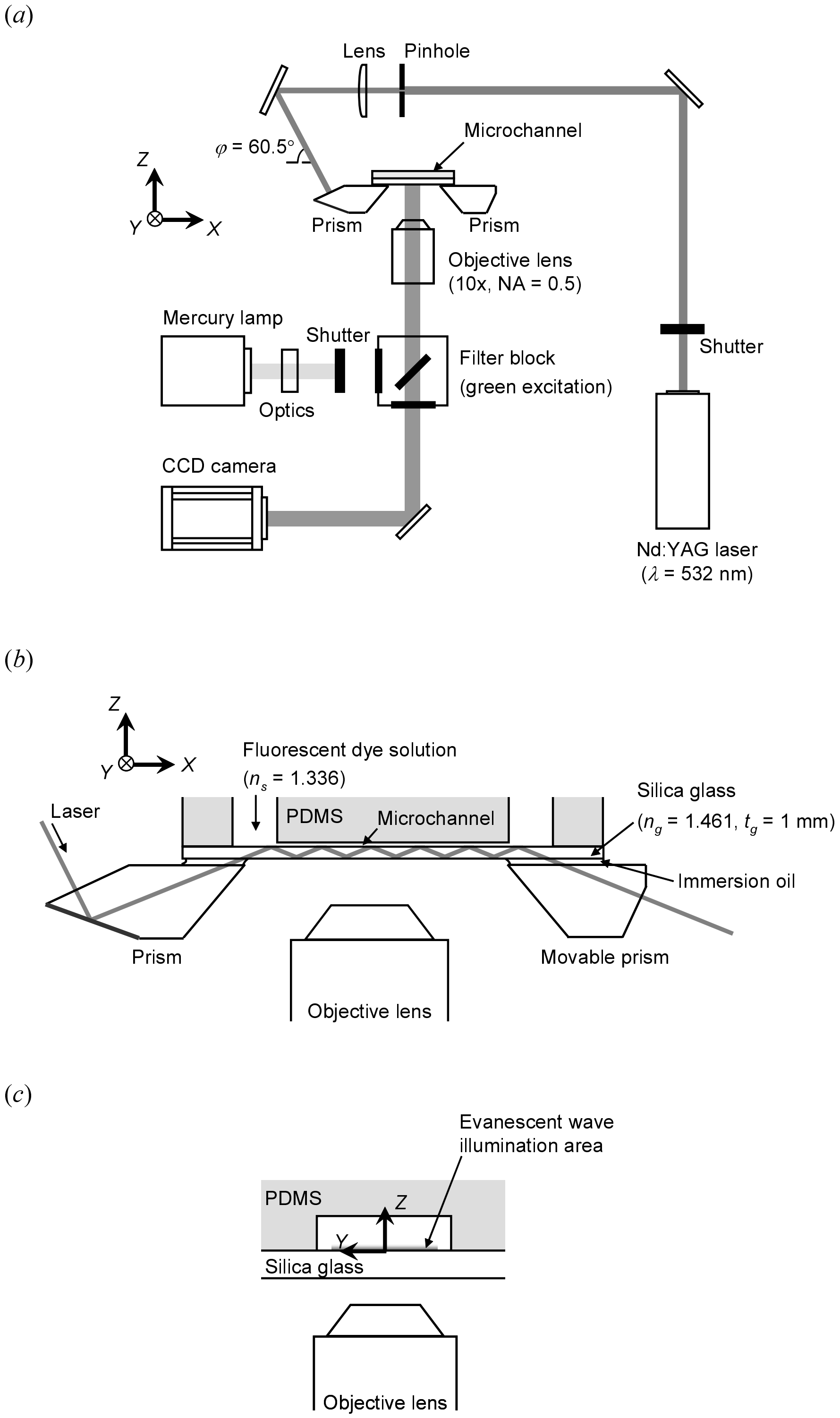

Figure 4.4. Schematic of (*a*) the experimental apparatus of the evanescent wave illumination system, (*b*) total internal reflection in the silica glass and (*c*) evanescent wave illumination in the microchannel.

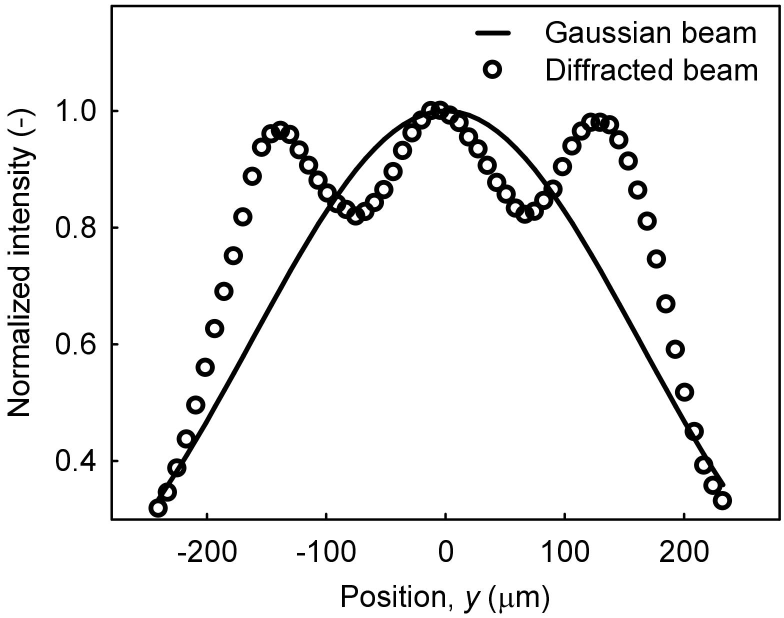

Figure 4.5. Normalized intensity profile of the diffracted laser beam at the silica glass wall compared with the Gaussian intensity profile. The Gaussian intensity profile was calculated from the beam diameter of 0.65 mm estimated by the geometrical optics.

detected with high signal to noise ratio. The fluorescence was captured by the CCD camera through the objective lens (10×, NA = 0.5, shown in table 2.5), the dichroic mirror and the barrier filter. The imaging region and the spatial resolution was 656 × 494 μm^2 and 1.0 × 1.0 μm^2, respectively, calculated from the pixel size and the magnification of objective lens. The depth of field of the measurement system, which is calculated from equation (2.59), was 4.26 μm. Compared with the penetration depth of the evanescent wave, z_p = 93 nm, the depthwise resolution is characterized by the evanescent wave rather than the recording optical system.

When the mercury lamp was selected as the light source by shutter units, the fluorescence detection with the volume illumination (shown in section 2.3) was performed. Since the entire fluorescent dye in the depthwise direction is illuminated by the volume illumination, the detected fluorescent intensity is an integrated value of in- and out of focus fluorescent intensities despite the depth of field of the recording optical system.

It is noted that the correction using equation (4.6) is based on the linear relationship between the fluorescent intensity excited by the evanescent wave and bulk fluorescent dye concentration as shown in equation (4.4). Hence, this linear relationship was verified experimentally by changing the concentration of Alexa Fluor 546 in the electrolyte solution. From the regression analysis, a plot of the fluorescent intensity excited by the evanescent wave versus

Table 4.1. Properties of electrolyte solution

Solution		A	B	C	D	E
HEPES	(mmol/l)	5	5	5	5	5
NaCl	(mmol/l)	0.1	0.5	2	5	10
pH	(-)	7.02	7.01	6.99	6.99	6.97
Conductivity	(μS/cm)	134	185	302	606	1161

the bulk fluorescent dye concentration had a slope of 1.005, $n = 4$, $r = 0.9992$, where n (-) is the number of data points and r (-) is the correlation coefficient.

4.5 Calibration Experiments for Nano-LIF Imaging

Prior to the nano-LIF imaging, the relationship between the fluorescent intensity excited by the evanescent wave and the zeta-potential at the wall was examined. The fluorescent intensity was detected at conditions with the uniform zeta-potential, which were prepared by adjusting the electrolyte concentration. The values of zeta-potential at each concentration were estimated from the results of the zeta-potential measurement by micro-resolution particle image velocimetry (micro-PIV).

4.5.1 Zeta-Potential Measurement by Micro-PIV

The zeta-potential at the wall in a straight microchannel made of silica glass was measured by micro-PIV. The particle velocity measured by micro-PIV in electrokinetic flow on an application of electric field is the summation of the electroosmotic and electrophoretic velocities as shown in equation (2.50). Since the wall zeta-potential is uniform in the microchannel, the zeta-potential at the silica glass wall is calculated from the Helmholtz-Smoluchowski equation (2.42) using the electroosmotic velocity, which is obtained by subtracting the electrophoretic velocity from the measured particle velocity. The particle electrophretic velocity is estimated by $u_{ep} = \mu_{ep}E$. The particle electrophoretic mobility is evaluated by the measurement technique using a closed cell and micro-PIV (Ichiyanagi *et al.*, 2005).

Five kinds of the electrolyte solution were prepared for the experiments as listed in table 4.1. Each solution was composed of a 5 mmol/l HEPES solution to keep pH in constant. Sodium chloride (NaCl) was added to the solutions to change the cation concentration. Fluorescent polystyrene particles with the diameter of 500 nm (details are described in section 3.1) were used as the tracer particles. An experimental apparatus was comprised of the flu-

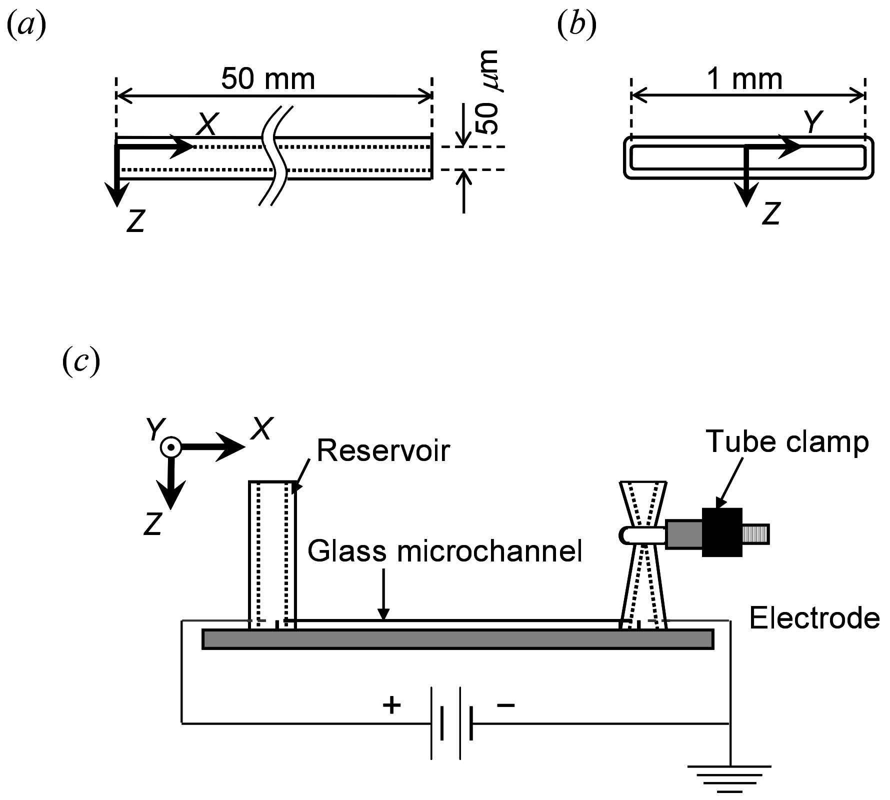

Figure 4.6. (*a*) Side and (*b*) cross-sectional views of the glass microchannel. (*c*) Schematic of the closed cell.

orescence microscope (figure 2.19(*a*)) with the filter block for blue excitation (table 2.4), the oil immersion objective lens (60×, NA = 1.4, table 2.5) and the cooled CCD camera (table 2.6). The excitation light was provided by the mercury lamp into the microchannel through the excitation filter and the dichroic mirror. Particle images were captured by the CCD camera through the objective lens, the dichroic mirror and the barrier filter. The particle diameter captured on the CCD camera calculated from d_e/e by equation (2.58) was 4.1 pixel. Velocity vectors were calculated from the particle images and the ensemble averaging technique was applied to the 100 instantaneous velocity vectors to avoid a measurement error associated with the Brownian motion of particles. The plane resolution of the velocity measurement was $11.6 \times 11.6\ \mu\text{m}^2$, which is equal to the size of the interrogation windows. The depthwise resolution was 2.1 μm calculated by equation (2.60).

First, the particle electrophoretic mobility was quantified by the measurement technique using the closed cell and micro-PIV. Figure 4.6 illustrates a schematic of the closed cell (the aspect ratio, k (-), was 20) comprised of a glass microchannel (VitroCom Inc., Large Ratio Rectangle Tubing RT5015) and silicon tubes used as the reservoirs. The electrolyte solution with the fluorescent particles at a number density of 3.06×10^{10} particles/ml was sealed in the microchannel by tube clamps. A DC electric field of 10 V/cm was applied through the electrodes submerged in the reservoirs. The particle images at $z = 4.4\ \mu$m, 8.8 μm, 13.2 μm, 17.6 μm, 22 μm, 26.4 μm, 30.8 μm, 35.2 μm, 39.6 μm, 44 μm and 48.4 μm ($y = 0$) were captured by the CCD camera by moving the focal plane of objective lens. Figure 4.7 shows the Z-direction profile of the spatially and temporally averaged particle velocity (X-direction), when the Na^+ concentration was 5 mmol/l. A circulating flow was generated to conserve the flux by electroosmotic flow in the closed cell and resulted in the parabolic velocity profile (Hunter, 1981; Probstein, 1994). The observed velocity is the superposition of the velocities of circulating flow and electrophoresis. Mori & Okamoto (1980) analyzed the circulating flow in the closed cell both experimentally and theoretically, and proposed a method in order to determine the particle electrophoretic velocity. The particle velocities in the closed cell, u_{cell} (m/s), were approximated by a quadratic curve using the least-squares method.

$$u_{cell} = C_2 z^{*2} + C_1 z^* + C_0 \tag{4.12}$$

where $z^* = (z - b)/2b$ (-) and C (-) is the coefficient of the equation. When $k > 20$, a viscosity effect from the side walls ($y = \pm 500\ \mu$m) is negligible at the center of the closed cell ($y = 0$) and the particle electrophoretic velocity was calculated from a following equation,

$$u_{ep} = C_0 + \left(\frac{1}{3} + \frac{0.42}{k}\right) C_2 \tag{4.13}$$

From the velocity profile shown in figure 4.7, the particle electrophoretic velocity was calculated to be $-60.9\ \mu$m/s by equation (4.13). Thus, the electrophoretic mobility was calculated to be -6.09×10^{-4} cm^2/V s.

The straight microchannel made of silica glass (VitroCom Inc., Vitrotubes Synthetic Fused Silica 5005S), whose width and depth was 500 μm and 50 μm, respectively, was used for the zeta-potential measurements as illustrated in figure 4.8. The electrolyte solution with the fluorescent particles was injected into the microchannel and a DC electric field of 20 V/cm was applied through the electrodes. Heights of the aqueous surface in the inlet and outlet of the channel were adjusted to be equal, and thus the pressure at the inlet and outlet was the atmospheric pressure. The electroosmotic velocity was obtained from equation (2.50) by using the particle electrophoretic mobility. Figure 4.9 shows the profile of the spatially and temporally averaged electroosmotic velocity in the depthwise direction (Z-direction), when the Na^+ concentration was 5 mmol/l. The electroosmotic flow shows the plug flow at uniform zeta-potential (Probstein, 1994). The zeta-potential at the silica glass wall was calculated to be -67 mV from the electroosmotic velocity at $z = 26.4\ \mu$m. Table 4.2 summarizes the electrophoretic mobility and the zeta-potential at the silica glass wall with the measurement uncertainty in 95% confidence level (ISO, 1995) obtained from 6 measurements. It is noted that the uncertainty in the zeta-potential measurement was calculated by the law of propagation

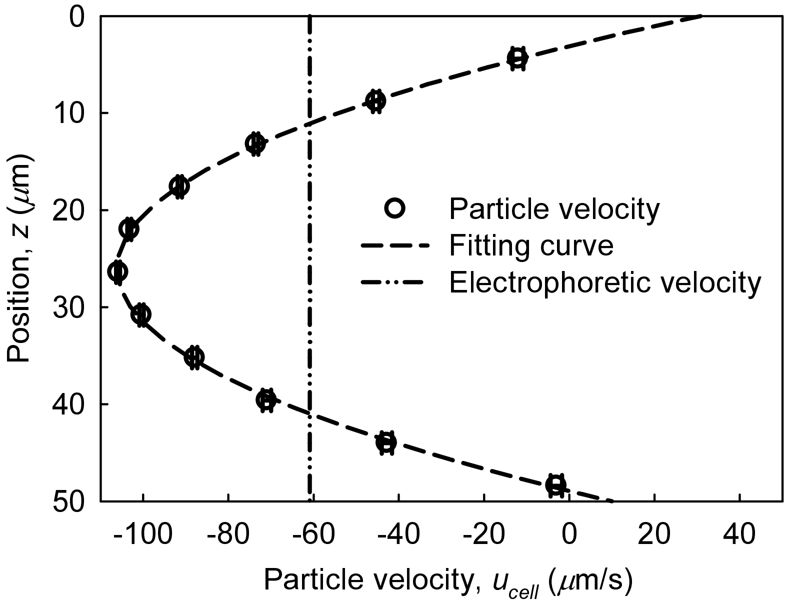

Figure 4.7. Profile of particle velocity with standard deviation in the Z-direction in the closed cell on an application of 10 V/cm. Dash line shows the fitting curve obtained by the least-squares method. Dash-dot-dot line shows the electrophoretic velocity calculated by equation (4.13).

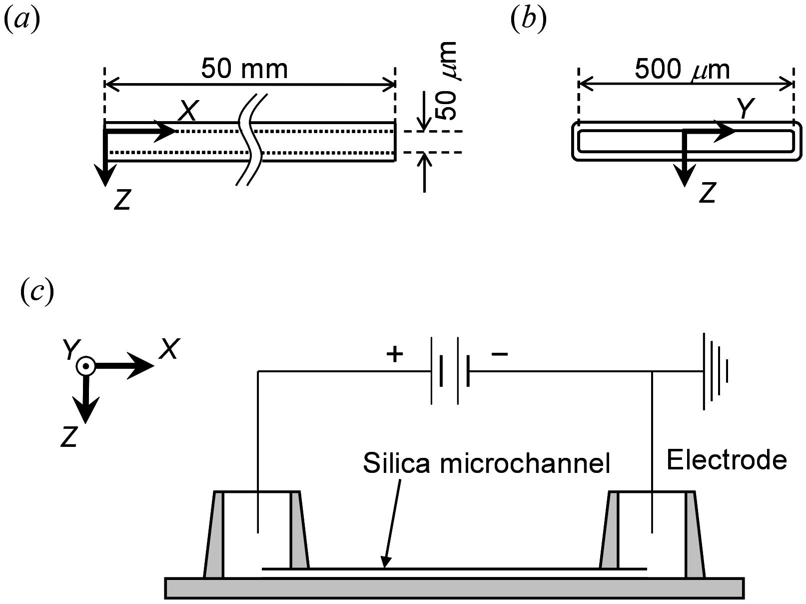

Figure 4.8. (*a*) Side and (*b*) cross-sectional views of the silica glass channel. (*c*) Schematic of the microchannel for the experiments.

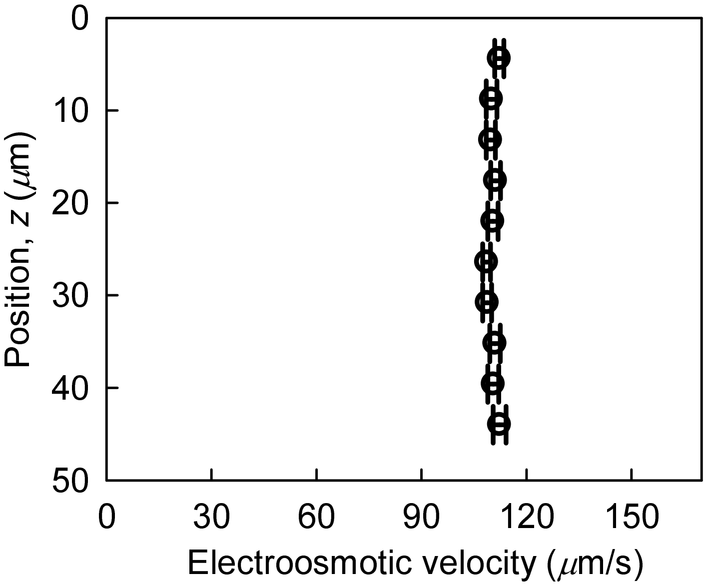

Figure 4.9. Profile of electroosmotic velocity with standard deviation in the Z-direction in the silica glass microchannel on an application of 20 V/cm.

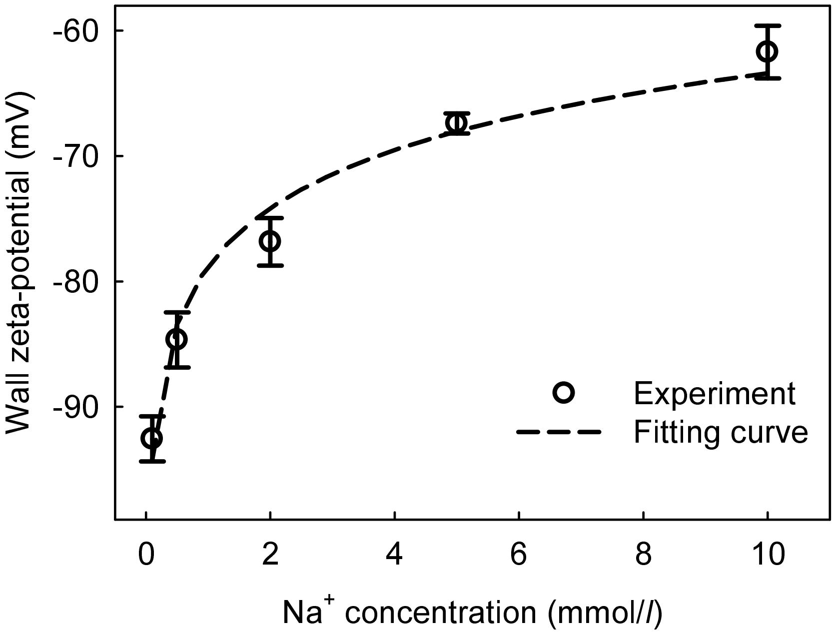

Figure 4.10. Relationship between the bulk Na^+ concentration and the zeta-potential at the silica glass wall.

Table 4.2. The particle electrophoretic mobility, μ_{ep} (m^2/V s), and the zeta-potential at the silica glass wall, ζ (V), with the measurement uncertainty in 95% confidence level obtained from 6 measurements

Solution	Na$^+$ concentration c_0 (mmol/l)	Electrophoretic mobility μ_{ep} ($\times 10^{-4}$ cm^2/V s)	Wall zeta-potential ζ (mV)
A	0.1	-6.21 ± 0.07	-92.6 ± 1.8
B	0.5	-5.74 ± 0.18	-84.7 ± 2.2
C	2	-6.21 ± 0.18	-76.8 ± 1.9
D	5	-6.07 ± 0.06	-67.4 ± 0.8
E	10	-6.00 ± 0.17	-61.7 ± 2.1

of uncertainty (ISO, 1995). The electrophoretic mobilities are almost independent of the bulk Na$^+$ concentration. Figure 4.10 is the relationship between the Na$^+$ concentration and the zeta-potential at the silica glass wall. The wall zeta-potential increases with increasing the bulk Na$^+$ concentration. From the experimental results, the relationship between the bulk Na$^+$ concentration, c_0 (mol/m^3), and the wall zeta-potential, ζ (V), was approximately obtained as $\zeta = -0.0788 + 0.0154 \log c_0$ by the linear fitting using the theoretical relationship given by equation 2.40.

4.5.2 Calibration Curve for Nano-LIF Imaging

A relationship between the fluorescent intensity excited by the evanescent wave and the zeta-potential at the silica glass wall was quantified as a calibration curve.

The electrolyte solution with a 15 μmol/l Alexa Fluor 546 was injected into a straight channel comprised of PDMS and the silica glass of 1 mm thickness. The fluorescent intensity excited by the evanescent wave was detected at each uniform zeta-potential over the range from -92.6 mV to -61.7 mV as shown in table 4.2. To reduce the CCD pixel error into negligible level, spatial averaging of the detected intensity per 8×8 pixel^2 was performed and resulted in the standard deviation of 0.32%. The influence of background noise in the CCD camera was removed by subtracting the background intensity from the detected intensity. Because the bulk fluorescent dye concentration was constant over the experiments, measurement errors associated with the excitation intensity was corrected by equation (4.5) using the fluorescent intensity at the reference zeta-potential of $\zeta_{ref} = -67.4$ mV. Figure 4.11 shows a relationship between the corrected fluorescent intensity and the zeta-potential. The corrected fluorescent intensity in figure 4.11 was spatially averaged value in the measurement area. The fluorescent

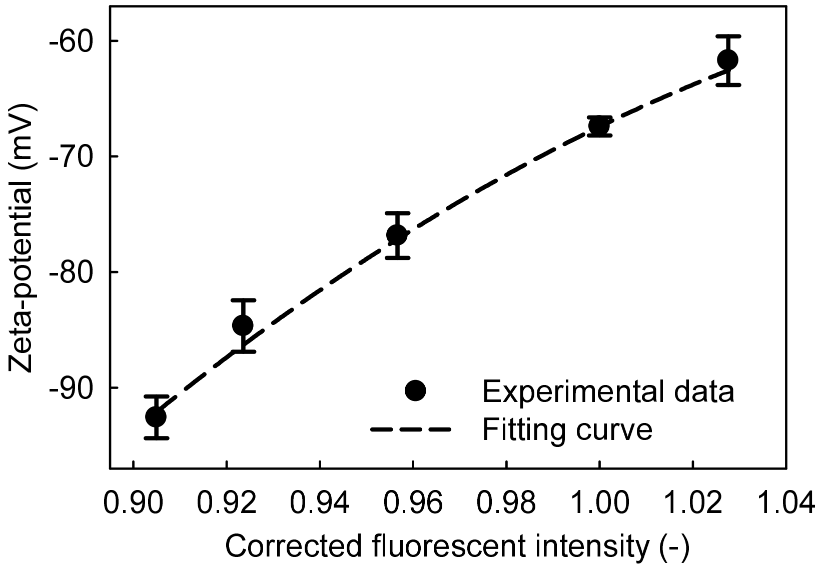

Figure 4.11. Calibration curve between the corrected fluorescent intensity and the zeta-potential. Error bars indicate the uncertainties of the zeta-potential as shown in table 4.2.

intensity increases with increasing the zeta-potential. The calibration curve was obtained as a quadratic curve by the least-squares method. Each experimental data was weighted considering the uncertainty of the zeta-potential as shown in table 4.2 (Bevington, 1969). The residual error in the fitting was evaluated as the standard deviation of 1.4 mV. When the calibration curve was applied to the corrected fluorescent intensity at uniform zeta-potential, the spatial variance of the corrected fluorescent intensity in the measurement area resulted in the standard deviation of 1.3 mV. Therefore, in the nano-LIF imaging, the measurement uncertainty in 95% confidence level was 4.7 mV based on the coverage factor of 2.53. The spatial resolution was $7.9 \times 7.9\ \mu\text{m}^2$ based on the pixel averaging.

4.6 Concluding Remarks

An optical measurement technique using the fluorescent dye and the evanescent wave, termed nanoscale laser induced fluorescence (nano-LIF) imaging, was developed for the two-dimensional distribution of zeta-potential at the microchannel wall. Fluorescent dye, which becomes ions in the electrolyte solution, was selected. The fluorescent dye was excited by the evanescent wave with total internal reflection of laser beam at the interface between the microchannel wall and the electrolyte solution. The wall zeta-potential is obtained from the fluorescent intensity due to the Boltzman distribution of the fluorescence ions related to the zeta-potential.

A two prisms-based evanescent wave illumination system was developed for the measurement. The evanescent wave was generated at the interface between the microchannel wall and the electrolyte solution, using the microchannel substrate as the optical waveguide. The laser beam was introduced into the microchannel material through the prism and underwent total internal reflections with the evanescent wave, and was thrown out from another prism to avoid the light scatter reducing the signal to noise ratio. This system achieves the low magnification measurement with the large area illumination, wide selectivity for the microchannel materials, easy access to the microchannel and high signal to noise ratio.

The calibration experiments were conducted to quantify a relationship between the fluorescent intensity and the zeta-potential at the silica glass wall. The relationship was estimated by detecting the fluorescent intensity at the uniform zeta-potential, which was prepared by adjusting the Na^+ concentration in the electrolyte solution. It is noted that the values of zeta-potential at each concentration were estimated from the results of the zeta-potential measurement by micro-resolution particle image velocimetry. The obtained calibration curve enables the two-dimensional measurement of wall zeta-potential. The measurement uncertainty and the spatial resolution by the evanescent wave illumination system and calibration curve was 4.7 mV in 95% confidence level and $7.9 \times 7.9\ \mu m^2$, respectively.

Chapter 5

Transient Structure of Electroosmotic Flow with Nonuniform Wall Zeta-Potential

This chapter presents a discussion of transient electroosmotic flow with nonuniform wall zeta-potential in microchannel. Time-series flow velocities are measured by the iterative measurement technique using particle tracking velocimetry (PTV). The velocity measurements are conducted to investigate electroosmotic flows with uniform zeta-potential, and nonuniform zeta-potential by the material heterogeneity, the surface modification with two step patterns perpendicular and parallel to the electric field. Momentum transport in the flow field and the volumetric flow rates with nonuniform zeta-potential are examined using the obtained results.

5.1 Theoretical Analysis of Electroosmotic Flow

In order to understand the dynamics of electroosmotic flow with nonuniform wall zeta-potential, a theoretical model was estimated and compared with the experimental results. A basic assumption is that the thickness of the electric double layer is negligible compared to the characteristic length. Thus, the slip velocity assumption can be applied to the theory of electroosmotic flow (section 2.1).

5.1.1 Order Estimation for Electroosmotic Flow with Nonuniform Wall Zeta-Potential

The effect of the nonuniform zeta-potential on the electroosmotic flow structure was approximately estimated. The analysis was conducted on assumptions as follows: (i) the Helmholtz-

Smoluchowski equation can be applied in the region where the zeta-potential is spatially distributed, (ii) the velocity is treated as a scalar variable. Consider a two-dimensional channel with step change zeta-potential ($\zeta = \zeta_0$ in $x < 0$ and $\zeta = 0$ in $x > 0$) at $y = 0$ and the zeta-potential with an arbitrary distribution at $y = L$ as illustrated in figure 5.1. The wall velocity at $y = 0$ has a step change distribution, and the shear stress, τ (Pa), at $y = 0$ has the delta function. The momentum generated from the wall at $y = 0$ is transported to the fluid in the channel, and the time required for the momentum transport over the characteristic length is the relaxation time of electroosmotic flow, τ_{eof} (s), as described in section 2.1. In parallel with the momentum transport in the direction normal to the wall (Y-direction), the momentum transport in the direction tangential to the wall (X-direction) due to the velocity gradient at $y = 0$ also occurs. The governing equation for the momentum transport is the diffusion equation (equation (2.7)). Thus, the solution of the equation is given by (Crank, 1975)

$$\rho u(x,\, t) = \frac{1}{2}\rho u_0 \,\mathrm{erfc}\frac{x}{2\sqrt{\nu t}} \tag{5.1}$$

The shear stress by the velocity gradient in the X-direction is obtained from the derivative

$$\tau = -\nu\frac{d\rho u}{dx} = \frac{\nu\rho u_0}{\sqrt{4\pi\nu t}}\exp\left(-\frac{x^2}{4\nu t}\right) \tag{5.2}$$

Equations 5.1 and 5.2 show that the momentum transport is treated as the diffusion problem with the penetration distance given by $\delta_p = \sqrt{2\nu t}$. Therefore, the length scale in the X-direction of the flow by the nonuniform wall zeta-potential at $y = 0$ is estimated by

$$\delta_p = \sqrt{2\nu\tau_{eof}} = \sqrt{2}L = O(L) \tag{5.3}$$

This shows that the step change zeta-potential (ideal variation) affects electroosmotic flow at the scale with the order of the characteristic length.

5.1.2 Two-dimensional Flow Model with Nonuniform Wall Zeta-Potential

The velocity profiles of electroosmotic flow in the region, where the wall zeta-potential can be assumed to be uniform, was estimated. From the velocity profiles, the volumetric flow rate with the nonuniform wall zeta-potential was calculated.

Consider a two-dimensional microchannel of the depth, H_c (m), and the length, L_c (m), composed of the walls with different zeta-potentials, ζ_1 (V) and ζ_2 (V), as depicted in figure 5.2(*a*). The slip velocities at the walls on an application of the electric field are obtained by the Helmholtz-Smoluchowski equation, $u_i = -\epsilon E\zeta_i/\mu$. Since the governing equation with the low Reynolds number (equation (2.5)) is linear and superposable, the velocity profile is simply

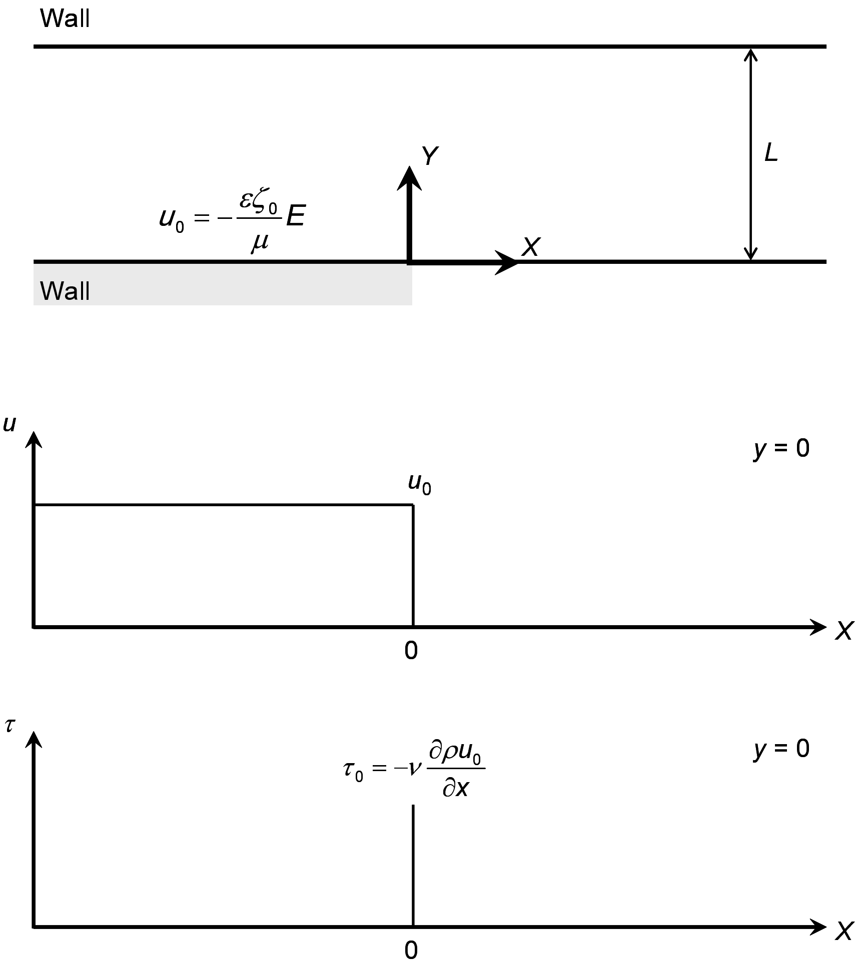

Figure 5.1. Two-dimensional channel with step change wall zeta-potential at $y = 0$.

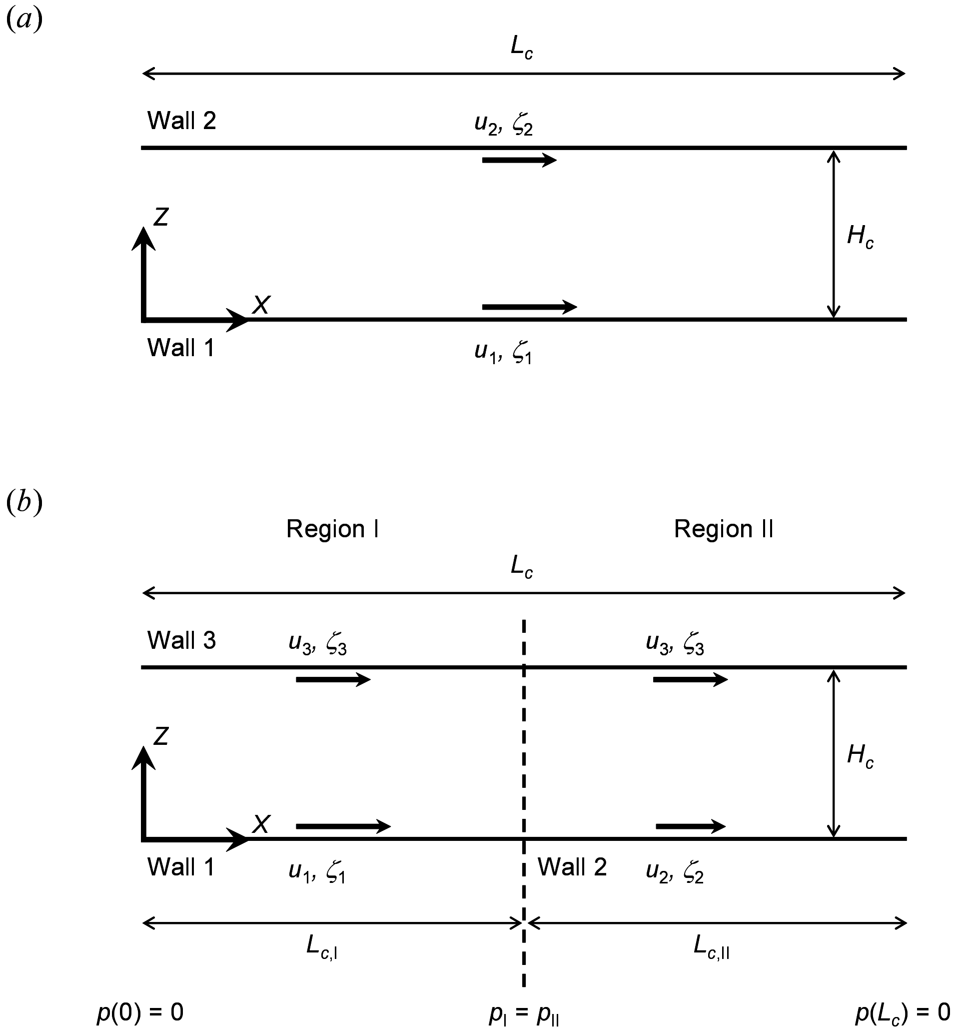

Figure 5.2. Two-dimensional models for electroosmotic flow with nonuniform zeta-potential. (*a*) Microchannel composed of walls with differnent zeta-potential. (*b*) Microchannel composed of walls with the zeta-potential distribution in the X-direction and uniform zeta-potential.

obtained by the superposition of the Couette flows given by equation (2.9)

$$\begin{aligned} u = & u_1 \left[\left(1 - \frac{z}{H_c} \right) - \sum_{n=1}^{\infty} \frac{2}{n\pi} \exp\left(-\frac{n^2\pi^2 t}{\tau_{eof}} \right) \sin\frac{n\pi z}{H_c} \right] \\ & + u_2 \left[\frac{z}{H_c} - \sum_{n=1}^{\infty} \frac{2}{n\pi} \exp\left(-\frac{n^2\pi^2 t}{\tau_{eof}} \right) \sin\left(n\pi - \frac{n\pi z}{H_c} \right) \right] \end{aligned} \tag{5.4}$$

The flow rate, Q_{2D} (m^2/s), is found by integrating equation (5.4) over the channel depth

$$Q_{2D} = -\frac{\epsilon E}{\mu} \frac{1}{2} \left(\zeta_1 + \zeta_2 \right) H_c C_q(t) \tag{5.5}$$

where C_q (-) is the coefficient determined by the time from the application of electric field

$$C_q(t) = 1 - \sum_{n=1}^{\infty} \frac{8}{(2n-1)^2\pi^2} \exp\left(-\frac{(2n-1)^2\pi^2 t}{\tau_{eof}} \right) \tag{5.6}$$

Next, a two-dimensional microchannel composed of the wall with the zeta-potential distribution in the streamwise direction (ζ_1 to ζ_2 at $x = L_{c,\mathrm{I}}$) and that with uniform zeta-potential, ζ_3 (V), is considered as shown in figure 5.2(*b*). The velocity profile and the flow rate are estimated on the basis of the model for steady electroosmotic capillary flow with the axial variation of wall zeta-potential, proposed by Herr *et al.* (2000). Only the flows far from the interface between region I and II are considered, and hence the slip velocities at each wall are also given by the Helmholtz-Smoluchowski equation. Electroosmotic velocity profiles with pressure gradients in region I and II are obtained from equation (5.4) on an assumption that pressure-driven flow is in the steady state

$$\begin{aligned} \text{Region I: } u = & u_1 \left[\left(1 - \frac{z}{H_c} \right) - \sum_{n=1}^{\infty} \frac{2}{n\pi} \exp\left(-\frac{n^2\pi^2 t}{\tau_{eof}} \right) \sin\frac{n\pi z}{H_c} \right] \\ & + u_3 \left[\frac{z}{H_c} - \sum_{n=1}^{\infty} \frac{2}{n\pi} \exp\left(-\frac{n^2\pi^2 t}{\tau_{eof}} \right) \sin\left(n\pi - \frac{n\pi z}{H_c} \right) \right] \\ & - \left. \frac{dp}{dx} \right|_{\mathrm{I}} \frac{1}{2\mu} \left(H_c z - z^2 \right) \end{aligned} \tag{5.7}$$

$$\begin{aligned} \text{Region II: } u = & u_2 \left[\left(1 - \frac{z}{H_c} \right) - \sum_{n=1}^{\infty} \frac{2}{n\pi} \exp\left(-\frac{n^2\pi^2 t}{\tau_{eof}} \right) \sin\frac{n\pi z}{H_c} \right] \\ & + u_3 \left[\frac{z}{H_c} - \sum_{n=1}^{\infty} \frac{2}{n\pi} \exp\left(-\frac{n^2\pi^2 t}{\tau_{eof}} \right) \sin\left(n\pi - \frac{n\pi z}{H_c} \right) \right] \\ & - \left. \frac{dp}{dx} \right|_{\mathrm{II}} \frac{1}{2\mu} \left(H_c z - z^2 \right) \end{aligned} \tag{5.8}$$

For the incompressible liquid, the flow rate is conserved in the channel due to the continuity, $Q_{2D,\mathrm{I}} = Q_{2D,\mathrm{II}}$. The pressure at the inlet and outlet are equal, and the continuous pressure distribution demands a condition, $p_{\mathrm{I}} = p_{\mathrm{II}}$ at $x = L_{c,\mathrm{I}}$. From these conditions and equations (5.7) and (5.8), the flow rate and the pressure gradients are obtained as follows

$$Q_{2D} = -\frac{\epsilon E}{\mu}\frac{1}{2}\left(\frac{L_{c,\mathrm{I}}}{L_c}\zeta_1 + \frac{L_{c,\mathrm{II}}}{L_c}\zeta_2 + \zeta_3\right) H_c C_q(t) \tag{5.9}$$

$$\begin{aligned} \left.\frac{dp}{dx}\right|_{\mathrm{I}} &= \frac{6\mu L_{c,\mathrm{II}}}{H_c^2 L_c}\left(u_1 - u_2\right) C_q(t) \\ \left.\frac{dp}{dx}\right|_{\mathrm{II}} &= -\frac{6\mu L_{c,\mathrm{I}}}{H_c^2 L_c}\left(u_1 - u_2\right) C_q(t) \end{aligned} \tag{5.10}$$

Considering the two-dimensional flow rate with nonuniform zeta-potential by equations (5.5) and (5.9), the flow rate is dependent on the summation of the ratios of a wall length multiplied with a zeta-potential to the total length of the wall in the channel, $2L_c$ (m). Therefore, the volumetric flow rate in a three-dimensional microchannel without considering the side walls is described as follows

$$Q_{3D} = -\frac{\epsilon E}{\mu}\frac{\sum_{i=1}^{n} A_i \zeta_i}{A_{total}} A_{cross} C_q(t) \tag{5.11}$$

where A_i (m^2) is the area of the ith wall with the zeta-potential of ζ_i (V), A_{total} (m^2) is the total area of the wall in the microchannel and A_{cross} (m^2) is the area of cross-section of the microchannel. Equation (5.11) theoretically shows that the volumetric flow rate is not dependent on the pattern of the zeta-potential at the wall but on the average zeta-potential in the microchannel, $\zeta_{ave} = \sum_{i=1}^{n} A_i \zeta_i / A_{total}$ (V), even in the transient state.

5.2 Experimental Setup

Four kinds of microchannel with the high aspect ratio were prepared for the experiments as illustrated in figure 5.3. All channels were fabricated by the replica molding using poly (dimethylsiloxane) (PDMS) (section 2.2), and sealed with a cover glass. The microchannel with uniform zeta-potential (channel length: $L_c = 30$ mm, channel width: $W_c = 700\ \mu$m, channel depth: $H_c = 78\ \mu$m, aspect ratio: $k = 8.97$) as shown in figure 5.3(a) was fabricated by sealing the PDMS microchannel with a cover glass on which PDMS was spincoated. The microchannel composed of the walls made of different material ($L_c = 30$ mm, $W_c = 700\ \mu$m, $H_c = 78\ \mu$m, $k = 8.97$, figure 5.3(b)) was normally fabricated by the replica molding. The microchannel with the surface modification of the step pattern perpendicular to the channel axis ($L_c = 30$ mm, $W_c = 700\ \mu$m, $H_c = 78\ \mu$m, $k = 8.97$, figure 5.3(c)) was prepared by the microcontact printing of octadecyltrichlorosilane (OTS) on the cover glass (section 2.2). The microchannel with the OTS modification of the step pattern parallel to the channel axis ($L_c = 27.6$ mm, $W_c = 1000\ \mu$m, $H_c = 63\ \mu$m, $k = 15.9$) was also prepared as depicted in figure 5.3(d).

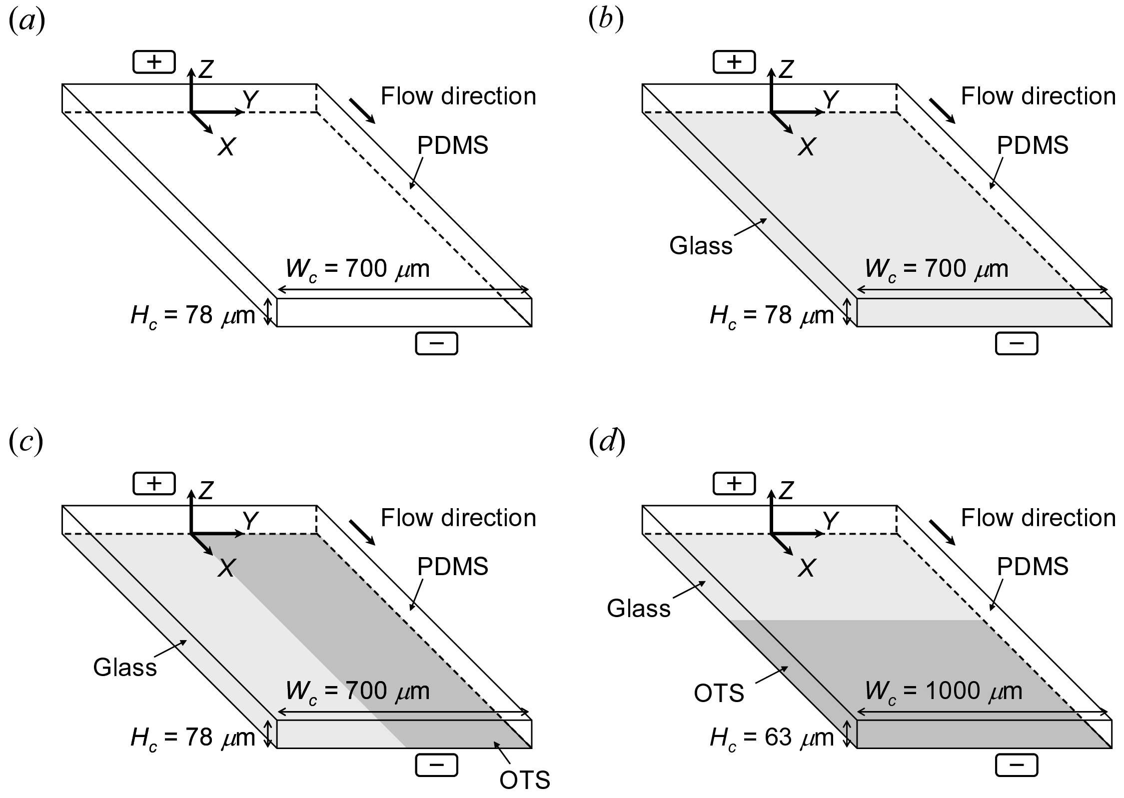

Figure 5.3. Schematics of microchannels (*a*) made of PDMS and (*b*) made of glass and PDMS, and those with the OTS modification of the step pattern (*c*) perpendicular to the electric field and (*d*) parallel to the electric field.

Table 5.1. List of uncertainties in 95% confidence level in the measurement of electroosmotic velocity

Uncertainty (95% confidence)		Excitation light source Mercury lamp	 Evanescent wave
Bias error (X-direction)	(μm/s)	97	97
Random error	(μm/s)	30.1	52.8
Total uncertainty (X-direction)	(μm/s)	102	110
Total uncertainty (Y-direction)	(μm/s)	30.1	52.8

The working fluid composed of a 5 mmol/l HEPES buffer and a 1 mmol/l KCl with the tracer particles (sections 3.1 and 3.2) was injected into the microchannel. The thickness of the electric double layer (the Debye length) was 9.6 nm and negligible compared with the channel width and length. Heights of the aqueous surface in the inlet and outlet of the channel were adjusted to be equal, and thus the pressure at the inlet and outlet was the atmospheric pressure. A DC voltage was applied into the microchannel to induce electroosmotic flow at $t = 0$. The voltage was adjusted to generate the electric field of 250 V/cm calculated using the channel length. The velocity measurements were conducted, and the particle electrophoretic mobility of $\mu_{ep} = -5.34\times10^{-4}$ cm^2/V s (section 3.5) was used to obtain the electroosmotic velocity from the measured particle velocity by equation (3.2). In the bulk velocity measurement, the electroosmotic velocities at different depths were measured by moving the focal plane of objective lens in the Z-direction with the interval of 4.4 μm. When the wall zeta-potential is assumed to be uniform, the zeta-potential was estimated from the obtained electroosmotic velocity by the Helmholtz-Smoluchowski equation (equation (2.42)). It is noted that the electrophoretic mobility also has the uncertainty of 0.39×10^{-4} cm^2/V s in 95% confidence level. This uncertainty contributes to the electroosmotic velocity as a bias error, but is independent of the error of the velocity profile. The uncertainty of electrophoretic velocity was 97.0 μm/s calculated using the magnitude of electric field by $u_{ep} = \mu_{ep}E_x$. On the other hand, since the bias error due to PTV was negligible compared with the random errors of the measurement system as described in section 3.4, the uncertainty due to the measurement system contributes to the electroosmotic velocity as the random errors. Thus, the uncertainty in 95% confidence level of the electroosmotic velocity was estimated to be 102 μm/s in the bulk velocity measurement and 110 μm/s in the near-wall velocity measurement. It is noted that spanwise velocity is independent of the electric field and the uncertainty remained to be 30.1 μm/s in the bulk velocity measurement and 52.8 μm/s in the near-wall velocity measurement. Table 5.1 lists the uncertainties in 95% confidence level in the measurement of electroosmotic velocity.

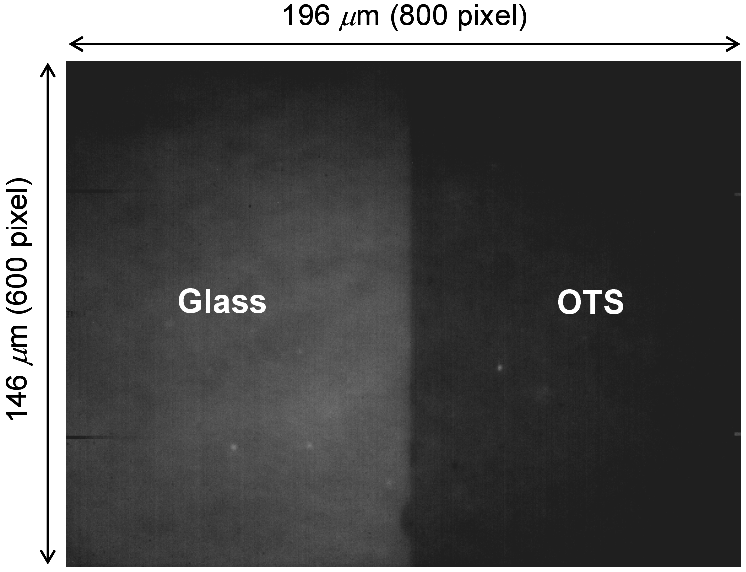

Figure 5.4. Evanescent wave illumination image of the surface modification pattern using the Ru(Phen) solution.

In the measurements using the microchannel with the step change zeta-potential, it is difficult to locate the interface between glass and OTS modified areas, from the particle images. Thus, prior to the velocity measurements, the interface was found by the nanoscale laser induced fluorescence imaging (chapter 4). The aqueous solution of a 100 μmol/l dichlorotris(1,10-phenanthroline)ruthenium(II) hydrate (Ru(Phen)), which becomes divalent cation, was injected in the microchannel. The evanescent wave was selected as the excitation light, and illuminated the fluorescent dye in the vicinity of the wall. Figure 5.4 shows the fluorescence image of the surface modification pattern, captured by the CMOS camera. The interface between the OTS modified area and the glass area was clearly observed. Since the magnitude of negative zeta-potential at the glass area was larger than the OTS modified area by the difference of the chemical endgroups between -SiO^- (glass) and -CH_3 (OTS), the fluorescent intensity became higher in the glass area due to the attraction of fluorescence cations to the wall.

When the total internal reflection of laser beam occurs at the interface between the OTS-modified wall and the electrolyte solution, the evanescent wave and its intensity can be affected by the OTS monolayers with the 5 $\sim$ 7 nm thickness as described in section 2.2. Axelrod (2001) pointed out that the penetration depth of the evanescent wave in the electrolyte solution is affected and the light scatter is induced by the existence of such the intermediate layer, but these effects are small when the layer thickness is less than 10 nm. In addition, from the captured fluorescence images, significant influences on the evanescent wave were not observed.

5.3 Electroosmotic Flow with Uniform Zeta-Potential Compared with Theoretical Model

The electroosmotic velocities in the microchannel made of PDMS (figure 5.3(*a*)) were measured. Since the evanescent wave was difficult to be generated at the interface between the PDMS spincoated on the cover glass and the working fluid, only the measurement using the volume illumination was conducted. The measurement technique was verified from the comparison of the experimental results to the theoretical model with uniform zeta-potential, proposed by Yang *et al.* (2004).

Figure 5.5 shows velocity vector maps at $t = 0.5$ ms, $t = 1.3$ ms and $t = 7.7$ ms ($z = 39.6$ μm). The electroosmotic velocities were successfully measured with a high spatial resolution of 39.1×9.8 μm^2 to increase the resolution in the spanwise direction (Y-direction). Due to the 50% overlapping of the reference regions, the vector interval was 19.6×4.9 μm. The fluid started to move in response to the application of electric field, and the flow reached to the steady state at about $t = 6$ ms. The velocities near the side wall were higher than other region at $t = 0.5$ ms (figure 5.5(*b*)). This shows that the momentum due to the electric body force was generated near the wall, and transported to the center of the channel. The electroosmotic velocities at $t = 7.7$ ms have almost uniform distribution with the variation under the random error at each time in the center of the channel (figure 5.5(*a*)). The zeta-potential at the PDMS walls was calculated to be -61.3 mV from the averaged velocity of 1247 μm/s by the Helmholtz-Smoluchowski equation.

The experimental results were compared with the analytical model of transient electroosmotic flow with uniform zeta-potential, which was experimentally verified using a square glass channel of a 300 μm width (Yan *et al.*, 2006). The slip boundary condition was estimated from the obtained zeta-potential of PDMS wall. From the hydraulic diameter of $D_h = 140$ μm, the relaxation time for electroosmotic flow was calculated to be $\tau_{eof} = D_h^2/\nu = 22.1$ ms by equation (2.43). These parameters were substituted in the analytical solution by equation (2.44). Figure 5.6 shows time-series electroosmotic velocity profiles in the spanwise direction (Y-direction) at $z = 39.6$ μm, compared with the analytical model. The values of the velocity were obtained by averaging the velocity vectors in the streamwise direction (X-direction). Error bars were the square-root of sum of squares of the standard deviation by the averaging in the streamwise direction, that due to the random error reduced by the averaging and that by the bias error due to the uncertainty of electrophoretic mobility. The experimental results quantitatively agree with the analytical model, especially in the center of the microchannel. Thus, it is concluded that the present technique successfully measured the velocity of transient electroosmotic flow.

The results shows that electroosmotic flow reached the steady state at a time faster than (*a*) Center of the channel

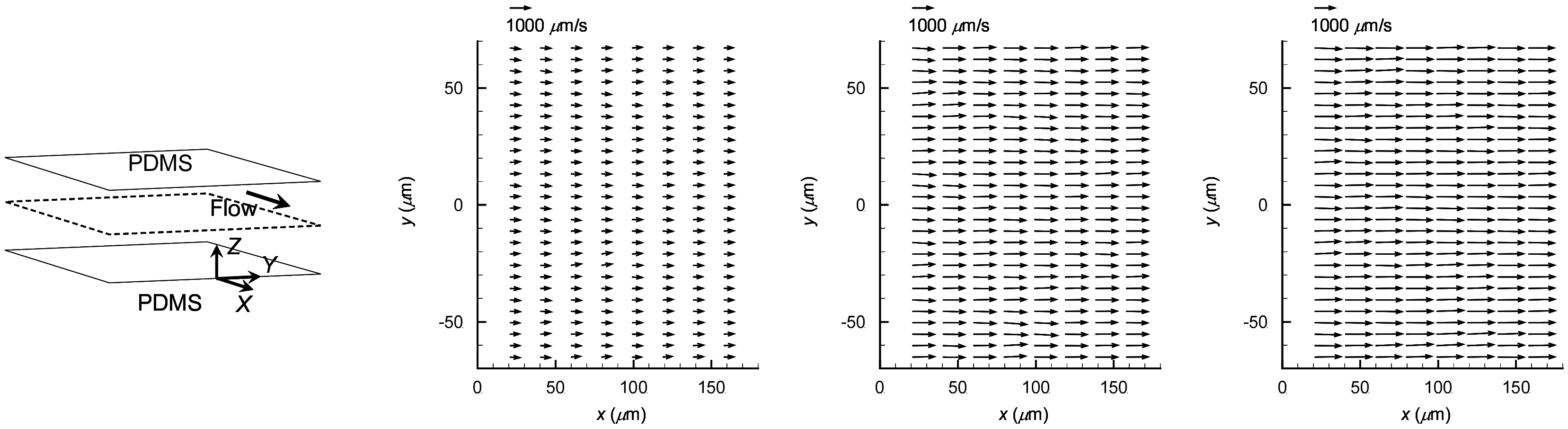

(*b*) Near the side wall

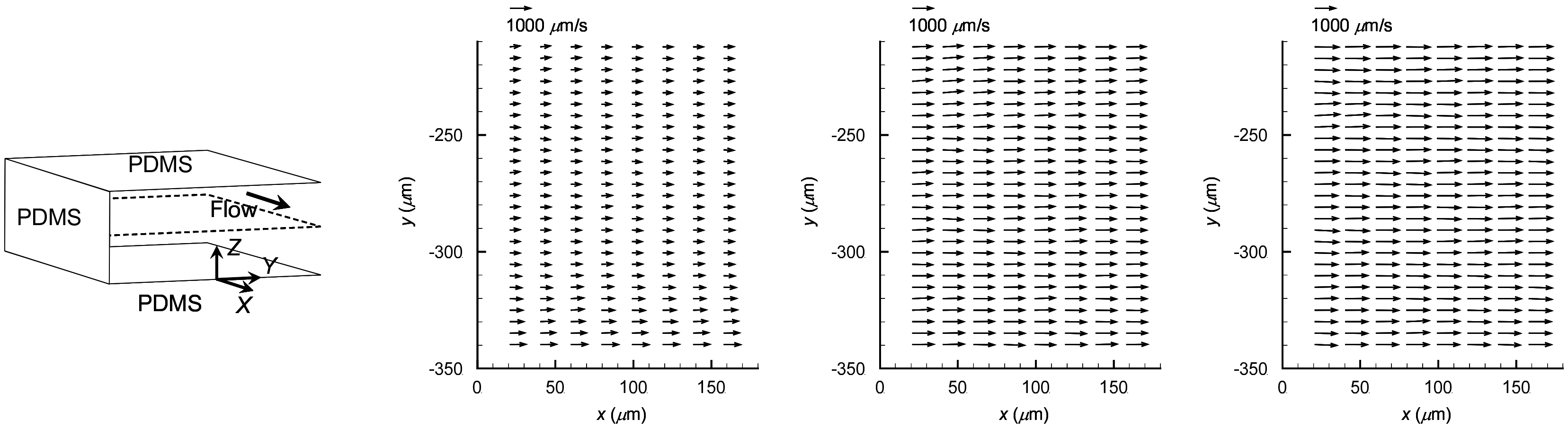

$t = 0.5$ ms

$t = 1.3$ ms

$t = 7.7$ ms

Figure 5.5. Velocity vector maps at $z = 39.6\ \mu$m (*a*) in the center of the channel and (*b*) near the side wall, when the microchannel was composed of PDMS walls.

(*a*)

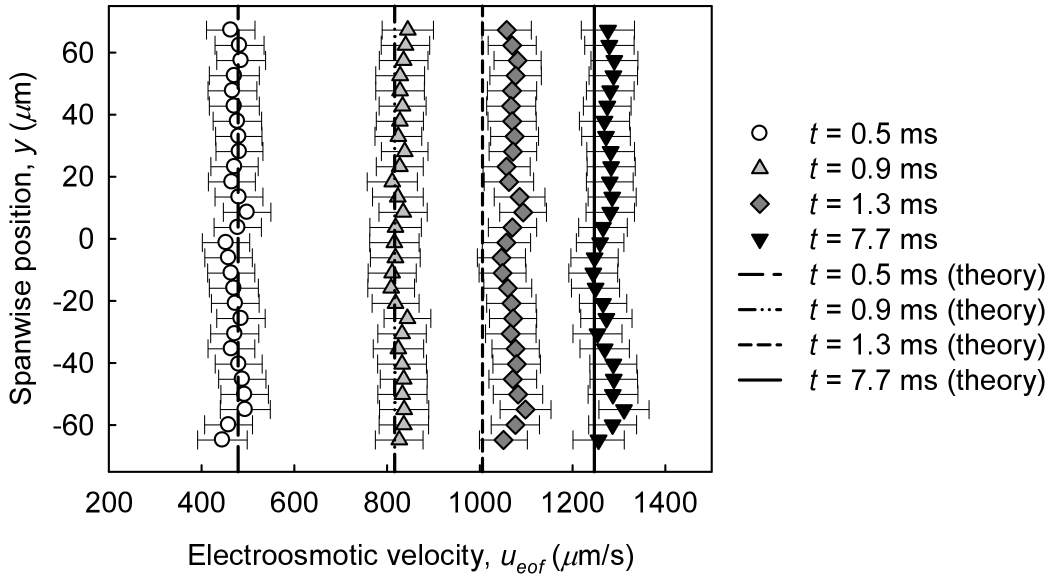

(*b*)

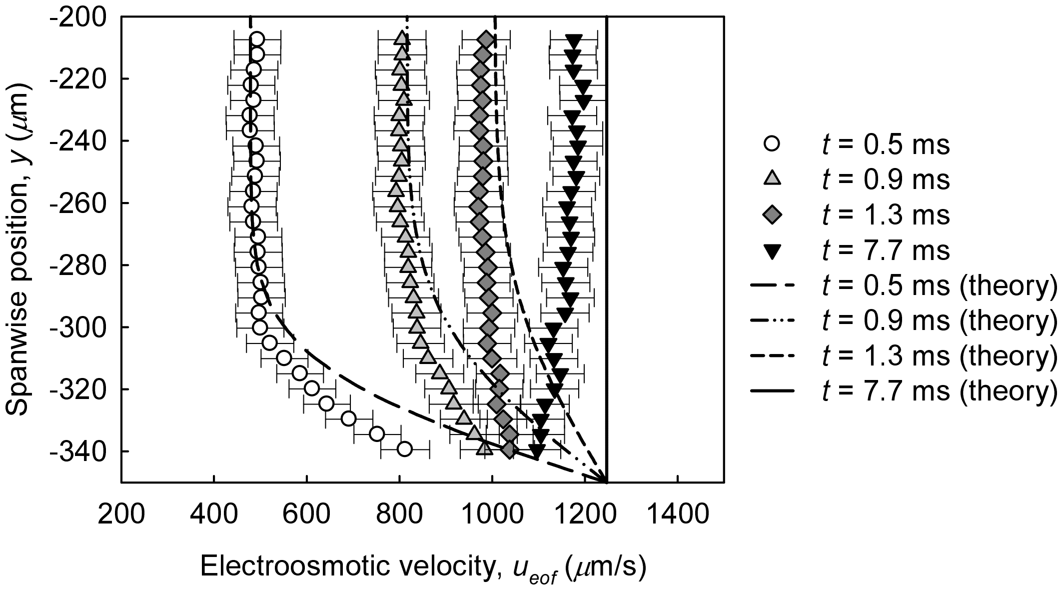

Figure 5.6. Time-series electroosmotic velocity profiles in the Y-direction at $z = 39.6$ μm (*a*) in the center of the microchannel and (*b*) near the side wall, compared with the theoretical model.

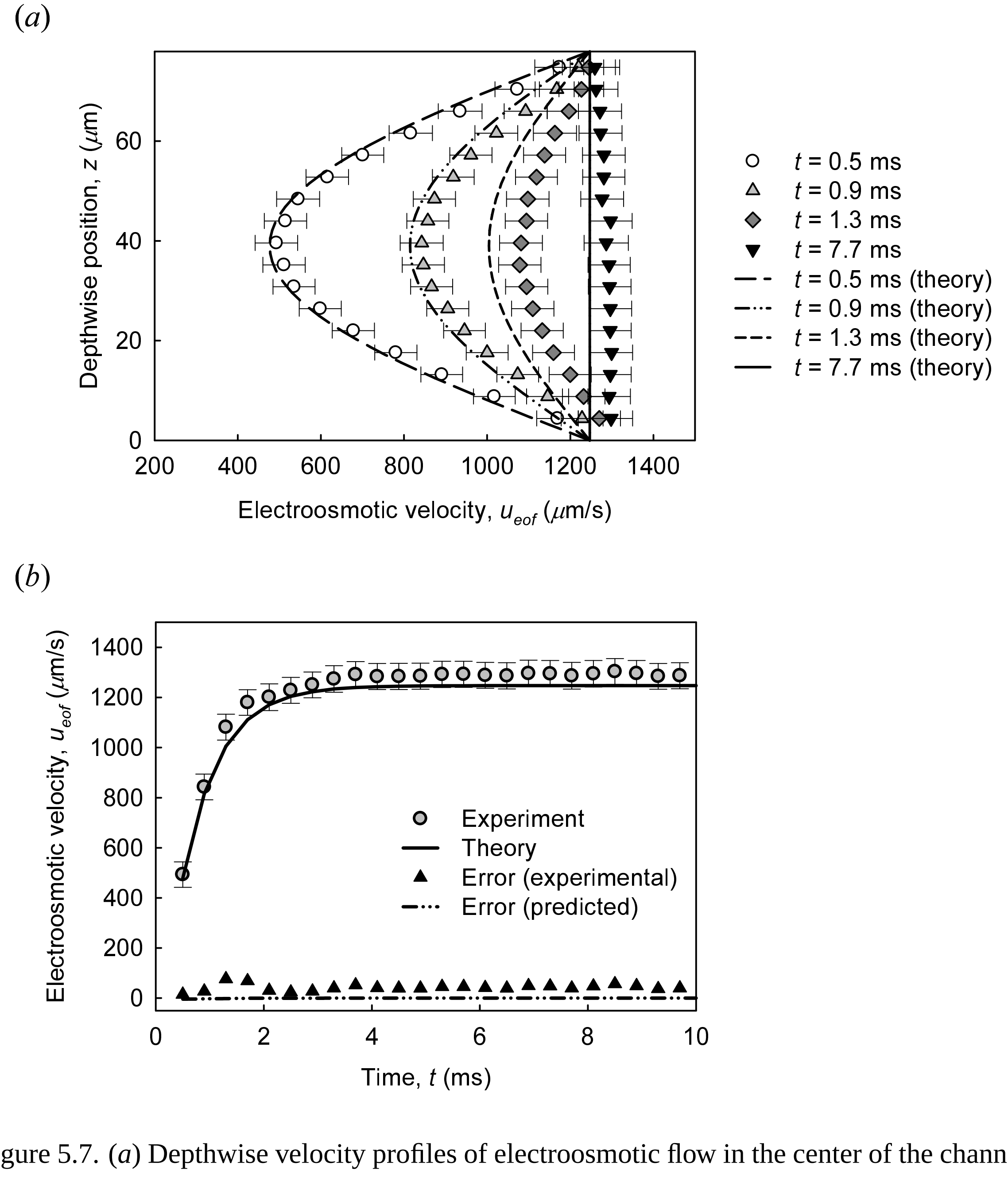

Figure 5.7. (*a*) Depthwise velocity profiles of electroosmotic flow in the center of the channel, compared with the theoretical model. (*b*) Time-series measured and theoretical velocities at $z = 39.6\ \mu$m, and errors of the measured velocities from the theoretical values and those by the approximation based on the central difference.

the relaxation time by the hydraulic diameter. This is because the flow is regarded as the two-dimensional flow independent of the spanwise position, y (m), due to the high aspect ratio. From the velocity profiles shown in figure 5.6, the effect of the momentum transport from the side wall on the flow structure appears only near the side wall about 100 μm. Thus, the relaxation time of electroosmotic flow was given by $\tau_{eof} = H_c^2/\nu = 6.83$ ms, which is approximately equal to the experimental results. Figure 5.7(*a*) shows the depthwise profiles of electroosmotic velocities in the center of the channel, compared with the two-dimensional model calculated by equation (5.4). The velocity profiles show the parabolic profiles in the transient state and nearly the plug profile in the steady state. The agreements of the results with the two-dimensional model shows that electroosmotic flow in the center of the channel is considered as the superposition of the Couette flows. However, there are slightly differences between the experimental results and the theoretical model with uniform zeta-potential. The measured electroosmotic velocity near the bottom wall is larger than that near the top wall about 50 μm/s. It is considered that the zeta-potential of the PDMS spincoated on the cover glass was different from that of the PDMS microchannel fabricated by the replica molding, and this resulted in disagreements between the experiment and theory in the depth wise velocity profiles and the spanwise velocity profiles near the side wall (figure 5.6(*b*)).

The measurement error caused by the calculation of the velocity, $u = \Delta x/\Delta t$, based on the central difference (equation (3.3)) was evaluated. Figure 5.7(*b*) shows the time-series measured and theoretical velocities at $z = 39.6$ μm, errors of the measured velocities from the theory, and predicted errors by the approximation using the central difference, given by $\Delta x/\Delta t - u = 1/24(\partial^3 f/\partial t^3)\Delta t^2$ where $x = f(t)$. The experimental error from the theory was 42.6 μm/s and the predicted error was -0.45 μm/s, at the average value. Therefore, the predicted errors are negligible, and it is concluded that the time resolution is enough to measure the flow velocity in transient electroosmotic flow.

5.4 Electroosmotic Flow Structure with Nonuniform Zeta-Potential

Near-wall and bulk velocity measurements were conducted using the microchannels with nonuniform zeta-potential. In the microchannel as shown in figure 5.3(*b*), the each wall was made of uniform materials, glass and PDMS. In the microchannels with the surface modification (figures 5.3(*c*) and (*d*)), the step change zeta-potential is considered to be generated on the channel wall.

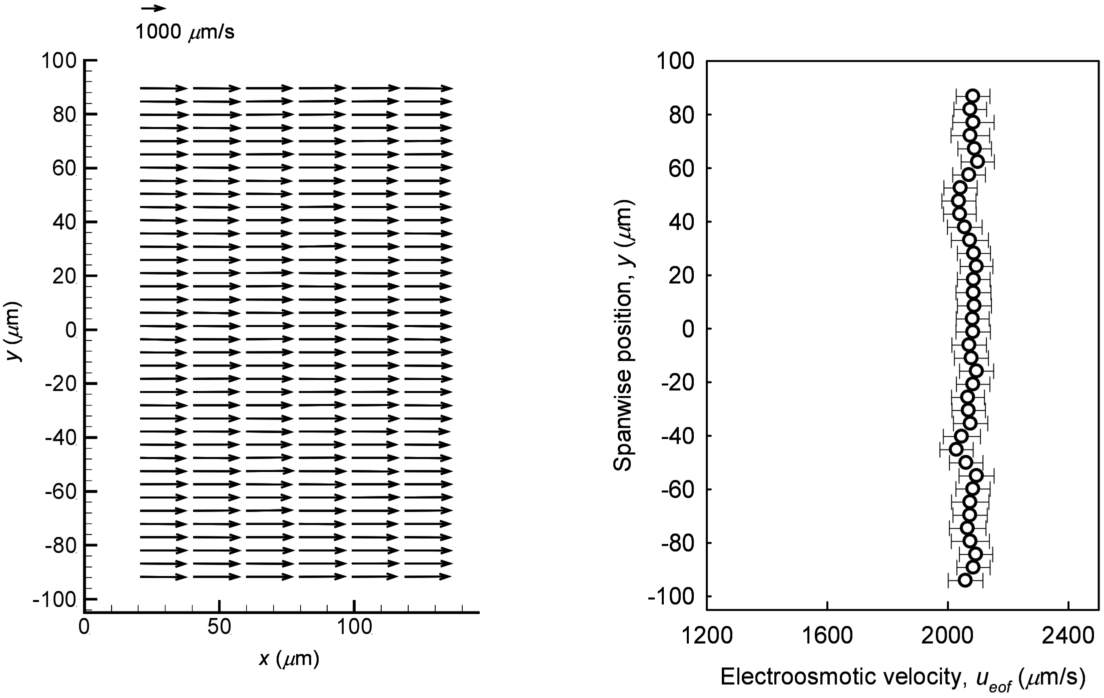

Figure 5.8. Near-wall velocity vector map at the glass wall, and velocity profile obtained by averaging the velocities in the X-direction.

5.4.1 Nonuniform Zeta-Potential with Material Heterogeneity

Figure 5.8 shows the electroosmotic velocity vector map in the vicinity of the glass wall and the velocity profile in the spanwise direction (Y-direction), obtained by the near-wall velocity measurement using the microchannel as illustrated in figure 5.3(*b*). The spatial resolution was $39.1 \times 9.8\ \mu\text{m}^2$ and the vector interval was $19.6 \times 4.9\ \mu$m. The near-wall velocities were successfully obtained as well as the bulk velocities. The velocities show the uniform profile due to the homogeneous zeta-potential at the glass wall. The velocities were independent of the time at the time resolution of 400 μs. Considering the relaxation time of electroosmotic flow in the evanescent wave illumination area given by $\tau_v = \delta z_{eva}{}^2/\nu = 0.6\ \mu$s (equation (2.8)), the obtained near-wall velocities are assumed to be in the steady state. The measurement depth by the evanescent wave illumination of 720 nm is sufficiently large compared with the thickness of the electric double layer of 9.6 nm. Therefore, it is considered that the electroosmotic velocities measured using the evanescent wave illumination were those outside the electric double layer. From the near-wall velocities, the zeta-potential at the glass wall was estimated to be -103 mV.

Figure 5.9 shows the time dependent depthwise velocity in the center of the channel compared with the two-dimensional flow model by equation (5.4). The relaxation time of $\tau_{eof} = 6.83$ ms and the zeta-potential of glass and PDMS were applied to equation (5.4). The

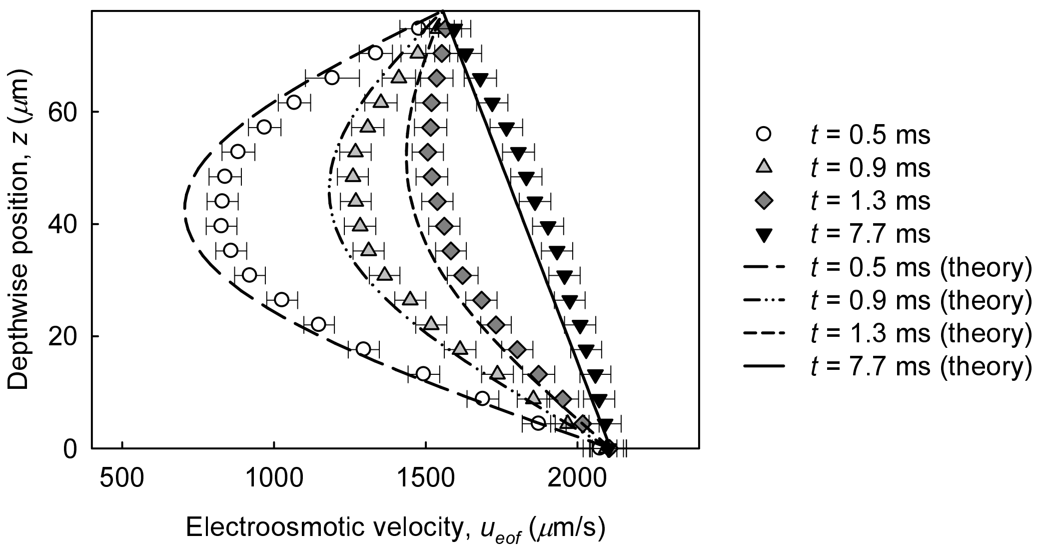

Figure 5.9. Time dependent velocity profiles of electroosmotic flow in the depthwise direction in the center of channel.

zeta-potential at the PDMS wall was estimated to be −77 mV from the velocity at the PDMS wall obtained by the approximation of the velocity profile using the least square method. The electroosmotic velocities show the parabolic profiles in the transient state and the linear profile at the steady state due to the difference of material between the bottom and top walls. The experimental results show quantitative agreements with the flow model. Hence, it is concluded that electroosmotic flow in the center of the channel is assumed to be two-dimensional flow by the superposition of the Couette flows with the different wall velocities.

Effect of the momentum transport from the side wall on the flow field was evaluated. Figure 5.10 shows the spanwise velocity profiles near the side wall at different depthwise positions. In the transient state, the values and profiles of velocity are different at each depth due to the material heterogeneity and the degree of the momentum transport, but the velocities near the PDMS side wall were nealy constant about 1500 μ/s approximately equal to the velocity at the PDMS wall. In the steady state, the difference of material between the glass at the bottom wall and PDMS at the side and top walls generated the spanwise velocity profile near the side wall. Figure 5.11 shows the time-series velocity profiles in the depthwise direction (Z-direction) at different spanwise positions. Near the PDMS side wall at $y = -342$ μm, the electroosmotic velocities were almost steady as shown in figure 5.11(a), since the effect of the side wall was dominant. The electroosmotic velocity significantly decreases with increasing the depthwise position, and the velocity profiles become flat at the velocity about 1500 μm/s. On the other hand, at the distance from the side wall of 100 μm ($y = -250$ μm as shown in figure 5.11(b)),

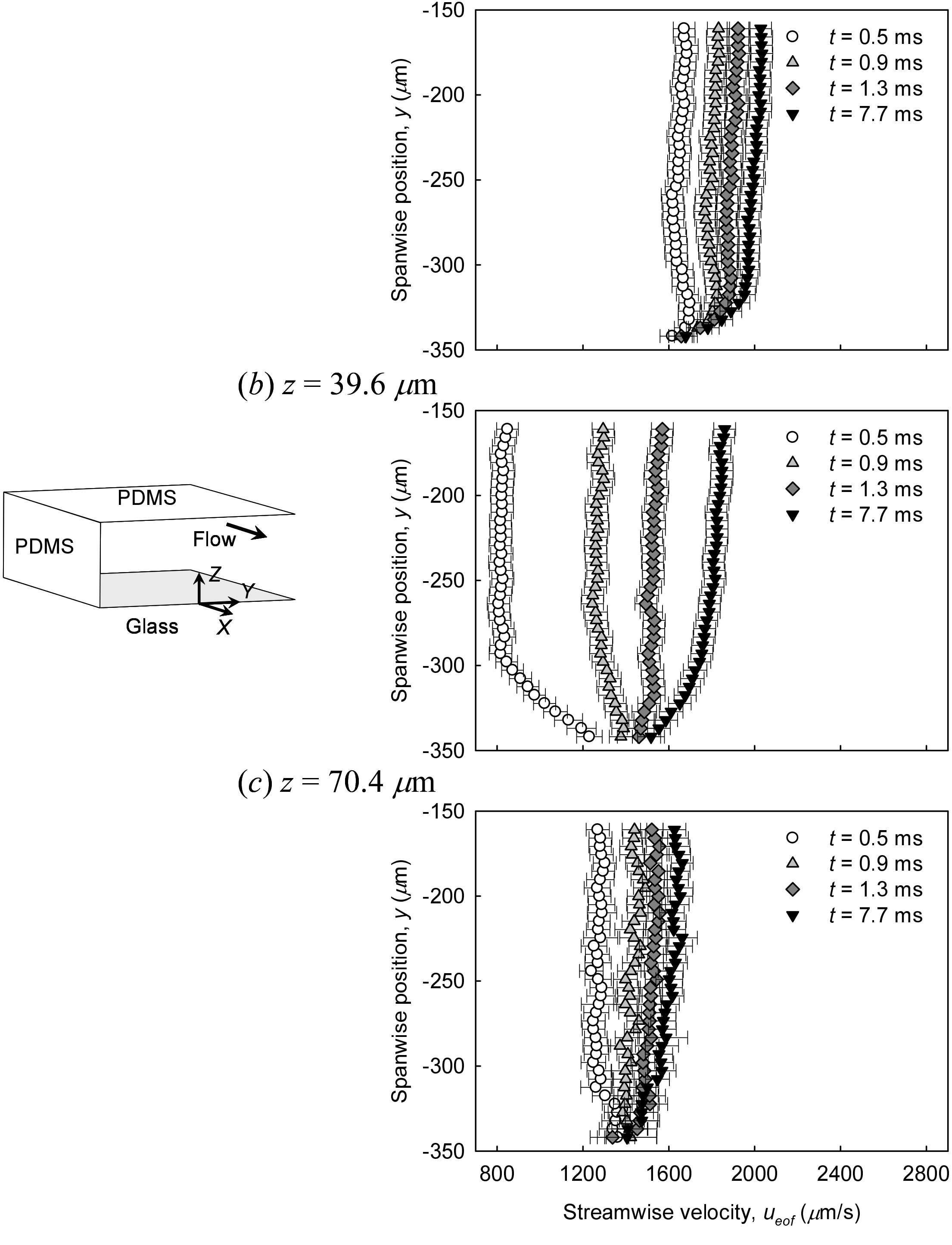

(a) $z = 8.8$ μm

(b) $z = 39.6$ μm

(c) $z = 70.4$ μm

Figure 5.10. Spanwise velocity profiles of electroosmotic flow near the side wall at (a) $z = 8.8$ μm, (b) $z = 39.6$ μm and (c) $z = 70.4$ μm.

(a) $y = -342$ μm

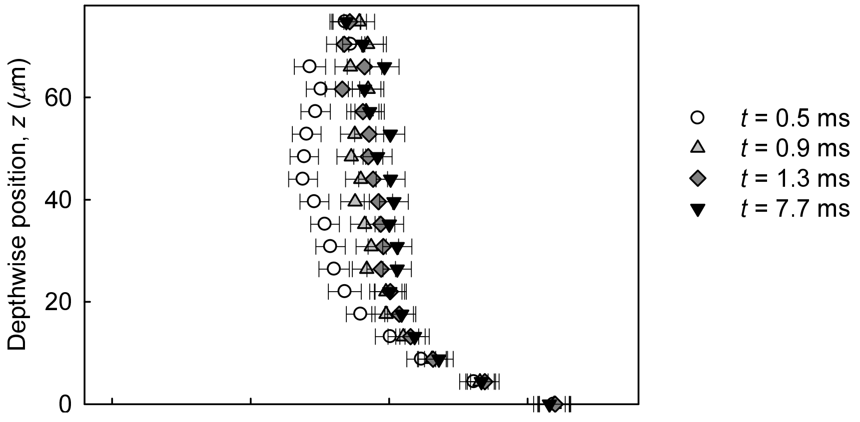

(b) $y = -250$ μm

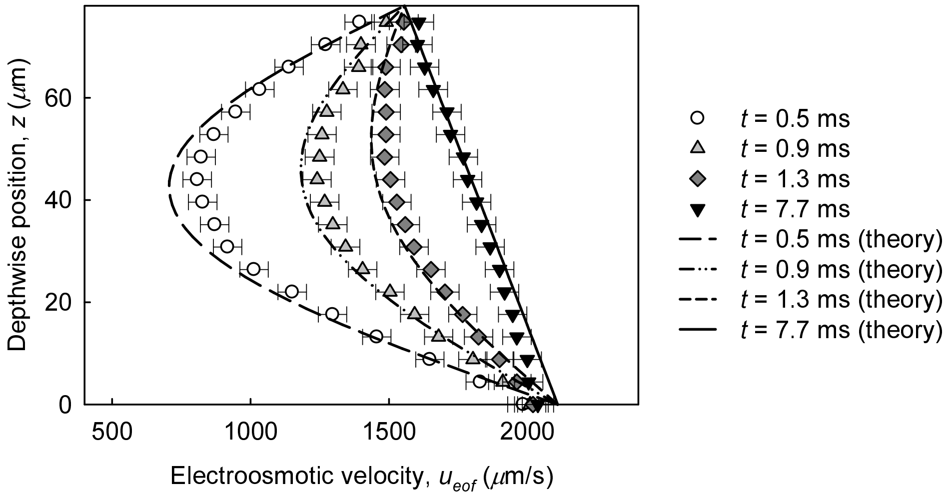

Figure 5.11. Depthwise velocity profiles of electroosmotic flow at different spanwise positions ((a) $y = -342$ μm and (b) $y = -250$ μm.

the depthwise velocity profiles are almost same as those in the center of the channel (figure 5.9) and nearly correspond to the flow model. Thus, it is concluded that the effect of the side wall was small in the high aspect ratio channel with the material heterogeneity and the flow in the region except near the side wall was nearly two-dimensional flow.

5.4.2 Step Change Zeta-Potential Perpendicular to Electric Field

Figure 5.12 shows the near-wall electroosmotic velocities and spanwise velocity profile in the vicinity of the wall, where OTS was modified on the glass wall at $y > 0$ as illustrated in figure 5.3(c). The velocities show the uniform distribution in the streamwise direction (X-direction) and the variation in the spanwise direction (Y-direction). Although the step change

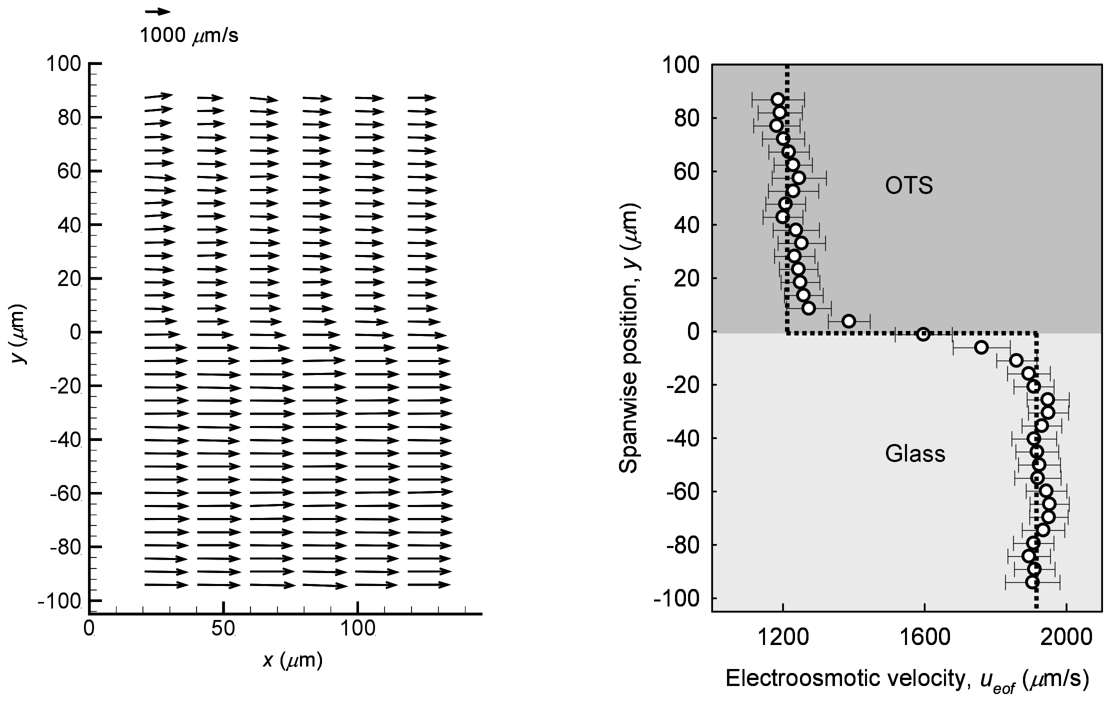

Figure 5.12. Near-wall velocity vector map with the step change zeta-potential perpendicular to the electric field, and velocity profile obtained by averaging the velocities in the *X*-direction.

zeta-potential perpendicular to the electric field is considered to be generated by the suface modification, the velocities do not show the step change profile but the profile with the steep gradient in the region of $-20 < y < 20$ μm. The velocity profile is almost flat in the region except near the interface between glass and OTS. From the velocities in the region with the flat flow profiles, the zeta-potential at the glass and OTS walls were estimated to be −94.7 mV and −59.9 mV, respectively. Since the concentration of ions in the electric double layer is different with the wall charge, it is considered that the ion diffusion in the electric double layer will occur at the interface between glass and OTS walls. This will result in the gradient of the electric body force and affect the velocity profile. However, due to the small thickness of electric double layer of 9.6 nm, the diffusion effect on the velocity profile is considered to be small and negligible. Therefore, it is concluded that the velocity gradient with the length scale of 40 μm was generated due to the viscous effect of the fluid. The momentum generated in the vicinity of the wall was examined using the obtained results. At the region of $-85 < y < 85$ μm, the total momentum in the vicinity of the wall was estimated by the integral of $\rho u_{eof}(y)$ (kg/m^{2}s) over the spanwise direction. The momentum obtained from the results was 2.73×10^{-4} kg/m^{2}s and almost equal to that calculated from the ideal step change velocity profile shown in figure 5.12 as dotted line predicted by the Helmholtz-Smoluchowski equation, 2.67×10^{-4} kg/m^{2}s. This shows that the total momentum was conserved and equal to that generated by the step change zeta-potential.

Figure 5.13 shows the streamwise velocity profiles at the cross-sectional plane (XZ-plane) in the center of the channel, obtained by the bulk and near-wall velocity measurements. The time to reach the steady state was approximately equal to the relaxation time calculated from the channel depth, $\tau_{eof} = 6.83$ ms. The velocities show the spanwise distribution near the bottom wall with the step change zeta-potential, and the flat velocity profile near the top wall made of PDMS. The zeta-potential at the PDMS wall was estimated to be −62.2 mV from the electroosmotic velocity near the PDMS wall. Figure 5.14 shows the time-series velocity profiles in the spanwise direction (Y-direction) at different depths. The velocity gradient in the spanwise direction becomes smaller with increasing the depthwise position due to the effect of the uniform zeta-potential at the PDMS wall. It is considered that the momentum diffusion in the spanwise direction also contributed to the reduction of the velocity gradient, since the range of the spanwise velocity gradient is expanded with increasing the depthwise position from $-30 < y < 30$ μm at $z = 8.8$ μm to $-50 < y < 50$ μm at $z = 39.6$ μm. Figure 5.15 shows the time-series velocity profiles in the depthwise direction (Z-direction) at different spanwise positions. In the transient state at $t < 1.3$ ms, the velocities show the paraboric profile in the all region but the magnitude is different at each position with the step change zeta-potential at the bottom wall. In the steady state, the velocities at the area far from the interface between glass and OTS walls ($y = -75$ μm and $y = 77$ μm) show the linear profiles due to the difference in the zeta-potential between the top and bottom walls. Thus, it is considered that the two flows in the same direction (flows in the glass-PDMS region and the OTS-PDMS region) were generated by the step change zeta-potential perpendicular to the electric field, and a transitional region was generated between the two flows.

In order to evaluate the effect of the step change zeta-potential perpendicular to the electric field on the flow field, the shear stress exerted on the fluid, which shows the momentum diffusion by the velocity gradient, was estimated from the measured velocities. The shear stress exerted in the X-direction caused by the spanwise velocity gradient, τ_{yx} (Pa), is given by

$$\tau_{yx} = -\mu \frac{\partial u}{\partial y} \tag{5.12}$$

Figure 5.16 shows spanwise profiles of the shear stress added on the fluid at different depthwise positions. It is noted that the profiles of the shear stress were almost independent of time. The shear stress was generated around the interface between glass and OTS at $y = 0$. The positive values show that the momentum was trasnported from the glass-PDMS region ($y < 0$) to the OTS-PDMS region ($y > 0$) because the near-wall velocity by the glass wall was larger than that by the OTS wall. The value of shear stress is large near the wall ($z = 0$) and decreases with increasing the depthwise position, but the region where the shear stress was generated becomes broader. This shows that the momentum diffusion in the spanwise direction occured

(a) t = 0.5 ms

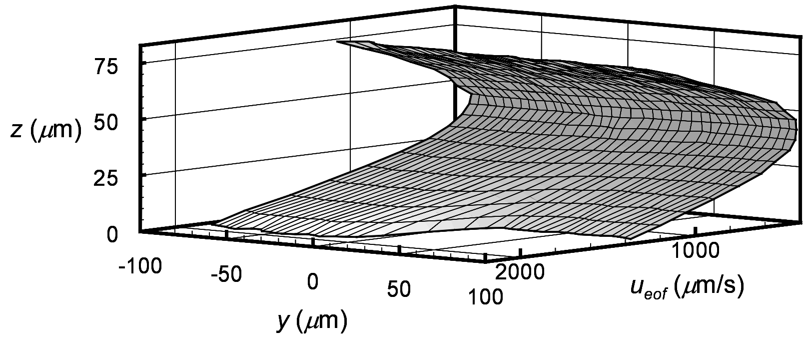

(b) t = 1.3 ms

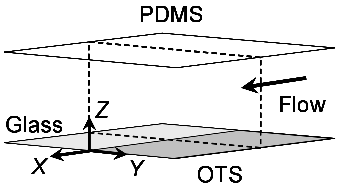

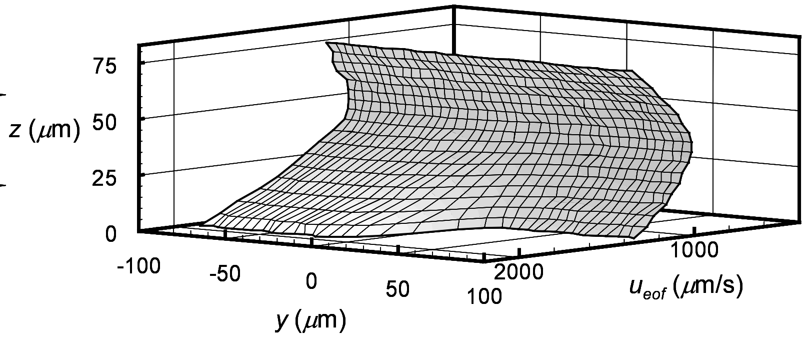

(c) t = 7.7 ms

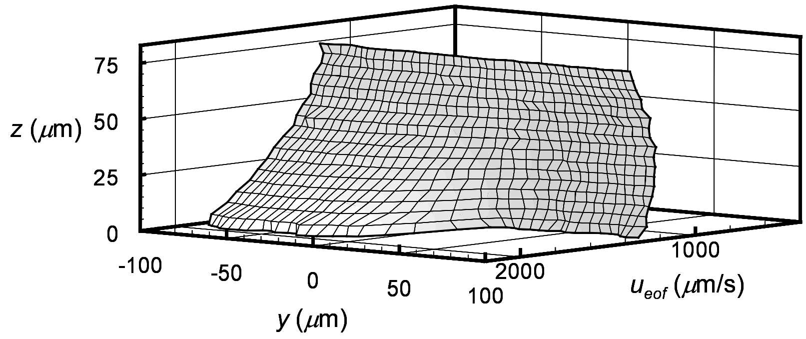

Figure 5.13. Streamwise velocity profiles in the YZ-plane at (a) t = 0.5 ms, (b) t = 1.3 ms and (c) t = 7.7 ms.

(a) $z = 8.8\ \mu$m

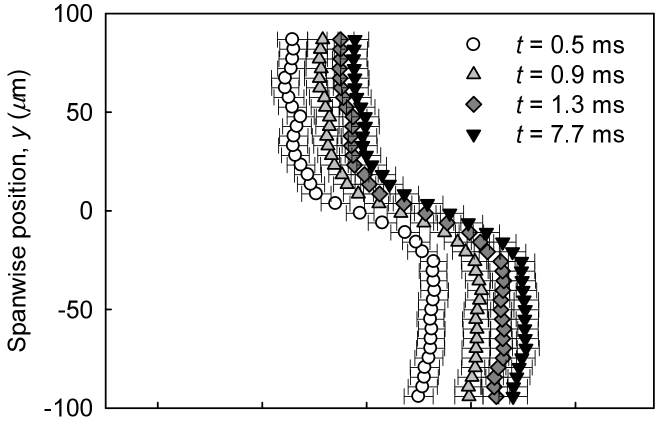

(b) $z = 39.6\ \mu$m

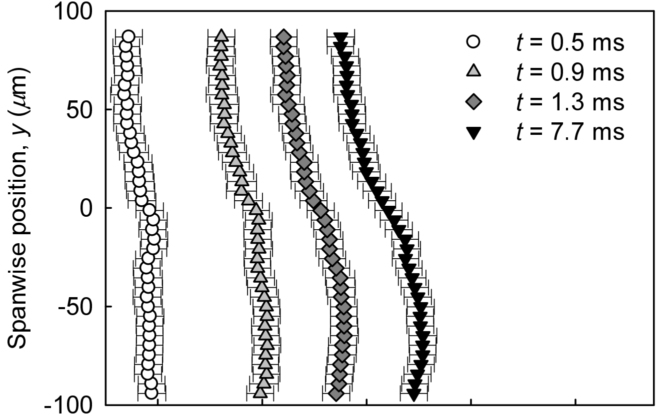

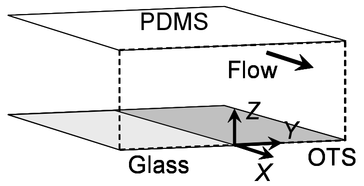

(c) $z = 70.4\ \mu$m

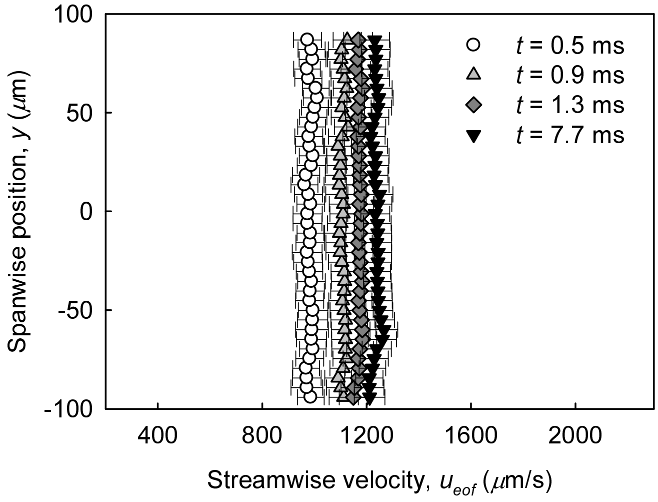

Figure 5.14. Time-series velocity profiles of electroosmotic flow in the Y-direction at (a) $z = 8.8\ \mu$m, (b) $z = 39.6\ \mu$m and (c) $z = 70.4\ \mu$m.

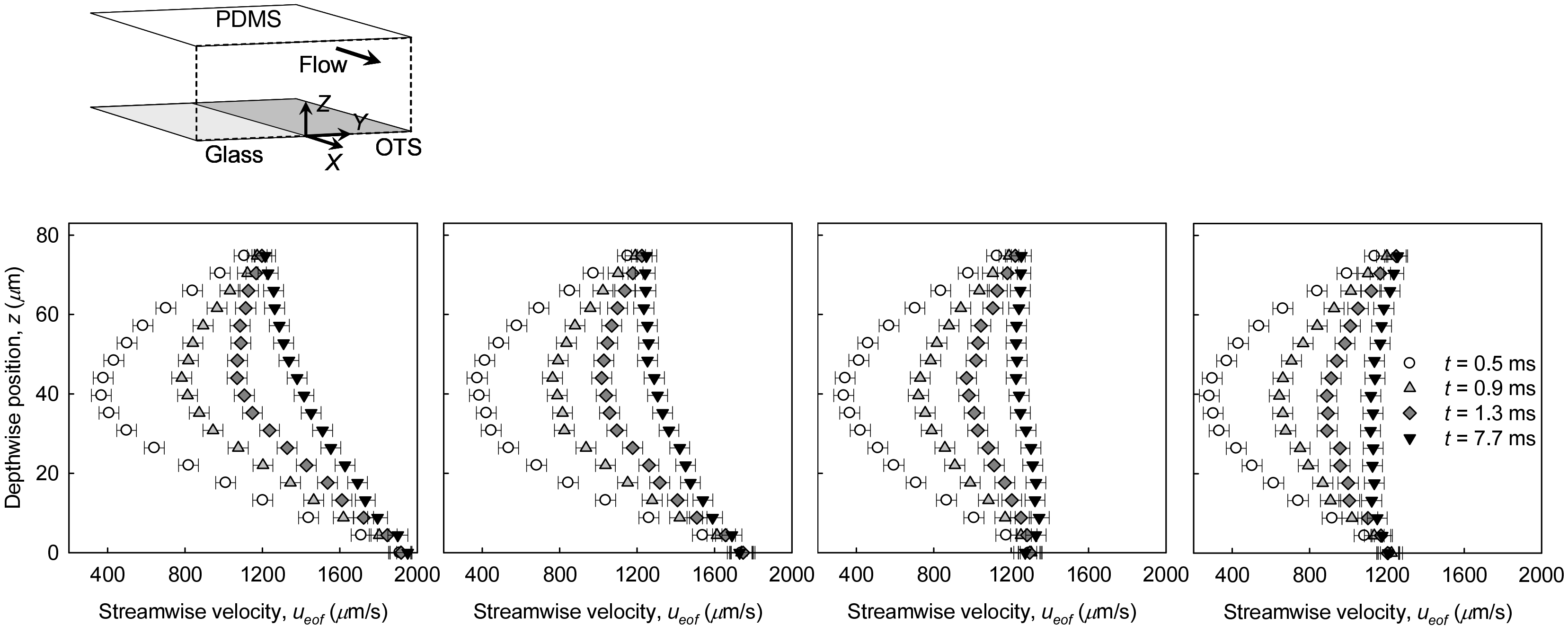

(a) $y = -75$ μm (b) $y = -6.1$ μm (c) $y = 8.6$ μm (d) $y = 77$ μm

Figure 5.15. Time-series electroosmotic velocity profiles in the Z-direction at (a) $y = -75$ μm (glass-PDMS), (b) $y = -6.1$ μm (glass-PDMS), (c) $y = 8.6$ μm (OTS-PDMS) and (d) $y = 77$ μm (OTS-PDMS).

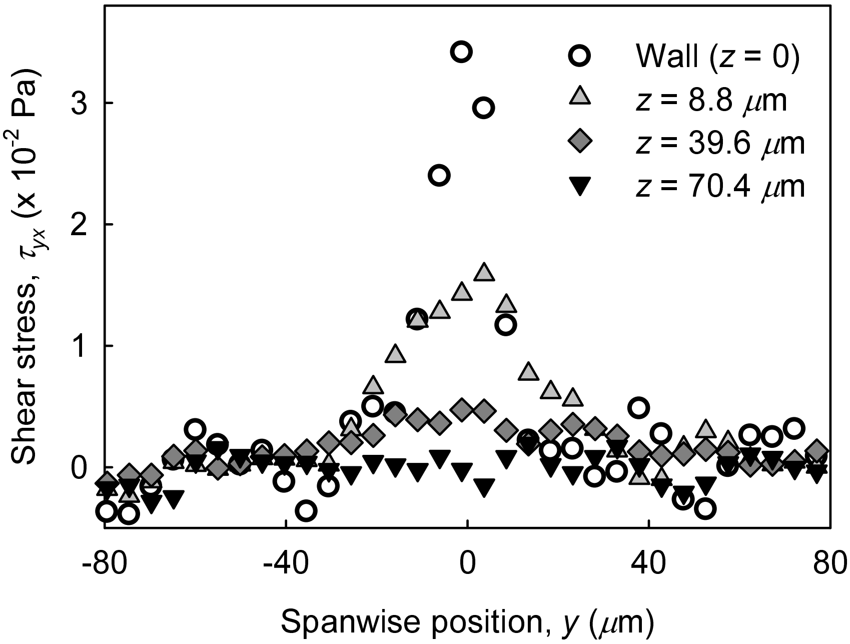

Figure 5.16. Spanwise profiles of the shear stress on the fluid, τ_{yx} (Pa), at different depthwise positions (t = 7.7 ms), obtained from the velocity profiles.

in parallel with that in the depthwise direction. The length scale of the flow affected by the step change zeta-potential was about 100 μm observed in the profiles of the shear stress and the velocity profiles shown in figure 5.14. Although the profile of the shear stress near the wall ($z = 0$) by the velocity gradient as shown in figure 5.12 was not the ideal delta function, the length scale of the flow in the transitional region is approximately equal to that of 110 μm obtained by equation (5.3) using the channel depth.

5.4.3 Step Change Zeta-Potential Parallel to Electric Field

Figure 5.17 shows the near-wall electroosmotic velocities and streamwise velocity profile in the vicinity of the wall (center of the channel), where OTS was modified on the glass wall as illustrated in figure 5.3(d). The spatial resolution was determined to be 9.8 × 39.1 μm^2 to increase the resolution in the streamwise direction (X-direction), and the vector interval was 4.9 × 19.6 μm. The near-wall velocities were independent of time, almost constant in the spanwise direction (Y-direction), but steeply decreased in the streamwise direction. The interface between the glass and OTS was located at $x = 88$ μm, and the velocity gradient in the X-direction is observed around the interface about 50 μm. Thus, the velocity profile was generated by the step change zeta-potential parallel to the electric field, which was induced by

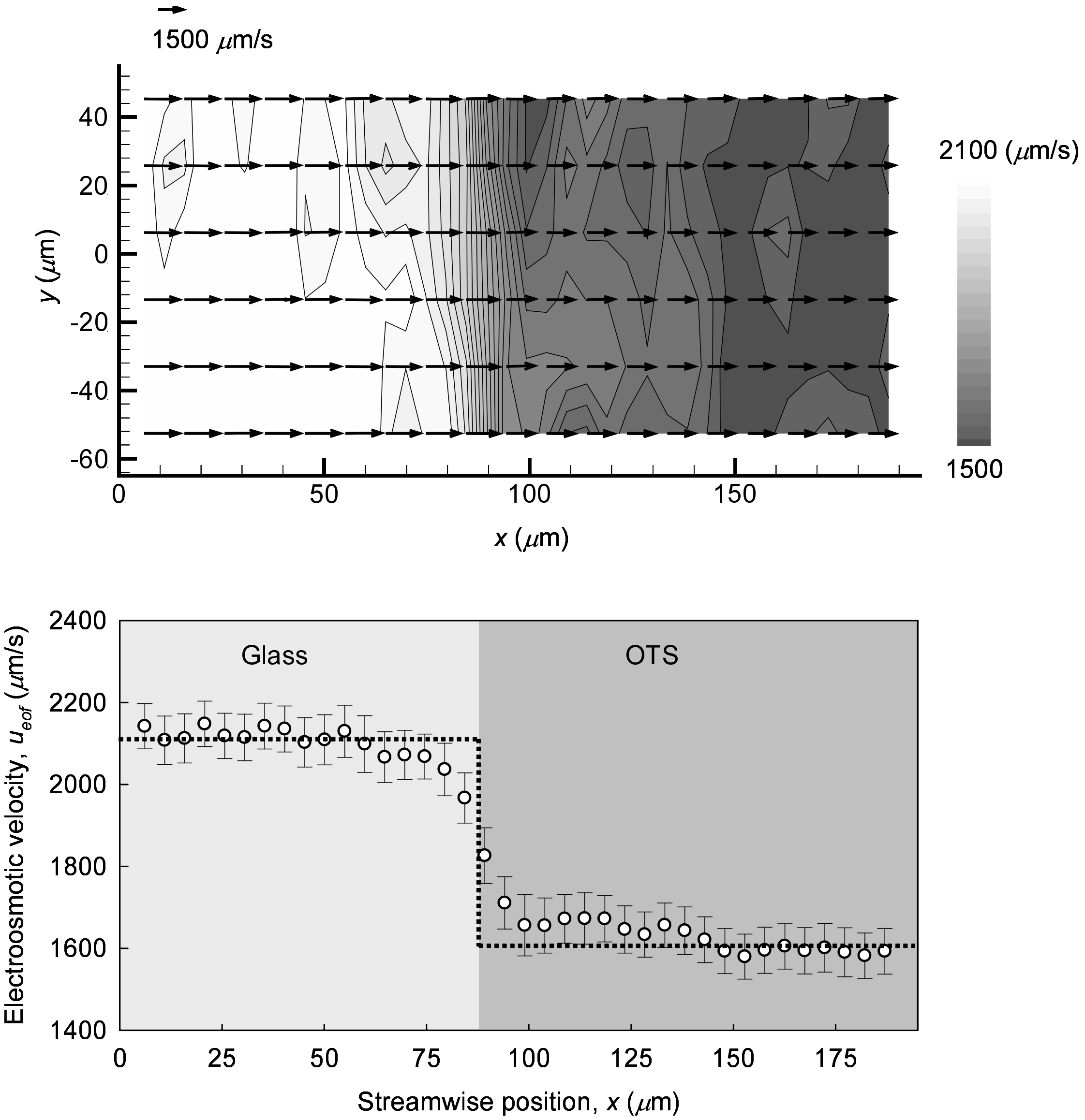

Figure 5.17. Near-wall velocity vector map with the step change zeta-potential parallel to the electric field, and velocity profile obtained by averaging the velocities in the Y-direction. Contours show the vector magnitudes.

the surface modification. From the velocities in the region with the flat flow profiles, the zeta-potential at the glass and OTS walls were estimated to be −104 mV and −79.2 mV, respectively. Due to the difference of the ion concentration in the electric double layer, an effect of the diffusive, advective and electrokinetic transport of ions in the electric double layer at the glass-OTS interface on the flow structure will occur. However, from the thickness of the electric double layer (9.6 nm) and the symmetric flow profile about the glass-OTS interface, the effect of ion motion in the electric double layer is considered to be enough small and negligible. Therefore, it is concluded that the velocity gradient in the streamwise direction was generated by the viscous effect. The total momentum induced by the step change zeta-potential was estimated as well as the flow with the step change zeta-potential perpendicular to the wall as mentioned above. The estimated momentum was 3.19×10^{-4} kg/m^{2}s and almost equal to that calculated from the predicted step change velocity profile shown in figure 5.17 as dotted line, 3.16×10^{-4} kg/m^{2}s. Thus, it is considered that the momentum generated by the step change zeta-potential was conserved in the vicinity of the wall.

Since the electroosmotic velocity is varied in the streamwise direction but kept constant in the spanwise direction as shown in figure 5.17, it is easily predicted that depthwise velocities were generated due to the mass conservation of fluid. Hence, the depthwise electroosmotic velocity was estimated by the equation of continuity (equation (2.1)), using the experimental results. In order to reduce the effect of measurement errors, the depthwise velocities were calculated by

$$\frac{\partial w}{\partial z} = -\frac{\partial u}{\partial x}, \tag{5.13}$$

using the streamwise velocities averaged in the spanwise direction. The near-wall velocities were used as the boundary velocities for the calculation. Figure 5.18 shows the velocity vector maps in the XZ-plane at different times. On an application of electric field, electroosmotic flow was induced from the regions near the top and bottom walls, and reached to the steady state at about $t = 3$ ms, which is approximately equal to the relaxation time of electroosmotic flow, $\tau_{eof} = H_c^2/\nu = 4.5$ ms. The zeta-potential at the PDMS wall was estimated to be −71.7 mV from the electroosmotic velocity near the PDMS wall. The flow structures are different between the upstream and downstream flows from the interface between the glass and OTS walls ($x = 88$ μm). From the contours as shown in figures 5.18(b) and (c), it is observed that the reduction of the streamwise velocity near the bottom wall ($z = 0$) due to the step change zeta-potential is complemented in the flow field, and this results in the increase of the flow velocities near the top wall ($z = 63$ μm). Figure 5.19 shows the profiles of the depthwise velocity at different depthwise positions. The depthwise velocities are generated around the glass-OTS interface with the streamwise length scale of 80 μm, almost independent of the time, and keep positive values over the depthwise positions. The magnitude of the depthwise velocity is about 100 μm/s at $z = 8.8$ μm, and decreases with increasing the depthwise position. Figure 5.20

(*a*) *t* = 0.5 ms

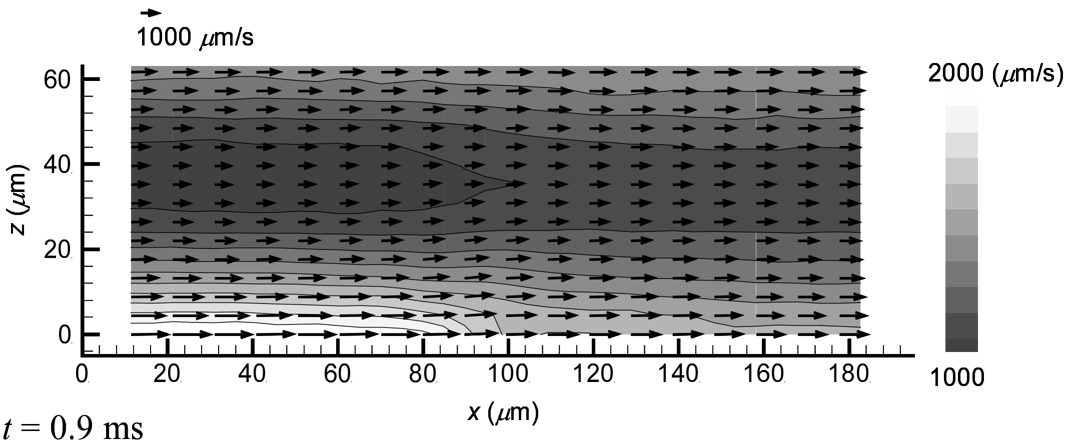

(*b*) *t* = 0.9 ms

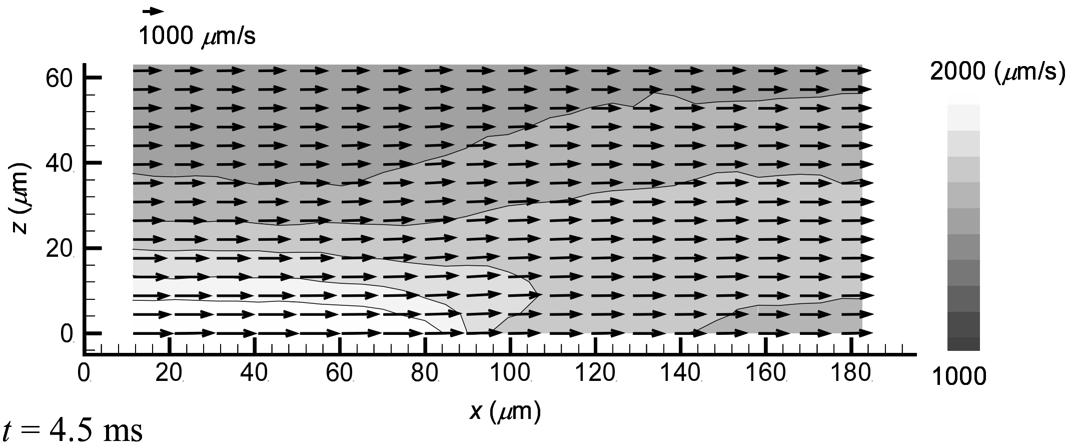

(*c*) *t* = 4.5 ms

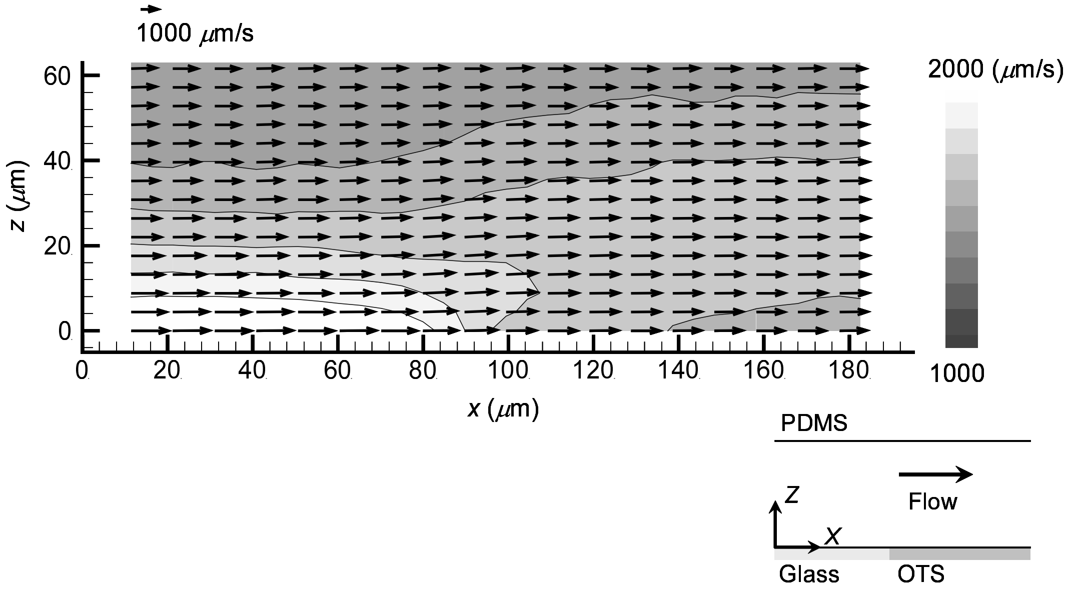

Figure 5.18. Velocity vector maps in the XZ-plane at (*a*) $t = 0.5$ ms, (*b*) $t = 0.9$ ms and (*c*) $t = 4.5$ ms. Contours show the vector magnitudes.

(a) $z = 8.8\ \mu$m

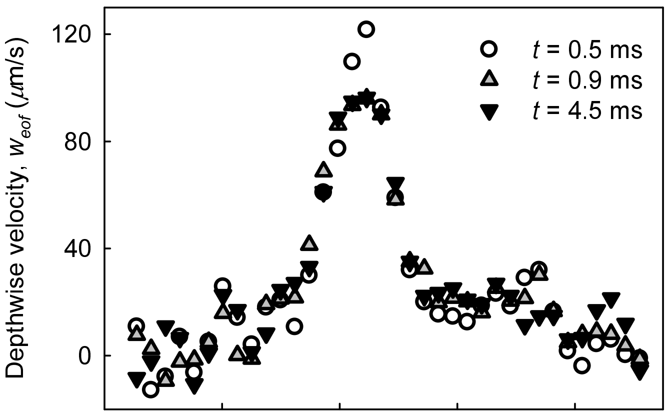

(b) $z = 30.8\ \mu$m

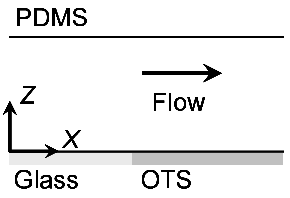

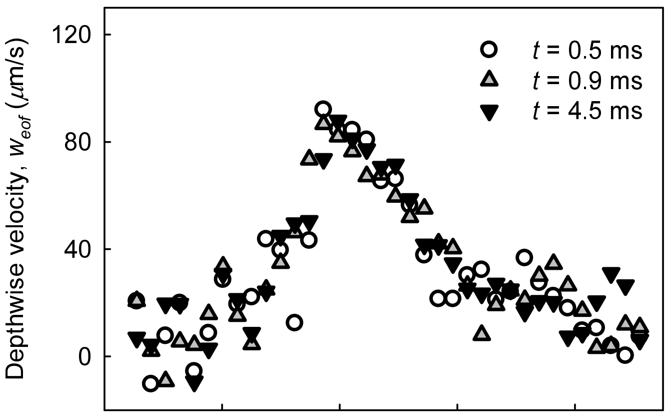

(c) $z = 52.8\ \mu$m

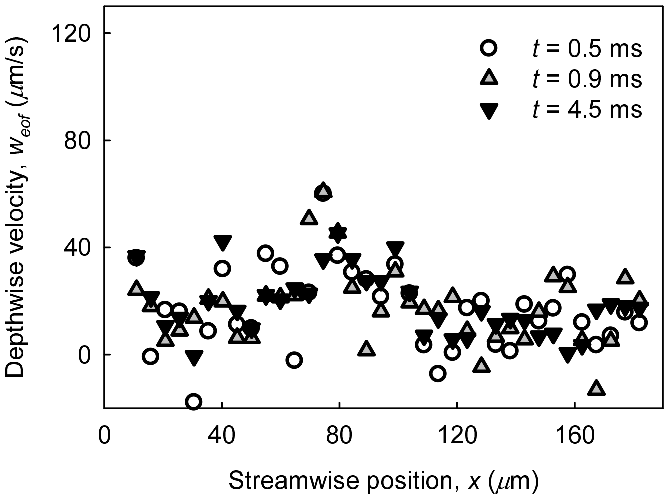

Figure 5.19. Time-series depthwise velocity profiles in the X-direction at (a) z = 8.8 μm, (b) z = 30.8 μm and (c) z = 52.8 μm.

(a) $z = 8.8\ \mu$m

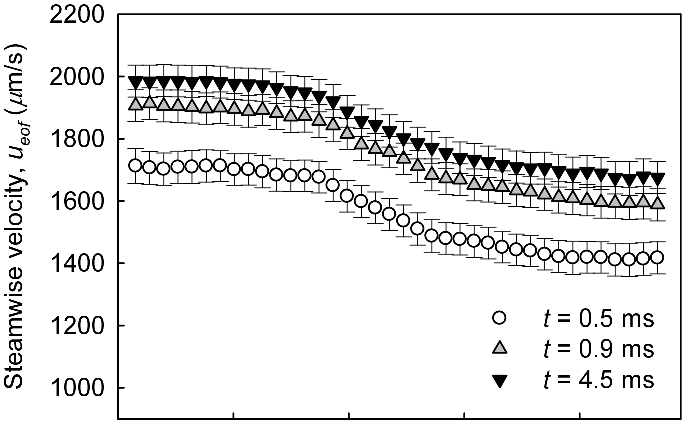

(b) $z = 30.8\ \mu$m

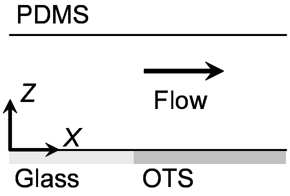

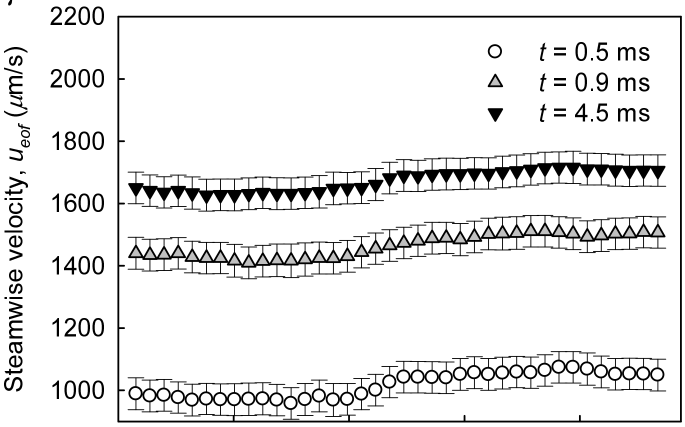

(c) $z = 52.8\ \mu$m

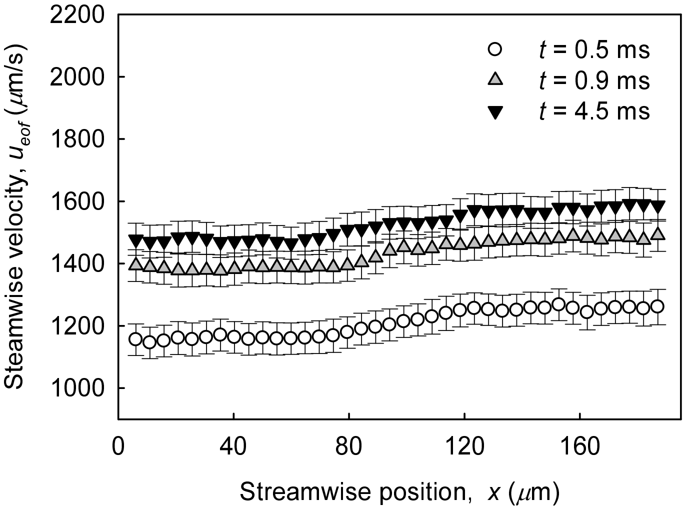

Figure 5.20. Time-series streamwise velocity profiles in the X-direction at (a) $z = 8.8\ \mu$m, (b) $z = 30.8\ \mu$m and (c) $z = 52.8\ \mu$m.

shows the profiles of the streamwise velocity at different depthwise positions. Near the bottom wall with the step change zeta-potential (z = 8.8 μm), the streamwise velocities decrease with increase the streamwise position due to the effect of the zeta-potential distribution. On the other hand, in the middle position (z = 30.8 μm) and near the top wall with the uniform zeta-potential (z = 52.8 μm), the streamwise velocities show the inverse profile, which was generated by the depthwise flow due to the mass conservation. The velocities keep the same streamwise profile due to the depthwise velocities independent of time. Figure 5.21 shows time-series electroosmotic velocity profiles in the Z-direction at different streamwise positions. The profiles far from the glass-OTS interface as shown in figures 5.21(a) and (d) were compared with the flow model by the superposition of the Couette flows and pressure-driven flow by equations (5.7) and (5.8). The estimated zeta-potential at the glass, OTS and PDMS walls were substituted into the equations as ζ_1, ζ_2 and ζ_3, respectively. The length of the glass wall, $L_{c,\mathrm{I}}$ = 12 mm, and that of the OTS wall, $L_{c,\mathrm{II}}$ = 15.6 mm, were used for the calculation. The profiles far from the glass-OTS interface show the quantitative agreements with the flow model at each time. This show that internal pressure gradients were generated to keep the constant flow rate between the upstream and downstream flows from the glass-OTS interface. In the upstream flow, the negative pressure gradient was generated to decrease the flow rate by electroosmotic flow. Near the glass-OTS interface, the pressure gradient is considered to be nearly zero due to the linear velocity profile in the steady state at x = 84.3 μm, but the velocity profiles are significantly distorted near the bottom wall at x = 94.1 μm due to the steep decrease in the near-wall velocities. In the downstream flow, the positive pressure gradient was generated to increase the suppressed flow rate by the reduced near-wall velocities at the bottom wall (OTS region). Thus, a transitional region between the upstream and downstream flows was induced with the step change zeta-potential parallel to the electric field, where the pressure gradient was varied and the depthwise velocities were generated.

The pressure gradients with the step change zeta-potential was investigated using the experimental results. Since the streamwise velocity was assumed to be constant in the spanwise direction (Y-direction), the pressure gradients in the streamwise direction, $-dp/dx$ (Pa/m), was estimated using the Stokes equation (equation (2.5))

$$-\frac{dp}{dx} = \rho\frac{\partial u}{\partial t} - \mu\left(\frac{\partial^2 u}{\partial x^2} + \frac{\partial^2 u}{\partial z^2}\right) \tag{5.14}$$

It is noted that the velocity profiles were smoothed using the polynominal approximation by the least square method to calculate the viscous terms, because the measurement errors significantly affects the second-order derivative. The obtained pressure gradients were averaged over the depthwise direction to reduce the influence of the errors. Figure 5.22 shows the profiles of the pressure gradient at t = 4.5 ms compared with the predicted values by equation (5.10). The values of the pressure gradient in the upstream and downstream flows from the glass-OTS

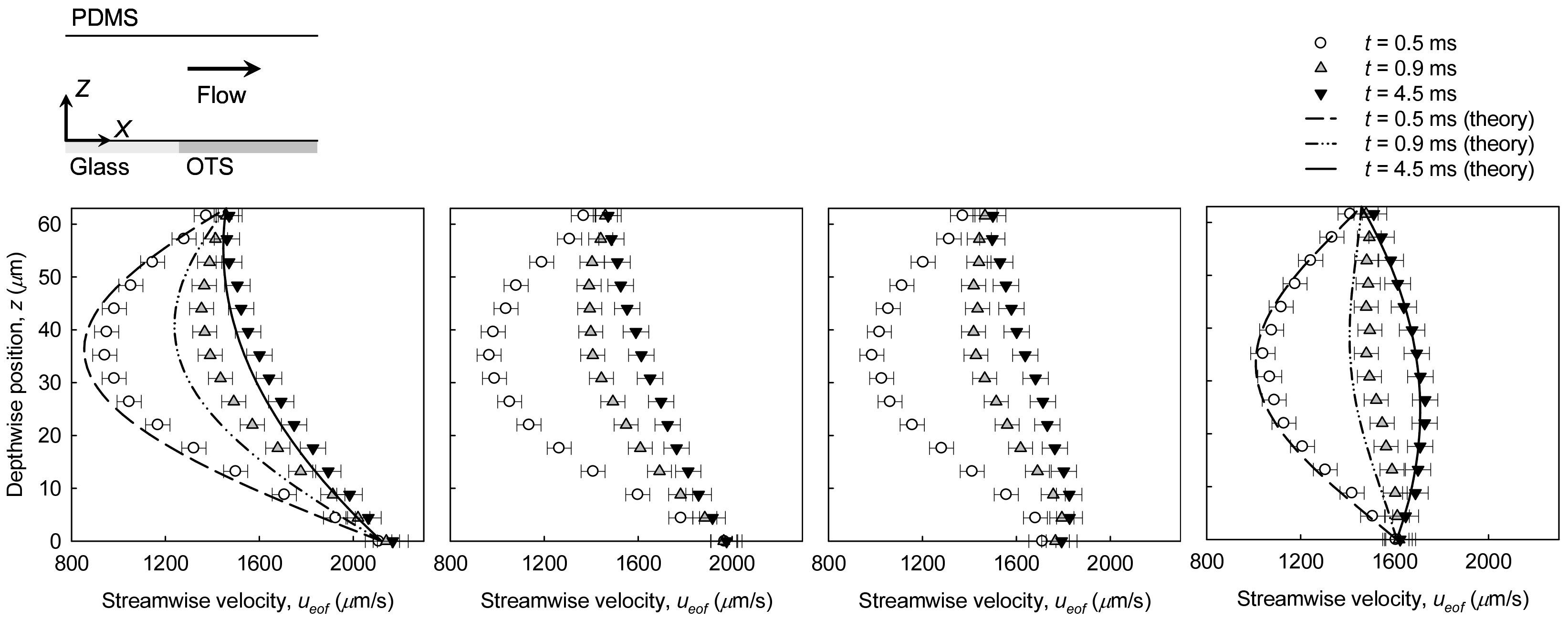

(*a*) $x = 11\ \mu$m (*b*) $x = 84.3\ \mu$m (*c*) $x = 94.1\ \mu$m (*d*) $x = 167\ \mu$m

Figure 5.21. Time-series electroosmotic velocity profiles in the Z-direction at (*a*) $x = 11\ \mu$m (glass-PDMS), (*b*) $x = 84.3\ \mu$m (glass-PDMS), (*c*) $x = 94.1\ \mu$m (OTS-PDMS) and (*d*) $y = 167\ \mu$m (OTS-PDMS).

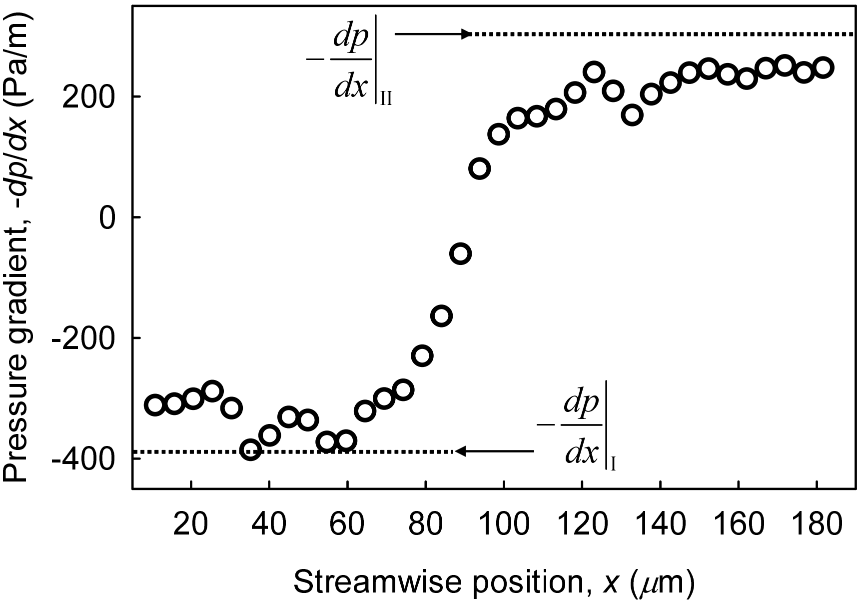

Figure 5.22. Streamwise profile of the pressure gradient at $t = 4.5$ ms obtained by averaging over the depthwise direction, $-dp/dx$ (Pa/m).

interface approximately agree with those predicted theoretically. The transition of the pressure gradient is observed around the glass-OTS interface with the length scale of about 80 μm, which is equal to the length scale of the region where the depthwise velocities were induced (figure 5.19) and the gradients of the streamwise velocity in the X-direction were observed (figure 5.20).

Finally, the shear stress caused by the velocity gradient in the streamwise direction was evaluated to examine the effect of the step change zeta-potential on the flow field. The shear stress exerted in the X-direction due to the velocity gradient, τ_{xx} (Pa), is given by

$$\tau_{xx} = -\mu \frac{\partial u}{\partial x} \tag{5.15}$$

Figure 5.23 shows streamwise profiles of the shear stress added on the fluid at different depthwise positions, obtaned from the measured velocities. The shear stress was generated around the interface between glass and OTS at $x = 88$ μm. The values of the shear stress show that the momentum diffusion occured from the upstream region (glass-PDMS) to the downstream region (OTS-PDMS) due to the near-wall velocity profile ($z = 0$) as shown in figure 5.17, but the momentum was transported in the inverse direction at $z = 39.6$ μm and $z = 70.4$ μm. This is because the internal pressure with the mass conservation also contributes to the momentum transport in the streamwise direction. The length scale of the transitional region by the step change zeta-potential parallel to the electric field was about 80 μm from the profiles of

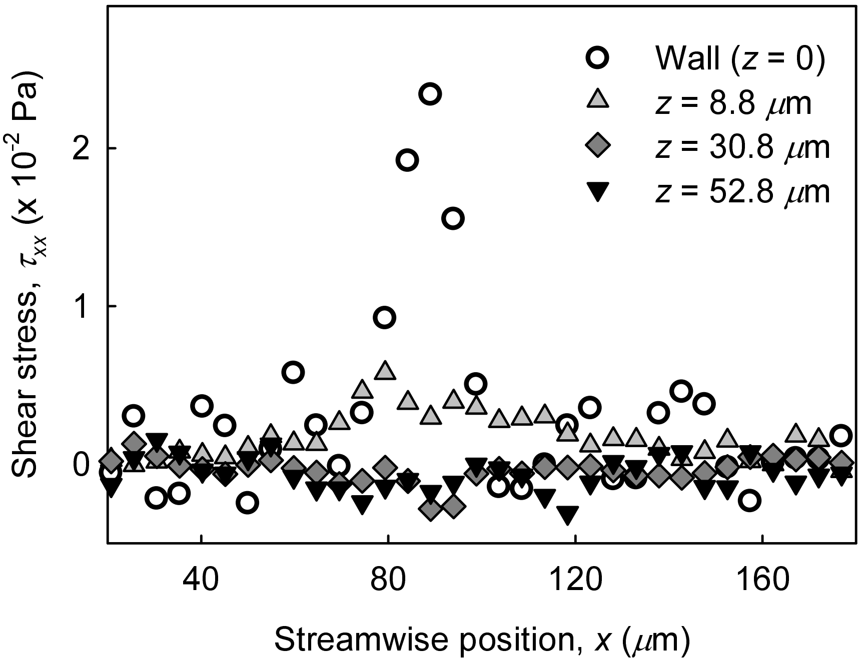

Figure 5.23. Streamwise profiles of the shear stress on the fluid, τ_{xx} (Pa), at different depthwise positions (t = 4.5 ms), obtained from the velocity profiles.

the shear stress, the velocity profiles shown in figures 5.19 and 5.20, and the pressure gradients shown in figure 5.22. This is approximately equal to that of 89 μm obtained by equation (5.3) using the channel depth, although the near-wall velocity profile was not the ideal delta function.

5.5 Volumetric Flow Rate Dependent on Zeta-Potential Distribution

A relationship between the volumetric flow rate of electroosmotic flow and the zeta-potential distribution at the wall was investigated using the experimental results. Only the flow field in the center of the channel, where the effect of the side walls are negligible, was considered.

The volumetric flow rates were estimated by the integral of the electroosmotic velocities obtained by the measurements. The obtained flow rates were normalized by that in the steady state to focus the time-dependent charasteristic of the flow rate. Figure 5.24(*a*) shows the volumetric flow rate with different wall zeta-potential with the normalized time given by $t^* = t/\tau_{eof}$, compared with the theoretical model by equation (5.11). The profile of time-series volumetric flow rates obtained from the experimental results are independent of the pattern and magnitude of wall-zeta-potential, and show quantitative agreements with the theoretical model. This theoretically and experimentally shows that the time-dependent characteristic of the flow rate is independent of the zeta-potential distribution, even in the step change zeta-potential parallel to the electric field where the secondary pressure-driven flow is induced. Next, a relationship between the volumetric flow rate and the average zeta-potential in the microchannel was examined. In order to neglect the difference of the cross-section area of the microchannel, the averaged electroosmotic velocities were estimated by $u_{ave} = Q_{3D}/A_{cross}$. Averaged wall zeta-potential, $\zeta_{ave} = \sum_{i=1}^{n} A_i \zeta_i / A_{total}$ (V), were calculated to be −61.3 mV (PDMS microchannel), −90 mV (glass-PDMS microchannel), −69.8 mV in the microchannel with the step change zeta-potential perpendicular to the wall and −80.9 mV in that parallel to the wall. Figure 5.24(*b*) shows the relationship between the averaged zeta-potential and the averaged electroosmotic velocity, which are normalized by the values at the PDMS microchannel. The relationships are almost independent of the normalized time, and show the proportional relationship. Therefore, it is concluded that the time-dependent characteristic of the volumetric flow rate is independent of the pattern of the wall zeta-potential, and the magnitude of the volumetric flow rate is proportional to the average zeta-potential even in the transient state.

5.6 Concluding Remarks

Transient electroosmotic flow with nonuniform wall zeta-potential was investigated by the iterative velocity measurement technique using particle tracking velocimetry. Microchannel made of PDMS, microchannel made of glass and PDMS, and those with the surface modification by OTS were employed. The time-series bulk and near-wall velocities of transient electroosmotic flow with nonuniform zeta-potential were firstly measured with the spatial resolution of 383 μm^2. Considering the bias error of 97.0 μm/s by the uncertainty of electrophoretic velocity, the uncertainty of the electroosmotic velocity in 95% confidence level was 102 μm/s in the bulk velocity measurement and 110 μm/s in the near-wall velocity measurement. The pattern of the surface modification was located using the nanoscale laser induced fluorescence imaging.

First, measurements were conducted using the microchannel made of PDMS with the high aspect ratio. Electroosmotic flow with the plug profile was induced in response to the application of electric field. Due to the high aspect ratio, the effect of the side wall was small and the flow was assumed to be two-dimensional in the center of the channel. Thus, the relaxation time of electroosmotic flow was given by using the channel depth. The experimental results well agreed with the theoretical model by Yang *et al.* (2004) and that by the superposition of the Couette flows. From the comparison with the theoretical model, it is concluded that the time resolution of 400 μs is enough small to measure the flow velocity of transient electroosmotic

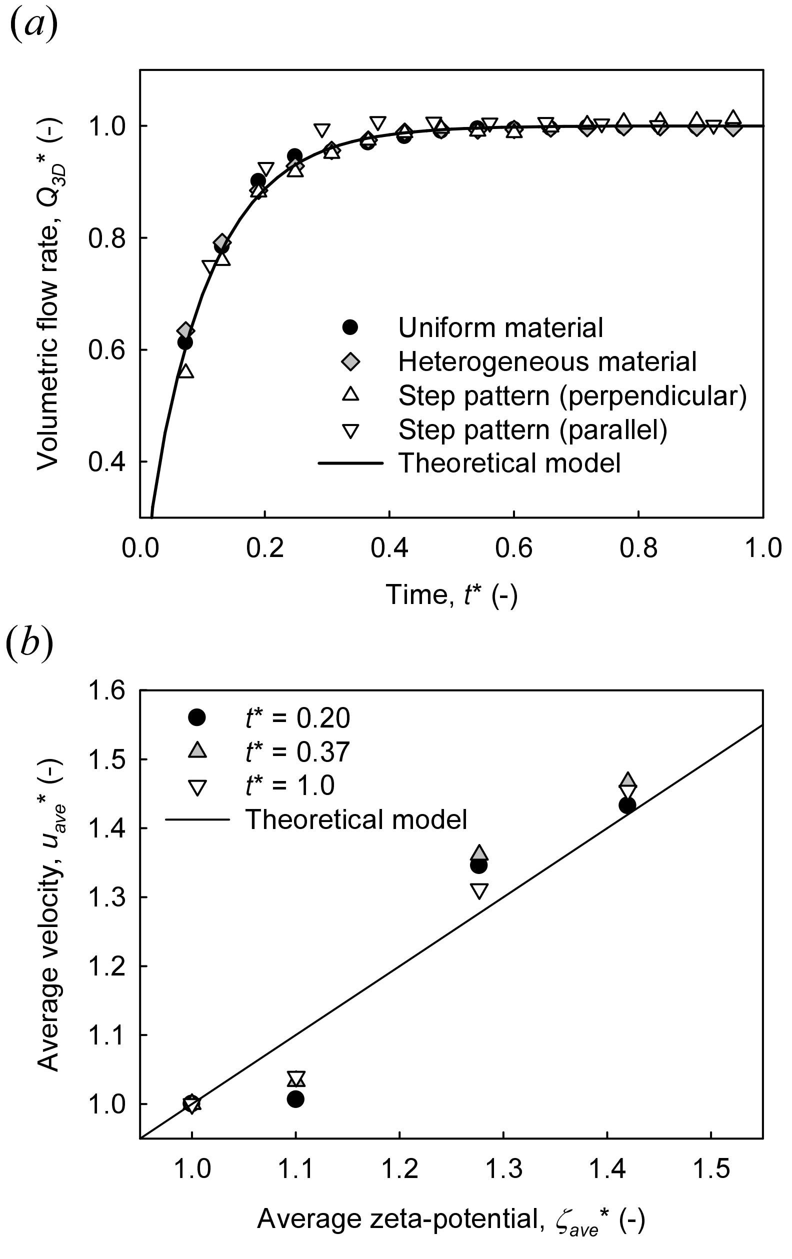

Figure 5.24. (*a*) Volumetric flow rate normalized by that at the steady state with the normalized time, $t^* = t/\tau_{eof}$ (-). (*b*) Relationships between the averaged electroosmotic velocity and the average zeta-potential at different times, t^* (-).

flow with the relaxation time at the order of 10^{-3} s.

In the microchannel made of glass and PDMS, the electroosmotic velocities with the linear profile was observed due to the nonuniform zeta-potential with the material heterogeneity. The effect of the side walls on the flow structure was also small because of the high aspect ratio. The electroosmotic velocities in the center of the channel quantitatively agreed with the theoretical model by the superposition of the Couette flows with different wall velocities.

In the microchannel with the OTS modification of the step pattern perpendicular to the electric field, two electroosmotic flows of the different velocities were induced parallel to the channel axis. The steep velocity gradient in the spanwise direciton near the wall was generated by the step change zeta-potential perpendicular to the electric field. The flow field was formed with the influences of the step change zeta-potential perpendicular to the electric field at the bottom wall and the uniform zeta-potential at the top wall. The momentum diffusion was evaluated by the shear stress estimated using the experiemental results. The flow structure was varied in the region near the step change zeta-potential with the length scale about 80 μm, and the flows in the rest regions were approximately considered as the flow approximated as the superposition of the Couette flows. The order of the length scale in the transition of the flow structure was nearly equal to that of the channel depth, which was estimated considering the momentum diffusion.

In the microchannel with the OTS modification of the step pattern parallel to the electric field, the different flow structures were generated in the upstream and downstream regions of the step change zeta-potential due to the mass conservation. The steep velocity gradient in the streamwise direction was generated in the vicinity of the wall, and this induced the depthwise velocities. The internal pressure was induced to keep the constant flow rate with the mass conservation. The flow fields in the upstream and downstream regions quantitatively agreed with the theoretical model by the superposition of the Couette flows and pressure-driven flow. The transitional region of the flow structure was observed between the upstream and downstream regions around the step change zeta-potential parallel to the electric field. The pressure gradient was varied in the transitional region, where the depthwise flow was generated. From the analysis using the shear stress, it is concluded that the length scale of the transitional region with the step change zeta-potential parallel to the electric field was equal to the order of the channel depth.

Finally, the relationship between the volumetric flow rate and the zeta-potential distribution was investigated. The volumetric flow rates were estimated using the measured electroosmotic velocities. The time-dependent characteristic of the volumetric flow rate was independent of the pattern of the wall zeta-potential, and the volumetric flow rate was proportional to the average zeta-potential even in the transient state.

Chapter 6

Effect of Ion Motion on Zeta-Potential Distribution at Microchannel Wall Obtained from Nanoscale Laser Induced Fluorescence Imaging

This chapter presents a discussion of electroosmotic flow with mixing of two aqueous solutions at different electrolyte concentrations in a microchannel. The zeta-potential distribution at the microchannel wall was measured by nanoscale laser induced fluorescence (nano-LIF) imaging. The ion motion in the microchannel is estimated by the numerical analysis using the velocity information obtained by micron-resolution particle image velocimetry (micro-PIV). Velocity measurement by micro-PIV is also conducted in electrokinetic flow field. This chapter especially concentrates on a relationship between the spatially distributed ion concentration in the mixing flow field and the wall zeta-potential. A relationship between the ion transport in the flow field, the distribution of wall zeta-potential and the electroosmotic flow structure is examined.

6.1 Experimental Setup

Two kinds of electrolyte solution were prepared for the experiments. One is a 5 mmol/*l* HEPES solution with sodium chloride (NaCl) of 0.1 mmol/*l*, and the another is that with NaCl of 10 mmol/*l*. Properties of solutions are listed in table 4.1. In the nano-LIF imaging, the fluorescent dye, Alexa Fluor 546 as shown in section 4.2, was dissolved into the solutions at 15 μmol/*l*. In the micro-PIV measurement, fluorescent tracer nanoparticles as described in section 3.1 were added into the solutions with a number density of 1.53×10^{10} particles/m*l*.

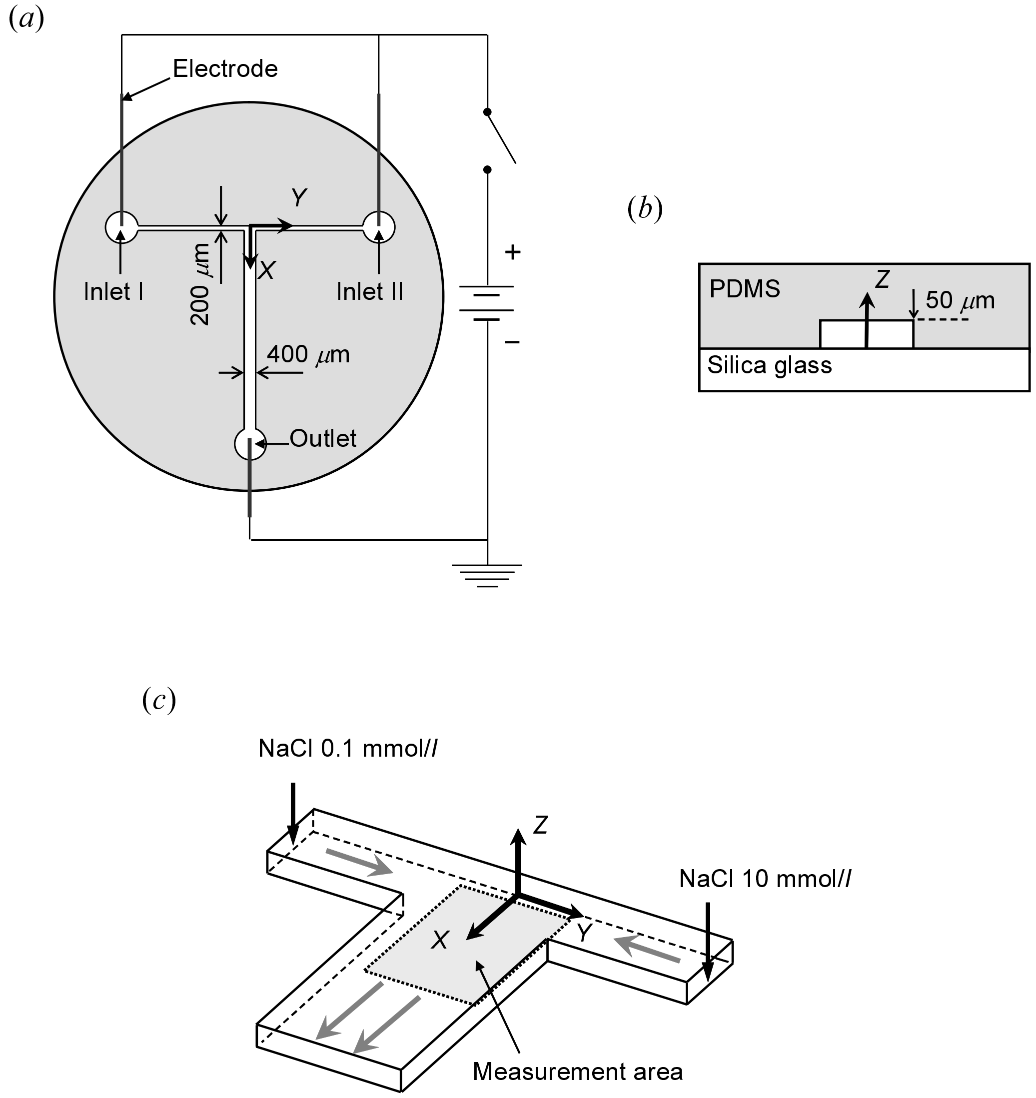

Figure 6.1. (*a*) Top and (*b*) cross-sectional views of T-shaped microchannel. The thickness of the silica glass was 1 mm for the nano-LIF imaging and 0.18 mm for the micro-PIV measurements. (*c*) Experimental setup for T-shaped microchannel.

Figure 6.1 shows a schematic of a T-shaped microchannel made of silica glass and poly (dimethylsiloxane) (PDMS). Prior to the experiments, the PDMS microchannel chip and the silica glass were rinsed by ion exchanged water after the ultrasonic cleaning with ethanol. The electrolyte solutions with NaCl concentration of 0.1 mmol/l and with that of 10 mmol/l were injected into the reservoirs of the T-shaped microchannel, inlet I and II, respectively. Both solutions were driven by pressure-driven flow generated from the difference in the height of aqueous surface between the inlets and the outlet. The mixing of two electrolyte solutions in the junction area were conducted at the equal flow rate. The experiments were performed at two conditions in which the average velocity of pressure-driven flow, U_{ave}, is 174 μm/s and 420 μm/s, respectively. The average velocity of pressure-driven flow was estimated from the experimental results obtained by micro-PIV and equation (2.11). Platinum electrodes were submerged into the reservoirs and a DC voltage of 150 V was applied from inlets to the outlet of the microchannel. In the nano-LIF imaging, as shown in figure 6.1(*c*), the fluorescent intensity was detected in the measurement area of 350 × 300 μm^2 at the silica glass wall by using the measurement system as shown in figure 4.4 (section 4.4).

A measurement system for micro-PIV was comprised of the inverted fluorescence microscope (figure 2.19(*b*)) with the filter block for blue excitation (table 2.4), the oil immersion objective lens (40×, NA = 1.3, table 2.5) and the cooled CCD camera (table 2.6). The excitation light was provided by the mercury lamp into the microchannel through the excitation filter and the dichroic mirror. Particle images were captured by the CCD camera through the objective lens, the dichroic mirror, the barrier filter and a 0.6× magnification TV lens to expand a measurement area. The particle diameter captured on the CCD camera calculated from d_e/e by equation (2.58) was 1.7 pixel. Velocity vectors were calculated from the particle images and the ensemble averaging technique was applied to the 100 instantaneous velocity vectors to avoid a measurement error associated with the Brownian motion of particles. The plane resolution of the velocity measurement was 20.6 × 20.6 μm^2, which is equal to the size of the interrogation windows. The depthwise resolution was 2.5 μm calculated by equation (2.60).

6.2 Zeta-Potential Distribution at the Wall Obtained by Nano-LIF Imaging

The zeta-potential distribution at the silica glass wall in the T-shaped microchannel was measured by the nano-LIF imaging. The DC voltage of 150 V was applied to the microchannel at $t = 0$. In order to determine the correction form of the detected fluorescent intensity excited by the evanescent wave (equations (4.5) or (4.6)), the bulk fluorescent dye concentration was examined by laser induced fluorescence (LIF) with the volume illumination. The standard

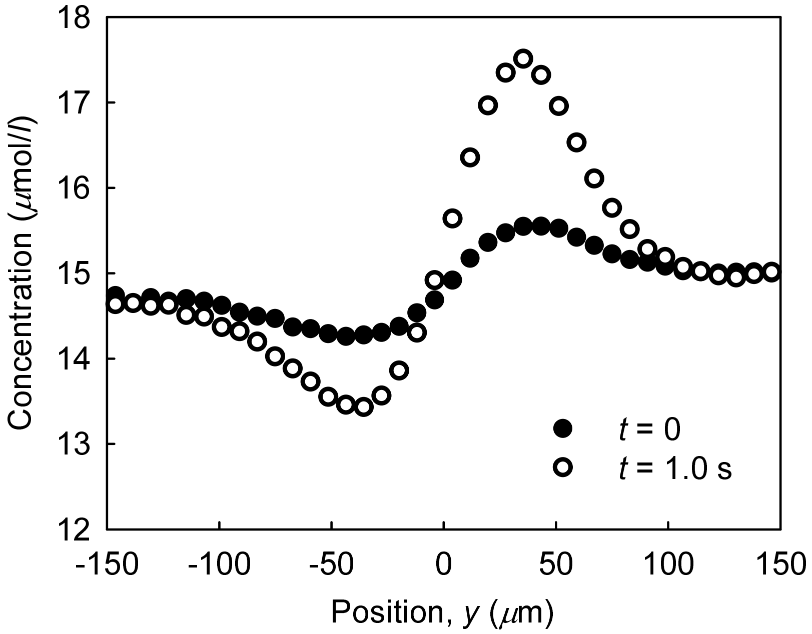

Figure 6.2. Bulk concentration profile of Alexa Fluor 546 in the spanwise direction (Y-direction) at $x = 200$ μm when $U_{ave} = 174$ μm/s.

deviation of the fluorescent intensity obtained by LIF was 0.26%. Figure 6.2 shows the profiles of bulk fluorescent dye concentration in the spanwise direction (Y-direction) at $x = 200$ μm. The bulk fluorescent dye concentration was not uniform in the center of the junction area. This concentration profiles were caused by the difference in diffusivity of ions and electrical conductivity of two solutions proportional to the electrolyte concentration as shown in equation (2.19). The difference in diffusivity between Na^+ ($D = 1.33 \times 10^{-9}$ m^2/s) and Cl^- ($D = 2.03 \times 10^{-9}$ m^2/s) as listed in table 2.2 generates the liquid junction potential (Munson *et al.*, 2002; Park *et al.*, 2006). Since the diffusion of Na^+ is less significant than that of Cl^-, the electrical neutrality based on equal concentrations of Na^+ and Cl^- is locally hindered even in the bulk region at the junction area, and this induces the small electric potential field. The electromigration of fluorescent dye by the liquid junction potential resulted in the bulk fluorescent dye distribution at $t = 0$. On an application of 150 V, due to the difference in electrical conductivity of two solutions as shown in table 4.1, the gradient of electrical conductivity with the diffusion of electrolyte generated an asymmetric electric field in the junction area (Devasenathipathy *et al.*, 2003). The electromigration of fluorescent dye induced by the asymmetric electric field resulted in the bulk fluorescent dye distribution at $t = 1.0$ s.

The fluorescent intensity excited by the evanescent wave was corrected by equation (4.6). Then, the calibration curve shown in figure 4.11 (section 4.5) was applied to the corrected

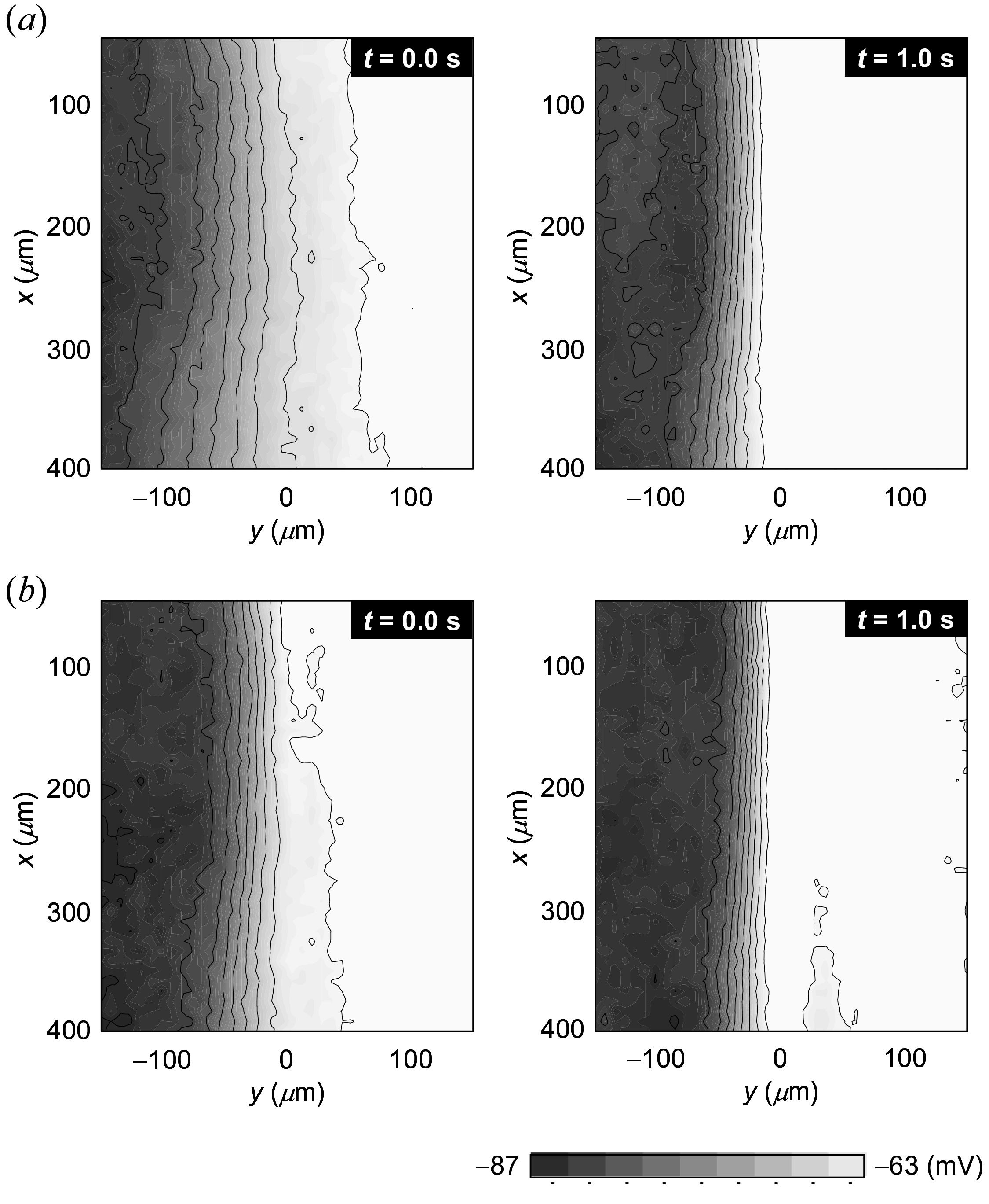

Figure 6.3. Two-dimensional distributions of zeta-potential at the silica glass wall in the junction area in (*a*) $U_{ave} = 174\,\mu$m/s and (*b*) $U_{ave} = 420\,\mu$m/s, respectively. The DC voltage of 150 V was applied at $t = 0$.

fluorescent intensity excited by the evanescent wave. Figure 6.3 shows the two-dimensional distributions of zeta-potential at the silica glass wall in the junction area. The distribution of wall zeta-potential in the mixing flow field was successfully obtained by the nano-LIF imaging. The zeta-potential distributions at the wall have the gradients in the Y-direction under the mixing of the two solutions. The gradient of the zeta-potential in U_{ave} = 420 μm/s was larger than that in U_{ave} = 174 μm/s. Since the silica glass surface is negatively charged, the wall zeta-potential depends on the concentration of counterion, Na^+, as described in section 2.1. Thus, the results indicate qualitatively that the zeta-potential distribution was determined by the spatial distribution of Na^+ in the mixing flow field, which was governed by the conservation equation of charged species (equation 2.16). On an application of 150 V, electroosmotic flow and the net flux of ions were induced and the zeta-potential gradients became larger than that at $t = 0$. The timescale of the change in the zeta-potential distribution was about 1.2 s. It is considered that this time scale is equal to the time to balance the mass transports by convection, diffusion and electromigration, and the zeta-potential distributions at $t = 1.0$ s were generated by the Na^+ distribution affected by the electric field.

6.3 Relationship between Wall Zeta-Potential and Ion Motion in Microchannel

The motion of Na^+ in pressure-driven flow was estimated from the measured velocity vectors to investigate the formation of the zeta-potential distribution at the wall. Velocity vectors in the junction area at z = 4.4 μm, 8.8 μm, 13.2 μm, 17.6 μm, 22 μm and 26.4 μm were obtained by moving the focal plane of objective lens. Figure 6.4(a) shows the velocity vector map at z = 26.4 μm when U_{ave} = 174 μm/s. The two solutions flow without mixing due to the laminar flow at the Reynolds number of 1.73×10^{-2}. When the effect of the liquid junction potential is not considered, the motion of Na^+ is governed by the convective diffusion equation. Thus, the Na^+ concentration in the flow field was calculated by the finite volume method using the discretized form of equation (2.12) (Patankar, 1980).

In the numerical analysis, control volumes were located at the coordinate of velocity vectors. The Na^+ concentration of two solutions were used as the inlet boundary condition. The velocity vector maps obtained by micro-PIV were applied to equation (2.12) considering the symmetric structure of pressure-driven flow in the depthwise direction (Z-direction). It is noted that the depthwise velocity, w (m/s), which was not measured by the micro-PIV, was assumed to be zero because the mass conservation law was completed by the streamwise velocity (X-direction), u (m/s), and spanwise velocity (Y-direction), v (m/s). Figure 6.4(b) shows the distribution of Na^+ concentration at z = 26.4 μm obtained by the numerical analysis when

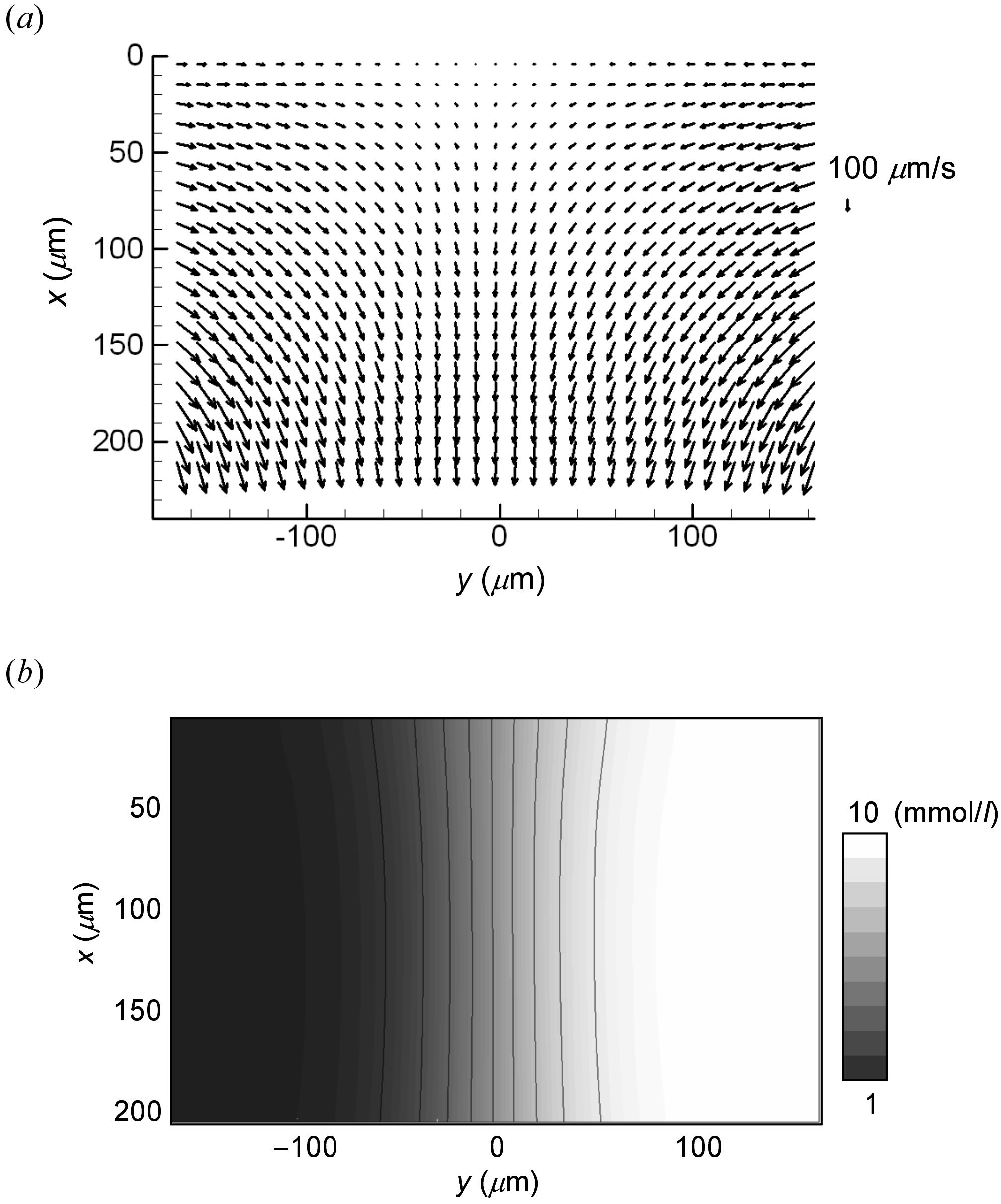

Figure 6.4. (*a*) Velocity vector map at $z = 26.4$ μm obtained by micro-PIV. (*b*) Two-dimensional distribution of Na^+ concentration at $z = 26.4$ μm obtained by the numerical analysis using the micro-PIV results. The averaged velocity, U_{ave}, was 174 μm/s.

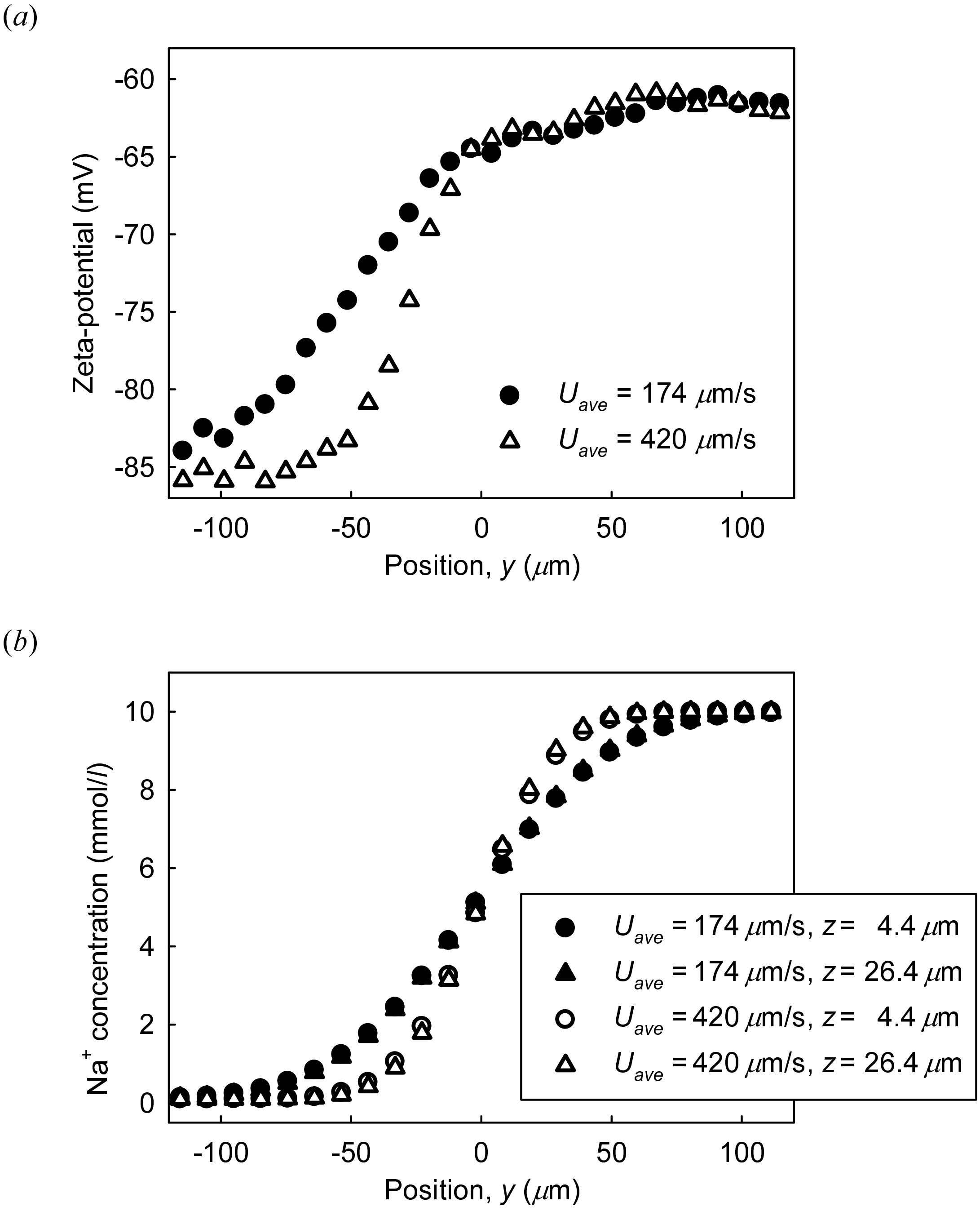

Figure 6.5. Comparison of (*a*) zeta-potential profiles at the wall obtained by nano-LIF to (*b*) Na$^+$ concentration profiles at $z = 4.4$ μm and $z = 26.4$ μm obtained by the numerical analysis in the Y-direction ($x = 150$ μm).

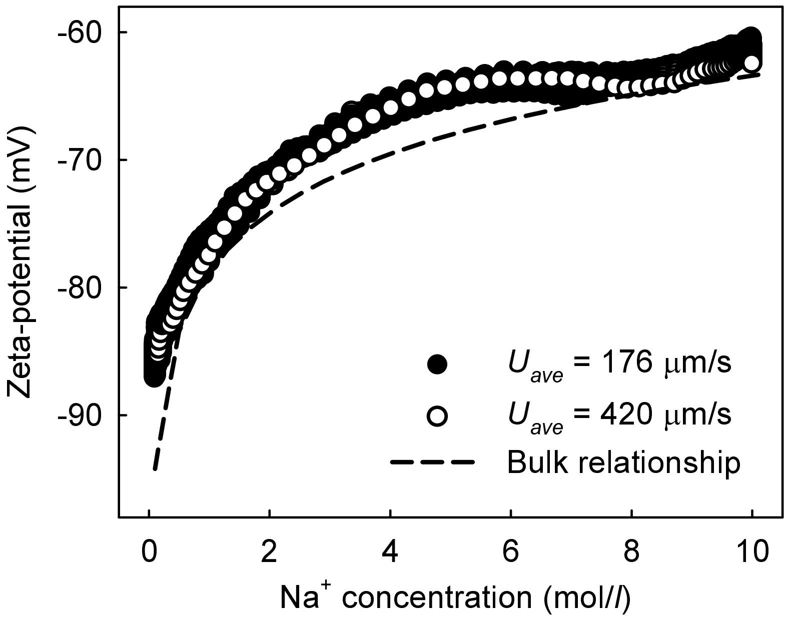

Figure 6.6. Relationship between the zeta-potential and Na$^+$ concentration in $U_{ave} = 174\,\mu$m/s and $U_{ave} = 420\,\mu$m/s.

$U_{ave} = 174\,\mu$m/s. Na$^+$ diffuses at the interface between two solutions and the concentration gradient in the Y-direction is generated. Figure 6.5 shows the comparison of the zeta-potential at the wall ($t = 0$) obtained by nano-LIF with the Na$^+$ concentration in the flow field ($x = 150\,\mu$m). The Na$^+$ concentration was kept almost constant in the Z-direction due to the molecular diffusion. The profiles of the zeta-potential have same tendency with those of Na$^+$ concentration. To evaluate quantitatively, a relationship between the zeta-potential at the wall and Na$^+$ concentration at $z = 4.4\,\mu$m in a location (x, y) were plotted in figure 6.6. The difference of the position coordinate between the zeta-potential and the Na$^+$ concentration was corrected by the linear interpolation. This relationship was also compared to that obtained by the calibration experiments (section 4.5) when the bulk Na$^+$ concentration is uniform in the microchannel. The relationship in $U_{ave} = 174\,\mu$m/s statistically agrees with that in $U_{ave} = 420\,\mu$m/s. In addition, the relationships in the mixing flow field where the Na$^+$ concentration is spatially distributed show the same tendency to that at uniform Na$^+$ concentration. Therefore, it is concluded that the zeta-potential distribution at the wall was formed by the motion of Na$^+$ governed by the convection and diffusion, depending on the relationship between the Na$^+$ concentration and the wall zeta-potential as same as that with uniform Na$^+$ concentration. From the results of previous work using the nano-LIF imaging (Kazoe & Sato, 2006), the same conclusion was obtained about the relationship between the K$^+$ concentration and the wall zeta-potential. However, there is a difference between the relationships in the case when the Na$^+$ concentration is uniform and nonuniform. Several reasons are considered such as the measurement error of the nano-LIF imaging and the neglect of the liquid junction potential in the numerical simulation, and further investigations are required in the future work.

6.4 Effect of Wall Zeta-Potential Distribution on Electroosmotic Flow

The structure of electrokinetic flow induced by the DC voltage was analyzed from the experimental results. Figure 6.7(a) shows the velocity vector map at $z = 8.8$ μm in the downstream of the microchannel ($x = 300$ μm) obtained by micro-PIV when $U_{ave} = 174$ μm/s. The observed velocity vector is superposition of electroosmotic, pressure-driven and electrophoretic components, $\boldsymbol{u_p} = \boldsymbol{u_{eof}} + \boldsymbol{u_{pre}} + \boldsymbol{u_{ep}}$ (Devasenathipathy & Santiago, 2002). In order to investigate the electroosmotic flow field, the streamwise electroosmotic velocity was estimated by subtracting the streamwise velocity of pressure-driven flow and particle electrophoresis from the streamwise observed velocity

$$u_{eof} = u_p - u_{ep} - u_{pre} \tag{6.1}$$

The streamwise electrophoretic velocity of particle was calculated by $u_{ep} = \mu_{ep} E_x$. The electrophoretic mobility was assumed to be -6.0×10^{-4} cm^2/V s considering the values shown in table 4.2, and the streamwise electric field, E_x, was 39.5 V/cm calculated from the microchannel length of 38 mm and the applied DC voltage of 150 V. Figure 6.7(b) shows the profile of streamwise electroosmotic velocity in the Y-direction at $z = 8.8$ μm ($x = 400$ μm, $U_{ave} = 174$ μm/s) estimated by equation (6.1). The profile of electroosmotic velocity has the gradient in the Y-direction, which shows the same trend with the profile of the magnitude of negative zeta-potential at the silica glass wall shown in figure 6.3(b). Considering electroosmotic flow with the zeta-potential of the variation perpendicular to the electric field as described in section 5.4, this spanwise velocity gradient was generated by the zeta-potential distribution at the silica glass wall.

In order to evaluate the effect of the zeta-potential distribution on the electroosmotic flow field quantitatively, the electroosmotic mobility, μ_{eof} (cm^2/V s), was calculated from the experimental results. From the micro-PIV results, the electroosmotic mobility was calculated using the streamwise electroosmotic velocity by $\mu_{eof} = u_{eof}/E_x$. From the results of the nano-LIF imaging, the electroosmotic mobility was calculated from the zeta-potential at the silica glass wall ($t = 1.0$ s) by $\mu_{eof} = -\epsilon\zeta/\mu$ (the Helmholtz-Smoluchowski equation). Figure 6.8 shows the profiles of electroosmotic mobility at the silica glass wall, $z = 8.8$ μm, $z = 26.4$

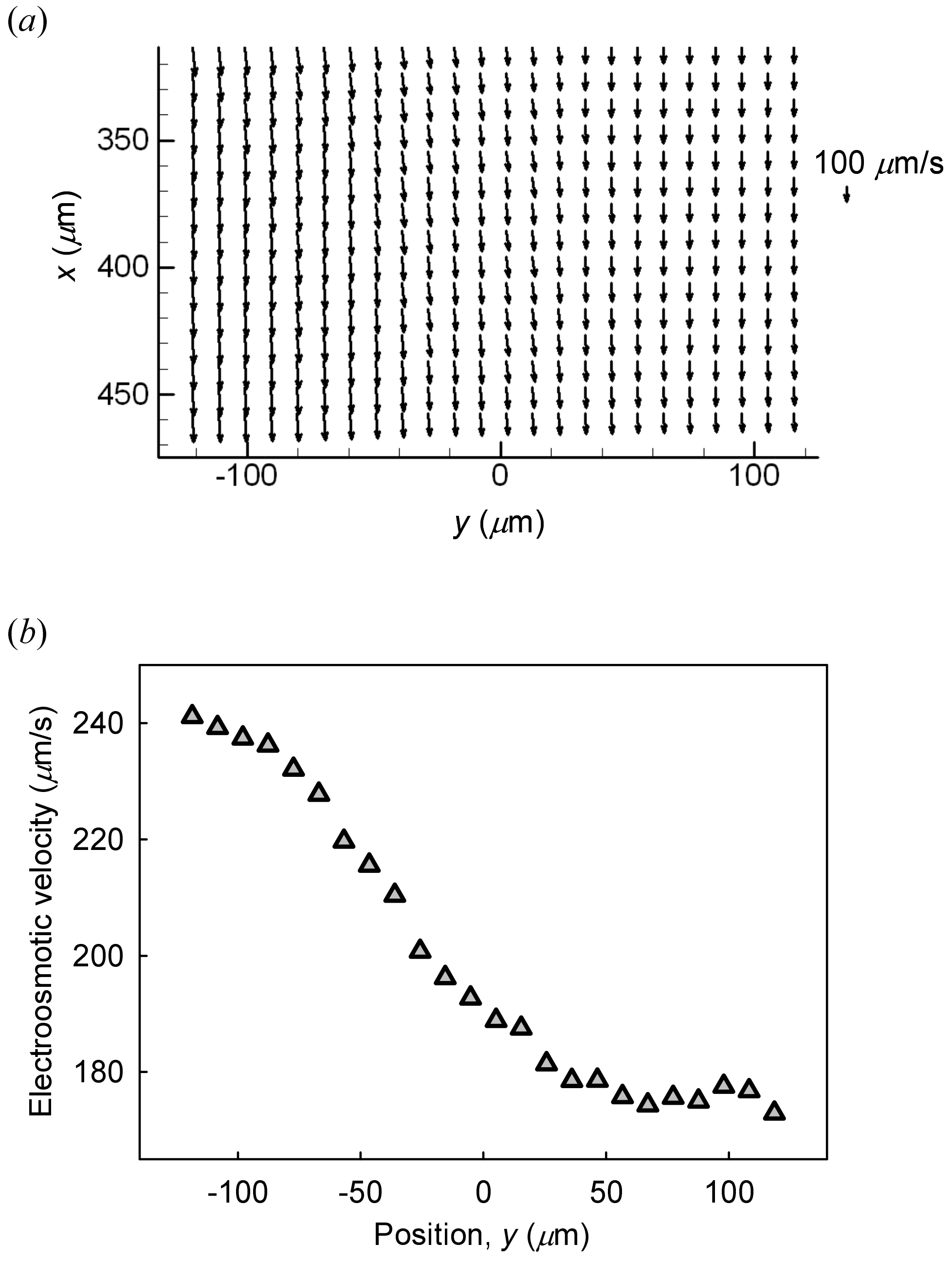

Figure 6.7. (*a*) Velocity vector map in electrokinetic flow at $z = 8.8\ \mu$m induced by the DC voltage of 150 V obtained by micro-PIV. (*b*) Profile of streamwise electroosmotic velocity at $z = 8.8\ \mu$m in the Y-direction ($x = 400\ \mu$m). The averaged velocity, U_{ave}, was 174 μm/s.

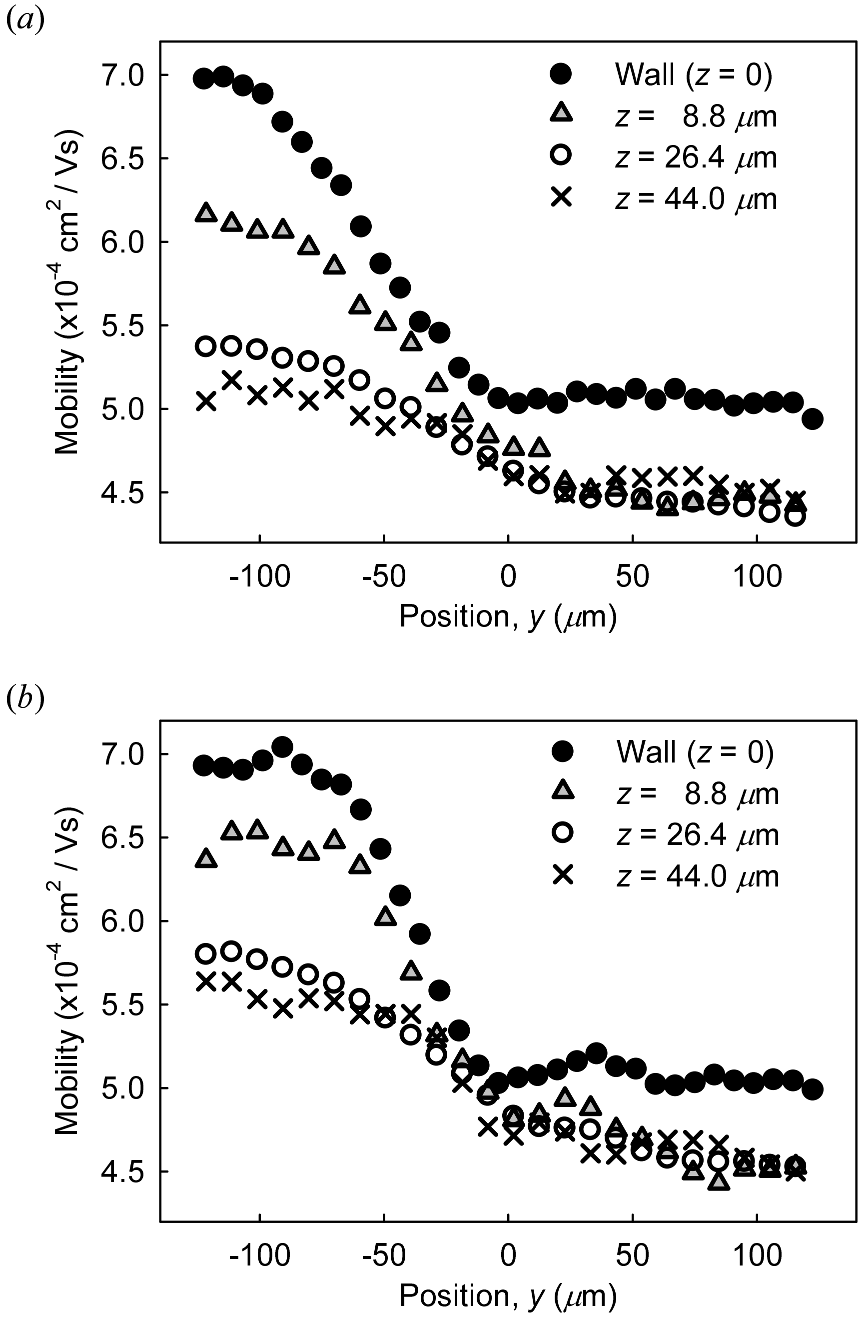

Figure 6.8. Profiles of the electroosmotic mobility at the silica glass wall (z = 0), z = 8.8 μm, z = 26.4 μm and z = 44 μm (near the PDMS wall) in the Y-direction (x = 400 μm). The averaged velocity, U_{ave}, was (*a*) 174 μm/s and (*b*) 420 μm/s, respectively.

μm and $z = 44$ μm (near the PDMS wall) in the Y-direction ($x = 400$ μm). The profiles of electroosmotic mobility at $z = 8.8$ μm are close to that at the silica glass wall. The electroosmotic mobility and its gradient decrease with increasing the depthwise position, z (m), due to the effect of electroosmotic mobility at the PDMS wall ($z = 50$ μm). However, the profiles of electroosmotic mobility near the PDMS wall also show the gradient in the Y-direction. Considering the dependence of the zeta-potential at PDMS surface on the cation concentration (Kirby & Hasselbrink, 2004*b*) (described in section 2.2), it is presumed that the zeta-potential at the PDMS wall also has the two-dimensional distribution depending on the motion of Na^+ in the flow field, which has the same tendency at the silica glass wall. The electroosmotic mobility in the high Na^+ concentration ($y > 80$ μm) at $z = 44$ μm approximately correspond to that at PDMS surface with the cation concentration of 10 mmol/l at pH 7 obtained by Ocvirk *et al.* (2000). This ensures that the difference in electroosmotic mobility in the Z-direction was caused by that in the zeta-potential distribution between the silica glass and PDMS wall. The profiles of electroosmotic mobility in $U_{ave} = 420$ μm/s (figure 6.8(*b*)) have larger gradients than those in $U_{ave} = 174$ μm/s (figure 6.8(*a*)) due to the effect of the convection of Na^+ as mentioned above. Therefore, it is concluded that the electroosmotic flow field in the T-shaped microchannel was generated by the zeta-potential distribution at the wall, which was governed by the motion of Na^+ in the mixing flow field.

6.5 Concluding Remarks

Electroosmotic flow with mixing of two solutions at different electrolyte concentrations was investigated. The T-shaped microchannel was comprised of PDMS and silica glass, and two kinds of solution with different Na^+ concentration were mixed in the junction area. The zeta-potential distribution at the silica glass wall was measured by the nano-LIF imaging. Velocity measurement by micro-PIV was performed to analyze pressure-driven and electrokinetic flow field. The Na^+ concentration was estimated by the numerical analysis using the micro-PIV results. The electroosmotic mobilities were estimated from the experimental results.

The distribution of wall zeta-potential in the mixing flow field was successfully obtained by the nano-LIF imaging. The gradient of the zeta-potential distribution in the mixing flow field was increased with increasing the convective flux of Na^+ dependent on the average velocity of pressure-driven flow. In addition, the zeta-potential gradient was also increased on an application of electric field due to the electromigration of Na^+ and the convective flux by electroosmotic flow.

The wall zeta-potential measured by the nano-LIF imaging and the Na^+ concentration obtained by the numerical analysis show a quantitative relationship in the flow field. Thus, the zeta-potential distribution at the wall was generated by the spatially distributed Na^+ dependent on the convection, diffusion and electromigration in the microchannel. It is presumed that the relationship between the Na^+ concentration and the wall zeta-potential in the mixing field is same as that when the Na^+ concentration is uniform in the channel.

The electroosmotic mobilities in the flow field were affected by the zeta-potential distribution at the wall. The difference in electroosmotic mobility in the depthwise direction was caused by that in the zeta-potential distribution between the silica glass and PDMS wall. Finally, it is concluded that electroosmotic flow with mixing of two solutions in the microchannel was generated by the zeta-potential distribution at the wall, which was dependent on the Na^+ transport in the flow field.

Chapter 7

Conclusions and Recommendations

Microscale liquid flows under electric field, i.e., electroosmotic flows, have been applied to the microscale flow systems such as capillary electrophoresis, liquid chromatography and microfluidic devices. Due to the dependence of electroosmotic flows on the wall zeta-potential, knowledge about the dynamics of electroosmotic flows with the wall zeta-potential is fundamental for the development of novel applications and flow control techniques by regulating the zeta-potential and electric field. However, experimental approaches have been restricted by the absence of (i) time-resolved bulk and near-wall velocity measurement technique with the high spatial resolution and (ii) the two-dimensional measurement technique for the wall zeta-potential. The present study developed novel measurment technqiues for the electroosmotic velocity and the wall zeta-potential, and experimentally investigated the structure of electroosmotic flow with nonuniform zeta-potential. The conclusions are described below.

7.1 Conclusions

The velocity measurement technique for transient electroosmotic flow and the measurement technique for nonuniform wall zeta-potential were developed on the basis of microscopic fluorescence imaging. Epi-fluorescence microscopy using the volume illumination was employed for the measurements with the micrometer order resolution. In order to achieve the nanometer order resolution, the evanescent wave with exponential decay from the wall of the order of 100 nm, which is generated by total internal reflection of laser beam, was used as the excitation light.

Using the developed measurement techniques, experimental investigations of the electroosmotic flow structure with nonuniform wall zeta-potential were conducted. Transient electroosmotic flows with inhomogeneous wall zeta-potential were examined using the time-resolved velocity measurement technique. Electroosmotic flow with mixing of two electrolyte solutions were investigated using the measurement technique for nonuniform wall zeta-potential and the conventional velocity measurement technique, i.e., micron-resolution particle image velocimetry.

7.1.1 Development of Measurement Technique for Electroosmotic Velocity

The time-resolved velocity measurement technique using fluorescent submicron particles and a high speed CMOS camera was developed to examine the transient structure of electroosmotic flow. Particle tracking velocimetry at low particle number density, which measures the flow velocity by tracing the individual particles, was employed and achieved the high signal to noise ratio in the fluorescent particle image. In order to increase the spatial resolution, an iterative measurement method was developed on the basis of the reproducibility of low Reynolds number flows. The time resolution of 400 μs was determined considering the relaxation times of electroosmotic flow and electrophoresis.

A measurement system with a timing control system for the iterative measurement was developed to realize the conbined measurement of the bulk and near-wall velocities with the volume illumination and the evanescent wave illumination, respectively. The objective lens-based total internal reflection fluorescence microscopy was employed to achieve the combined measurement. The measurement depth was 1.94 μm in the volume illumination and 0.72 μm in the evanescent wave illumination. The spatial resolution of 383 μm^2 ($19.6 \times 19.6\ \mu m^2$ at the square region) was achieved by the iterative measurement method. The measurement uncertainty in 95% confidence level was 30.1 μm/s in the measurement with the volume illumination and 52.8 μm/s in that with the evanescent wave illumination.

This technique firstly realized the time-resolved combined measurement of bulk and near-wall velocities of electroosmotic flow with the high spatial resolution.

7.1.2 Development of Measurement Technique for Zeta-Potential at Microchannel Wall

The optical measurement technique using the fluorescent dye and the evanescent wave, termed nanoscale laser induced fluorescence imaging, was developed for the spatial and temporal distribution of wall zeta-potential. Since the fluorescence ions are distributed by the wall zeta-potential, the fluorescent intensity excited by the evanescent wave is related to the zeta-potential. The nanoscale laser induced fluorescence imaging firstly realized the measurement of spatial and temporal distribution of the wall zeta-potential.

An evanescent wave illumination system using two prisms was developed for the measurement. The evanescent wave was generated using the microchannel substrate and the prisms as the optical waveguide. This system achieved the low magnification measurement with the large area illumination, wide selectivity for the microchannel materials, easy access to the microchannel and high signal to noise ratio with low magnitude of scattered light. A relationship between the fluorescent intensity and the wall zeta-potential was estimated by the calibration experiments. The obtained calibration curve enables the two-dimensional measurement of wall zeta-potential. The measurement uncertainty and the spatial resolution by the evanescent wave illumination system and calibration curve was 4.7 mV in 95% confidence level and 7.9×7.9 μm^2, respectively.

7.1.3 Investigation of Transient Electroosmotic Flow with Nonuniform Zeta-Potential

The velocity measurements were conducted to investigate transient electroosmotic flows in the microchannel with the uniform zeta-potential, and the nonuniform zeta-potential by the material heterogeneity and the surface modification of the step patterns perpendicular and parallel to the electric field. Considering the bias error of 97.0 μm/s by the uncertainty of electrophoretic velocity, the uncertainty of the electroosmotic velocity in 95% confidence level was 102 μm/s in the bulk velocity measurement and 110 μm/s in the near-wall velocity measurement. The pattern of the surface modification was located using the nanoscale laser induced fluorescence imaging. The effect of the momentum diffusion by the nonuniform zeta-potential on the flow structure was approximately estimated. In addition, the two-dimensional flow model based on the time-dependent Couette flow was presented and compared with the experimental results.

The validation of the measurement technique for transient electroosmotic flow was evaluated using the experimental results in electroosmotic flow with uniform zeta-potential.

The flow was assumed to be two-dimensional in the center of the channel due to the high aspect ratio and the relaxation time of electroosmotic flow at the order of 10^{-3} s was given by using the channel depth. Electroosmotic flow with the material heterogeneity showed the linear velocity profile due to difference of the wall zeta-potential between the bottom and top walls, and the velocities well agreed with the model by the superposition of the Couette flows with different wall velocities. Two electroosmotic flows of the different velocities in the same direction were induced parallel to the channel axis with the step change zeta-potential perpendicular to the electric field. The near-wall velocities showed the profile with the steep velocity gradient by the step change zeta-potential and the viscous effect of fluid. The flow structure was varied in the spanwise direction at the region near the step change zeta-potential with the length scale nearly equal to the channel depth, and the flows in rest regions were approximately considered as the flow by the superposition of the Couette flows. The different electroosmotic flow structures were generated in the upstream and downstream regions of the step change zeta-potential parallel to the electric field due to the mass conservation of fluid, which are approximately considered as the superposition of the Couette flows and pressure-driven flow. The internal pressure was induced to keep the constant flow rate between the upstream and down stream regions. The steep velocity gradient in the streamwise direction was generated in the vicinity of the wall by the step change zeta-potential, and this induced the depthwise velocities. The transitional region of the flow structure was observed between the upstream and downstream regions around the step change zeta-potential parallel to the electric field. The length scale of the transitional region, where the pressure gradient was varied and the depthwise flow was induced, was about the order of the channel depth.

The time-dependent characteristic of the volumetric flow rate was independent of the pattern of the wall zeta-potential, and the volumetric flow rate was proportional to the average zeta-potential even in the transient state.

These results show that electroosmotic flows have different velocity profiles by the pattern and magnitude of wall zeta-potential, but the volumetric flow rate and the averaged zeta-potential shows a proportional relationship.

7.1.4 Investigation of Electroosmotic Flow Affected by Ion Motion in Mixing Flow Field

Electroosmotic flow with mixing of two solutions at different electrolyte concentrations was investigated. A T-shaped microchannel comprised of PDMS and silica glass was employed for the experiments, and two kinds of solution with different Na^+ concentration were mixed in the junction area by pressure-driven and electroosmotic flows. The zeta-potential distribution at the silica glass wall was measured by the nanoscale laser induced fluorescence imaging. Velocity measurement by micron-resolution particle image velocimetry was performed to analyze pressure-driven and electrokinetic flow field. The Na^+ concentration was estimated by the numerical analysis using the velocity information obtained experimentally. The electroosmotic mobilities were estimated from the experimental results.

The zeta-potential distribution showed the gradient in the spanwise direction, which was varied by the flux of Na^+ related to pressure-driven and electroosmotic flows and the electromigration of Na^+ in the mixing flow field. The wall zeta-potential and the Na^+ concentration show a quantitative relationship in the flow field. Thus, the zeta-potential distribution at the wall was generated by the spatially distributed Na^+ dependent on the convection, diffusion and electromigration in the microchannel. The relationship between the Na^+ concentration and the wall zeta-potential in the mixing field is considered to be same as that when the Na^+ concentration is uniform in the channel.

The electroosmotic mobilities in the flow field were affected by the zeta-potential distribution at the silica glass and PDMS walls. It is concluded that electroosmotic flow with mixing of two solutions in the microchannel was generated by the zeta-potential distribution at the wall, which was dependent on the Na^+ transport in the flow field. Since the gradient of the wall zeta-potential perpendicular to the electric field was generated in the mixing field, the flow profile showed the spanwise velocity gradients as well as the flows with the step change zeta-potetnial perpendicular to the electric field.

7.2 Recommendations for Future Research

Finally, applications of the developed measurement techniques and knowledge obtained from this work are described for the future research.

The iterative velocity measurement technique using particle tracking velocimetry is useful for the investigation of the dynamics of micro- and nanoscale fluid flow with the reproducibility by the low Reynolds numbers. The time-series velocities of fluid, particles and suspended substrates in both the bulk and near-wall regions are measured with the high spatial resolution. This technique can be applied to examine electrokinetic flows with various patterns of the wall zeta-potential, AC electrokinetic flow with dielectrophoresis of substrates, microscale liquid flows in microchannels with the complecated shape, the motion of the suspended substrates such as particles, colloids, cells, proteins, microbubbles and droplets in the bulk and near-wall regions.

The nanoscale laser induced fluorescence imaging enables the two-dimensional measurement of the wall zeta-potential, which has not been achieved by the conventional measurement techniques. This technique can be applied to investigate the wall zeta-potential in the mixing and chemical reactive flow with the ion and the thermal transports, and to evaluate the pattern of the surface modification on the channel wall. A combined measurement with another technique such as velocity measurement technique is considered. By using the fluorescent dye and fluorescent particles with the different fluorescence wavelengths, a simultaneous measurement technique of the near-wall velocity and the wall zeta-potential using the evanescescent wave illumination have been developed (Miyakawa *et al.*, 2007). Disadvantages of this technique are the requirements of the evanescent wave and the reference value. Due to the requirement of the evanescent wave, the measurements must be conducted at the wall where the surface is clear and enough flat with the small roughness. The reference zeta-potential at the wall is required for the measurements to obtain the absolute value. However, it is difficult to know the reference zeta-potential at the wall where the surface modification is conducted due to the low repeatability. In order to achieve the zeta-potential measurement without the reference value, a measurement technique using two fluorescent dyes with different fluorescence wavelengths have been developed and will be presented in the future work.

The important knowledge about electroosmotic flow obtained from this work is listed as follows: (i) transient electroosmotic flows with different flow structure are generated by the zeta-potential distributions at the wall, (ii) the volumetric flow rate of electroosmotic flow is independent of the pattern of the zeta-potential but proportional to the average zeta-potential, and (iii) electroosmotic flow in a mixing flow is generated by the zeta-potential distribution, which depends on the local ion concentration in the flow field governed by the convection and diffusion, based on the relationship as same as that obtained when the ion concentration is uniform. Using the knowledge about electroosmotic flow with the wall zeta-potential of the typical patterns, the flow structure of electroosmotic flow in the practical devices can be approximately predicted. If the average zeta-potential in the microchannel is known, the volumetric flow rates in transient and steady electroosmotic flow will be estimated. In the development of the devices with mixing and chemical reaction, the knowledge obtained from the present study ensures that the distribution of ion concentration can be applied to predict the zeta-potential distribution at the wall based on the relationship between the ion concentration and the zeta-potential, which has been obtained in previous work. Therefore, the knowledge obtained from this work will contribute to the optimal design of the microscale flow systems using electrokinetics, the precise flow control technique using electrokinetics, and the novel applications such as mixing and separation by regulating the electric field and the zeta-potential. However, since the investigations conducted in the present study are restricted to electroosmotic flows with the typical patterns of the zeta-potential under the constant electric field, further investigations are required in the future researches.

Acknowledgement

I would like to express gratitude to my supervisor Associate Professor Yohei Sato for his enthusiastic encouragement, guidance and suggestions throughout this study.

I would also like to express gratitude to Professor Koichi Hishida at Keio University for his enthusiastic encouragement, guidance and suggestions and to Professors Kazuo Tanishita, Yuji Nagasaka and Kotaro Oka at Keio University for their enthusiastic guidance and suggestions.

I would also like to express gratitude to Assistant Professors Norihisa Miki and Yasuhiro Kakinuma at Keio University and to Assistant Professor Masahiro Motosuke at Tokyo University of Science for their enthusiastic guidance and suggestions.

I would also like to acknowledge Doctor Tomohiko Tanaka at Hitachi, Ltd. for his enthusiastic guidance and suggestions. I would also like to acknowledge Doctor Mitsuhisa Ichiyanagi at Keio University. No work has been done without his encouragement, guidance and suggestions.

I would also like to thank former and current graduate students Gentaro Irisawa, Seijiro Inaba, Takahiro Yamamoto, Koichiro Saiki, Hiroya Ishida, Naoyuki Hasegawa, Koki Yoshimura, Hiroki Fukumura, Seiichi Sasaki, Yuichiro Kawamoto, Takatsugu Moriya, Issei Tsutsui, Shu Miyakawa, Tsubasa Nakamura, Mitsuaki Fushimi and other members in Hishida & Sato laboratory at Keio University.

I would also like to express gratitude to financial supports by Scholarship from Japan Student Services Organization, Fujiwara Scholarship Fund, the 21st Century COE for ”System Design: Paradigm Shift from Intelligence to Life” and Research Fellowship for Young Scientists from Japan Society for the Promotion of Science.

Finally, I would like to express special thanks to my father Masaji Kazoe and my mother Noriko Kazoe for their continuous encouragement and financial support.

References

ADRIAN, R. J. 1991 Particle-imaging techniques for experimental fluid mechanics. *Annu. Rev. Fluid. Mech.* **23**, 261–304.

AJDARI, A. 1995 Electro-osmosis on inhomogeneously charged surfaces. *Phys. Rev. Lett.* **75** (4), 755–758.

AXELROD, D. 2001 Total internal reflection fluorescence microscopy in cell biology. *Traffic* **2**, 764–774.

AXELROD, D., BURGHARDT, T. P. & THOMPSON, N. L. 1984 Total internal reflection fluorescence. *Ann. Rev. Biophys. Bioeng.* **13**, 247–268.

BANERJEE, A. & KIHM, K. D. 2005 Experimental verification of near-wall hindered diffusion for the Brownian motion of nanoparticles using evanescent wave microscopy. *Phys. Rev. E* **72**, 042101.

BAO, N., XU, J. J., ZHANG, Q., HANG, J. L. & CHEN, H. Y. 2005 Electroosmotic flow in poly(dimethylsiloxane) microchannels. *J. Chromatogr. A* **1099**, 203–206.

BARKER, S. L. R., ROSS, D., TARLOV, M. J., GAITAN, M. & LOCASCIO, L. E. 2000 Control of flow direction in microfluidic devices with polyelectrolyte multilayers. *Anal. Chem.* **72**, 5925–5929.

BAROUD, C. N., OKKELS, F., MÉNÉTRIER, L. & TABELING, P. 2003 Reaction-diffusion dynamics: Confrontation between theory and experiment in a microfluidic reactor. *Phys. Rev. E* **67**, 060104.

BECKER, H. & LOCASCIO, L. E. 2002 Polymer microfluidic devices. *Talanta* **56**, 267–287.

BECKER, R. S. 1969 *Theory and Interpretation of Fluorescence and Phosphorescence*. New York: John Wiley & Sons.

BENOR, A., WAGNER, V. & KNIPP, D. 2007 Microstructuring by microcontact printing and selective surface dewetting. *J. Vac. Sci. Technol. B* **25** (4), 1321–1326.

BEVAN, M. A. & PRIEVE, D. C. 2000 Hindered diffusion of colloidal particles very near to a wall: Revisited. *J. Chem. Phys.* **113** (3), 1228–1236.

BEVINGTON, P. R. 1969 *Data Reduction and Error Analysis for the Physical Sciences*, 1st edn. New York: McGraw-Hill.

BEYNON, R. J. & EASTERBY, J. S. 1996 *Buffer Solutions*. New York: IRL Press at Oxford University Press.

BORN, M. & WOLF, E. 1999 *Principles of Optics: Electromagnetic Theory of Propagation, Interface and Diffraction of Light*, 7th edn. New York: Cambridge University Press.

BRENNER, H. 1961 The slow motion of a sphere through a viscous fluid towards a plane surface. *Chem. Eng. Sci.* **16**, 242–251.

BRODY, J. P., YAGER, P., GOLDSTEIN, R. E. & AUSTIN, R. H. 1996 Biotechnology at low Reynolds numbers. *Biophys. J.* **71**, 3430–3441.

BUCH, J. S., WANG, P. C., DEVOE, D. L. & LEE, C. S. 2001 Field-effect flow control in a polydimethylsiloxane-based microfluidic system. *Electrophoresis* **22**, 3902–3907.

CARASSO, M. L., ROWLANDS, W. N. & KENNEDY, R. A. 1995 Electroacoustic determination of droplet size and zeta potential in concentrated intravenous fat emulsions. *J. Colloid Interface Sci.* **174**, 405–413.

CHABINYC, M. L., CHIU, D. T., MCDONALD, J. C., STROOCK, A. D., CHRISTIAN, J. F., KARGER, A. M. & WHITESIDES, G. M. 2001 An integrated fluorescence detection system in poly(dimethylsiloxane) for microfluidic applications. *Anal. Chem.* **73**, 4491–4498.

CHI, L. F., JOHNSTON, R. R. & RINGSDORF, H. 1991 Fluorescence microscopy investigations of the domain formation of fatty acid monolayers induced by polymeric gegenions. *Langmuir* **7**, 2323–2329.

CHIUMAN, W. & LI, Y. 2007 Efficient signaling platforms built from a small catalytic DNA and doubly labeled fluorogenic substrates. *Nucleic Acids Res.* **35** (2), 401–405.

CLIFT, R., GRACE, J. R. & WEBER, M. E. 1978 *Bubbles, Drops, and Particles*. New York: Academic Press.

CONIBEAR, P. B. & BAGSHAW, C. R. 2000 A comparison of optical geometries for combined flash photolysis and total internal reflection fluorescence microscopy. *J. Microsc.* **200**, 218–229.

Coppeta, J. & Rogers, C. 1998 Dual emission laser induced fluorescence for direct planar scalar behavior measurements. *Exp. Fluids* **25**, 1–15.

Cowen, E. A. & Monismith, S. G. 1997 A hybrid digital particle tracking velocimetry technique. *Exp. Fluids* **22**, 199–211.

Crank, J. 1975 *The Mathematics of Diffusion*, 2nd edn. London: Oxford University Press.

Debusschere, B. J., Najm, H. N., Matta, A., Knio, O. M., Ghanem, R. G. & Maître, O. P. L. 2003 Protein labeling reactions in electrochemical microchannel flow: Numerical simulation and uncertainty propagation. *Phys. Fluids* **15** (8), 2238–2250.

Deen, W. M. 1998 *Analysis of Transport Phenomena*. New York: Oxford University Press.

Deng, T., Wu, H., Brittain, S. T. & Whitesides, G. M. 2000 Prototyping of masks, masters, and stamps/molds for soft lithography using an office printer and photographic reduction. *Anal. Chem.* **72**, 3176–3180.

Devasenathipathy, S. & Santiago, J. G. 2002 Particle tracking techniques for electrokinetic microchannel flows. *Anal. Chem.* **74**, 3704–3713.

Devasenathipathy, S., Santiago, J. G., Yamamoto, T., Sato, Y. & Hishida, K. 2003 Electrokinetic particle separation. In *Proc. μTAS 2003*, , vol. 1, pp. 845–848. Transducers Research Foundation, San Diego.

Dittrich, P. S. & Manz, A. 2006 Lan-on-a-chip: Microfluidics in drug discovery. *Nat. Rev. Drug Discovery* **5**, 210–218.

Doremus, R. H. 1973 *Glass Science*. New York: John Wiley & Sons.

Dubois, L. H. & Nuzzo, R. G. 1992 Synthesis, structure, and properties of model organic surfaces. *Annu. Rev. Phys. Chem.* **43**, 437–463.

Dutta, D., Ramachandran, A. & Leighton, Jr., D. T. 2006 Effect of channel geometry on solute dispersion in pressure-driven microfluidic systems. *Microfluid Nanofluid* **2**, 275–290.

Erickson, D. & Li, D. 2003 Three-dimensional structure of electroosmotic flow over heterogeneous surfaces. *J. Phys. Chem. B* **107**, 12212–12220.

Erickson, D., Sinton, D. & Li, D. 2003 Jole heating and heat transfer in poly(dimethylsiloxane) microfluidic systems. *Lab Chip* **3**, 141–149.

Fletcher, P. D. I., Haswell, S. J. & Zhang, X. 2001 Electrical currents and liquid flow rates in micro-reactors. *Lab Chip* **1**, 115–121.

DE FORNEL, F. 2001 *Evanescent Waves: From Newtonian Optics to Atomic Optics*. Berlin: Springer.

FU, L. M., LIN, J. Y. & YANG, R. J. 2003 Analysis of electroosmotic flow with step change in zeta potential. *J. Colloid Interface Sci.* **258**, 266–275.

GESCHKE, O., KLANK, H. & TELLEMAN, P. 2004 *Microsystem Engineering of Lab-on-a-chip Devices*. Weinheim: Wiley-VGH Verlag GmbH & Co. KGaA.

GHOSAL, S. 2006 Electrokinetic flow and dispersion in capillary electrophoresis. *Annu. Rev. Fluid Mech.* **38**, 309–338.

GOLDEN, J. P. & LIGLER, F. S. 2002 A comparison of imaging methods for use in an array biosensor. *Biosens. Bioelectron.* **17**, 719–725.

GOLDMAN, A. J., COX, R. G. & BRENNER, H. 1967 Slow viscous motion of a sphere parallel to a plane wall-I motion through a quiescent fluid. *Chem. Eng. Sci.* **22**, 637–651.

GU, Y. & LI, D. 2000 The ζ-potential of glass surface in contact with aqueous solutions. *J. Colloid Interface Sci.* **226**, 328–339.

HAIN, R., KÄHLER, C. J. & TROPEA, C. 2007 Comparison of CCD, CMOS and intensified cameras. *Exp. Fluids* **42**.

HARLEPP, S., ROBERT, J., DARNTON, N. C. & CHATENAY, D. 2004 Subnanometric measurements of evanescent wave penetration depth using total internal reflection microscopy combined with fluorescent correlation spectroscopy. *Appl. Phys. Lett.* **85**, 3917–3919.

HARRISON, D. J., FLURI, K., SEILER, K., FAN, Z., EFFENHAUSER, C. S. & MANZ, A. 1993 Micromachining a miniaturized capillary electrophoresis-based chemical analysis system on a chip. *Science* **261**, 895–897.

HARRISON, D. J., MANZ, A., FAN, Z., LÜDI, H. & WIDMER, H. M. 1992 Capillary electrophoresis and sample injection systems integrated on a planar glass chip. *Anal. Chem.* **64**, 1926–1932.

HAUGLAND, R. P. 2005 *The Handbook: A Guide to Fluorescent Probes and Labeling Technologies*, 10th edn. Invitrogen.

HEFTMANN, E. 1992 *Chromatography: Fundamentals and Applications of Chromatography and Related Differential Migration Methods, Part A: Fundamentals and Techniques*, 5th edn. Amsterdam: Elsevier.

Herr, A. E., Molho, J. I., Santiago, J. G., Mungal, M. G., Kenny, T. W. & Garguilo, M. G. 2000 Electroosmotic capillary flow with nonuniform zeta potential. *Anal. Chem.* **72**, 1053–1057.

Horiuchi, K. & Dutta, P. 2006 Electrokinetic flow control in microfluidic chips using a field-effect transistor. *Lab Chip* **6**, 714–723.

Hosokawa, K. & Maeda, R. 2001 In-line pressure monitoring for microfluidic devices using a deformable diffraction grating. In *Proc. 14th IEEE Int. Conf.*, pp. 174–177. IEEE, New York.

Huang, X., Gordon, M. J. & Zare, R. N. 1988 Current-monitoring method for measuring the electroosmotic flow rate in capillary zone electrophoresis. *Anal. Chem.* **60**, 1837–1838.

Hunter, R. J. 1981 *Zeta Potential in Colloid Science*. London: Academic Press.

Ichiyanagi, M., Sato, Y. & Hishida, K. 2005 Evaluation of electroosmotic velocity and zeta-potential in microchannel using submicron fluorescent particles. *Trans. JSME. Ser. B* **71** (709), 104–111.

Ichiyanagi, M., Sato, Y. & Hishida, K. 2007 Optically sliced measurement of velocity and pH distribution in microchannel. *Exp. Fluids* **43**, 425–435.

Inoué, S. & Spring, K. R. 1997 *Video Microscopy: The Fundamentals*, 2nd edn. New York: Plenum Press.

ISO 1995 *Guide to the Expression of Uncertainty in Measurement*, 2nd edn. International Organization for Standardization, Geneve.

Jacobson, S. C., Hergenröder, R., Koutny, L. B. & Ramsey, J. M. 1994 High-speed separations on a microchip. *Anal. Chem.* **66**, 1114–1118.

Jung, B., Bharadwaj, R. & Santiago, J. G. 2003 Thousandfold signal increase using field-amplified sample stacking for on-chip electrophoresis. *Electrophoresis* **24**, 3476–3483.

Kazoe, Y. & Sato, Y. 2006 Measurement of zeta-potential at microchannel wall by a nanoscale laser induced fluorescence imaging. *Trans. JSME. Ser. B* **72** (722), 127–134.

Kihm, K. D., Banerjee, A., Choi, C. K. & Takagi, T. 2004 Near-wall hindered Brownian diffusion of nanoparticles examined by three-dimensional ratiometric total internal reflection fluorescence microscopy (3-D R-TIRFM). *Exp. Fluids* **37**, 811–824.

KIM, M. J., BESKOK, A. & KIHM, K. D. 2002 Electro-osmosis-driven micro-channel flows: A comparative study of microscopic particle image velocimetry measurements and numerical simulations. *Exp. Fluids* **33**, 170–180.

KIRBY, B. J. & HASSELBRINK, JR., E. F. 2004*a* Zeta potential of microfluidic substrates: 1. theory, experimental techniques, and effects on separations. *Electrophoresis* **25**, 187–202.

KIRBY, B. J. & HASSELBRINK, JR., E. F. 2004*b* Zeta potential of microfluidic substrates: 2. data for polymers. *Electrophoresis* **25**, 203–213.

KRISHNAMOORTHY, S., FENG, J., HENRY, A. C., LOCASCIO, L. E., HICKMAN, J. J. & SUNDARAM, S. 2006 Simulation and experimental characterization of electroosmotic flow in surface modified channels. *Microfluid Nanofluid* **2**, 345–355.

KUMAR, A. & WHITESIDES, G. M. 1993 Features of gold having micrometer to centimeter dimensions can be formed through a combination of stamping with an elastomeric stamp and an alkanethiol ”Ink” followed by chemical etching. *Appl. Phys. Lett.* **63** (14), 2002–2004.

KUMAR, S. & BANERJEE, S. 1998 Development and application of a hierarchical system for digital particle image velocimetry to free-surface turbulence. *Phys. Fluids* **10**, 160–177.

LEE, D. W. & CHO, Y. H. 2007 A continuous electrical cell lysis device using a low dc voltage for a cell transport and rupture. *Sens. Act. B* **124**, 84–89.

LEE, G. B., FU, L. M., LIN, C. H., LEE, C. Y. & YANG, R. J. 2004 Dispersion control in microfluidic chips by localized zeta potential variation using the field effect. *Electrophoreis* **25**, 1879–1887.

LEE, J. N., PARK, C. & WHITESIDES, G. M. 2003 Solvent compatibility of poly(dimethylsiloxane)-based microfluidic devices. *Anal. Chem.* **75**, 6544–6554.

LEE, S., IBEY, B. L., COTÉ, G. L. & PISHKO, M. V. 2008 Measurement of pH and dissolved oxygen within cell culture media using a hydrogel microarray sensor. *Sens. Act. B* **128**, 388–398.

LEONG, J. C., TSAI, C. H., CHANG, C. L., LIN, C. F. & FU, L. M. 2007 Rapid microfluidic mixers utilizing dispersion effect and interactively time-pulsed injection. *Jpn. J. Appl. Phys.* **46**, 5345–5352.

LI, P. C. H. & HARRISON, D. J. 1997 Transport, manipulation, and reaction of biological cells on-chip using electrokinetic effects. *Anal. Chem.* **69**, 1564–1568.

Li, S. F. Y. 1992 *Capillary Electrophoresis: Principles, practice and applications*. Amsterdam: Elsevier.

Lide, D. R. 2007 *CRC Handbook of Chemistry and Physics*, 88th edn. Boca Raton, FL: CRC Press.

Lin, H., Storey, B. D., Oddy, M. H., Chen, C. H. & Santiago, J. G. 2004 Instability of electrokinetic microchannel flows with conductivity gradients. *Phys. Fluid* **16** (6), 1922–1935.

Liu, Y., Fanguy, J. C., Bledsoe, J. M. & Henry, C. S. 2000 Dynamic coating using polyelectrolyte multilayers for chemical control of electroosmotic flow in capillary electrophoresis microchips. *Anal. Chem.* **72**, 5939–5944.

López, G. P., Biebuyck, H. A., Frisbie, C. D. & Whitesides, G. M. 1993*a* Imaging on features on surfaces by condensation figures. *Science* **260**, 647–649.

López, G. P., Biebuyck, H. A. & Whitesides, G. M. 1993*b* Scanning electron microscopy can form images of patterns in self-assembled monolayers. *Langmuir* **9**, 1513–1516.

Lyklema, J. 1995 *Fundamentals of Interface and Colloid Science: Volume II Solid-Liquid Interfaces*. San Diego: Academic Press.

Lyklema, J. & Minor, M. 1998 On surface conductance and its role in electrokinetics. *Coll. Surf. A* **140**, 33–41.

Maoz, R., Sagiv, J., Degenhardt, D., Moöhwald, H. & Quint, P. 1995 Hydrogen-bonded multilayers of self-assembling silanes: Structure elucidation by combined Fourier transform infra-red spectroscopy and X-ray scattering techniques. *Supramol. Sci.* **2**, 9–24.

McDonald, J. C., Duffy, D. C., Anderson, J. R., Chiu, D. T., Wu, H., Schueller, O. J. A. & Whitesides, G. M. 2000 Fabrication of microfluidic systems in poly(dimethylsiloxane). *Electrophoresis* **21**, 27–40.

McDonald, J. C. & Whitesides, G. M. 2002 Poly(dimethylsiloxane) as a material for fabricating microfluidic devices. *Acc. Chem. Res.* **35** (7), 491–499.

McGovern, M. E., Kallury, K. M. R. & Thompson, M. 1994 Role of solvent on the silanization of glass with octadecyltrichlorosilane. *Langmuir* **10**, 3607–3614.

Meinhart, C. D., Wereley, S. T. & Gray, M. H. B. 2000*a* Volume illumination for two-dimensional particle image velocimetry. *Meas. Sci. Technol.* **11**, 809–814.

Meinhart, C. D., Wereley, S. T. & Santiago, J. G. 1999 PIV measurements of a microchannel flow. *Exp. Fluids* **27**, 414–419.

Meinhart, C. D., Wereley, S. T. & Santiago, J. G. 2000*b* A PIV algorithm for estimating time-averaged velocity fields. *J. Fluids Eng.* **122**, 285–289.

Minor, M., van der Linde, A. J., van Leeuwen H. P. & Lyklema, J. 1997 Dynamic aspects of electrophoresis and electroosmosis: A new fast method for measuring particle mobilities. *J. Colloid Interface Sci.* **189**, 370–375.

Miyakawa, S., Kazoe, Y. & Sato, Y. 2007 Simultaneous measurements of near-wall velocity and wall zeta-potential by evanescent wave illumination. In *Proc. μTAS 2007 Conf.*, pp. 1667–1669. Chemical and Biological Microsystems Society, Paris.

Moreau, W. M. 1988 *Semiconductor Lithography: Principles, Practices, and Materials*. New York: Plenum Press.

Mori, S. & Okamoto, H. 1980 A unified theory of determining the electrophoretic velocity of mineral particles in the rectangular micro-electrophoresis cell. *Fusen* **27**, 117–126.

Mosier, B. P., Molho, J. I. & Santiago, J. G. 2002 Photobleached-fluorescence imaging of microflows. *Exp. Fluids* **33**, 545–554.

Mrksich, M. & Whitesides, G. M. 1996 Using self-assembled monolayers to understand the interactions of man-made surfaces with proteins and cells. *Annu. Rev. Biophys. Biomol. Struct.* **25**, 55–78.

Munson, M. S., Cabrera, C. R. & Yager, P. 2002 Passive electrophoresis in microchannels using liquid junction potentials. *Electrophoresis* **23**, 2642–2652.

Nelstrop, L. J., Greenwood, P. A. & Greenway, G. M. 2001 An investigation of electroosmotic flow and pressure pumped luminol chemiluminescence detection for cobalt analysis in a miniaturized total analytical system. *Lab Chip* **1**, 138–142.

Ng, J. M. K., Gitlin, I., Stroock, A. D. & Whitesides, G. M. 2002 Components for integrated poly(dimethylsiloxane) microfluidic systems. *Electrophoresis* **23**, 3461–3473.

Ocvirk, G., Munroe, M., Tang, T., Oleschuk, R., Westra, K. & Harrison, D. J. 2000 Electrokinetic control of fluid flow in native poly(dimethylsiloxane) capillary electrophoresis devices. *Electrophoresis* **21**, 107–115.

Oddy, M. H. & Santiago, J. G. 2001 Electrokinetic instability mixing. *Anal. Chem.* **73**, 5822–5832.

Oddy, M. H. & Santiago, J. G. 2004 A method for determining electrophoretic and electroosmotic mobilities using AC and DC electric field particle displacements. *J. Colloid Interface Sci.* **269**, 192–204.

Ohmi, K. & Li, H. Y. 2000 Particle-tracking velocimetry with new algorithms. *Meas. Sci. Technol.* **11**, 603–616.

Oldham, I. B., Young, F. J. & Osterle, J. F. 1963 Streaming potential in small capillaries. *J. Colloid Sci.* **18**, 328–336.

O'Neal, D. P., Meledeo, M. A., Davis, J. R., Ibey, B. L., Gant, V. A., Pishko, M. V. & Coté, G. L. 2004 Oxygen sensor based on the fluorescence quenching of a ruthenium complex immobilized in a biocompatible poly(ethylene glycol) hydrogel. *IEEE Sens. J.* **4**, 728–734.

Osbourn, D. M., Weiss, D. J. & Lunte, C. E. 2000 On-line preconcentration methods for capillary electrophoresis. *Electrophoresis* **21**.

Pallandre, A., de Lambert, B., Attia, R., Jonas, A. M. & Viovy, J. L. 2006 Surface treatment and characterization: Perspectives to electrophoresis and lab-on-chips. *Electrophoresis* **27**, 584–610.

Park, H. M. & Lee, J. S. 2007 Estimation of inhomogeneous zeta potential using velocity measurements of EOF. *Electrophoresis* **28**, 1499–1507.

Park, H. M., Lee, J. S. & Kim, T. W. 2007 Comparison of the Nernst-Planck model and the Poisson-Boltzmann model for electroosmotic flows in microchannels. *J. Colloid Interface Sci.* **315**, 731–739.

Park, J., Huh, K. Y. & Li, X. 2006 Lattice Boltzmann simulation on the liquid junction potential in a microchannel. *J. Electroanal. Chem.* **591**, 141–148.

Pashley, R. M. & Karaman, M. E. 2004 *Applied Colloid and Surface Chemistry*. John Wiley & Sons.

Patankar, S. V. 1980 *Numerical Heat Transfer and Fluid Flow*. Washington: Hemisphere.

Paul, P. H., Garguilo, M. G. & Rakestraw, D. J. 1998 Imaging of pressure- and electrokinetically driven flows through open capillaries. *Anal. Chem.* **70**, 2459–2467.

Prieve, D. C. & Frej, N. A. 1990 Total internal reflection microscopy: A quantitative tool for the measurement of colloidal forces. *Langmuir* **6**, 396–403.

PROBSTEIN, R. F. 1994 *Physicochemical Hydrodynamics*, 2nd edn. New York: John Wiley & Sons.

QUIGLEY, W. W. C. & DOVICHI, N. J. 2004 Capillary electrophoresis for the analysis of biopolymers. *Anal. Chem.* **76**, 4645–4658.

REN, L. & LI, D. 2001 Electroosmotic flow in heterogeneous microchannels. *J. Colloid Interface Sci.* **243**, 255–261.

REN, X., BACHMAN, M., SIMS, C., LI, G. P. & ALLBRITTON, N. 2001 Electroosmotic properties of microfluidic channels composed of poly(dimethylsiloxane). *J. Chromatogr. B* **762**, 117–125.

REVIL, A., PEZARD, P. A. & GLOVER, P. W. J. 1999 Streaming potential in porous media 1. theory of the zeta potential. *J. Geophys. Res.* **104**, 20021–20031.

ROESGEN, T. & TOTARO, R. 1995 Two-dimensional on-line particle imaging velocimetry. *Exp. Fluids* **19**, 188–193.

ROSS, D., GAITAN, M. & LOCASCIO, L. E. 2001*a* Temperature measurement in microfluidic systems using a temperature-dependent fluorescent dye. *Anal. Chem.* **73**, 4117–4123.

ROSS, D., JOHNSON, T. J. & LOCASCIO, L. E. 2001*b* Imaging of electroosmotic flow in plastic microchannels. *Anal. Chem.* **73**, 2509–2515.

ROSS, D. & LOCASCIO, L. E. 2003 Effect of caged fluorescent dye on the electroosmotic mobility in microchannels. *Anal. Chem.* **75**, 1218–1220.

RUDINGER, G. 1980 *Fundamentals of Gas-Particle Flow*. Amsterdam: Elsevier.

SADR, R., LI, H. & YODA, M. 2005 Impact of hindered Brownian diffusion on the accuracy of particle-image velocimetry using evanescent-wave illumination. *Exp. Fluids* **38**, 90–98.

SADR, R., YODA, M., GNANAPRAKASAM, P. & CONLISK, A. T. 2006 Velocity measurements inside the diffuse electric double layer in electro-osmotic flow. *Appl. Phys. Lett.* **89**, 044103.

SADR, R., YODA, M., ZHENG, Z. & CONLISK, A. T. 2004 An experimental study of electro-osmotic flow in rectangular microchannels. *J. Fluid Mech.* **506**, 357–367.

SAKAKIBARA, J. & ADRIAN, R. J. 1999 Whole field measurement of temperature in water using two-color laser induced fluorescence. *Exp. Fluids* **26**, 7–15.

SANTIAGO, J. G. 2000 Electroosmotic flows in microchannels with finite inertial and pressure forces. *Anal. Chem.* **73**, 2353–2365.

Santiago, J. G., Wereley, S. T., Meinhart, C. D., Beebe, D. J. & Adrian, R. J. 1998 A particle image velocimetry system for microfluidics. *Exp. Fluids* **25**, 316–319.

Sasaki, S. & Sato, Y. 2006 Effect of surface modification on electroosmotic flow and zeta potential in microchannel. In *Proc. μTAS 2006 Conf.*, pp. 239–241. Society for Chemistry and Micro-Nano Systems, Tokyo.

Sato, Y., Inaba, S., Hishida, K. & Maeda, M. 2003*a* Spatially averaged time-resolved particle-tracking velocimetry in microspace considering Brownian motion of submicron fluorescent particles. *Exp. Fluids* **35**, 167–177.

Sato, Y., Irisawa, G., Ishizuka, M., Hishida, K. & Maeda, M. 2003*b* Visualization of convective mixing in microchannel by fluorescence imaging. *Meas. Sci. Technol.* **14**, 114–121.

Scales, P. J., Grieser, F., Healy, T. W., White, L. R. & Chan, D. Y. C. 1992 Electrokinetics of the silica-solution interface: A flat plate streaming potential study. *Langmuir* **8**, 965–974.

Schasfoort, R. B. M., Schlautmann, S., Hendrikse, J. & van den Berg, A. 1999 Field-effect flow control for microfabricated fluidic networks. *Science* **286**, 942–945.

Schreiber, F. 2000 Structure and growth of self-assembling monolayers. *Prog. Surf. Sci.* **65**, 151–256.

Seller, K., Fan, Z. H., Flurl, K. & Harrison, D. J. 1994 Electroosmotic pumping and valveless control of fluid flow within a manifold of capillaries on a glass chip. *Anal. Chem.* **66**, 3485–3491.

Shinohara, K., Sugii, Y., Hibara, A., Tokeshi, M., Kitamori, T. & Okamoto, K. 2005 Rapid proton diffusion in microfluidic devices by means of micro-LIF technique. *Exp. Fluids* **38**, 117–122.

Shinohara, K., Sugii, Y., Okamoto, K., Madarame, H., Hibara, A., Tokeshi, M. & Kitamori, T. 2004 Measurement of pH field of chemically reacting flow in microfluidic devices by laser-induced fluorescence. *Meas. Sci. Technol.* **15**, 955–960.

Sinton, D. 2004 Microscale flow visualization. *Microfluid Nanofluid* **1**, 2–21.

Sinton, D., Canseco, C. E., Ren, L. & Li, D. 2002 Direct and indirect electroosmotic flow velocity measurements in microchannels. *J. Colloid Interface Sci.* **254**, 184–189.

Sinton, D. & Li, D. 2003 Electroosmotic velocity profiles in microchannels. *Colloid Surf. A* **222**, 273–283.

Sniadecki, N. J., Lee, C. S., Sivanesan, P. & DeVoe, D. L. 2004 Induced pressure pumping in polymer microchannels via field-effect flow control. *Anal. Chem.* **76**, 1942–1947.

Spehar, A. M., Koster, S., Linder, V., Kulmala, S., de Rooij, N. F., Verpoorte, E., Sigrist, H. & Thormann, W. 2003 Electrokinetic characterization of poly(dimethylsiloxane) microchannels. *Electrophoresis* **24**, 3674–3678.

Stitou, A. & Riethmuller, M. L. 2001 Extension of PIV to super resolution using PTV. *Meas. Sci. Technol.* **12**, 1398–1403.

Stone, H. A., Stroock, A. D. & Ajdari, A. 2004 Engineering flows in small devices. *Annu. Rev. Fluid Mech.* **36**, 381–411.

Stroock, A. D., Weck, M., Chiu, D. T., Huck, W. T. S. & Kenis, P. J. A. 2000 Patterning electro-osmotic flow with patterned surface charge. *Phys. Rev. Lett.* **84** (15), 3314–3317.

Stroock, A. D. & Whitesides, G. M. 2003 Controlling flows in microchannels with patterned surface charge and topography. *Acc. Chem. Res.* **36**, 597–604.

Sun, Y., Lim, C. S., Liu, A. Q., Ayi, T. C. & Yap, P. H. 2007 Design, simulation and experiment of electroosmotic microfluidic chip for cell sorting. *Sens. Act. A* **133**, 340–348.

Sze, A., Erickson, D., Ren, L. & Li, D. 2003 Zeta-potential measurement using the Smoluchowski equation and the slope of the current-time relationship in electroosmotic flow. *J. Colloid Interface Sci.* **261**, 402–410.

Tay, F. E. H. 2002 *Microfluidics and BioMEMS Applications*. Boston: Kluwer Academic Publishers.

Taylor, J. A. & Yeung, E. S. 1993 Imaging of hydrodynamic and electrokinetic flow profiles in capillaries. *Anal. Chem.* **65**, 2926–2932.

Tripp, C. R., Veregin, R. P. N. & Hair, M. L. 1993 Effect of fluoroalkyl substituents on the reactions of alkylchlorosilanes with silica surfaces. *Langmuir* **9**, 3518–3522.

Tropea, C., Yarin, A. L. & Foss, J. F. 2007 *Springer Handbook of Experimental Fluid Mechanics*. Berlin: Springer.

Tsuda, T., Ikedo, M., Jones, G., Daddo, R. & Zare, R. N. 1993 Observation of flow profiles in electroosmosis in a rectangular capillary. *J. Chromatogr.* **632**, 201–207.

Valeur, B. 2002 *Molecular Fluorescence: Principles and Applications*. Weinheim: Wiley-VCH.

VILKNER, T., JANASEK, D. & MANZ, A. 2004 Micro total analysis systems. Recent developments. *Anal. Chem.* **76**, 3373–3386.

VAN WAGENEN, R. A., COLEMAN, D. L., KING, R. N., TRIOLO, P., BROSTROM, L., SMITH, L. M., GREGONIS, D. E. & ANRADE, J. D. 1981 Streaming potential investigations: Polymer thin films. *J. Colloid Interface Sci.* **84**, 155–161.

WALKER, D. A. 1987 A fluorescence technique for measurement of concentration in mixing liquids. *J. Phys. E: Sci. Instrum.* **20**, 217–224.

WALLDAL, C. 2001 Electrokinetic study of silica particles flocculated by two cationic polyelectrolytes; Sequential and simultaneous addition. *Colloid Surf. A* **194**, 111–121.

WANG, B., ABDULALI-KANJI, Z., DODWELL, E., HORTON, J. H. & OLESCHUK, R. D. 2003 Surface characterization using chemical force microscopy and the flow performance of modified polydimethylsiloxane for microfluidic device applications. *Electrophoresis* **24**, 1442–1450.

WANG, L., XU, W., BACHMAN, M., LI, G. P. & CHEN, Z. 2004*a* Imaging and quantifying of microflow by phase-resolved optical Doppler tomography. *Opt. Commu* **232**, 25–29.

WANG, L., XU, W., BACHMAN, M., LI, G. P. & CHEN, Z. 2004*b* Phase-resolved optical Doppler tomography for imaging flow dynamics in microfluidic channels. *Appl. Phys. Lett.* **85** (10), 1855–1857.

WASSERMAN, S. R., TAO, Y. T. & WHITESIDES, G. M. 1989 Structure and reactivity of alkylsiloxane monolayers formed by reaction of alkyltrichlorosilanes on silicon substrates. *Langmuir* **5**, 1074–1087.

WESTERWEEL, J. 1997 Fundamentals of digital particle image velocimetry. *Meas. Sci. Technol.* **8**, 1379–1392.

WHEELER, A. R., TRAPP, G., TRAPP, O. & ZARE, R. N. 2004 Electroosmotic flow in a poly(dimethylsiloxane) channel dose not depend on percent curing agent. *Electrophoresis* **25**, 1120–1124.

WHITE, F. M. 1986 *Fluid Mechanics*, 2nd edn. New York: McGraw-Hill.

WHITE, F. M. 2006 *Viscous Fluid Flow*, 3rd edn. New York: McGraw-Hill.

WHITESIDES, G. M., OSTUNI, E., TAKAYAMA, S., JIANG, X. & INGBER, D. E. 2001 Soft lithography in biology and biochemistry. *Annu. Rev. Biomed. Eng.* **3**, 335–373.

WILBUR, J. L., BIEBUYCK, H. A., MACDONALD, J. C. & WHITESIDES, G. M. 1995 Scanning force microscopies can image patterned self-assembled monolayers. *Langmuir* **11**, 825–831.

WILKES, J. O. 2006 *Fluid Mechanics for Chemical Engineers*, 2nd edn. Upper Saddle River, NJ: Prentice Hall Professional Technical Reference.

WU, C. H., CHEN, J. K. & YANG, R. J. 2007 Electrokinetically driven flow control using bare electrodes. *Microfluid Nanofluid* **3**, 485–494.

WU, H. Y. & LIU, C. H. 2005 A novel electrokinetic micromixer. *Sens. Act. A* **118**, 107–115.

XIA, Y. & WHITESIDES, G. M. 1998 Soft lithography. *Angew. Chem. Int. Ed.* **37**, 550–575.

YAN, D., NGUYEN, N. T., YANG, C. & HUANG, X. 2006 Visualizing the transient electroosmotic flow and measuring the zeta potential of microchannels with a micro-PIV technique. *J. Chem. Phys.* **124**, 021103.

YAN, D., YANG, C., NGUYEN, N. T. & HUANG, X. 2007 Diagnosis of transient electrokinetic flow in microfluidic channels. *Phys. Fluids* **19**, 017114.

YANG, M. C., OOI, K. T., WONG, T. N. & MASLIYAH, J. H. 2004 Frequency-dependent laminar electroosmotic flow in a closed-end rectangular microchannel. *J. Colloid Interface Sci.* **275**, 679–698.

YANG, X. M., TRYK, D. A., HASIMOTO, K. & FUJISHIMA, A. 1996 Surface enhanced Raman imaging of a patterned self-assembled monolayer formed by microcontact printing on a silver film. *Appl. Phys. Lett.* **69** (26), 4020–4022.

ZETTNER, C. M. & YODA, M. 2003 Particle velocity field measurements in a near-wall flow using evanescent wave illumination. *Exp. Fluids* **34**, 115–121.